Dark Matter Genesis

Russell Kirk

Department of Physics

Royal Holloway, University of London

A thesis submitted to the University of London for the

Degree of Doctor of Philosophy

Declaration

I confirm that the work presented in this thesis is my own. Where information has been derived from other sources, I confirm that this has been indicated in the document.

Russell Kirk

Abstract

There is abundant evidence pointing to an unseen component of the Universe comprising approximately 80% of its mass; this *dark matter* cannot be any known particle, and so demands new physics. Very little is known about dark matter, however from the cosmic microwave background, its abundance has been accurately measured. How this is produced then dictates the requirements placed on a theory of dark matter. Here four works [1–4] are described where theories of dark matter genesis are explored. The first mechanism considers an additional source of dark matter from decaying topological defects in the early Universe. Topological defects are massive structures formed during spontaneous symmetry breaking phase transitions, which evolve under their own tension and decay, possibly producing dark matter during freeze-out. This allows the annihilation cross-section to rise above what is required in standard freeze-out, as the losses in abundance it predicts, may be recuperated by the contributions from the decaying defects. Given this, the constraints standard freeze-out imposes on dark matter models can be loosen. This is illustrated by implementing the mechanism in an example theory, the Inert Doublet Model, where it opens up large swathes of parameter space and allows for lighter dark matter masses. Furthermore this mechanism is employed to resolve issues with dark matter interpretations of the galactic centre γ-ray excess seen by Fermi-LAT. The cross-section required to produce this signal is in tension with limits from searches in dwarf spheroidal satellite galaxies. Using this mechanism in a p-wave annihilating model of dark matter, this tension is avoided while producing the correct relic abundance of dark matter. Additionally we examine the direct detection signatures in upcoming detectors, DEAP-3600 and XENON1T, of nuclear dark matter: bound states of strongly-interacting dark nucleons, formed during a synthesis period in the early Universe. Scatterings of states in this model produce characteristic recoil spectra, which we find can be distinguished to $3\,\sigma$ confidence level from WIMP spectra with as few as ~ 24 events. Subsequently there is potential for discovery in the not too distant future.

Acknowledgements

First and foremost I would like to thank my supervisor Dr Stephen West for providing exceptional help, guidance and support throughout my studies, going above and beyond what was required. Many of the research staff in the particle physics group have also gone out of their way to help me during this time and I would like to thank them here: Dr Veronique Boisvert, Prof Glen Cowan, Mr Barry Green, Dr Nikolas Kauer, and Prof Pedro Teixeira-Dias. I would also like to thank all the staff in the Royal Holloway physics department for helping me along the way and cultivating a great environment in which to work.

The fellow students I've met during my time have made it highly enjoyable, so I would like to thank Ian, Claire, Joshuha, Will, Alistair, and lastly (and coincidently leastly) Graham. I would like to thank my parents, their unwavering support in the face of my sometimes unwavering stupidity has made me the man I am today. I would like to thank Ksenija and Nevenko, hvala za sve, for welcoming me into their lives. Forgiving his murderous tendencies, I am grateful for the support I received from Gojko, a jack-russell terrier. Good boy.

Lastly I would like to thank Sara for all her love and support, and for making sure I maintain at least the minimal cleanliness required for a civil society.

I like relativity and quantum theories
because I don't understand them
and they make me feel as if space shifted about
like a swan that can't settle,
refusing to sit still and be measured;
and as if the atom were an impulsive thing
always changing its mind.

Relativity

D. H. Lawrence

Contents

List of Figures **9**

List of Tables **16**

Prologue **18**

1 Dark Matter **21**

1.1 Origins and Evidence 22

1.1.1 Galaxy and Galaxy Cluster Rotation Curves 22

1.1.2 Gravitational Lensing and the Bullet Cluster 27

1.1.3 Cosmic Microwave Background Radiation 29

1.2 Genesis and Relic Density 35

1.2.1 Freeze-Out and the WIMP Miracle 35

1.2.2 Asymmetric Freeze-Out 43

1.2.3 Freeze-In 44

1.3 Candidates and Models 45

1.3.1 SUSY and the Neutralinos 46

1.3.2 Building Simple Models 49

1.4 Searches and Signals 50

1.4.1 Direct Detection 50

1.4.2 Indirect Detection 54

1.4.3 Collider Searches 56

1.4.4 Theoretical Bounds 58

2 Topological Defects **61**

2.1 Spontaneously Breaking a Symmetry 63

2.1.1 In the Abelian Higgs Model 64

2.1.2 In the Standard Model 66

2.2 Forming a Topological Defect 69

2.2.1 Homotopy Groups 72

2.3 Cosmic Strings 74

2.3.1 Gravitational Interactions 77

2.3.2 Condensates and Superconductivity 79

2.4 Cosmic String Evolution and Decay 81

2.4.1 Abelian Higgs Field Simulations 82

2.4.2 Nambu-Goto Strings 83

3 Dark Matter from Topological Defect Decays **85**

3.1 Top-Down Dark Matter Production from Topological Defects 86

3.1.1 Adding Defects to the Boltzmann Equation 87

3.2 Solving the Boltzmann Equation 89

3.2.1 Numerical Solutions 89

3.2.2 Analytic Solutions 93

3.3 Constraints 97

4 The Inert Doublet Model with Topological Defects **104**

4.1 The Inert Doublet Model 106

4.1.1 Theoretical Bounds and Electroweak Precision Tests 109

4.2 An Inert Doublet Model with a $U(1)'$ Gauge Symmetry 111

4.3 Increasing the Relic Abundance 114

4.4 Constraints 119

4.4.1 Bounds from Dark Matter Physics 119

4.4.2 Bounds from Cosmic String Physics 122

4.4.3 Results 124

4.5 Discussion 129

5 The Galactic Centre Excess with Topological Defects 131

5.1 The Galactic Centre Excess and dSph Limits 133

5.1.1 P-wave Annihilating Dark Matter 135

5.2 A Toy Model 137

5.2.1 Higgs Portal Couplings 138

5.3 Generating Cosmic Strings 139

5.4 Fitting and Constraining 140

5.4.1 Implications for Cosmic Strings 143

5.5 Discussions 144

6 Direct Detection Signatures of Nuclear Dark Matter 146

6.1 Nuclear Dark Matter Recoil Spectrum 149

6.2 Nuclear Dark Matter in Tonne-Scale Direct Detection Experiments 152

6.2.1 Energy Resolutions, Efficiencies and Energy Windows. 152

6.2.2 Example Recoil Spectra 153

6.2.3 Current and Projected Exclusion Limits 157

6.3 Identifying Nuclear Dark Matter 159

6.3.1 Discovery Potential 167

6.4 Discussions 168

Epilogue 171

Appendix A Particle Radiation from Cosmic Strings 176

A.1 FT Scenario 178

A.2 CE Scenario 178

Appendix B Pure Gauge Limit 181

Appendix C Cascade Annihilation Model: Higgs Mixing 184

List of Figures

1.1 The rotation curve of the galaxy NGC 6503. The measured contributions from luminous and gaseous matter is shown by the dashed and dotted lines respectively. The dot-dashed line is the predicted contribution from a DM halo. One can see that by summing all three contributions the predicted rotation curve (the solid line) matches the measured well. Taken from [12] and annotated with line labels. 24

1.2 An X-ray heat map image of the Bullet Cluster as seen by the Chandra X-ray Observatory overlaid with gravitational potential contours reconstructed from weak lensing measurements shown in green. Taken from [30]. 29

1.3 A full sky map of the anisotropies seen in the CMB by Planck [41], where K_{cmb} is the deviation from the mean temperature. 30

1.4 Angular Power Spectrum of the CMB as measured by Planck [17]. Here, $\mathcal{D}_l^{TT} = \frac{l(l+1)}{2\pi}\langle|a_{lm}|^2\rangle$. 32

1.5 A plot of Y_χ vs x illustrating how the yield evolves when a particle undergoes freeze-out with dominant s-wave annihilations, which highlights key moments in the thermal history. The yields for several σ_0 values were plotted (coloured lines), as well as $Y_{\chi,\text{eq}}$ (the black line). These were found by numerically solving (1.21) when $m_\chi = 500$ GeV. 39

1.6 A plot of yield against x illustrating DM production via freeze-in. It plots the yield in thermal equilibrium (black) and the freeze-in yield for various interaction strengths (colours), whose relative values are indicated within. . . 45

1.7 An illustrative plot of typical interaction cross-section σ_{int} against DM mass showing regions covered by a selection of popular DM models, taken from [78]. 46

1.8 Contributions to the Higgs boson's self-energy from fermion (left) and sfermion (right) loops. 47

1.9 A summary of SI WIMP scattering limits from past and future direct detection experiments, taken from [104]. Also shown are the neutrino background threshold (orange dashed line), fits to claimed signals (shaded regions with outlines), and the regions of where signals of various models are expected to be found (shaded regions without outlines). 53

1.10 Monojet 90% CL limits using 8 TeV LHC data on the DM-nucleon scattering cross-section against mass in the case of SI (left) and SD (right) interactions. This uses a simplified model of Dirac fermion DM with vector (SI) or axial-vector (SD) interactions taken from [152]. The blue lines represent limits for two choices of couplings in the simplified model, while the green line gives the limit when using an effective field theory approach. These limits are shown alongside those from LUX (red) [95]. 58

2.1 An illustration of the Abelian Higgs potential, taken from [165]. 65

2.2 An illustration showing the potential in a ϕ^4 theory (2.13) where ϕ is odd under a $\mathbb{Z}_2$ symmetry. The system here has two choices of VEV ($\langle\phi\rangle = \pm\eta$) into which it can fall. 70

2.3 Spatial configurations of post-symmetry breaking vacuum states in a theories predicting cosmic strings (left), shown in a 2D plane, and monopoles (right). The position on the vacuum manifold is represented by arrows, and the points of normal phase are the central dots. 71

2.4 An illustration of contractible and non-contractible loops in a vacuum manifold. The green shaded region represents the vacuum manifold, which contains a hole. Loops not enclosing this hole, such as the blue loop shown, are contractible (to a point). Otherwise if it encloses the loop, such as the red one shown, then it is non-contractible. 73

2.5 Radial string functions $f(\rho)$ and $P(\rho)$ from (2.22) in the case that $\beta = 1$ representing the cosmic string solutions to an Abelian Higgs model with a local U(1) symmetry. 76

2.6 An illustration of how the conical space around a cosmic string allows the gravitational lensing of light. A cylindrical space (represented in red) has a slice of angular width θ removed from it. The edges are then pushed together "stretching" the space and transforming the geodesic path of light (shown as blue lines) travelling nearby. 78

2.7 A diagram showing the mechanism for loop formation by the intersection of long strings. The top diagram shows formation through self-intersection, and the bottom shows formation from two different strings. 82

2.8 Illustrations of kinks and cusps on strings. 84

3.1 The yield of DM against $x = m_\chi/T$ from numerical evaluations of (3.4), which describes freeze-out with an additional source of DM from decaying topological defects. Each sub-figure is for one of the four different cases of (n, p) considered: $(0, 1)$ (a), $(1, 1)$ (b), $(0, 7/6)$ (c), and $(1, 7/6)$ (d). Plotted in each case are curves for when $q_X = 0$ (red), *i.e.* standard freeze-out, $q_X = 10^{-9}$ (purple), $q_X = 10^{-8}$ (blue), and $q_X = 10^{-7}$ (green). Also shown is the thermal equilibrium curve (black). In all cases, $m_\chi = 500$ GeV, $r_\chi = 0.5$, and σ_0 was chosen such that one obtains the observed relic abundance [17] in standard freeze-out; this is 2.0×10^{-26} cm^3 s^{-1} for dominant s-wave annihilations and 9.9×10^{-25} cm^3 s^{-1} for p-wave. 90

3.2 Contours of constant yield in (σ_0, q_X) space showing the required values in order to produce 1σ either side of the observed abundance of DM [17]. Four cases are considered: $(0, 1)$ (purple), $(1, 1)$ (blue), $(0, 7/6)$ (red), and $(1, 7/6)$ (black). 91

3.3 Contours of constant DM yield in (σ_0, q_X) space, fixed to the the observed abundance [17]. Shown are contours derived by three means: numerical analysis (red), using (3.9), an approximate analytic solution (dashed blue), and using (3.10), the analytic solution in the high AB limit (dotted blue). This is in the $(1, 1)$ scenario, where the disagreement between numerical and analytic results is maximal. 95

3.4 Contours of constant $(x_{\rm d}/x_{\rm fr})\%$ in (σ_0, q_X) space alongside those of constant yield set to 1σ either side of the observed abundance [17]. The point of departure, $x_{\rm d}$, was found using the recursive analytic approximation (3.14) and the yield contours were plotted using the approximate analytic solution (3.9). This was for the $(0, 1)$ scenario, chosen as an illustrating example. 97

3.5 Plots of (σ_0, q_X) space constrained by unitarity (blue dotted) and Fermi-LAT (red dashed) bounds in four cases of (n, p); $(0, 1)$ (a), $(1, 1)$ (b), $(0, 7/6)$ (c), and $(1, 7/6)$ (d). The double black lines are contours of constant yield set to 1σ either side of the observed relic abundance [17], which were applied using the approximate analytic solution (3.9). The Fermi-LAT bound is from a combined analysis of several dSphs [228] and assumes dominant annihilations into W bosons. The unitarity bound (3.16) was taken from [154]. 99

4.1 Plots of the predicted relic abundance against m_{H^0} in the FT scenario for four different benchmark points of $(\Delta m^2, \lambda_L)$; (1000 GeV^2, 0) (a), (10000 GeV^2, 0) (b), (1000 GeV^2, 0.1) (c), and (10000 GeV^2, 0.1) (d). Each plot shows the predicted relic abundance for the IDM with topological defects for various values of q_0, as well as for standard freeze-out. The horizontal dotted line is the observed relic abundance [17]. 117

4.2 Plots of the predicted relic abundance against m_{H^0} in the CE scenario for four different benchmark points of $(\Delta m^2, \lambda_L)$; (1000 GeV^2, 0) (a), (10000 GeV^2, 0) (b), (1000 GeV^2, 0.1) (c), and (10000 GeV^2, 0.1) (d). Each plot shows the predicted relic abundance for the IDM with topological defects for various values of q_0, as well as for standard freeze-out. The horizontal dotted line is the observed relic abundance [17]. 118

4.3 Plots of the q_0 values which generate the measured relic density, against m_{H^0} in the FT (a) and CE (b) scenarios. In each plot four benchmark cases of (Δm^2, λ_L) are shown; (1000 GeV^2, 0) (green), (1000 GeV^2, 0.1) (black), (10000 GeV^2, 0) (purple), and (10000 GeV^2, 0.1) (red). In the FT plot, the gray shaded region represents DGRB bounds and in the CE plot it represents BBN bounds. Where the lines are dashed and dot dashed, are where they are ruled out by Fermi-LAT limits from dSphs [130] and LUX limits [95] respectively. The regions where the lines are dotted or solid are ruled out by both or neither respectively. 125

4.4 Plots in (m_{H^0}, λ_L) space for $\Delta m^2 = 1000$ GeV^2 (left) and $\Delta m^2 = 10000$ GeV^2 (right) in the FT (top) and CE (bottom) scenarios. The shaded regions show 90% CL limits from LUX (shaded green) and 95% CL limits from Fermi-LAT (shaded blue). Contours of constant yield set to the measured abundance for different values of $-\log_{10}[q_0]$ are shown in red, along with that in the case of standard freeze-out, seen in gray. When the contours become dotted, they are no longer consistent with DGRB and BBN bounds. The blue contour shows when the required q_0 value hits one of these cosmic string bounds, *i.e.* DGRB in the FT scenario and BBN in the CE scenario. 128

4.5 Plots in (m_{H^0}, Δm^2) space for $\lambda_L = 0$ (left) and $\lambda_L = 0.1$ (right) in the FT (top) and CE (bottom) scenarios. The shaded regions show 90% CL limits from LUX (shaded green) and 95% CL limits from Fermi-LAT (shaded blue). Contours of constant yield set to the measured abundance for different values of $-\log_{10}[q_0]$ are shown in red, along with that in the case of standard freeze-out, seen in gray. When the contours become dotted, they are no longer consistent with DGRB and BBN bounds. The blue contour shows when the required q_0 value hits one of these cosmic string bounds, *i.e.* DGRB in the FT scenario and BBN in the CE scenario. 130

5.1 A fit of $(m_\chi,\langle\sigma v\rangle)$ space via a χ^2 analysis of GCE data [265] to a model of DM with dominant s-wave annihilations, assuming $\bar{b}b$ final states only. The cross shows the point of best fit, while the red bold, dashed, and dotted lines are contours highlighting $1\,\sigma$, $2\,\sigma$, and $3\,\sigma$ significance. Also shown are the thermal values of $\langle\sigma v\rangle$ required to produce the observed relic abundance according to standard freeze-out [17] (dashed gray), and the Fermi-LAT 95% limits from dSphs [131] (blue). 135

5.2 A fit of $(m_\chi,\ \sigma_0)$ space via a χ^2 analysis of GCE data [265] to a cascade annihilation model of DM where $\bar{\chi}\chi \to \phi\phi \to \bar{b}b\bar{b}b$ for $m_\phi = 15$ GeV (green) and 40 GeV (red). The crosses show the points of best fit, while the bold, dashed, and dotted lines represent the $1\,\sigma$, $2\,\sigma$, and $3\,\sigma$ CL contours respectively. Also shown are the Fermi-LAT 95% CL limits from dSphs [131] (blue) and the Virgo Cluster [294] (purple). Contours along which the correct relic abundance is generated are plotted for various values of $-\log_{10}[q_X]$ (gray dashed lines) in the FT scenario. 141

6.1 (a): Comparison of the recoil energy spectra for NDM along with that of a 100 GeV WIMP for DEAP-3600. Spectra are plotted for three different k values: 10^3 (red), 10^4 (blue), and $k^{\rm D}_{\rm max} = 6.5 \times 10^6$ (purple). (b): Comparison of the recoil energy spectra for NDM along with that of a 100 GeV WIMP for XENON1T. Spectra are plotted for three different k values: 10^3 (red), 10^4 (blue), and $k^{\rm X}_{\rm max} = 5.8 \times 10^5$ (green). The bold and dashed lines represent the spectra with and without the finite energy resolution taken into account for each experiment using the experimental parameters in (6.10) and (6.11) for DEAP-3600 and XENON1T respectively. In the NDM cases we have set $R_1 = 1$ fm and $m_1 = 1$ GeV. Vertical dashed lines represent the limits of the energy windows of the two experiments. The WIMP-SM nucleon scattering cross-section was fixed to be 10^{-46} cm^2 and the NDM cross-sections were scaled such that the integrated rates were equal to that of the WIMP across the energy window of each experiment. 155

6.2 Projected limits at 90% CL for σ_0, the DN-SM nucleon scattering cross-section (in bold), against the DM mass for DEAP-3600 (blue) [98] and XENON1T (green) [96], and compared with the strongest current limits from LUX (red) [316]. Also shown are the WIMP limits in the same detectors (dashed lines). For the NDM limits we have taken $m_1 = 1$ GeV and $R_1 = 1$ fm. 158

6.3 (a): The CL up to $N_{\rm obs} = 92$ for $k = 10^4$ ($m_1 = 1\,\text{GeV}$) compared to a 53.2 GeV WIMP (which gives the most indistinguishable spectrum. 10^5 pseudo-experiments were used to generate the $g(\lambda|N_{\rm obs})$ distribution for each $N_{\rm obs}$. (b): A subset of $N_{\rm obs}$ values, function (6.19) was fit to these points, shown as the solid line. 161

6.4 Example NDM spectra (black) reconstructed in DEAP-3600 along with the most indistinguishable WIMP spectra (red) resulting in the number of events shown in Figure 6.5. Inset into each plot are the k values, the mass of the best fitting WIMP ($m_{\rm WIMP}$), and the number of events required to distinguish the spectra to a 3 σ confidence level. This is plotted across the energy window, where the total rate integrated over the window is equal for both WIMP and NDM. 162

6.5 The number of events required to distinguish between values of k and all WIMP masses to the stated confidence level in DEAP-3600 (above) and XENON1T (below). Here the confidence level given by (6.19) is shown by the colour scale with 1, 2, and 3 σ shown as dot-dashed, dashed, and solid lines respectively. 163

6.6 The maximum number of events that could be seen at DEAP-3600 (above) and XENON1T (below) against DM mass for NDM (red) and WIMPs (blue), plotted alongside the 1,2, & 3σ CL lines (the dotdashed, dashed, and bold lines respectively) for distinction as seen in Figure 6.5. 166

B.1 Feynman diagrams for $H^0H^0 \to W^+W^-$ (a) and $H^0H^0 \to ZZ$ (b) processes which dominate the annihilation cross-section in the early Universe in the high mass region $m_{H^0} > 100$ GeV. 182

List of Tables

2.1 A list of conditions on the homotopy groups of the vacuum manifold $\pi_n(\mathcal{M})$, in order for defects of the listed types to form. 74

3.1 Limits on q_X in four different (n, p) scenarios. The second column gives the values required to produce the measured relic abundance, using (3.12), where $\sigma_0^{23} = \sigma_0/10^{-23}$ cm^3 s^{-1}. The third and fourth columns are limits from unitarity and Fermi-LAT respectively. 100

3.2 Limits on the string tension parameter, $G\mu$, in four different (n, p) scenarios. The second column gives the values required to produce the measured relic abundance, while the third and fourth are limits from unitarity and Fermi-LAT respectively. These are translated from the q_X values presented in Table 3.1, using the relations (A.8) and (A.21). $P_{\rm FT}$ and $P_{\rm CE}$ are order unity parameters, which are defined in Appendix A. 101

4.1 A table listing the possible mass ranges and maximum q_0 values allowed in an IDM in which cosmic strings arise. These are given for FT and CE scenarios for the four benchmark values of (Δm^2, λ_L). The second column lists the range of m_{H^0} values consistent with all experimental bounds, in which the observed relic density may be produced. The third column lists the maximum q_0 allowed in each of the cases, beyond this value q_0 is ruled out by either BBN or DGRB bounds, or requires $\langle\sigma v\rangle$ to be an unacceptably large value (*i.e.* conflicts with direct or indirection bounds) in order produce the observed relic density. . . . 126

4.2 A table listing the maximum allowed values of $G\mu$ in the four benchmark (Δm^2, λ_L) points in the FT and CE scenarios. These were translated from the q_0 values seen in Table 4.1 using the same formulae for q_X in (A.8) and (A.21), although now $P_{\rm FT}$ and $P_{\rm CE}$ are defined differently, as shown in (4.43) and (4.44) respectively. Both parameters are still $\mathcal{O}(1)$. 127

5.1 Values of q_X required to produce the observed relic abundance of DM [17] when the annihilation cross-section is fitted to the GCE signal, as seen in Figure 5.2. This is for $m_\chi = 15$ and 40 GeV, and is found for both the FT and CE scenarios. 143

C.1 Limits on $\sin\theta$, the mixing between the mediator ϕ, and the SM Higgs boson h. These take $\lambda_\chi = 4.1$ and 5.1 for $m_\chi = 15$ and 40 GeV respectively, provided by fits to the GCE. Bounds from direct detection, monojet searches, direct searches for ϕ, invisible Higgs decays, and BBN are listed. See the text for a discussion of these limits and references there within. 186

Prologue

> For the moment we might very well can them DUNNOS (for Dark Unknown Nonreflective Nondetectable Objects Somewhere).
>
> — Bill Bryson

This thesis details the original work in four papers produced as part of my PhD research [1–4]. These are all related at least in part to atypical models of dark matter production in the early Universe, which is the core theme of this thesis. We start by dedicating Chapter 1 to reviewing dark matter physics — studying the evidence, production mechanisms, phenomenology, and popular models. Within this chapter we explore the motivation for dark matter to be a beyond the standard model particle, and discuss the ways it can be produced in the early Universe; detailing freeze-out, the oft assumed production mechanism. This places restrictions on some models, which can be relieved if an alternative mechanism is considered. Furthermore, this chapter will briefly discuss arguably the most popular dark matter candidate, the neutralino, in context in supersymmetric models. This is followed by a section on model building using effective field theories and simplified models. Concluding this chapter, we shall take a look at the status of dark matter searches in direct and indirect detection, and collider experiments.

Topological defects play a crucial role in the works described here and comprise a large part of the discussion, as such Chapter 2 provides a review of the subject, which begins with a summary of symmetry breaking and the Higgs mechanism. We will also discuss defect formation during these phase transitions and how the vacuum manifold's topology dictates the type of defect arising. Proceeding this, the focus shifts onto cosmic strings, a particular type of defect, as they are of greater significance to our research. The evolution and decay of cosmic strings is then examined, along with the condensates that form upon them.

The next four chapters detail each piece of research in turn. Chapter 3 will examine an alternative production mechanism of dark matter presented in [1], which used decaying defects as a source of dark matter. The Boltzmann equation governing the evolution of the dark matter yield in this scenario is derived and numerically analysed in order to study the mechanism. Approximate analytic solutions to this equation are also presented in this chapter. Lastly, constraints on the mechanism will be explored in a model-independent fashion, and how these then limit the cosmic strings is discussed.

Chapter 4 studies how this mechanism may be realised in an example dark matter theory: the Inert Doublet Model. After first reviewing the model, cosmic strings are then implemented into it by adding a scalar field charged under an additional local $\mathrm{U}(1)'$ symmetry. The strings form during the spontaneous breaking of this symmetry by the scalar field, and the remnant particle model is studied. Relevant experimental bounds from both dark matter and cosmic string physics are then reviewed and applied to the model. We subsequently examine in what regions of parameter space the correct relic abundance of dark matter can be produced, while not conflicting with phenomenological limits. The work presented here is from [2].

In a second example of how the defect mechanism may be utilised, the work of [3] is discussed in Chapter 5. Here the mechanism is used to deal with issues facing dark matter interpretations of the galactic centre excess. First outlining the nature of the excess and how dark matter can accommodate it, we then discuss its tension with searches in dwarf spheroidal galaxies. Following on from this, it will be shown how a model with p-wave dominant dark matter annihilation avoids this tension, but requires an annihilation cross-section too large to produce the correct abundance according to standard freeze-out. The defect mechanism is then used to resolve this new issue, and we build a toy model in which cosmic strings can arise and the dark matter candidate has dominant p-wave annihilations. We then consider the experimental constraints on this model and the consequences for cosmic string physics.

Finally Chapter 6 considers the direct detection phenomenology of nuclear dark matter, a composite model of dark matter, which was the subject of [4]. Nuclear dark matter is built on the ideas of standard model nuclear physics, *i.e.* it assumes dark matter consists of strongly-interacting bound states of dark nucleons, and is reviewed here. We will then study its signatures in two upcoming tonne-scale detectors, DEAP-3600 and XENON1T, by first examining the recoil spectra. Proceeding this, the projected limits on the scattering

cross-section will be found and compared to the existing limits from LUX. Using likelihood tests, the number of events required to distinguish nuclear dark matter recoils from those of a WIMP will also be found. Concluding this chapter, we comment on the chances for nuclear dark matter to be discovered by these detectors.

Chapter 1

Dark Matter

> If this would be confirmed we would get the surprising result that dark matter is present in much greater amounts than luminous matter.
>
> — Fritz Zwicky

It is now widely believed that the Universe contains a significant abundance of new undetected particles called *dark matter* (DM), whose existence is essential to form the Universe as we know it. The evidence so far suggests it is massive, interacts gravitationally and does not scatter light (and is thus dark), but very little else is known; its spin, mass, and couplings have yet to be measured. Huge numbers of beyond the standard model (BSM) theories containing DM candidates have been suggested and studied, and each year more and more are presented. While there is much not known about DM, a lot is known about what it is not; a variety of experiments are searching (and have searched) for DM and many more are planned which allow us to constrain DM theories, and have even provided a number of possible signals.

This chapter will deliver a brief review of DM physics — the motivation, theories, and phenomenology, with an aim to create a foundation of knowledge from which one could delve deeper into this vast subject. In Section 1.1 the evidence for DM is discussed, alongside alternate theories which may also give rise to some of the observations, but are in tension with others. Proceeding this, Section 1.2 reviews a selection of mechanisms through which DM could have been produced, and considers the implications on the relic density. Section 1.3 takes a look at DM models, focusing on arguably the most popular candidate, the neutralino,

and discusses model building using effective field theories and simplified models. Lastly, Section 1.4 looks at DM searches and signals in direct detection, indirect detection, and collider studies, while also considering theoretical limits.

1.1 Origins and Evidence

The well established pieces of evidence for DM all originate from the collective gravitational effects of a large body of DM, which can manifest in the rotation curves of galaxies and galaxy clusters, measurements of gravitational lensing, and in the structure and formation of the Universe. Here each piece of evidence is reviewed in approximate chronological order allowing one to follow a line of reasoning, so that the motivation for DM can be clear.

1.1.1 Galaxy and Galaxy Cluster Rotation Curves

A galaxy is a celestial body primarily made up of stars, dust, and gas (and DM, we will later assume), with a supermassive black hole thought to be at the centre. These can be part of larger gravitationally bound systems called *groups* and *clusters*, which typically contain $\mathcal{O}(10)$ and $\mathcal{O}(10^2\text{-}10^3)$ galaxies respectively. Clusters and groups can then be part of superclusters, which are amongst the largest systems in the observable universe. Superclusters and smaller systems are not uniformly spread out, but rather are part of a network of filaments (vast chains of galaxies) and walls with voids in between. With any gravitationally bound system, the mean rotation velocity $v(r)$ of its components as a function of distance to the centre r may be estimated by considering the balancing of gravitational and centrifugal forces. Doing so one finds

$$v(r) = \sqrt{\frac{GM(r)}{r}}, \tag{1.1}$$

where $G = 6.674 \times 10^{-11}$ m^3 kg^{-1} s^{-2} is the gravitational constant and $M(r)$ is the mass contained within a sphere of radius r around the gravitational centre of the system. Crudely modelling the luminous matter in a system as a hard shell core of uniform density, we then expect the mean rotational velocity to be proportional to r inside the core and to drop as $r^{-1/2}$ outside. Any significant deviations from this behaviour suggests that either our understanding of gravity is wrong, or our ideas on the composition of galaxies and systems thereof are incomplete.

Arguably, the first evidence for DM came in around 1933[1] when Fritz Zwicky used measurements from the 100-inch telescope at the Mount Wilson Observatory to infer the total mass of the Coma cluster, then compared the result to the total luminous matter (estimated from the number of nebulae). The total mass of the cluster was determined from the rotational velocity of the orbiting galaxies, which in turn was inferred from the redshift of their spectral features, *i.e.* the H, K, and G-band Fraunhofer lines. It was found that the total mass was $\sim$ 400 times larger [9] than the luminous prompting the response quoted at the beginning of this chapter.

The next major step came in 1970 when Rubin & Ford measured the rotation curve of the Andromeda (M31) galaxy [10] using the so-called 21cm or HI line; a spectral line created by the decay of excited hydrogen atoms in the interstellar medium (ISM). This provided convincing evidence for a flat curve outside the core of the galaxy, and thus a deviation from the $r^{-1/2}$ behaviour expected from the luminous matter. More ambiguous results had been found earlier, *e.g.* in 1939 Babcock [11] measured Andromeda's rotation curve and saw it to be constantly rising, although he had too few measurements outside the core to firmly establish its shape.

In order for DM to give rise to the observed flatness in the rotation curve, it must be distributed approximately as a large halo centred on the core, but extending out much further than it. This is illustrated in Figure 1.1, where an example measured rotation curve is shown to be in good agreement with a model combining the luminous and gaseous matter with such a DM halo. This plot is not Rubin & Ford's own results, but rather taken from later work by Begeman, Broeils & Sanders on the NGC 6503 galaxy [12]. For simplicity and in keeping with the theme, our discussions thus far have assumed DM as the source of the discrepancies in rotation curves, however it is just one possible explanation.

Alternative Explanations: MACHOs

Taking a broader view, the postulated missing mass in these bodies needs not be a new BSM particle (DM); it is only required that the matter be non-luminous. Astronomical objects

[1] While Zwicky is often credited with providing the first evidence, in the preceding decades others [5–8] were working on comparing the total mass to the luminous mass of galaxies and galaxy clusters with varied results and conclusions. For example, in 1922 Jeans found from the motions of stars in the Milky Way, that two "dark" stars would be needed for every luminous one in the vicinity of the galactic plane.

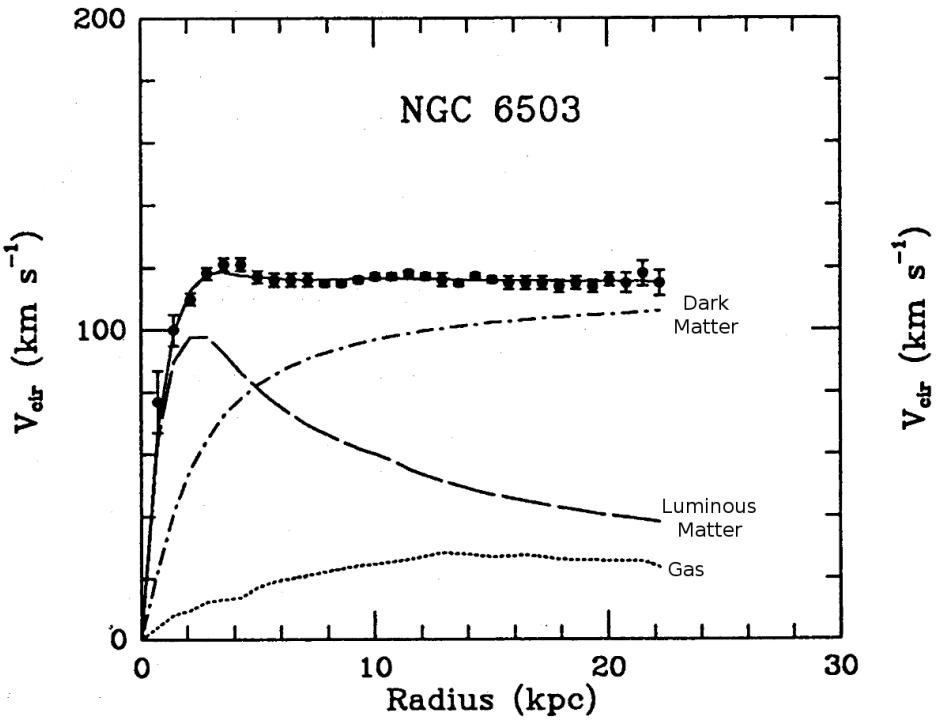

Figure 1.1: The rotation curve of the galaxy NGC 6503. The measured contributions from luminous and gaseous matter is shown by the dashed and dotted lines respectively. The dot-dashed line is the predicted contribution from a DM halo. One can see that by summing all three contributions the predicted rotation curve (the solid line) matches the measured well. Taken from [12] and annotated with line labels.

emitting little to no light, such as brown dwarfs, neutron stars, and black holes are all large baryonic structures and could provide the required mass, these are referred to as Massive Compact Halo Objects (MACHOs[1]).

Alternative Explanations: SM Neutrinos

Alternatively SM neutrinos (being neutral particles) could also provide the missing mass. The three neutrinos in the SM are massless by definition, however observations of neutrino oscillations tell us this is not so. Tritium decay experiments give us a direct measurement of the electron-neutrino mass, limiting it to be $\lesssim 1$ eV [13]. While direct limits on the

[1]The name was chosen to contrast with WIMPs, one of the main candidates for non-baryonic DM. These will be discussed later in Section 1.2.1.

muon- and tau-neutrino masses are significantly greater (around the MeV scale [14, 15]), measurements on the mass splitting from observations of neutrino oscillations indicate much smaller values. From a global fit of neutrino oscillation data [16], we have best fit values of $\Delta m^2_{21} = 7.37 \times 10^{-5}$ eV^2 and $|\Delta m^2_{32}| \approx 2.5 \times 10^{-3}$ eV^2. Furthermore, there are limits on the summed masses coming from the cosmic microwave background (discussed later in Section 1.1.3), which mean $\sum m_\nu \leq 0.57$ eV [17]. Given all this, we expect these three generations of neutrinos to be very light and assuming they were produced thermally in the early Universe, would have been relativistic during freeze-out (this production mechanism will be discussed in greater detail in Section 1.2). This is an example of a Hot Dark Matter (HDM) candidate. In this case, the number density per comoving volume is constant, and the relic abundance only depends upon the mass, requiring the DM candidate to be ~ 9 eV to produce the measured amount. Such a neutrino mass value is in slight tension with neutrino mass limits, but more importantly we will see in Section 1.1.3 that HDM candidates pose serious challenges for structure formation.

One might instead consider a fourth generation of neutrino that is sufficiently heavy to be non-relativistic during freeze-out (*i.e.* a cold dark matter (CDM) candidate). Limits on the summed masses from the cosmic microwave background, discussed above, assumed three light neutrino species, thus the presence of a fourth much heavier state will not be constrained by this bound. Similarly measurements of the Z boson decay width indicating three families of neutrinos [18], are blind to additional states of greater mass than half that of the Z boson, as these final states will be kinematically inaccessible.

In the case of CDM, the number density per comoving volume is not constant, and the relic abundance predicted by freeze-out, depends on both the candidates mass and couplings. Taking the fourth generations' couplings to be the same as the first three, its mass needs to be ~ 6 GeV in order to produce the measured abundance (known as the Lee-Weinberg bound [19]). This would be in tension with the Z decay width measurements mentioned above. Given this, SM neutrinos as DM candidates are often disfavoured. However sterile neutrinos, BSM states which are not charged under any SM gauge group, are possible DM candidates. They can also explain SM neutrino masses via the see-saw mechanism, and can even explain the baryon asymmetry via leptogenesis.

Alternative Explanations: MOND

As suggested earlier, discrepancies in velocity rotation curves could also arise when the gravitational interactions are no longer well described by Newtonian gravity. The theory of MOdified Newtonian Dynamics (MOND) is in keeping with this notion, and was suggested by Milgrom [20, 21] as an alternative to DM.

As an ad hoc first attempt to resolve discrepancies in the velocity rotation curves of galaxies, cluster, and other such systems, one might wish to consider an alternate theory of gravity above some critical length scale. Doing so would explain why gravitational forces are Newtonian-like in our solar system, but differ with larger systems like the Coma cluster. Such a theory would suggest bigger discrepancies in larger systems, however significant deviations from Newtonian gravity have been observed in small systems like dwarf galaxies, and haven't been observed in large systems such as spiral galaxies [22]. MOND avoids this issue by recognising discrepancies within systems tend to arise for those with accelerations lower than $\sim 10^{-8}$ cm s^{-2}. MOND was actually defined by Milgrom in two ways. The first viewed it as a modification to inertia, where the force on a particle is not proportional to its acceleration, but rather a function of it. That is

$$\vec{F} = m\vec{a}\mu(|\vec{a}|/a_0), \tag{1.2}$$

where m is the particles mass, a is its acceleration, a_0 is new parameter dictating the crossover between regimes, and μ is a function with the behaviour: $\mu(x) \approx 1$ for $x \gg 1$ and $\mu(x) \approx x$ for $x \ll 1$.

The second interpretation of MOND takes these effects only to be relevant for gravitational interactions, in which case the true gravitational acceleration, $\vec{g}$, is related to the Newtonian gravitational acceleration $\vec{g}_n$ via

$$\vec{g}\mu(|\vec{g}|/a_0) = \vec{g}_n. \tag{1.3}$$

In either case, the flattening of velocity rotation curves is predicted when the acceleration is sufficiently low ($a \ll a_0$).

In the coming sections further observations are discussed which poise difficulties for MOND, SM neutrinos and MACHOs, but give further credence to the existence of DM. For a more detailed historical review of rotation curves, see [23, 24].

1.1.2 Gravitational Lensing and the Bullet Cluster

In 1916 Einstein [25] found a way to represent gravity using the geometry of spacetime, which would become "bent" around massive objects, a theory known as general relativity. A major consequence of this theory was that light (a massless particle) was expected to also feel the effects of gravity and thus be attracted to massive objects, giving rise to a phenomenon known as *gravitational lensing*. This occurs when light from a source is bent around a massive object, such as a galaxy and reaches an observer creating a translated and distorted image of the source, akin to an optical lens. This phenomenon was confirmed shortly after in 1919 when Dyson, Davidson & Eddington [26] observed the gravitational lensing of stars passing close to the sun (which was undergoing a total eclipse).

Gravitational lensing is typically categorised into three different types:

- Strong lensing: The most extreme form of lensing which typically results in the formation of multiple images of the source, or the source being distorted into arcs or circular images called Einstein rings. Here the lens is usually a galaxy or a cluster, with the source relatively close to it, and the distortions are easily visible.

- Weak lensing: In this case, the lensing is only strong enough to magnify and stretch images. Since it is hard to know the shape and size of single sources, the strength and nature of the weak lens is difficult to gauge. However by using a collection of sources and their averaged properties, more information about the lens may be found. For example the lensing of a cluster may be found by using the galaxies behind it as sources.

- Microlensing: Distortions in the image here are too small to be detected, but image may appear brighter. By measuring a source's brightness with time, one can track the appearance of a lens.

Measuring gravitational lensing effects allows us to infer the total mass of a system, which can then be compared to the luminous mass to find the abundance of non-luminous matter. The Sloan Digital Sky Survey started measuring the weak lensing around 1.6 million objects in 2000 [27] and has since found DM dominating in galaxies. Gravitational lensing effects have two other important consequences for DM: they can be used in MACHO searches, and in tests of MOND. In 1986 Paczyński suggested a novel way in which MACHOs can be detected using

microlensing events [28]; passing close to our line-of-sight with a distant star, they cause a time-symmetric rise and fall in the star's apparent magnitude. From the peak brightness and duration of the microlensing event, the mass and velocity of the MACHO may be inferred.

Two collaborations, MACHO and EROS, have both looked for microlensing events in order to limit MACHO content. In 2000 results from a 5.7 year study by the MACHO collaboration were published, which looked for microlensing events in 11.9 million stars in the Large Magellanic Cloud (LMC), a satellite galaxy of the Milky Way [29]. The study of microlensing events is best done using large numbers of stars, which are far away enough to allow as many MACHOs as possible to pass in front of them; making the LMC an excellent probe. A total of 13-17 microlensing events were seen, while this was larger than expected from the known stellar content, it still rules out to a 95% confidence level (CL) the possibility of the dark halo being entirely comprised of MACHOs. Interestingly their maximum likelihood analysis suggests MACHOs could comprise around 20% of the LMC's missing matter, however this depends on the dark halo model.

The EROS collaboration published the final results of the EROS-2 survey in 2006, studying 33 million stars in the LMC and the Small Magellanic Cloud (SMC). Using a subsample of bright stars from their results they found only a single microlensing event, where ~ 39 would have been expected for a dark halo comprised entirely of typical MACHOs.

To differentiate between the missing mass and modified gravity solutions to rotation curve anomalies, one must study a system where the luminous and dark matter could be spatially displaced. One such system is the Bullet Cluster, the product of two colliding clusters (the smaller one being the "bullet"). The gas plasma components of the colliding clusters interact sufficiently and slow down, while the galaxies pass through effectively unhindered. As the majority of the baryonic mass is in the plasma, one expects the gravitational potential (Newtonian or otherwise) to be centred there. However the weak lensing about the cluster shows this is not the case, revealing two centres of gravity unaligned with the distribution of plasma (found from X-ray data). This suggests there are invisible components of the clusters making up the majority of their mass which passed through each other unhindered.

This was first reported in 2006 by Clowe *et al.* [30], where they claim the spatial separation of the centres of total and baryonic mass to $8\,\sigma$ significance. Figure 1.2 shows the X-ray emission and gravitational lensing around the Bullet Cluster as presented in [30]. Here one

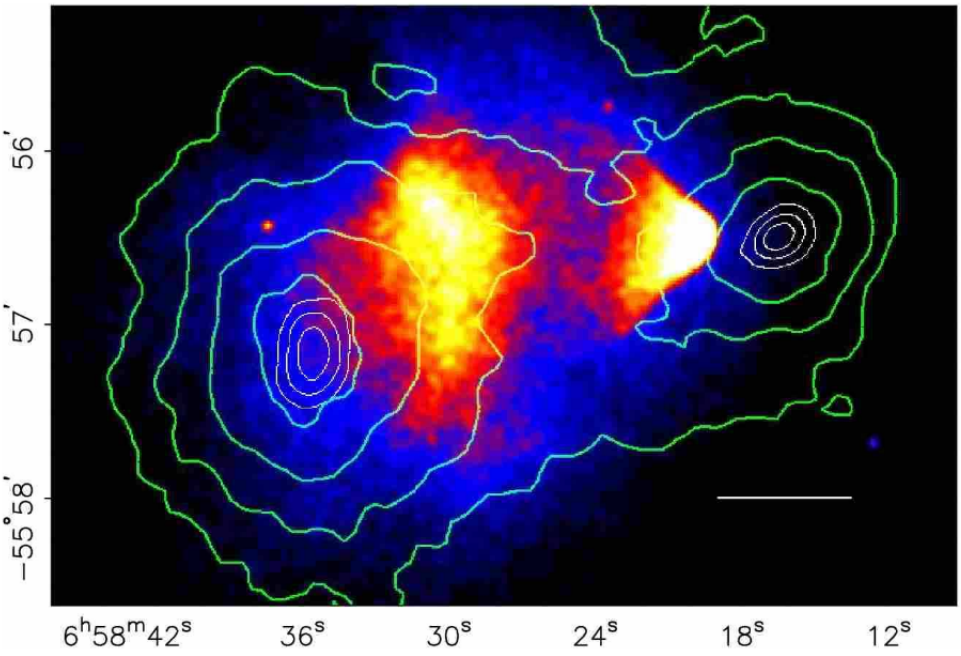

Figure 1.2: An X-ray heat map image of the Bullet Cluster as seen by the Chandra X-ray Observatory overlaid with gravitational potential contours reconstructed from weak lensing measurements shown in green. Taken from [30].

can clearly see the separation between the X-ray data depicting the luminous matter (the heat map), and the gravitational wells (green contours). Later, other systems were studied and found to have similar features, such as in [31] and [32]. In the latter they saw a cluster with a ring-like invisible halo, thought to be generated by two clusters colliding along our line-of-sight. Using numerical simulations of collisionless particles, they show how such rings form after the initial collision.

1.1.3 Cosmic Microwave Background Radiation

In 1964 Wilson and Penzias, while working with a 20 ft horn antenna, detected a strong extraterrestrial background noise of microwaves at a temperature of 3.5 ± 1.0 K [33], the so-called Cosmic Microwave Background (CMB). This discovery provided further evidence for a Big Bang cosmological model, which had been postulated by Lemaître in 1931 [34]. The CMB is typically spoken of as a "picture" of the Universe at approximately 380,000 years old, which was when the light last scattered. This occurs just after recombination, a period when protons and electrons fused to form the first atoms, which effectively ended photon scattering.

Prior to this epoch, photons are kept in thermal equilibrium via Thomson scattering with free electrons, thus the CMB is a blackbody spectrum. The dramatic drop in free electron density instigated by the formation of bound hydrogen states at recombination effectively terminates Thomson scattering and so photons cease interacting and will have streamed freely towards us, redshifting under the expanding Universe.

This radiation is (almost) isotropic, suggesting regions were once in contact with each other allowing them to thermalize. This was not expected by the standard cosmological model of the time, and so motivated a period of inflation (exponential expansion) to bring regions into causal contact [35–39]. Later in 1989 COBE, a satellite based experiment measuring the CMB, was launched and discovered tiny anisotropies (too small to discourage inflation) [40]; Figure 1.3 shows these anisotropies as found in a more recent survey by Planck [41]. By measuring these temperature fluctuations the abundance of baryonic and non-baryonic (dark) matter can be inferred.

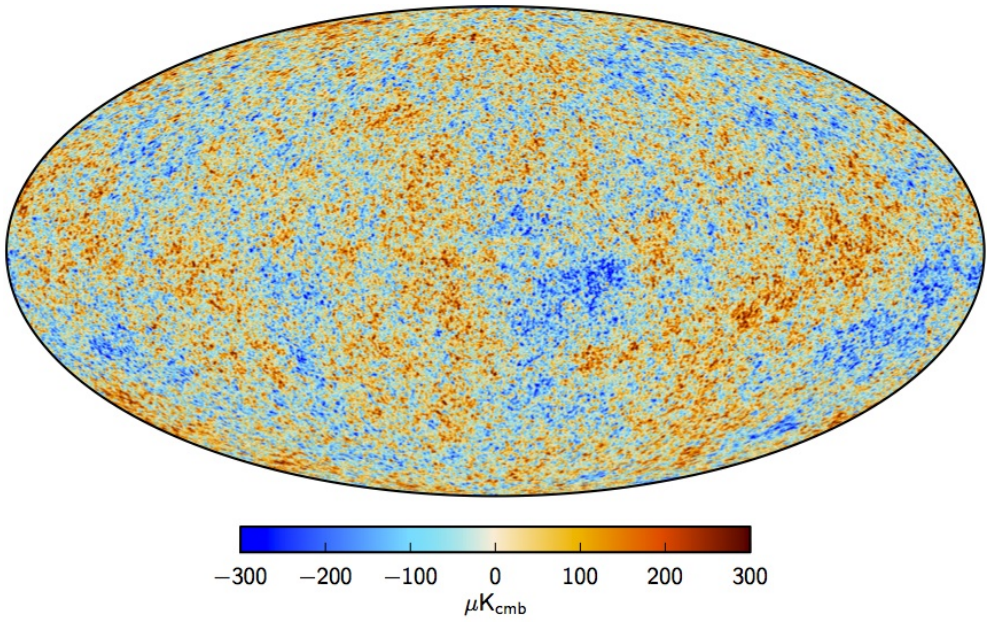

Figure 1.3: A full sky map of the anisotropies seen in the CMB by Planck [41], where K_{cmb} is the deviation from the mean temperature.

The temperature fluctuations reflect the distribution of matter at recombination, *e.g.* in a region of higher mass density the photons will have to escape a "deeper" gravitational well and so be at a lower temperature. These density fluctuations grow and the matter clusters, first creating small-scale structures (galaxies, *etc.*), then later the large-scale structures such

as filaments. These fluctuations are analysed as a function of the angular displacement between points on the map. To do so, a multipole analysis is utilised, where the temperature fluctuations as a function of angular displacement can be expanded in terms of spherical harmonics, *i.e.*

$$\frac{\delta T(\theta,\phi)}{T} = \sum_{l=1}^{\infty} \sum_{m=-l}^{l} a_{lm} Y_{lm}(\theta,\phi). \tag{1.4}$$

The anisotropies in the CMB are then considered as a function of the multipole l, with each term representing temperature fluctuations on differing angular scales. A general expansion in spherical harmonics would include an $l = 0$ term, which has been left out above. This, like the s-orbital of an atomic electron, is spherically symmetric, and so determines the overall scale of the temperature fluctuations, which is zero in our case by definition. The first non-zero term is then $l = 1$, which represents dipole anisotropies. Our solar system is moving with respect to the CMB, and so a large dipole contribution occurs due to the resulting Doppler shift. Any dipole contributions intrinsic to the CMB cannot be seen due to this dominating effect, and so one adjusts the measured CMB to remove this dipole term (which is the case in Figure 1.3) and is only interested in the terms with $l \geq 2$. At higher values of l, the scale being probed is of finer angles, in accordance with the approximate relation $\theta \sim \frac{180^{\circ}}{l}$.

To analysis the CMB in this manner, one is interested in determining the values of the coefficients a_{lm} required to produced the observed map. This cannot be done by determining the expectation value of the temperature fluctuation, $\langle \delta T/T \rangle$, as the average variation will be zero. Thus what one actually determines is the two-point correlation function

$$\left\langle \frac{\delta T(\hat{n})}{T} \frac{\delta T(\hat{n}')}{T} \right\rangle = \sum_{l} \frac{2l+1}{4\pi} \langle |a_{lm}|^2 \rangle, \tag{1.5}$$

where $\hat{n}$, $\hat{n'}$ represents unit vectors pointing to single points in the sky, such that $\hat{n}.\hat{n}' = \cos\theta$ with θ representing their angular displacement.

The angular power spectrum is not actually represented by the expression seen in (1.5), but rather $\frac{l(l+1)}{2\pi}\langle |a_{lm}|^2 \rangle$ by custom. Figure 1.4 shows this quantity as measured by Planck [17], as a function of l. We can see a definite structure in the spectrum, which has a series of peaks starting with the most dominant at $l \sim 200$, and further ones of decreasing amplitude as l is increased. The origin of these peaks lies in the acoustic oscillations of the photon-baryon plasma caused by the pressure and gravitational interactions of the fluid.

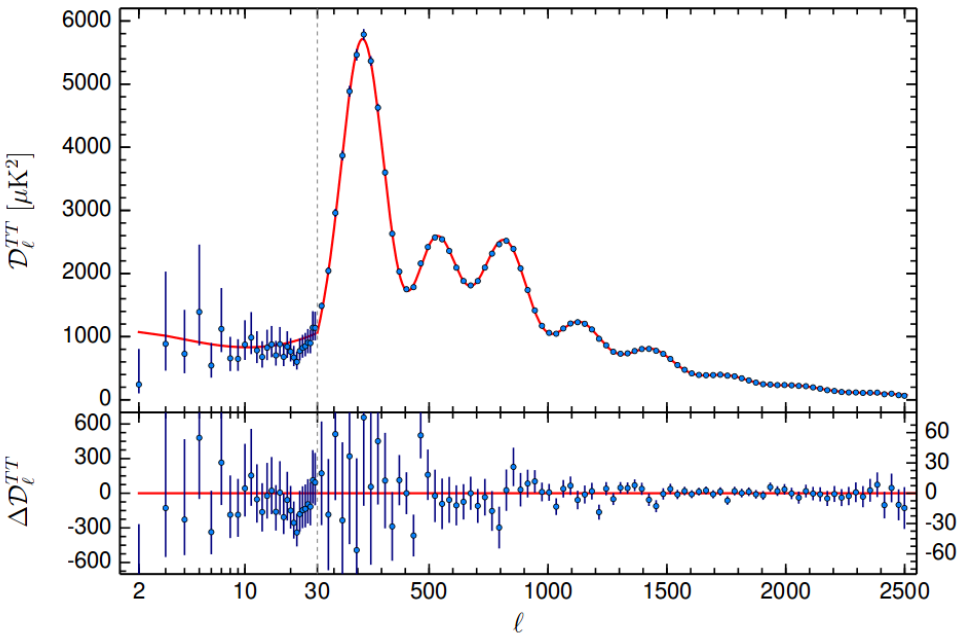

Figure 1.4: Angular Power Spectrum of the CMB as measured by Planck [17]. Here, $\mathcal{D}_l^{TT} = \frac{l(l+1)}{2\pi}\langle|a_{lm}|^2\rangle$.

The formation of the CMB starts with the creation and expansion (to cosmic sizes) of primordial fluctuations by inflation. This made a landscape of potential wells and hills, on which acoustic oscillations of a distribution of frequencies propagated. This system evolved up until the surface of last scattering, and the CMB is a frozen image of this epoch. The first, and largest peak of the CMB, represents the oscillation mode which since creation has had just enough to time to reach maximal compression for the first time in the potential wells. The second peak has exactly half the wavelength of the first, and so oscillated twice as fast. This means that at the surface of last scattering, it had just reached a point of maximum rarefaction in the well, having already undergone maximal compression before. This picture is also true for the subsequent peaks thereafter, which are higher harmonics of the fundamental first peak, having undergone several oscillations and reached an extremum at the surface of last scattering.

The position and amplitude of these peaks (amongst other features) reflects the composition of the early Universe. Baryonic matter experiences pressure through its electromagnetic interactions, and also gravity, whereas non-baryonic matter would only feel the latter. Consequently they affect the CMB in different ways and their abundance can be extracted from the

spectrum. To understand the contribution DM could make, one must note its importance in bringing about a matter-dominated Universe and consider the modes which start oscillating before or after this transition. Modes which start oscillating earlier in the radiation-dominated Universe (those of larger l), will be enhanced because their oscillations cause the decay of the potential wells. This is because if radiation is dominating the energy, then it is also responsible for the gravitational potential. It's own oscillations changes the potential. On the other hand, if the oscillations start later in the matter-dominated Universe (like those of lower l), then the gravitational potential will be held by the non-relativistic matter and this effect which boosts the amplitude does not occur. This means by comparing the higher and lower peaks, the abundance of non-relativistic matter (DM) can be determined.

In practice one has to consider the range of effects each component of a cosmological model could have, which will affect multiple features of the spectrum. Silk damping must be considered as well, this is an effect which results in the suppression of peaks of higher l. This is understood by acknowledging that the surface of last scattering is not an exact point at which photon scatterings were switched off, but rather occurred over a finite period of time. This means that during the decoupling from matter, light can still undergo a few scatterings before it finally starts free streaming. Before these final scatterings the light will travel a finite distance, and this means that temperature fluctuations on scales below this distance will be smeared out, dampening the peaks seen in the spectrum.

Thus from the angular variation of temperature fluctuations (seen in Figure 1.4) the composition of the early Universe can be determined, and we find it is best described by what is known as the ΛCDM cosmological model, which contains SM matter along with non-relativistic CDM and a non-zero cosmological constant. Values for the abundances of baryonic matter and CDM can then be extracted from this angular power spectrum. These measurements tell us the missing mass inferred by velocity rotation curves cannot come from MACHOs as there is too little baryonic matter. They also provide the best measurement for the abundance of DM, $\Omega_{\mathrm{DM}}h^2$, which is formally defined later in Section 1.2.1. Planck [17] found this to be

$$\Omega_{\mathrm{DM}}h^2 = 0.1186 \pm 0.0020, \tag{1.6}$$

which is approximately 25% of the energy of the Universe, while SM particles (moslty baryons)

are only 5%[1].

If there was no CDM, primordial density fluctuations in the plasma would need to be much larger than what is inferred from the CMB in order to get sufficient galaxy formation. By including CDM, density fluctuations start earlier and sufficient galaxy formation is allowed. As mentioned before, the missing mass in galaxies could also comprise of SM neutrinos, however they are an example of relativistic HDM, which also suffers from insufficient galaxy production.

The small scale density fluctuations required for galaxy formation are erased by the free streaming of neutrinos [42], *i.e.* they are moving at relativistic velocities and the distance they travel before becoming non-relativistic is larger than the scale of the fluctuations. In this scenario galaxy formation must have then occurred via the fragmentation of large-scale structures; numerical simulations [43] found that this must have happened fairly recently (z, the expected redshift to have occurred since that time, must be less than ~ 2). However measurements of galactic ages seem to be in excess of $z > 4$ [44], which makes SM neutrinos less attractive DM candidates (see [45] for further detail).

A third option, keV-scale "warm" dark matter (WDM) is also possible, where the candidate is still relativistic at freeze-out, like HDM, but becomes non-relativistic sufficiently quickly after, such that the free streaming length is ~ 4 Mpc. This however doesn't directly correspond to the minimum size of structures that can form in WDM scenarios. Post-decoupling, where the pressure from photon interactions with baryons dissipates, perturbations of this minimum size start evolving non-linearly. The perturbations become gravitational unstable and consequently collapse and virialize, *i.e.* become a stable gravitationally bound system. For an initial perturbation of ~ 4 Mpc in size, which will encapsulate a total mass of $\sim 10^{12} M_{\odot}$, the resulting bound system will be ~ 30 kpc; this is around the size and mass of a typical galaxy. Thus in WDM scenarios, sub-galactic structure formation is suppressed. An attribute which can be exploited to resolve some tensions facing CDM models on these scales, such as issues with satellite galaxy populations (the 'missing satellites' problem), density profiles in galactic and satellite cores (the 'core/cusp' problem), and the structure of subhalos (the 'too-big-to-fail' problem) [46–49].

[1]The remaining 70% is *dark energy*, postulated to be the driving force behind a non-zero cosmological constant, and so an accelerating expansion of the Universe.

From the evidence presented here, we are painted a picture of a Universe whose mass is dominated by a BSM particle as yet undiscovered. Theories of modified gravity face problems from colliding galaxies, while assuming neutrinos or MACHOs as the missing matter leads to issues with structure formation, and constraints from microlensing searches and the CMB. Many key results have been discussed here, but for a reader seeking further detail and evidence, there are many illuminating texts [23, 24, 50–52].

1.2 Genesis and Relic Density

Having established the evidence for DM in the Universe, we shall now discuss the means through which it may be produced by considering a selection of genesis mechanisms. As seen in Section 1.1.3, the CMB (as measured by Planck) provides the best measurement for the relic density of DM [17]. Without further information, there is no connection between the abundance and intrinsic properties of DM, and so no constraints. However by assuming a mechanism via which the relic density was produced, such a relation may be created. There are numerous mechanisms one could use, which allows the constraint to be manipulated, but it is typically assumed DM was created via a process known as *freeze-out* [53–55].

1.2.1 Freeze-Out and the WIMP Miracle

In freeze-out one assumes DM was in thermal equilibrium with the particle bath in the early Universe, where it was annihilated and created in equal rates. When the temperature drops below the DM mass, creation becomes suppressed as more and more bath particles no longer have enough energy, thus annihilations dominant and the abundance drops. Approximately when the annihilation rate matches the expansion rate of the Universe, the DM particles become too far apart and annihilations effectively cease (the DM falls out of chemical equilibrium), and we are left with a residual amount of DM, this is known as the point of freeze-out.

This process is described by a Boltzmann transport equation, which tells us the number density evolution of the particle freezing-out. In its most general and compact form this equation is written as

$$\hat{\mathbf{L}}[f] = \hat{\mathbf{C}}[f], \tag{1.7}$$

where $\hat{\mathbf{C}}$ is the collision operator and $\hat{\mathbf{L}}$ is the Liouville operator. In relativistic covariant

form

$$\hat{\mathbf{L}} = p^\alpha \frac{\partial}{\partial x^\alpha} - \Gamma^\alpha_{\beta\gamma} p^\beta p^\gamma \frac{\partial}{\partial p^\alpha}, \tag{1.8}$$

where $\Gamma^\alpha_{\beta\gamma}$ are the Christoffel symbols into which the gravitational effects enter. Using the Friedmann-Robertson-Walker (FRW) metric and assuming a homogeneous and isotropic Universe, the Liouville operator becomes

$$\hat{\mathbf{L}}[f(E,t)] = E\frac{\partial f}{\partial t} - H|\vec{p}|^2 \frac{\partial f}{\partial E}, \tag{1.9}$$

where $H \equiv \dot{R}/R$ is the Hubble parameter. Freeze-out occurs during the radiation-dominated era, and as such H as a function of temperature T, is given by

$$H(T) = \left(\frac{8\pi^3}{90}\right)^{1/2} \frac{T^2\sqrt{g_*}}{M_{\rm Pl}} \qquad \text{with} \qquad g_* = \sum_{\text{bosons}} g_i \left(\frac{T_i}{T}\right)^4 + \frac{7}{8}\sum_{\text{fermions}} g_i \left(\frac{T_i}{T}\right)^4, \tag{1.10}$$

where $M_{\rm Pl} = 1.22 \times 10^{19}$ GeV is the Planck mass, g_* is the relativistic degrees of freedom contributing to the energy density, and g_i and T_i are the internal degrees of freedom and temperature of that particle species respectively.

Inserting $\hat{\mathbf{L}}[f(E,t)]$ into the Boltzmann equation, with some manipulation, one gets

$$\frac{dn}{dt} + 3nH = \frac{g}{(2\pi)^3}\int \hat{\mathbf{C}}[f]\frac{d^3p}{E}, \tag{1.11}$$

where n is the number density, which in terms of $f(E,t)$, the phase space distribution, is $n(t) = \frac{g}{(2\pi)^3}\int d^3p f(E,t)$.

Labelling the DM particle species χ, and assuming a single annihilation and creation channel ($\chi + a + b + \ldots \leftrightarrow i + j + \ldots$), the collision term is

$$\begin{aligned}\frac{g}{(2\pi)^3}\int \hat{\mathbf{C}}[f]\frac{d^3p_\chi}{E_\chi} = -\int d\Pi_\chi d\Pi_a d\Pi_b \ldots d\Pi_i d\Pi_j \ldots \\ \times (2\pi)^4\delta^4(p_\chi + p_a + p_b \ldots - p_i - p_j \ldots) \\ [|\mathcal{M}|^2_{\chi+a+b+\ldots\to i+j+\ldots} f_a f_b \ldots f_\chi (1 \pm f_i)(1 \pm f_j)\ldots \\ - |\mathcal{M}|^2_{i+j+\ldots\to\chi+a+b+\ldots} f_i f_j \ldots (1 \pm f_a)(1 \pm f_b)\ldots(1 \pm f_\chi)],\end{aligned} \tag{1.12}$$

where (with α representing any particle involved) $d\Pi_\alpha \equiv \frac{g_\alpha}{(2\pi)^3}\frac{d^3p_\alpha}{2E_\alpha}$, and the $|\mathcal{M}|^2$ terms are the square matrix elements, averaged over initial and final state spins. In the $(1 \pm f_\alpha)$ terms, a $+(-)$ is used when α is a boson (fermion).

By assuming CP or T invariance, and a Maxwell-Boltzmann distribution $f_\alpha = e^{-(E_\alpha - \mu_\alpha)/T}$ for every particle, then

$$|\mathcal{M}|^2 \equiv |\mathcal{M}|^2_{\chi+a+b+\ldots\to i+j+\ldots} = |\mathcal{M}|^2_{i+j+\ldots\to\chi+a+b+\ldots} \tag{1.13}$$

and $(1 \pm f_\alpha) \approx 1$ (since the temperature has fallen below the χ mass, meaning f_α is small). With these assumptions the equation simplifies to

$$\begin{aligned}\dot{n}_\chi + 3Hn_\chi = -\int d\Pi_\chi d\Pi_a d\Pi_b \ldots d\Pi_i d\Pi_j \ldots (2\pi)^4 |\mathcal{M}|^2 \\ \times \delta^4(p_i + p_j \ldots - p_\chi - p_a - p_b \ldots)[f_a f_b \ldots f_\chi - f_i f_j \ldots].\end{aligned} \tag{1.14}$$

As the Universe is expanding the number density continues to fall even after the cessation of inelastic scattering processes. A more useful quantity would then be the number density per comoving volume, which would be independent of these dynamics. Furthermore it is convenient to consider the evolution in temperature as opposed to time, and so typically the Boltzmann equation is rewritten in terms of the yield Y and the variable x, which are given by

$$Y_\alpha \equiv \frac{n_\alpha}{s} \qquad \text{and} \qquad x \equiv \frac{m_\chi}{T}, \tag{1.15}$$

where s is the entropy density. This scales the same way under expansion as total entropy is conserved ($sR^3 = $ constant), and in the radiation-dominated era, can be approximated by

$$s = \frac{2\pi^2}{45} g_{*S} T^3 \qquad \text{with} \qquad g_{*S} = \sum_{\text{bosons}} g_i \left(\frac{T_i}{T}\right)^3 + \frac{7}{8} \sum_{\text{fermions}} g_i \left(\frac{T_i}{T}\right)^3. \tag{1.16}$$

where g_{*S} is the relativistic degrees of freedom contributing to the entropy density. During freeze-out, the effective relativistic degrees of freedom, g_* and g_{*S}, are approximately equal and constant, and so are taken as such.

Rewritten in terms of Y and x, the Boltzmann equation is

$$\begin{aligned}\frac{dY_\chi}{dx} = -\frac{1}{H(m_\chi)s(m_\chi)x^2} \int d\Pi_\chi d\Pi_a d\Pi_b \ldots d\Pi_i d\Pi_j \ldots (2\pi)^4 |\mathcal{M}|^2 \\ \times \delta^4(p_i + p_j \ldots - p_\chi - p_a - p_b \ldots)[f_a f_b \ldots f_\chi - f_i f_j \ldots].\end{aligned} \tag{1.17}$$

Typically in freeze-out calculations one considers DM pair annihilating via $2 \to 2$ inelastic scattering processes such as $\bar{\chi}\chi \leftrightarrow \bar{\psi}\psi$, where ψ represents all possible SM final states. In these cases, the Boltzmann equation reduces to the far simpler form

$$\frac{dY_\chi}{dx} = -\frac{\langle \sigma_{\bar{\chi}\chi\to\bar{\psi}\psi} v \rangle s(m)}{H(m)x^2} \left(Y_\chi Y_{\bar{\chi}} - Y_{\chi,\text{eq}} Y_{\bar{\chi},\text{eq}}\right), \tag{1.18}$$

where $\langle\sigma_{\bar{\chi}\chi\to\bar{\psi}\psi}v\rangle$ is the thermally-averaged annihilation cross-section times velocity, and $Y_{\alpha,\mathrm{eq}}$ is the yield in thermal equilibrium. This depends on both particle and antiparticle yields, however standard freeze-out is presumed to be symmetric (asymmetric DM is discussed later in Section 1.2.2), *i.e.* the yields of both are initially equal and no asymmetry is generated thereafter. Here, we will consider an even simpler case in which DM is its own antiparticle (*e.g.* a real scalar or Majorana fermion).

In general, the annihilation cross-section times relative velocity, σv, for most processes can be expanded as

$$\sigma v = a + bv^2 + \mathcal{O}(v^4). \tag{1.19}$$

If all terms of this expansion are non-zero, then the velocity-independent first term dominates (as $v \sim 0.3$ at freeze-out) and the annihilations are s-wave. However scenarios with dominant p-wave annihilations can arise in which $a = 0$, and so σv is velocity-suppressed. Taking the lowest order non-zero term as dominant, by thermally-averaging σv one then finds

$$\langle\sigma v\rangle \approx \frac{\sigma_0}{x^n}, \tag{1.20}$$

where $n = 0(1)$ and $\sigma_0 = a(6b)$ in the case of s(p)-wave dominant annihilations. The Boltzmann equation with this expansion becomes

$$\frac{dY_\chi}{dx} = -\frac{A}{x^{n+2}}\left(Y_\chi^2 - Y_{\chi,\mathrm{eq}}^2\right), \tag{1.21}$$

where $A = \sqrt{\frac{\pi}{45}}g_* m_\chi M_{\mathrm{Pl}}\sigma_0$, and

$$Y_{\chi,\mathrm{eq}} \approx 0.145(g/g_{*S})x^{3/2}e^{-x}, \tag{1.22}$$

which is an approximation valid in the non-relativistic regime.

This equation (1.21) has no known exact analytic solution, but can be solved numerically assuming the initial condition $Y_\chi(x_i) \approx Y_{\chi,\mathrm{eq}}(x_i)$ when x is below the point of freeze-out x_{fr}. In Figure 1.5, solutions (assuming dominant s-wave annihilation) for a range of σ_0 values are plotted which illustrate the yield's evolution during freeze-out. Here we see how the particles were once in thermal equilibrium, following $Y_{\chi,\mathrm{eq}}$ (the black curve) at high temperatures, before diverging at $x \sim 25$ (the point of freeze-out) and plateauing, leaving a residual yield. The size of the remnant yield decreases as the cross-section increases, since the annihilation rate is higher and so the system can stay in equilibrium longer.

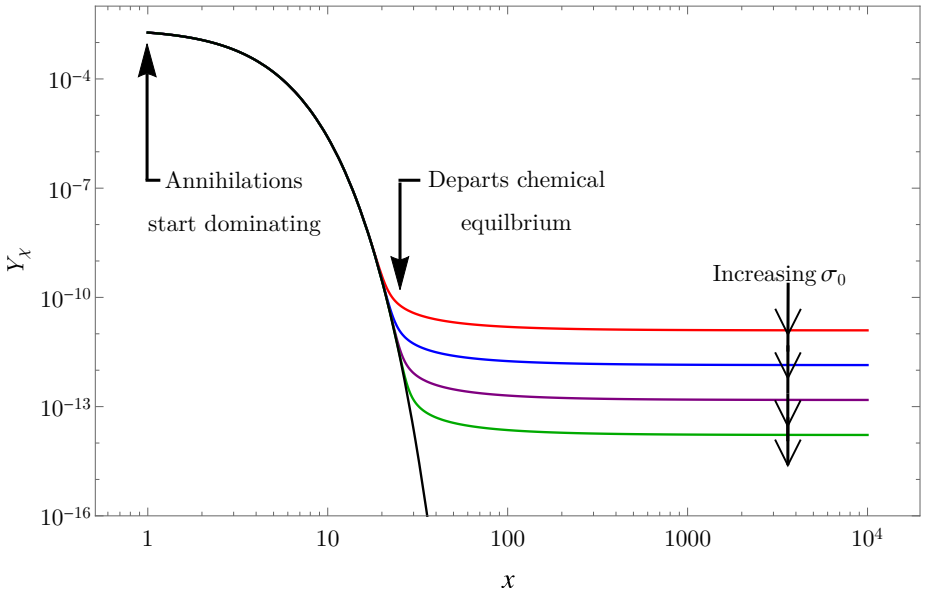

Figure 1.5: A plot of Y_χ vs x illustrating how the yield evolves when a particle undergoes freeze-out with dominant s-wave annihilations, which highlights key moments in the thermal history. The yields for several σ_0 values were plotted (coloured lines), as well as $Y_{\chi,\mathrm{eq}}$ (the black line). These were found by numerically solving (1.21) when $m_\chi = 500$ GeV.

While (1.21) does not permit an exact analytic solution, an approximation can be found. For the proceeding derivations, it is convenient to rewrite the equation in terms of $\Delta \equiv Y_\chi - Y_{\chi,\mathrm{eq}}$, obtaining

$$\frac{d\Delta}{dx} = -\frac{dY_{\chi,\mathrm{eq}}}{dx} - \frac{A}{x^{n+2}}\Delta(\Delta + 2Y_{\chi,\mathrm{eq}}). \tag{1.23}$$

In late times ($x > x_{\mathrm{fr}}$) we let $Y_{\chi,\mathrm{eq}} \approx 0$, an approximation which is justified upon inspection of Figure 1.5. This reduces (1.23) to

$$\frac{d\Delta}{dx} = -\frac{A}{x^{n+2}}\Delta^2, \tag{1.24}$$

which now possesses an analytic solution. Rearranging this into an integral between x_{fr} and ∞, and given $\Delta(x_{\mathrm{fr}}) \gg \Delta(\infty) \approx Y_\chi(\infty)$ one derives the relic yield

$$Y_\chi(\infty) \approx \frac{(n+1)x_{\mathrm{fr}}}{A}, \tag{1.25}$$

This can then be related to the relic abundance $\Omega_\chi h^2$, where $\Omega_\chi \equiv \frac{\rho_\chi}{\rho_c}$ and $h \equiv H_0/100$; in these definitions, ρ_χ is energy density of χ particles, ρ_c is the critical density, and $H_0 = 67.8 \pm 0.9$ km s^{-1}Mpc^{-1} is the present value of the Hubble parameter.

Using the result (1.25), this means the relic abundance is

$$\Omega_\chi h^2 = (2.76 \times 10^8) \frac{(n+1) x_{\rm fr}^{n+1}}{M_{\rm Pl} \sigma_0 \sqrt{g_*}} \sqrt{\frac{45}{\pi}}. \tag{1.26}$$

When calculating these abundances it is important to remember the total will be given by the sum of particle and anti-particle contributions.

Calculating the relic abundance from (1.26) requires knowledge of $x_{\rm fr}$; defining it as the point where $\Delta(x_{\rm fr}) = cY_{\chi,\rm eq}(x_{\rm fr})$ (c is a constant of order one) and taking $\frac{d\Delta}{dx} \approx 0$, an expression is found from (1.23)

$$x_{\rm fr} \approx \log[Ak(n+1)] - \left(n + \frac{1}{2}\right) \log[\log[Ak(n+1)]], \tag{1.27}$$

where $k = 0.145(g/g_{*S})$ (the coefficient in $Y_{\chi,\rm eq}$), and we have set $c(c+2) = (n+1)$ which fits best to numerical data [50].

Using (1.27) and (1.23), one can predict the DM relic abundance from freeze-out. Presuming the annihilations are dominantly s-wave, to get the observed abundance the cross-section would need to be

$$\sigma_0 \approx 3 \times 10^{-26} \text{ cm}^3 \text{ s}^{-1}. \tag{1.28}$$

Intriguingly, if a DM state with electroweak scale mass and coupling (G_F) is considered, one finds σ_0 values of around this size. This motivates DM to consist of Weakly Interacting Massive Particles (WIMPs) — a coincidence referred to as the WIMP miracle. However while freeze-out motivates a WIMP candidate, it is by no means restricted to such, as highlighted in [56]. For more details on the derivation of and analytic solutions to the Boltzmann equation for freeze-out, see [50].

Exceptions to Freeze-Out

When assuming DM genesis through freeze-out, there are three important exceptions highlighted by Griest and Seckel [57] that must be kept in mind:

1. Threshold effects
2. Resonances
3. Co-annihilations

If one (or more) of these exceptions takes place, then σv is no longer appropriately described by an expansion in v^2 as in (1.19), and the Boltzmann equation can take a different form.

Threshold effects arise when an annihilation channel is significantly more kinematically accessible during freeze-out than it is presently. For example consider the process $\bar{\chi}\chi \to \psi_1\psi_2$ when $2m_\chi < m_{\psi_1} + m_{\psi_2}$; there exists a minimum centre-of-mass energy required for it to proceed. At present this channel could be neglected as a minute fraction of χ particles will collide with enough energy, however during freeze-out when $T \sim m_\chi/25$, annihilation through this channel could be occurring at a significantly higher rate (and could even dominate the total cross-section).

Resonance effects occur when an annihilation channel is near a pole during freeze-out, *e.g.* when there is an s-channel annihilation process where the mediator's mass is approximately twice that of colliding DM particles ($m_{\text{med}} \sim 2m_\chi$). In such a case one uses the Breit-Wigner form for the propagator

$$\frac{1}{s - m_{\text{med}}^2 + i m_{\text{med}}\Gamma_{\text{med}}}, \tag{1.29}$$

which takes the finite width of the mediator, Γ_{med}, into account.

Co-annihilations become significant when the DM candidate is nearly mass degenerate with at least one different state. During freeze-out there will be a significant abundance of these other states still present and new scattering channels will be opened up. As an example, consider N new states (labelled χ_i) which are odd under a stabilising $\mathbb{Z}_2$ symmetry, taking χ_1 to be the lightest and therefore our DM candidate. If the mass splitting between χ_1 and the other odd sector states is much greater than the temperature at freeze-out, then only $\chi_1\chi_1 \leftrightarrow \psi_a\psi_b$ (with ψ_a representing SM final states) is important to consider; having frozen out and decayed away earlier, the additional degrees of freedom cannot contribute. If however the mass splittings are small enough (approximately the freeze-out temperature or less), the other odd sector states will freeze-out almost simultaneously with χ_1, and consequently co-annihilation processes such as $\chi_i\chi_j \leftrightarrow \psi_a\psi_b$, $\chi_i\psi_a \leftrightarrow \chi_j\psi_b$ and $\chi_j \to \chi_i\psi_a$ must be taken into account.

Following work in [58], the Boltzmann equation for each χ_i state is given by

$$\begin{aligned}\frac{dn_i}{dt} =& -3Hn_i - \sum_j \langle\sigma_{ij}v_{ij}\rangle(n_i n_j - n_{i,\mathrm{eq}}n_{j,\mathrm{eq}}) \\ &- \sum_{j\neq i}\left[\langle\sigma'_{ij}v_{ij}\rangle(n_i n_X - n_{i,\mathrm{eq}}n_{X,\mathrm{eq}}) - \langle\sigma'_{ji}v_{ij}\rangle(n_j n_{X'} - n_{j,\mathrm{eq}}n_{X',\mathrm{eq}})\right] \\ &- \sum_{j\neq i}\left[\Gamma_{ij}(n_i - n_{i,\mathrm{eq}}) - \Gamma_{ji}(n_j - n_{j,\mathrm{eq}})\right],\end{aligned} \tag{1.30}$$

where

$$\begin{gathered}\sigma_{ij} = \sum_{a,b}\sigma(\chi_i\chi_j \to \psi_a\psi_b), \qquad \sigma'_{ij} = \sum_{a,b}\sigma(\chi_i\psi_a \to \chi_j\psi_b), \\ \text{and} \qquad \Gamma_{ij} = \sum_a \Gamma(\chi_i \to \chi_j\psi_a).\end{gathered} \tag{1.31}$$

The first term is the familiar cosmological expansion term, the second represents creation and annihilation processes, the third is for scatterings and the last term is the contribution from decays.

Summing the Boltzmann equations together we obtain an expression describing the evolution of the number density of all odd sector particles;

$$\frac{dn}{dt} = -3Hn - \langle\sigma_{\mathrm{eff}}v\rangle(n^2 - n_{\mathrm{eq}}^2), \tag{1.32}$$

where $n = \sum_i n_i$ and

$$\langle\sigma_{\mathrm{eff}}v\rangle \equiv \sum_{ij}\langle\sigma_{ij}v_{ij}\rangle\frac{n_{i,\mathrm{eq}}n_{j,\mathrm{eq}}}{n_{\mathrm{eq}}^2}. \tag{1.33}$$

As we expect the other odd sector states to have decayed, the present total number density, $n(t_0)$, will be dominantly χ_1 states.

There is also a "fourth exception" to the standard freeze-out scenario, arising when the annihilation cross-section has an inverse dependence on the velocity, *i.e.* $\sigma v \sim 1/v$. As the present velocity of DM is far less than it was at freeze-out, the annihilation cross-section now can be far greater; this boost is called a Sommerfeld enhancement [59].

Such situations occur when there is a long-range attractive potential between the colliding DM states which can arise if light force-carrier particles are exchanged [60, 61]. Sommerfeld enhancements are typically applied when large indirect detection signals (discussed later in Section 1.4.2) are desired, but conflict with the small thermal cross-section values needed to produce the relic density. A Sommerfeld boost justifies a lower cross-section at freeze-out, however annihilations directly into the mediators can re-enhance it.

Only DM genesis via freeze-out and the associated caveats have been discussed thus far; by assuming this mechanism and requiring the correct abundance of DM to have been produced, theories of DM can be heavily constrained. However by considering a different production mechanism, these bounds will change and can make a theory more appealing. In the following sections we shall take a look at two alternative mechanisms: asymmetric freeze-out and freeze-in.

1.2.2 Asymmetric Freeze-Out

An asymmetry between baryonic matter and antimatter in the present Universe has long been established [62], leading to models of Baryogenesis [63–65] via which such an asymmetry could have been produced. Given this, it is reasonable for one to wonder if a similar situation could have arisen in the dark sector, and produced an asymmetric abundance of DM. However there is more than speculation; the abundance of DM is approximately five times that of baryons, which would seem too coincidental if they are generated by separate mechanisms. This suggests there could be a single process generating both baryon and DM asymmetries. In asymmetric freeze-out, the asymmetry is presumed to have been generated beforehand by some process at higher temperatures. During freeze-out DM particles and anti-particles annihilate away, leaving behind the excess of particles (the asymmetry).

The asymmetry in a particle species can be parameterised using

$$\eta_\psi = \frac{n_\psi - n_{\bar{\psi}}}{n_\gamma}, \tag{1.34}$$

where ψ is the particle species (baryons or DM), and n_ψ and n_γ are the ψ and photon number densities respectively. If the symmetric components of the abundances are efficiently annihilated away, *i.e.* the particle number densities are far greater than the antiparticle densities now, then the relic density of both baryons and DM is dictated by the asymmetry generated and

$$\Omega_{\rm DM} \approx \frac{m_{\rm DM}\eta_{\rm DM}}{m_p\eta_b}\Omega_b. \tag{1.35}$$

To get the observed ratio of relic densities then, we expect $1 \lesssim m_{\rm DM} \lesssim 10$ GeV, as baryon and DM asymmetries generated by the same mechanism will likely be of comparable value.

The Boltzmann equations describing asymmetric freeze-out will be of the same form as (1.18), however now subject to the constraint $Y_\chi - Y_{\bar{\chi}} =$ constant. The annihilation rate drops

faster in asymmetric freeze-out as fewer particle-antiparticle pairs are available; this means the annihilation cross-section will need to be greater than it is in standard freeze-out to insure the efficient annihilation of the symmetric component. Furthermore the annihilation cross-section may be increased pass this required value without causing any significant changes to the relic abundance. For a more precise treatment of asymmetric production, see [66].

By assuming asymmetric production of DM, indirect detection bounds are effectively removed as there will be too few antiparticles for DM to annihilate with. There are also other ways aside from via freeze-out, that an asymmetric DM abundance may be produced [67–69].

1.2.3 Freeze-In

Freeze-in [70] starts with the assumption that there is initially a negligible abundance of DM, and that while processes amongst the bath particles will produce DM, these will be insufficient for thermal equilibrium to be established. Instead the yield of DM will gradually build through these rare processes, and as the Universe cools and expands, they will come to a halt and we are left with a residual abundance of DM which has "frozen-in". DM candidates which are produced this way are referred to as Feebly Interacting Massive Particles (FIMPs).

There are several ways for a DM candidate to be frozen-in, such as via rare decays of bath particles, or their annihilations into DM final states. It may also be produced indirectly; the frozen-in particle could be another heavier state which then decays into DM. The inverse of these decays may also be the channel through which the parent state is produced. In this last example the DM particle is actually in thermal equilibrium, however it presumes the abundance generated via standard freeze-out is far less than that produced through the freeze-in of the heavier state.

Figure 1.6 shows a plot of the DM yield, Y_χ, against x, which illustrates how freeze-in generates the relic abundance. This is in the case that rare decays of heavier states are producing the DM. The DM yield for different coupling strengths is plotted (colours) along with the thermal equilibrium yield of the parent state (black). Before $x \sim 10$, the yield is increasing and heading towards thermal equilibrium as bath processes are in effect. As the parent particles are annihilated away, DM production via their decays ceases and we are left with a relic abundance of DM which is larger when the interaction is stronger. This contrasts with freeze-out, where a larger couplings mean a lower residual yield. One may also

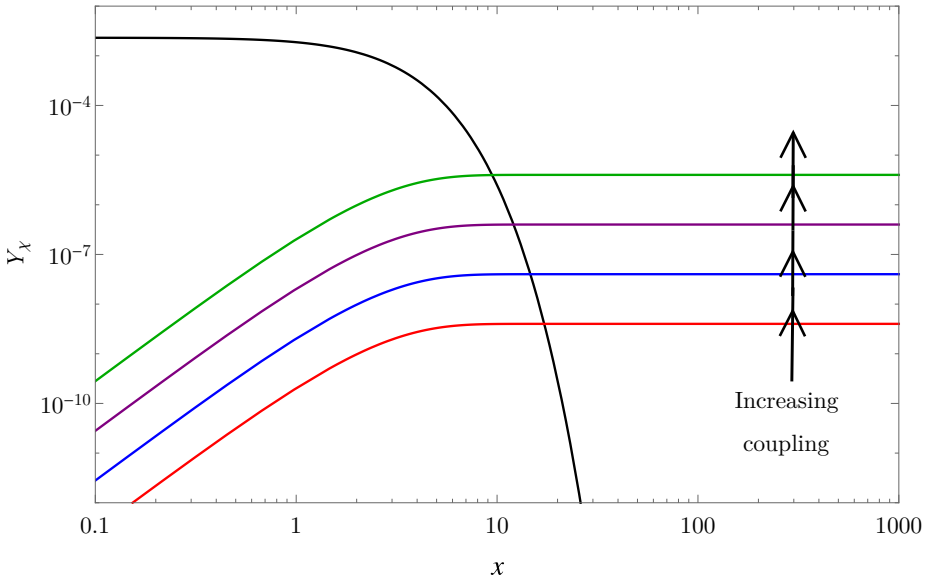

Figure 1.6: A plot of yield against x illustrating DM production via freeze-in. It plots the yield in thermal equilibrium (black) and the freeze-in yield for various interaction strengths (colours), whose relative values are indicated within.

have asymmetric freeze-in, where the asymmetry is generated by the mechanism, rather than presumed to already exist [69].

Here different mechanisms for DM genesis have been discussed, including standard freeze-out, the traditional mechanism of WIMP models. However other possibilities have also been highlighted, demonstrating how the requirements of relic density may be manipulated. Indeed atypical mechanisms are even necessary in various cases, especially when considering non-WIMP candidates, such as axions and sterile neutrinos, these are discussed more in [71, 72]. In Chapter 3 we will present an alternate mechanism in which DM is produced from the decays of topological defects, and in Chapters 4 & 5 we discuss works which utilise this mechanism.

1.3 Candidates and Models

Caution should be exercised when listing the criteria for a DM candidate, as one would be hard pressed to find a condition that is without exception. As a guide, a successful theory should permit a candidate that is stable, electrically neutral, and cold. However caveats exist: instability is allowed as long as the lifetime is of or above the age of the Universe, DM may couple very weakly to photons (see millicharged theories [73, 74]), and "warm" DM candidates

can still allow for sufficient galaxy formation [50, 75, 76]. Further rules could be added [77] such as compatiability with Big Bang nucleosynthesis (BBN), stellar evolution, and self-interactions, however broadly speaking one could put this in the category of phenomenological bounds.

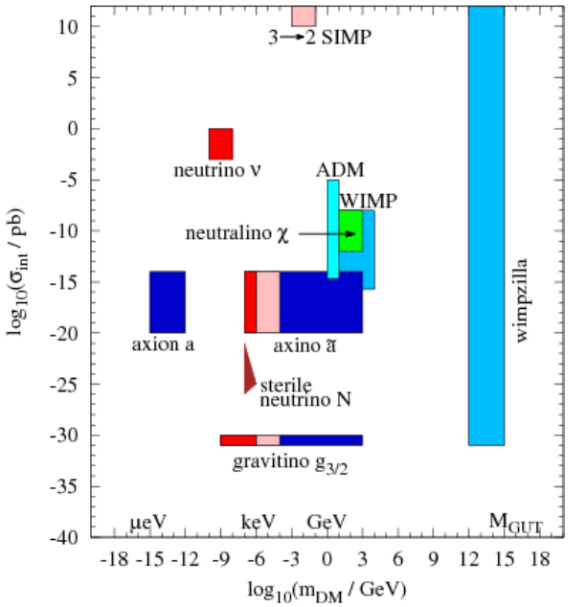

Figure 1.7: An illustrative plot of typical interaction cross-section σ_{int} against DM mass showing regions covered by a selection of popular DM models, taken from [78].

There are an enormous number of DM models permeating every nook and cranny of our theory-space. Figure 1.7 contains a popular illustrative plot showing the regions of typical interaction cross-section σ_{int}, against mass for a few DM models; this highlights the vast expanse of this space that DM models span. This section will first focus on the neutralino in supersymmetric (SUSY) theories, which has arguably received the most attention. Proceeding this we will discuss DM model building with simplified models and effective field theories.

1.3.1 SUSY and the Neutralinos

Arguably containing the most popular DM candidate (the *neutralino*), SUSY models encompass all theories which are invariant (or softly broken) under a supersymmetric transformation. This symmetry states that for every SM particle there is an associated state (its superpartner) with the same quantum numbers, but whose spin differs by 1/2. The main motivation for

SUSY theories is their ability to resolve the gauge hierarchy problem.

The SM has proven highly successful in describing many particle processes, but it does not address several other phenomena, *e.g.* gravity. Quantum gravitational effects are thought to become important at around the Planck scale, $M_{\mathrm{Pl}} = 1.22 \times 10^{19}$ GeV, which is orders of magnitude beyond the electroweak scale processes of the SM. Further new physics between these scales is to be expected as neutrino oscillations, the CP problem, and DM for example, all require BSM physics.

The issues with this expectation of new physics is the sensitivity of the Higgs field, H, to these new scales. Consider the contribution to the self-energy of the Higgs from a fermion, which has a Yukawa coupling $\lambda_f H \bar{f} f$, seen in Figure 1.8. If you regulate this using an ultraviolet momentum cutoff, Λ, a term quadratically divergent in the cutoff arises

$$\Delta m_H^2 = -\frac{|\lambda_f|^2}{8\pi^2}\left[\Lambda^2 + 2m_f^2 \log(\Lambda/m_f) + \ldots\right]. \tag{1.36}$$

The cutoff Λ can be physically interpreted as the scale at which new physics enters. If this is the Planck scale, then this correction to the mass is huge, and fine-tuning is required to bring the mass down to the electroweak scale. This is not just a problem for the Higgs, but for all the massive states in the SM, as their masses are determined from that of the Higgs field's (which dictates the VEV). Subsequently this suggests the cutoff is at a much lower scale ($\sim$ TeV), where the mass correction is small enough such that no tuning is required.

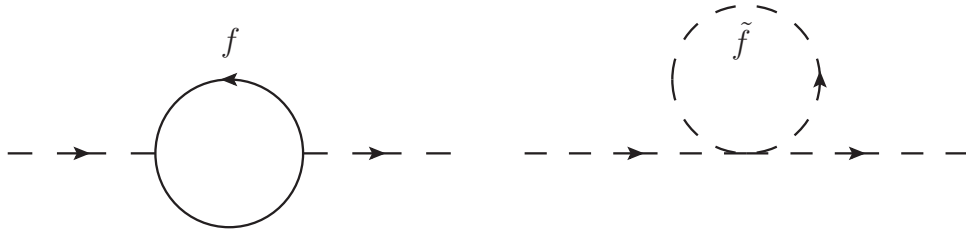

Figure 1.8: Contributions to the Higgs boson's self-energy from fermion (left) and sfermion (right) loops.

This problem cannot be avoided by regularising in a different way, such as by using dimensional regularisation. In this case, the first term is no longer present, but the second term is, which quadratically diverges with the fermion mass. So one also expects large mass corrections even with such regularisations, as new states are expected with masses above the

electroweak scale. Furthermore large mass corrections from new states are expected even if they do not couple directly to the Higgs, but rather through another particle.

In SUSY theories, this problem is resolved by considering the effect of the fermion's superpartner (called a sfermion[1]), a scalar particle which can also provide a loop correction to the Higgs mass (see Figure 1.8). The total mass correction from both these loops is then

$$\Delta m_H^2 = \frac{1}{8\pi^2}(\lambda_S - |\lambda_f|^2)\Lambda^2 + \dots, \tag{1.37}$$

where λ_S is the scalar coupling.

Invariance under SUSY requires $\lambda_S = |\lambda_f|^2$, thus there is a perfect cancellation between the corrections, which can be proven to all orders, and the hierarchy problem is solved. Although if the symmetry was perfect, the superpartners would have the same mass as their SM counterparts, and should have been observed by now. Therefore any realistic SUSY theory must be broken, but in such a way as to preserve its ability to solve the hierarchy problem; *i.e.* it must allow for unequal masses, though the cancellation of quadratic divergences must hold, this is called a softly broken SUSY theory. In such a scenario, there are still the logarithmically divergent terms to consider, which are

$$\Delta m_H^2 = m_{\text{soft}}^2 \left[\frac{\lambda}{16\pi^2} \log(\Lambda/m_{\text{soft}}) + \dots \right], \tag{1.38}$$

where m_{soft} determines the mass splitting between the fermion and its superpartner. This means the masses of the SM fermions' superpartners cannot be too large, as then the mass correction would be also and we would again need fine-tuning.

Amongst the ensemble of new terms added in a SUSY theory are those which violate baryon and lepton number. This presents a problem, as they predict processes which have not been observed, such as proton decay. To avoid this, one can implement R-parity, a $\mathbb{Z}_2$ symmetry under which SM particles are even and superpartners are odd, which forbids the unobserved processes. Coincidently this makes the lightest SUSY particle stable and if it is electrically neutral, then it is a DM candidate. Neutralinos are mixed states of the neutral

[1]The nomenclature in SUSY is to prefix every fermion's superpartner with s- (*e.g.* selectron, stop, *etc.*) and to affix -ino to the end of every boson's (*e.g.* gaugino, Higgsino, *etc.*).

Higgsinos[1] ($\tilde{H}_u^0, \tilde{H}_d^0$) and neutral gauginos ($\tilde{B}, \tilde{W}^0$). The lightest neutralino could be a DM candidate, and to many is the most promising. See [79] for a detailed introduction to SUSY.

1.3.2 Building Simple Models

Models of DM are often complex with large numbers of new states and interactions, however the channels relevant to DM searches can be much more limited. With this in mind, simpler theories can be constructed which contain the relevant terms and aptly describe the DM phenomenology; effective field theories and simplified models are made for this purpose, and can encapsulate the physics of many fuller theories.

Effective field theories are approximations of UV complete models valid below a particular cut-off scale. They typically contain one new state (DM), and a single non-renormalisable four-point interaction via which it communicates with the SM. In 1933 Fermi [80] suggested such an effective theory to describe β-decay with the interaction

$$\mathcal{L} = \frac{G_F}{\sqrt{2}} \bar{\nu_\mu} \gamma^\alpha (1 - \gamma^5) \mu \bar{e} \gamma_\alpha (1 - \gamma^5) \nu_e. \tag{1.39}$$

We now know β-decay is mediated by W bosons, however it is well described by this interaction at energies far below the W mass. At such energies the W can be integrated out, and this effective theory is derived.

In effective field theories of DM, the principle is the same: the new physics describing the interaction is at a scale much higher than what is being experimentally probed, and so an effective interaction can be used. For example a vector operator could be considered, given by

$$\mathcal{L} = \frac{1}{\Lambda^2} \bar{f} \gamma^\mu f \bar{\chi} \gamma_\mu \chi, \tag{1.40}$$

where χ is the DM candidate, f is any SM fermion, and Λ is cut-off scale of the interaction, beyond which the theory breaks down.

Effective field theories clearly have great appeal as they are arguably the simplest DM models one could construct and could represent many complete DM theories. However a

[1] Two Higgs doublets are required because the superpotential must be holomorphic in left-chiral superfields; one cannot generate up-type quark masses using the conjugate of a single Higgs doublet without spoiling SUSY. Thus a second doublet is introduced with opposite quantum numbers to resolve this issue, and to insure anomaly cancellation. For further details see [79].

problem arises when utilising effective field theories at colliders (which will be discussed in Section 1.4.3), motivating simplified models instead.

The fundamental idea of simplified models is the same as effective field theories; to create a simple theory, which can represent a plethora of more complex models. The difference with simplified models is that they do not use higher dimensional non-renormalizable operators to do so, requiring the mediators to be physical degrees of freedom. While such models are more complicated than effective field theories, they have a wider range of validity. For example, if the effective field theory considered above (1.40) was inadequate for a study, one might instead use the simplified model

$$\mathcal{L} = g_\chi V_\mu \bar{\chi}\gamma^\mu \chi + g_f V_\mu \bar{f}\gamma^\mu f, \tag{1.41}$$

where V is a new vector mediator. The cut-off of the effective theory is then related to the fundamental parameters via $\frac{1}{\Lambda^2} = \frac{g_\chi g_f}{m_V^2}$, where m_V is the mediator's mass.

Using higher dimensional operators and terms such as this, toy models of DM may be built. A successful theory will contain a new stable particle, which can be guaranteed if this state is odd under a $\mathbb{Z}_2$ symmetry and the terms added conserve this symmetry. Furthermore the particle should not be charged under the $\mathrm{U}(1)_{\mathrm{EM}}$ symmetry.

There are several DM candidates not discussed here which have received much attention, to name a few: axions [81–83], sterile neutrinos [71, 84], gravitinos [79, 85], and Kaluza-Klein DM [86]. We shall not discuss these further, but for the interested reader there is a review of DM candidates which details these models and more [45].

1.4 Searches and Signals

Thus far we have seen the evidence for DM, how it may be created, and examined a selection of particle models; in this final section we shall discuss attempts to detect it, and the subsequent constraints models must adhere to. Here collider, and direct and indirect detection searches will be briefly reviewed, as well as theoretical bounds.

1.4.1 Direct Detection

Our solar system is travelling through the Milky Way's DM halo at a velocity of $v_0 \sim 220$ km s^{-1}. Direct detection experiments aim to observe the scattering of this DM "wind"

off a target mass inside a detector. To optimise the sensitivity, backgrounds must be as low as possible; usually this means detectors are placed underground where they can be shielded from cosmic rays.

DM scattering events may be detected from three different products of a nuclear recoil:

- Phonons: Vibrations travelling through the target mass detected as a temperature rise.
- Scintillation: Light emitted from an excited nuclei.
- Ionization: Light emitted when an electron, freed by the scattering, recombines.

Electron recoils caused by background events also deposit their energy into these channels, although with differing fractions. To discriminate between electron and nuclear recoil events, there are two approaches: detect two different channels and use the relative energy deposition or detect only a single channel and use the signal's variation in time. Direct detection experiments are typically capable of detecting nuclear recoil energies (E_R) of $\mathcal{O}$(1-100) keV, which is optimal for WIMP searches.

Analyses of direct detection searches depend on the properties of the DM halo, *i.e.* the local density and velocity distribution. For consistency and comparability, these searches typically use the Standard Halo Model (SHM), where DM is distributed as an isotropic, isothermal sphere with a local density of $\rho_\odot = 0.3$ GeV cm^{-3} and a Maxwell-Boltzmann velocity distribution, but cut-off at the escape velocity of the galaxy, *i.e.*

$$f(\mathbf{v}) = \begin{cases} \frac{1}{N}(e^{-v^2/v_0^2} - e^{-v_{\rm esc}^2/v_0^2}) & v < v_{\rm esc} \\ 0 & v > v_{\rm esc} \end{cases}, \tag{1.42}$$

where N is a normalization constant, and v_0 in the SHM is same as defined at the start of the section. A recent RAVE survey measured the escape velocity to be $v_{\rm esc} = 533^{+54}_{-41}$ km s^{-1} [87], however direct detection analyses' dependence on the choice of $v_{\rm esc}$ is weak [88]. While a reasonable model, the actual DM halo is likely to deviate from the SHM, as was shown in numerical simulations [89–92].

Direct detection experiments are sensitive to both spin-independent (SI) and spin-dependent (SD) interactions, where former is dependent on the number of nucleons, and the latter on the nuclei's total spin. Whether the scatterings are SI, SD, or both, will depend on the theory.

These scattering cross-sections are defined as

$$\begin{aligned}\sigma^{\text{SI}}_{\chi\text{-}N} &= \frac{4\mu^2_{\chi N}}{\pi}[Zf_p + (A-Z)f_n]^2, \\ \sigma^{\text{SD}}_{\chi\text{-}N} &= \frac{32\mu^2_{\chi N}}{\pi}\frac{J+1}{J}[S_p a_p + S_n a_n]^2 G_F^2,\end{aligned} \tag{1.43}$$

where Z (A) is the atomic (nucleon) number, J is the nuclear spin, $S_{p,n}$ are the nucleon spin expectation values, and $f_{p,n}$ and $a_{p,n}$ are the effective DM-nucleon couplings. The form of the effective couplings is model-dependent, however as the nuclear recoils under study have low energy, effective interactions are often considered.

For example, in the case of a scalar interaction of the form $\mathcal{L} \supset \alpha_q \bar{\chi}\chi\bar{q}q$, the interactions are SI and the effective couplings are given by

$$f_{p,n} = \sum_{q=u,d,s} f^{(p,n)}_{T_q} \alpha_q \frac{m_{p,n}}{m_q} + \frac{2}{27} f^{(p,n)}_{TG} \sum_{q=c,b,t} \alpha_q \frac{m_{p,n}}{m_q}, \tag{1.44}$$

where

$$\begin{aligned} f^{(p)}_{T_u} &= 0.020 \pm 0.004, \quad f^{(p)}_{T_d} = 0.026 \pm 0.005, \quad f^{(p)}_{T_s} = 0.118 \pm 0.062, \\ f^{(n)}_{T_u} &= 0.014 \pm 0.003, \quad f^{(n)}_{T_d} = 0.036 \pm 0.008, \quad f^{(n)}_{T_s} = 0.118 \pm 0.062, \end{aligned} \tag{1.45}$$

and $f^{(p,n)}_{TG} = 1 - \sum_{q=u,d,s} f^{(p,n)}_{T_q}$ [93]. If instead there is a vector interaction $\mathcal{L} \supset \alpha_q \bar{\chi}\gamma_\mu\chi\bar{q}\gamma^\mu\bar{q}$, the interactions are still SI, but $f_p = 2\alpha_u + \alpha_d$ and $f_n = \alpha_u + 2\alpha_d$. For further information on SD scatterings see [94].

In the event an experiment does not find an excess of events signalling DM detection, limits may be placed on the scattering cross-section. A summary of SI WIMP scattering results is presented in Figure 1.9, showing limits from past studies along those projected by future detectors. Currently LUX offers the most stringent limit, whose 2013 analysis result [95] is shown in the figure; however since then there has been an improved analysis with a $\sim 20\%$ lower limit [96][1]. Of the future detectors, the first results will likely come from DEAP-3600 [98] and XENON1T [99], which expect at least an order of magnitude improvement in sensitivity. Further upgrades to these experiments are planned, as are several other detectors such as, DarkSide-G2 [100], DARWIN [101], LZ [102], and SuperCDMS at SNOLAB [103], which insure direct detection limits will go steadily further down over the coming years.

[1]Results from 332 new live-days of data were recently presented [97], and are expected to be published soon.

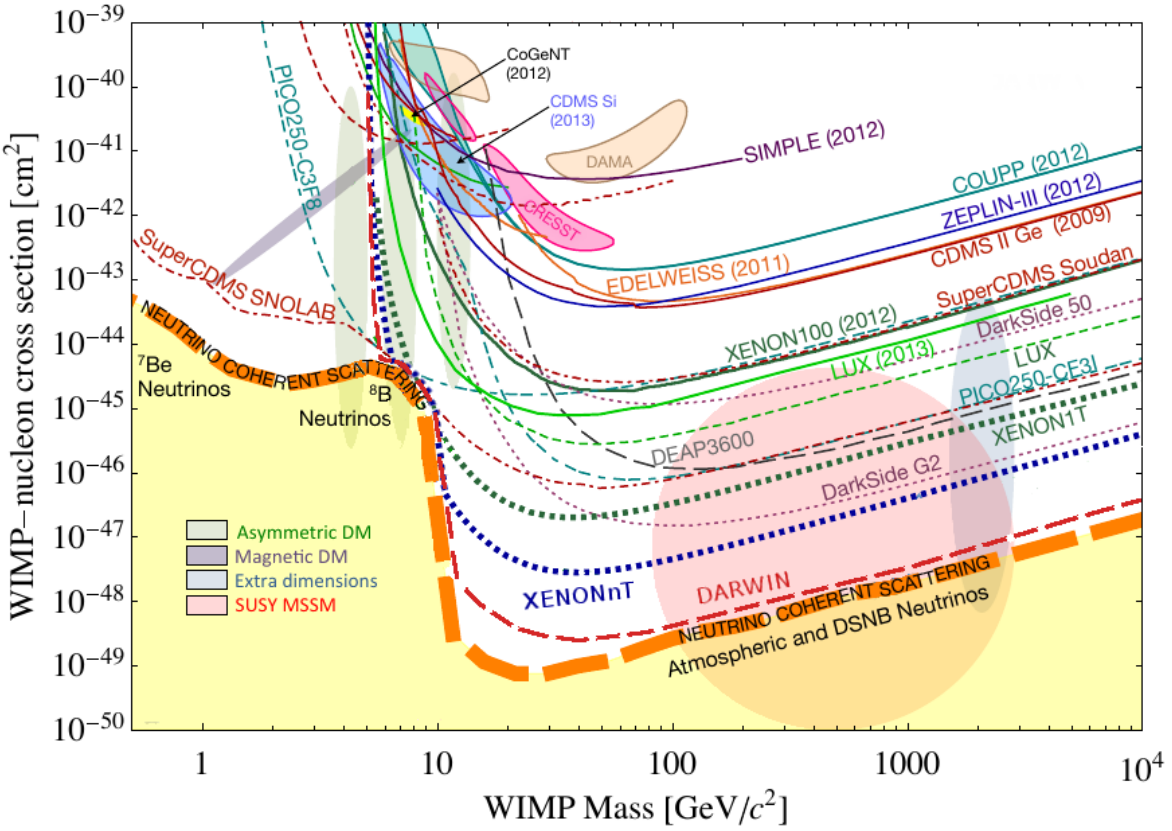

Figure 1.9: A summary of SI WIMP scattering limits from past and future direct detection experiments, taken from [104]. Also shown are the neutrino background threshold (orange dashed line), fits to claimed signals (shaded regions with outlines), and the regions of where signals of various models are expected to be found (shaded regions without outlines).

Detectors pushing the sensitivity limit will eventually encounter the "neutrino floor", where solar, atmospheric, and diffuse supernovae neutrinos produce a large background [105–108], shown in Figure 1.9. This poses a new challenge for direct detection searches, as these neutrino recoils will be indistinguishable from those of a WIMP. Conventional detectors are effectively limited by this neutrino bound, however detectors sensitive to the direction of the nuclear recoils will be able to distinguish much of this background, and so push pass the neutrino floor [109].

Possible candidate signals for DM have been seen by CRESST, CDMS Si, CoGeNT, and DAMA, the last of which being the most significant. DAMA/NAI, a NaI scintillation detector, reported an annual modulation in the event rate [110], which could be explained by the Earth moving with and against the DM "wind" flowing through the solar system. The Earth is

moving in the direction of the star Vega, meaning a signal of DM should peak around the beginning of June and be at its lowest in December. The phase and period of the DAMA/NAI modulation matched this well. Since then, the next generation detector, DAMA/LIBRA continued to measure this modulation, and the combined signal is now at $9.3\,\sigma$ CL [111]. The signal is well fitted by WIMPs with masses of ~ 10 GeV or ~ 80 GeV, depending on whether it is mostly sodium or iodine recoils respectively; DAMA/LIBRA cannot determine which nuclei is recoiling.

CoGeNT, a germanium ionization detector, also searched for this annual modulation and found one with a significance of $2.2\,\sigma$, however its amplitude was 4-7 times that expected in the SHM [112]. It also reported an small excess of low energy ionisation events [113, 114], consistent with $\sim$ 10 GeV WIMPS. CRESST found an excess of low-energy events with a 4σ significance [115], however it had problems with decaying polonium deposited in the clamps holding the detector, which has raised questions [116]. CDMS-II searched for annual modulation and found no such signal [117], however CDMS Si, looking WIMPs using the silicon detectors of CDMS-II, reported 3 low energy events with a 5.4% probability of being produced by known backgrounds, compatible with a ~ 10 GeV DM candidate [118].

While these signals offer some promise, their fits do not show good agreement with each other, as seen in Figure 1.9. However, the fits depend on the particle and astrophysical model, and by varying these some agreement may be restored [119–123]. Null results from other searches also give these signals issue; limits from LUX [96], SuperCDMS [103], and others [124] are in strong conflict with some or all of them. Furthermore the tension persists even when assuming SD couplings [125]. Although there are issues that need to be addressed, no clear alternate explanation for DAMA's annual modulation signal has emerged — this ongoing puzzle is one reason of many to keep a keen eye on direct detection searches.

1.4.2 Indirect Detection

As established in Section 1.1, the mass of the Universe is dominated by DM, as are most of the astronomical systems inhabiting it. Knowing this, motivation to search for the annihilation or decay products of DM within such systems is clear; this is called indirect detection. These searches typically look for evidence of DM by detecting photons, neutrinos, positrons, or antiprotons. Here, we will discuss a selection of experiments probing these channels, and any

possible signals of DM they may have seen.

The Fermi Gamma-ray Space Telescope (Fermi) was launched in 2008 and built to measure the γ-ray sky. Its main instrument is the Large Area Telescope (LAT), which measures γ-rays of about 20 MeV to over 300 GeV covering approximately 20% of the sky [126]. Such γ-rays may be produced in DM annihilations into (for example) quark final states; they are radiated during the hadronic cascades, and created in the decays (mainly from neutral pions). These indirect annihilations into γ-rays will produce a continuum, however line signals are also possible if DM annihilates/decays directly into γ-rays (*e.g.* via a charged particle loop). There are various astronomical objects whose γ-ray spectra we can search for DM in which have different advantages (and disadvantages) dependent on the DM model under study.

The Galactic Centre (GC) of the Milky Way is an excellent target for γ-ray searches as the density of DM is expected to be very large, and thus so is the signal. Indeed an excess peaking in the range 300 MeV to 10 GeV has been observed [127, 128], and shown to be consistent with DM annihilations. DM of ~ 10 GeV mass annihilating dominantly into leptons, or ~ 30 GeV DM annihilating dominantly into bottom quarks, could explain the excess. However the GC is a complex astrophysical region with poorly understood backgrounds, and as such the signal carries a degree of doubt. Unresolved millisecond pulsars distributed in a manner akin to the DM halo is the leading alternative explanation for the Galactic Centre Excess (GCE) [129]. There are other issues with dark interpretations of the GCE, which motivated our work in [3]; this is discussed in Chapter 5.

Given the challenges with backgrounds, it is appropriate to study astrophysical objects for which this problem is minimal: dwarf spheroidal galaxies (dSphs) make excellent such candidates. These are small DM dominated satellite galaxies with low astrophysical backgrounds orbiting larger galaxies (such as the Milky Way). Combined analyses of several of the Milky Way's dSphs [130, 131] often provide the most stringent indirect detection limits on a DM model.

One can also search for DM in other parts of the photon spectrum, such as in X-rays, and recently these searches have presented interesting results. In [132, 133] a weak 3.5 keV line was seen in the X-ray spectrum of various galaxies, using XMM-Newton X-ray data. Such a signal could be generated from the decays of sterile neutrinos [134] or axions [135], amongst others [136]. However other searches, expecting a clear signal, found no evidence of the 3.5

keV line [137, 138], casting doubt on the signal.

Cosmic rays comprise mostly of nuclei and electrons, with antimatter, like antiprotons and positrons, making up a small fraction as they are seldom generated in standard astrophysical processes. Thus antiparticle contributions from new physics, such as DM annihilations, could easily emerge above known sources in cosmic ray searches. An excess in the positron fraction was first reported by PAMELA in 2009 [139], and later confirmed with an improved analysis by AMS-02 [140]. Both saw a rise in the positron fraction spectrum above 10 GeV, which is consistent with DM annihilations [141], but could also be explained by nearby pulsars [142]. To distinguish between these hypotheses the spectrum must be measured at higher energies; pulsars predict the positron fraction to plateau with a gradual decrease thereafter, however if DM annihilations are responsible for the excess, then there should be a sharp drop. The AMS-02 mission will run for several more years, and its future results could probe this high energy region.

With neutrino telescopes one can search for DM in the same sources as γ-ray searches, however they are also capable of detecting the annihilations of DM captured in the Sun. These annihilations produce high energy neutrinos (~ 1 GeV) distinct from the background solar neutrinos. The measured annihilation rate tells us the capture rate, as the two are in equilibrium [143], and subsequently the scattering cross-section can be limited. As the Sun is predominantly hydrogen, capture will be largely due DM-proton scattering, which allows for both SI and SD analyses. While limits on SI scattering are weaker than those from direct detection searches, SD limits can give more stringent bounds in some cases [144–146].

Indirect detection searches benefit from a huge choice of sources and channels in which to explore, and furthermore they exploit the large DM abundances within systems more than direct detection searches[1]. However, they also suffer the most from astronomical uncertainties and backgrounds, which hamper efforts to find a clear cut signal of DM.

1.4.3 Collider Searches

A final way to search for DM is in the products of high-energy particle collisions. Accelerators can take particles to TeV scale energies before colliding them together in the heart of a detector

[1] The signal rates in indirect detection searches go as the square of the DM density, whereas direct detection rates are linearly proportional to the density.

which can identify the products and their kinematic properties. The Large Hadron Collider (LHC) outside Geneva is the most powerful built so far; in its first run it collided protons with a centre-of-mass energy of up to 8 TeV, which has now risen to 13 TeV in its ongoing second run. Its two main detectors ATLAS and CMS are currently the best in the field for DM searches.

The major advantage of collider searches, over direct and indirect detection studies, is the absence of astrophysical backgrounds, which (as we have seen) have created significant hurdles for the latter studies. However the drawback is that in the event of a DM candidate signal being detected, they provide no way in which to tell if the particle being created is the same as the DM dominating the mass of Universe.

If DM is created in a collision, it will not interact with the detector or decay within it into particles which will. However if produced alongside some "visible" matter, it can be inferred by the missing energy in the event. Typically the best way to search for DM is to look at mono-X events [147], where (for example) only one jet, photon, Z or W is seen in the detector. Such events usually involve the production of two DM particles, due the requisite stabilising symmetry in most theories.

Past ATLAS and CMS analyses often implemented an effective field theory approach to DM searches [148, 149], but it was recently pointed out [150] that there are limitations to this approach. The bounds these searches derive on the cut-off scale of the theory (beyond which it breaks down) can be comparable to the centre-of-mass energy of the collisions they study. This motivated the use of simplified DM models instead, as discussed in [151].

Monojet limits often provide the most stringent DM collider bounds; to illustrate the implementation of such limits in an example model, and how they compare to direct direction limits, we will consider the analysis in [152]. Here, a simplified model is used, where DM is a Dirac fermion which communicates to the SM quarks via a vector or axial-vector mediator. Figure 1.10 shows the monojet limits using 8 TeV LHC data translated into SI and SD WIMP-nucleon scattering cross-section bounds (blue lines), which are compared with the 2013 LUX bounds (red). As we increase in mass, monojet bounds have a sharp drop off, as the energy of the collisions limits the masses that can be probed. In the lower mass region, direct detection limits fall off, as the recoil energy of the collisions is too small to be detected within the energy window of the detector.

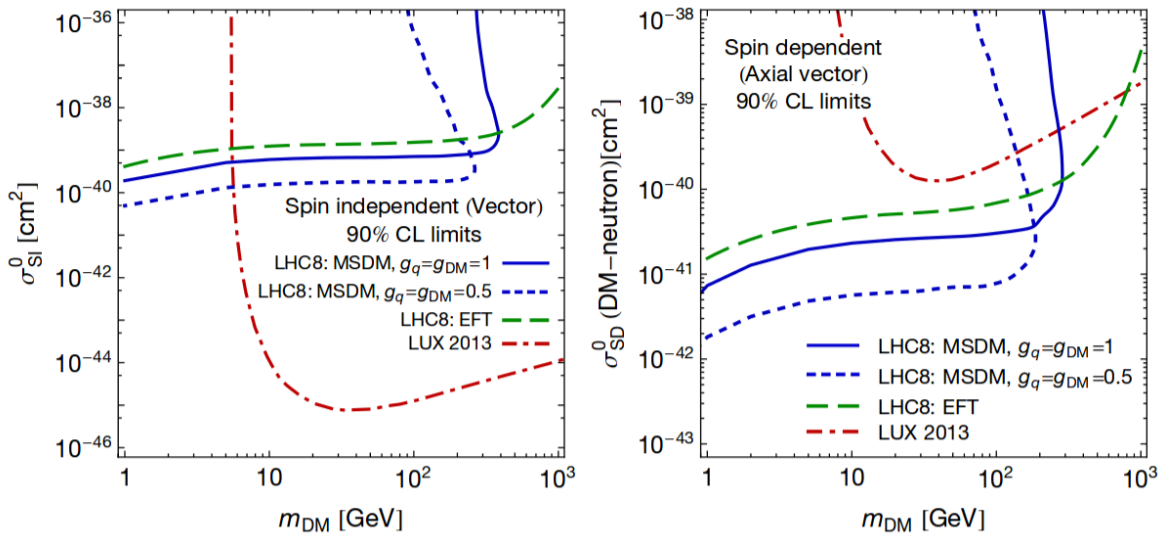

Figure 1.10: Monojet 90% CL limits using 8 TeV LHC data on the DM-nucleon scattering cross-section against mass in the case of SI (left) and SD (right) interactions. This uses a simplified model of Dirac fermion DM with vector (SI) or axial-vector (SD) interactions taken from [152]. The blue lines represent limits for two choices of couplings in the simplified model, while the green line gives the limit when using an effective field theory approach. These limits are shown alongside those from LUX (red) [95].

In the case of SI scattering, the overall scale of direct detection limits is far greater, thus only in the low mass region can monojet limits surpass them. For SD scattering the situation is more balanced; monojet limits are more stringent before their drop off. The disagreement between effective field theory (green line) and simplified model limits is also apparent in Figure 1.10, which highlights the issues with using effective field theories in collider searches.

1.4.4 Theoretical Bounds

While not under the umbrella of DM searches, it is appropriate here to also mention theoretical bounds. Issues can arise in DM models when perturbativity, unitarity, and vacuum stability bounds are violated.

A matrix element can be written as a series of successively higher order diagrams, where it may be well approximated by the first few terms (perturbation theory). The validity of this method relies on the convergence of the series, which is guaranteed so long as the couplings involved do not surpass a critical value. As an illustrative example consider a $2 \to 2$ scattering

process which depends on a single coupling λ, such that the tree-level diagram is proportional to λ^2, and the higher order terms go as integer powers of this factor. Naivety would lead us to believe unity the boundary beyond which perturbativity breaks down, however loop factors are introduced at higher orders which means the limit is instead $\lambda^2 \leq 4\pi$ [153]. Perturbativity is not a strict physical bound, as this limit may still be exceeded, however in such cases the theory would become strongly coupled and bound states would arise.

The probability for a particle reaction must never be greater than one, this is the unitarity bound. This concept was used in [154] to limit the thermally-averaged annihilation cross-section $\langle \sigma v \rangle$ to be

$$\langle \sigma v \rangle \lesssim \frac{4\pi(2n+1)}{m_\chi^2}\sqrt{\frac{x}{\pi}}, \tag{1.46}$$

where the parameters are the same as in Section 1.2.1. Assuming standard freeze-out with dominant s-wave annihilations, and requiring the correct relic density, they used this unitarity bound to provide an (almost) model-independent limit of ~ 340 TeV on the DM mass.

Unstable vacua in any theory are to be avoided, *i.e.* the potential of the theory must be bound from below in order to avoid an infinite vacuum expectation value (these are discussed in the coming chapter). Vacuum stability limits are model-dependent, *e.g.* in the Abelian Higgs model the vacuum is stable so long as the quartic coupling is not negative.

A vast breadth of DM searches provide us with an almost continual stream of results, reflecting the concerted efforts and zeal of the community. This helps make DM phenomenology a rich and varied topic, whose key subjects and findings have been touched upon here. In the coming chapters we will use the results presented here throughout the works discussed.

In this chapter, we have provided a brief introduction to one of the scientific world's biggest challenges — dark matter. Section 1.1 presented the case for its existence, highlighting evidence in rotation curves, colliding galaxies, and the CMB. MOND and MACHO interpretations of the evidence were put into question by other results raised here. In Section 1.2 we looked at how DM could have been produced, discussing freeze-out and its caveats in detail, as well as asymmetric production and freeze-in. This demonstrated that by considering different production mechanisms, different requirements are made on a DM theory. In Chapter 3 we will introduce one such mechanism which utilises decaying topological defects as a source of DM.

There exists a huge range of theories with DM candidates, a selection of these were briefly

reviewed in Section 1.3. After discussing SUSY and the neutralino, arguably the most popular candidate, we looked at effective field theories and simplified models. Finally in Section 1.4 the searches and signals for DM were summarised, including direct and indirection detection experiments, and collider seaches, as well theoretical bounds. Several possible signals were discussed, including the γ-ray excess in the GC, which is the subject of the work presented in Chapter 5. Dark matter is a broad subject encompassing a colossal body of work, here we have provided but a brief review; for further information there are a number of other works, such as [45, 50, 51, 94, 155, 156].

Chapter 2

Topological Defects

> It is very gratifying to realise that an idea and a theory that we worked on nearly 50 years ago has such huge relevance to actual physics.
>
> — Gerald Guralnik

Symmetries play a crucial role in particle physics — the SM was built using them and you will be challenged to find a modern particle theory in which a symmetry is not integral. Symmetries largely emerged as a driving force of theoretical physics in the early 20th century, with the inception of special relativity [157], when the idea that nature could be defined by symmetries became prominent [158].

Later, special relativity was reconciled with quantum mechanics, and quantum field theory was born. From this grew gauge theories: the quantum theories of the fundamental forces of nature, derived from ideas of invariance under a symmetry. The SM comprises of three gauge theories (although we will see the situation is a little more complex than that), describing the electromagnetic, weak, and strong forces. To further understand gauge theories, consider the free fermion field Lagrangian

$$\mathcal{L} = \overline{\psi}(i\partial\!\!\!/ - m)\psi, \tag{2.1}$$

where $\partial\!\!\!/ = \gamma^\mu \partial_\mu$ and m is the mass. The Lagrangian is invariant under what is called a U(1) global symmetry, where if $\psi \to e^{-i\alpha}\psi$ then it is left unchanged.

The case is more complex when α is spacetime dependent; this is referred to as a *local* or

gauge U(1) transformation, and under this the Lagrangian becomes

$$\mathcal{L} \to \mathcal{L}' = \overline{\psi}(i\not{\partial} - \not{\partial}\alpha(x) - m)\psi, \tag{2.2}$$

which is not what we started with. To insure invariance under this transformation, one must introduce a new field which couples to the fermions and transforms itself. This is done by promoting the derivative to a covariant derivative, *i.e.* $\partial^\mu \to D^\mu = \partial^\mu + igA^\mu$ (where g is a coupling constant), and allowing the new vector field (called the gauge boson) to transform as $A^\mu \to A^\mu - \frac{1}{g}\partial^\mu\alpha(x)$.

Our Lagrangian is still incomplete however, as a kinetic term for the gauge field must also be added, which preserves the gauge symmetry. Doing so, the full gauge invariant Lagrangian is

$$\mathcal{L} = \overline{\psi}(i\not{D} - m)\psi - \frac{1}{4}F^{\mu\nu}F_{\mu\nu}, \tag{2.3}$$

where the field strength tensor $F_{\mu\nu} = \partial_\mu A_\nu - \partial_\nu A_\mu$. One might also consider a mass term for the gauge boson, however such a term is not gauge invariant. This means the gauge boson must be massless if the symmetry holds, which is true of all gauge theories.

Quantum Electrodynamics (QED), the quantum field theory of electromagnetic interactions, is a gauge theory which uses such a local U(1) symmetry. In QED all electrically charged fermions transform under the symmetry and couple to the photon (the gauge boson) with a strength proportional to the charge. Weak and strong interactions can also be formulated as gauge theories, although they use more complex symmetry groups. The gauge theory of the strong force is called Quantum Chromodynamics (QCD) and uses the group SU(3) to transform triplets comprising of the three colour states (typically called red, green, and blue) of a quark. The number of new bosons required for gauge invariance is equal to the number of generators of the symmetry. The group SU(3) has eight generators, and so QCD requires as many gauge bosons, called gluons.

QCD possesses a curious property: interactions between coloured states strengthen as the distance between them increases. While the theory is not fully understood, it is thought that this quality is behind the non-observability of free coloured states, *i.e.* the principle of confinement which states that only colourless bound states can exist as free particles.

We understand this from a physical picture where one trys to separate quarks in a bound state. Eventually the energy required to push them further apart will be sufficient for quark

pair production, and thus one gets two new bound states rather than two free quarks. As the energy of the interaction increases (or equivalently the distance decreases) the interaction weakens, a quality, true of all non-abelian gauge theories, called asymptotic freedom [159,160]. This means that at high energies and inside hadrons quarks can be treated as free particles.

For weak interactions the case is more complex; they could be described by a SU(2) gauge theory which contains three new gauge bosons, however these would be massless and the observed weak vector bosons are not. This suggests the symmetry is broken and in such a manner as to generate the boson masses. A dynamical way through which this may occur in a gauge theory was first presented in the 60s by Higgs [161], Englert & Brout [162], and Kibble, Guralnik & Hagen [163] — through a phenomenon known as spontaneous symmetry breaking.

In this chapter we shall review spontaneous symmetry breaking and topological defects, massive structures which can arise through the breaking, and are important to the works discussed here. In the proceeding section spontaneous symmetry breaking is discussed, along with the Higgs mechanism. The latter is implemented in the Abelian Higgs model as an illustrating example, before its place in the SM is discussed. Following on from this, Section 2.2 details how topological defects can form after a spontaneous symmetry breaking phase transition. The types of defects are reviewed, as well as their relation to the symmetry which is broken.

Cosmic strings are a type of topological defect, and are the most relevant to the works presented here. This being so, Section 2.3 discusses their formation from the field theory, their gravitational interactions, and the condensates which can form on the string. Finally, in Section 2.4 we look at the evolution and decay of strings, and discuss two schools of thought on how these occur.

2.1 Spontaneously Breaking a Symmetry

Spontaneous symmetry breaking is a mechanism by which a symmetry of a theory is broken, or perhaps more correctly, hidden. Within the context of the SM, it is responsible for generating the masses of the W and Z weak gauge bosons, as well as the fermion masses (excluding the neutrinos). One can have a local or global symmetry within a theory, which they wish to extend with a term which is forbidden under the symmetry; one way to do this is to simply add

the term, and "ignore" the symmetry requirements, this is referred to as explicit symmetry breaking. If we use this to generate the W and Z boson masses, issues with unitarity arise in $WW \to WW$ scattering. Examining just the scattering of the longitudinal components, one finds the cross-section goes as

$$\sigma(W_L^+ W_L^- \to W_L^+ W_L^-) \approx \frac{G_F^2 s}{16\pi}, \tag{2.4}$$

which diverges with the centre-of-mass energy. This only occurs with the longitudinal components, with the dangerous divergences arising from their polarisation terms, $\epsilon_L \sim \frac{E}{M_W}$. Therefore in the low energy regime, the longitudinal component is suppressed over the transverse terms and there is no problem. However in the high energy regime, the longitudinal term dominates and violates the unitarity bound at approximately 1 TeV. New physics is therefore required to unitarize this process. With the additional of a SM Higgs boson, new WW scattering diagrams are opened up, in which a Higgs is exchanged; these new diagrams cancel the dangerous divergences and the issue is resolved. The cancellation is assured owing to the restoration of gauge symmetry to the theory. In addition to this issue with unitary, a theory of weak interactions with explicit symmetry breaking is also non-renormalizable.

One consequence of breaking a continuous symmetry is the emergence of (at least one) new degree of freedom, this is known as Goldstone's Theorem. This theorem states that for every generator of the symmetry that is broken, there is a new massless scalar, called the Goldstone boson. When it became desirous to use symmetry breaking to create massive particles, this theorem presented an impasse [164]. The Higgs mechanism resolved this issue by showing that when the symmetry is local, the Goldstone bosons are "eaten" by the gauge bosons of the symmetry, which subsequently become massive. To illustrate how the mechanism works, we will first consider it in action in the Abelian Higgs model.

2.1.1 In the Abelian Higgs Model

At the beginning of this chapter one of the simplest gauge theories was constructed, which was based on a local U(1) symmetry. Continuing to work with this example here, it will be shown how the gauge boson can become massive via the Higgs mechanism. This first requires the introduction of a new complex scalar (the Higgs field), which is charged under the same

symmetry:

$$\mathcal{L} \supset |D^\mu \phi|^2 - V(\phi) - \frac{1}{4} F^{\mu\nu} F_{\mu\nu}, \qquad \text{where} \qquad V(\phi) = \mu^2 |\phi|^2 + \frac{1}{2}\lambda(|\phi|^2)^2. \tag{2.5}$$

Spontaneous symmetry breaking arises from changes in the vacuum state, where the energy of the system is minimal. This will be where the kinetic terms are zero, and so the minimum is found from that of the potential $V(\phi)$. To insure vacuum stability, the quartic coupling λ, must be positive, however μ^2 need not be. If $\mu^2 > 0$, then the minimum is at zero, that is to say, the vacuum expectation value (VEV) $\langle\phi\rangle \equiv \langle 0|\phi|0\rangle = 0$. In this case the theory is as it appears and we just have a new scalar particle of mass μ. If instead $\mu^2 < 0$, then the minimum is now at $|\phi|^2 = -\mu^2/\lambda$ and the situation is more complex. Figure 2.1 shows the shape of this potential (often referred to as a Mexican hat potential), where it is evident that the minimum is no longer at zero, but lies along the circular trough, $\langle\phi\rangle = \sqrt{\frac{-\mu^2}{\lambda}} e^{i\theta}$. One can move between points in the trough using gauge transformations, which are all equivalent, as only the magnitude dictates what the physical theory will be.

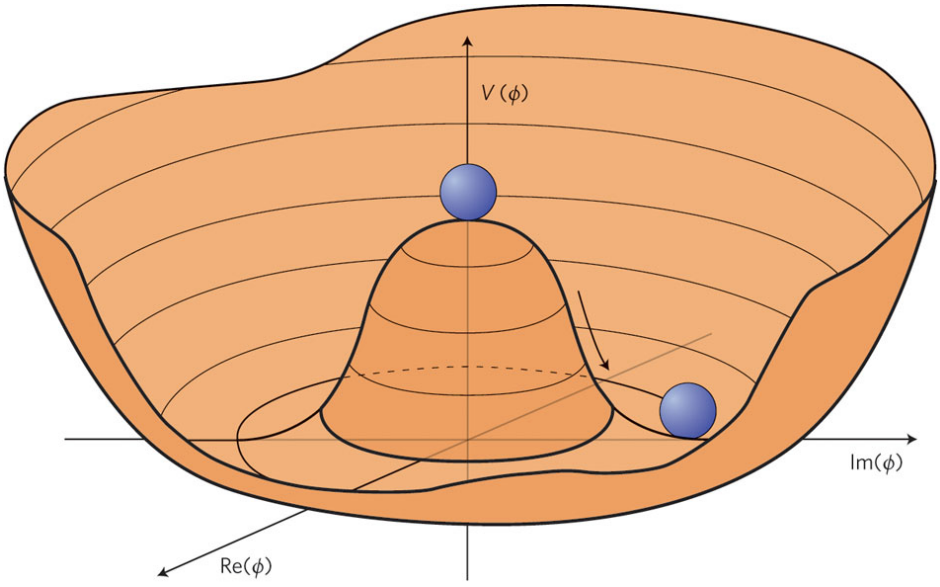

Figure 2.1: An illustration of the Abelian Higgs potential, taken from [165].

To rewrite the Lagrangian in terms of the physical degrees of freedom we must expand the Higgs field about its minimum, however this requires us to pick a particular vacuum state — this inevitable choice breaks the symmetry. Expanding about a generic point on the vacuum

manifold, ϕ may be rewritten as

$$\phi = \frac{1}{\sqrt{2}}(\eta + h)e^{i\xi}, \tag{2.6}$$

where $\eta = \sqrt{2}\langle\phi\rangle = \sqrt{-2\mu^2/\lambda}$, and h and ξ are real scalar fields. However ξ (the Goldstone boson) is an unphysical degree of freedom, as it can be removed via a transformation into the unitary gauge, *i.e.* $\phi \to e^{-i\xi}\phi$. Expanding ϕ in this gauge, our Lagrangian becomes

$$\begin{aligned}\mathcal{L} =& \frac{1}{2}(\partial_\mu h)^2 - \frac{1}{2}\lambda\eta^2 h^2 - \frac{1}{2}\lambda\eta h^3 - \frac{1}{8}\lambda h^4 \\ &- \frac{1}{4}F_{\mu\nu}F^{\mu\nu} + \frac{1}{2}e^2\eta^2 A_\mu A^\mu \\ &+ e^2\eta h A_\mu A^\mu + \frac{1}{2}e^2 h^2 A_\mu A^\mu.\end{aligned} \tag{2.7}$$

Inspecting (2.7) one sees a gauge mass term (with $m_A = e\eta$) has arose from the coupling to the original Higgs field. The massive gauge boson now has three degrees of freedom (before it had two), and knowing this, one can further see the necessity for the removal of ξ: to insure the total degrees of freedom are unchanged by symmetry breaking. Typically one says ξ has been "eaten" by the gauge field, becoming its longitudinal component.

In summary, a scalar field charged under a gauge symmetry generated the mass term for the associated gauge boson after it gained a VEV and broke the symmetry. Consequently this also introduced a new field h (a Higgs boson), which couples to the gauge boson. While this is one of the simplest models in which to implement the Higgs mechanism, it illustrates the key features true in any case.

2.1.2 In the Standard Model

Now the basics of spontaneous symmetry breaking and the Higgs mechanism have been established, it is appropriate to discuss their place in the SM. As previously mentioned, the SM before the Higgs was incomplete as there was no explanation for the masses of the W and Z bosons. Furthermore parity was seen to be maximally violated in weak interactions, and so left-handed and right-handed fermion chiral states must be charged differently under the electroweak gauge group; *i.e.* left-handed fermion states form doublets charged under an $\mathrm{SU(2)_L}$ symmetry, whereas the right-handed states are singlets. This meant fermion mass terms, $m\bar{f}f = m(\bar{f}_L f_R + \bar{f}_R f_L)$, were also forbidden by the gauge symmetry. By implementing the Higgs mechanism into the SM the problems with mass terms can be eloquently solved.

In the SM, weak and electromagnetic forces become unified above a scale in accordance with the electroweak theory [166–168], and only after a symmetry breaking phase transition do the electromagnetic and weak interactions emerge as separate forces. The electroweak theory is formulated with the left-handed doublets

$$L_L = \begin{pmatrix} \nu_e \\ e \end{pmatrix}_L , \qquad \text{and} \qquad Q_L = \begin{pmatrix} u \\ d \end{pmatrix}_L , \tag{2.8}$$

which are charged under an $\mathrm{SU(2)_L} \times \mathrm{U(1)_Y}$[1] symmetry, as well as right-handed singlets e_R, u_R, and d_R (but no ν_{eR}), which are charged under the $\mathrm{U(1)_Y}$. Here e, ν_e, u, and d can represent any electron-, neutrino-, up-, and down-type fermion respectively, however within a doublet the fermions must be of the same generation.

A scalar doublet H (the Higgs field), also charged under the $\mathrm{SU(2)_L} \times \mathrm{U(1)_Y}$ symmetry is added to the SM:

$$\mathcal{L}_\phi \supset |D_\mu H|^2 - V(H), \tag{2.9}$$

where $D_\mu = \partial_\mu + igW_\mu^a T^a + ig'YB_\mu$ with the index $a = 1, 2, 3$, and the form of V is the same as in (2.5). W^a and B are the massless gauge bosons, T_a are the generators of the $\mathrm{SU(2)_L}$ gauge group, g and g' are coupling constants, and Y is the hypercharge. The same covariant derivative appears in the kinetic terms of the doublets.

At the electroweak phase transition, H gains a VEV which breaks $\mathrm{SU(2)_L} \times \mathrm{U(1)_Y} \to \mathrm{U(1)_{EM}}$. In the unitary gauge, H is expanded about the VEV v to be

$$H = \frac{1}{\sqrt{2}} \begin{pmatrix} 0 \\ v + h \end{pmatrix}, \tag{2.10}$$

where h is the Higgs boson. As in the Abelian Higgs model, this expansion breaks the symmetry and generates gauge boson mass terms, however now the situation is more involved. Firstly, W^1 and W^2 gain the same mass and are recast into physical states via $W_\mu^\pm = \frac{1}{\sqrt{2}}(W_\mu^1 \mp W_\mu^2)$. Secondly a mixing is induced between W^3 and B giving rise to the physical mass eigenstates Z and A, the latter being massless. While the Higgs field breaks the symmetry, it does not do so perfectly; there is a remnant $\mathrm{U(1)_{EM}}$ symmetry of which A is the gauge boson (thus why it is massless). Fermions then couple to A with a strength proportional to

[1] $\mathrm{U(1)_Y}$ is not the same symmetry that represents QED; this emerges after symmetry breaking.

$Q = T^3 + Y$, which is the electric charge of the particle. Therefore we can see the remnant gauge theory is QED, and A is the photon.

Via the Higgs mechanism we have seen how W and Z boson mass terms arise, however fermion mass generation has yet to be addressed. These are produced via Yukawa terms

$$\mathcal{L} \supset y_e^{ij} \overline{L}_L^i . H e_R^j + y_d^{ij} \overline{Q}_L^i . H d_R^j + y_u^{ij} \overline{Q}_L^i . \tilde{H} u_R^j + \text{h.c}, \tag{2.11}$$

where i, j labels the generation, and $\tilde{H} = i\sigma_2 H^*$ (σ_2 being the Pauli matrix). Post-symmetry breaking, these terms generate the electron-, up-, and down-type fermion masses, however the neutrinos remain massless as there are no right-handed fields ν_R. Given the form of (2.11), we see the Yukawa couplings set both the fermion masses and couplings to h, which means the $h\bar{f}f$ coupling is proportional to the mass of the fermion; this is a key phenomenology consequence of electroweak symmetry breaking in the SM. This behaviour has been seen by ATLAS and CMS [169, 170] suggesting the Higgs boson found is at least SM-like.

One can also see from (2.11) that terms which mix generations are permitted, *i.e.* the Yukawa coupling matrices y_e, y_u, and y_d need not be diagonal. However we can diagonalize them, transforming the mixing fields into their mass eigenstates, *e.g.* $u_L^i \to U_{i\alpha}^u u_L^\alpha$, $d_L^i \to U_{i\alpha}^d d_L^\alpha$, *etc.* These transformations do not effect the photon and Z couplings, as they are diagonal in flavour, however $W^\pm$ couplings are between different flavours and so the transformations need not cancel out. For quarks, the interaction in terms of mass eigenstates becomes

$$\mathcal{L} \supset -\frac{g}{\sqrt{2}} \overline{u}_L^\alpha \gamma^\mu V_{\alpha\beta}^{\text{CKM}} d_L^\beta W_\mu^+ + \text{h.c.}, \tag{2.12}$$

where $V_{\alpha\beta}^{\text{CKM}} = U_{\alpha i}^{u\dagger} U_{i\beta}^{d\dagger}$ is called the CKM matrix [171, 172].

In the $W^\pm$ couplings to leptons, the same mixing does not arise however. Neutrinos are massless and as such there is no Yukawa matrix to diagonalize and therefore one can always choose a transformation that allows the current to be unchanged.

This brief overview of spontaneous symmetry breaking and the Higgs mechanism highlights some key features of the phenomena. The latter has now become a well ingrained device in modern particle physics, implemented in many theories. Furthermore, from this theory arose another relevant to this work — topological defects.

2.2 Forming a Topological Defect

Given the wide use of spontaneous symmetry breaking in BSM theories, we are well motivated to believe that as the Universe cooled it underwent a number of such phase transitions, not just the electroweak. The dynamics of these transitions are described using finite-temperature field theory, which formulates particle interactions in the non-zero temperature regime. We will first consider the simple example of a symmetry breaking phase transition in the Abelian Higgs model. For this discussion we need only concern ourselves with a single result of finite-temperature field theory: there is a temperature-dependent contribution to the mass, which by dimensional analysis must be proportional to T^2. Including this contribution, the Lagrangian may be written in the form

$$\mathcal{L} = |\partial_\mu \phi|^2 + m_0^2 \left(1 - \frac{T^2}{T_\mathrm{c}^2}\right) |\phi|^2 - \frac{1}{2}\lambda(|\phi|^2)^2, \tag{2.13}$$

where T_c is the critical temperature of the phase transition.

As the temperature drops below T_c the quadratic term changes sign, that is when $T \geq T_\mathrm{c}$ the VEV is zero (the normal phase) and when $T < T_\mathrm{c}$ it is non-zero (the ordered phase), *i.e.* $|\phi|^2 = \eta^2 \equiv \frac{m_0^2}{\lambda}$. Below T_c, the potential is as seen in Figure 2.1, where the vacuum state may lie anywhere on a circular vacuum manifold. Upon entering into the ordered phase, the system at different points in space needs not fall onto the same point on this vacuum manifold, but rather it can be a function of spacetime. Just after the phase transition, the temperature is still high enough to allow for fluctuations back to the normal phase, but as the temperature drops further the fluctuations diminish and the vacuum state settles onto a point on the manifold for each point in space.

During this process configurations of normal phase can become trapped within the vacuum structure. To illustrate this we will consider the case when ϕ is breaking a $\mathbb{Z}_2$ symmetry, under which it is odd. The potential in this case is akin to a flatten Mexican hat potential (see Figure 2.2), which has two possible VEVs $\langle\phi\rangle = \pm\eta$. Suppose there are two neighbouring spatial regions whose vacuum states, upon the phase transition, fall into opposing minima. To cross over the interface between these regions the vacuum state must change continuously, but as seen in Figure 2.2, this cannot be done while remaining in the vacuum manifold as the points are disconnected. Therefore in order to get a continuously varying $\langle\phi\rangle$, we are required to move through the normal phase as we pass over the boundary. In our Euclidean space this

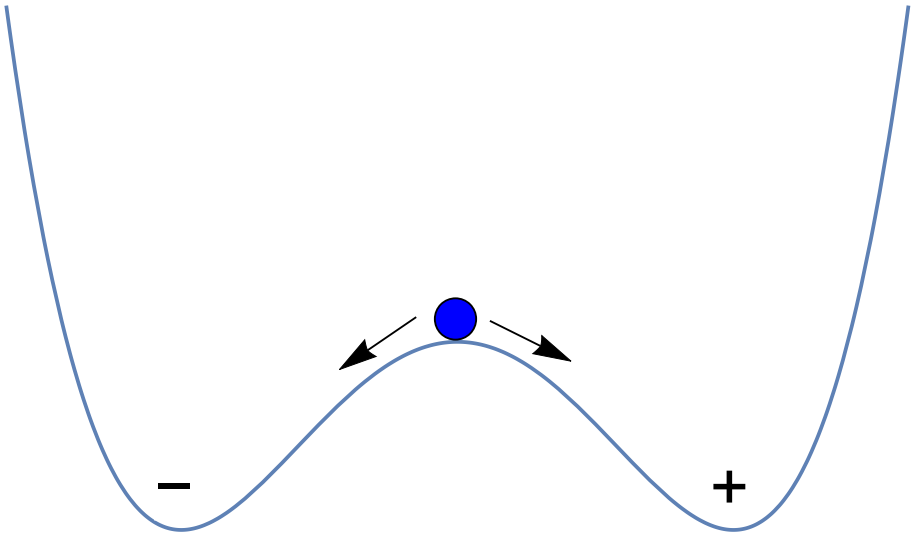

Figure 2.2: An illustration showing the potential in a ϕ^4 theory (2.13) where ϕ is odd under a $\mathbb{Z}_2$ symmetry. The system here has two choices of VEV ($\langle\phi\rangle = \pm\eta$) into which it can fall.

will produce 2D structures of normal phase (or *false vacuum*, if you will) called domain walls.

How gradually the vacuum evolves to the normal phase (and onto the other ordered phase) is derived from ϕ's equation of motion; one finds ϕ varies smoothly from one phase to the other with a characteristic width of $\sim (\sqrt{\lambda}\eta)^{-1}$ [173]. The normal phase is at a higher potential energy than the ordered, thus these structures are massive. Consequently it is energetically favourable for domain walls to minimise their surface area; *i.e.* they evolve under their own surface tension, $\sigma \sim \sqrt{\lambda}\eta^3$.

Domain walls are arguably the simplest topological defects, and have been useful here to illustrate the key features of topological defect formation. Phenomenologically speaking though, domain walls are heavily constrained and typically disfavoured. Their energy density falls slower than the matter or radiation contributions, and so it comes to dominant the energy of the Universe, thus overclosing it. Consequently, domain walls would also have left a significant imprint on the CMB, unless the VEV is below $\sim$ 1 MeV [174]. Domain walls always arise when a discrete symmetry is broken, so typically theories where this occurs are avoided, or else a work around is required [173, 175, 176].

Let us now consider the case when (2.13) is invariant under a U(1) symmetry, which is an increment more complex than our $\mathbb{Z}_2$ symmetry breaking model. Here the vacuum manifold

is now continuous and connected (see Figure 2.1), *i.e.* it can be represented by the group S^1 (a circle). This allows for the vacuum state to remain in an ordered phase as it pasts between two regions by moving through the vacuum manifold. However normal phase trapping can still occur via more intricate spatial configurations of the vacuum state. Figure 2.3 shows a configuration of vacuum states in a 2D plane which traps a point of normal phase at the center, in 3D space this is extended to a line defect called a *cosmic string*. Akin to domain walls, cosmic strings evolve under a characteristic string tension which in most cases is equivalent to its mass per unit length $\mu \sim \eta^2$ (where η is the magnitude of the VEV, as before).

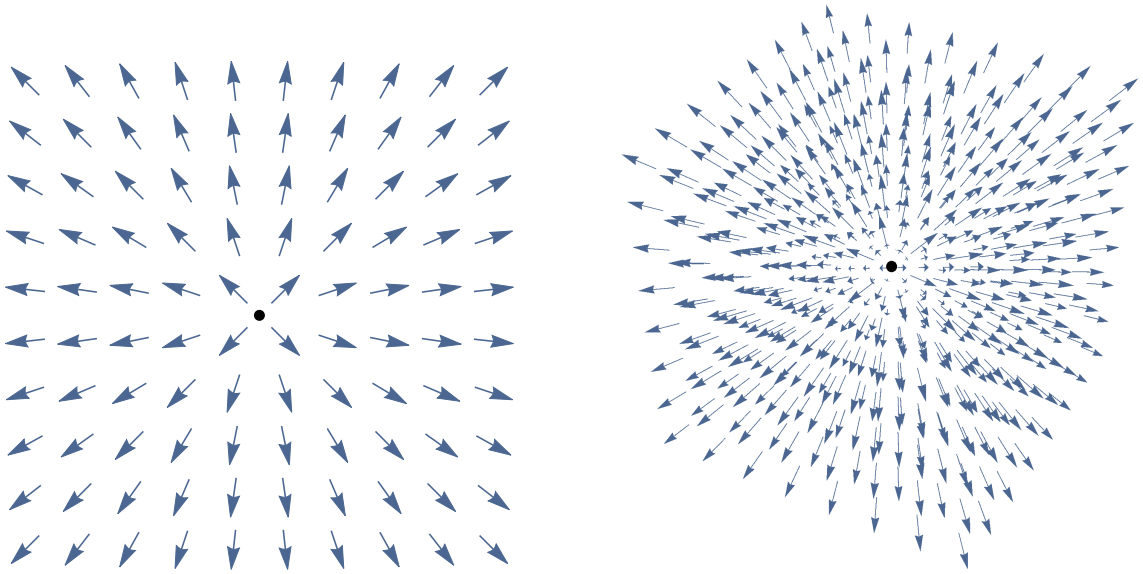

Figure 2.3: Spatial configurations of post-symmetry breaking vacuum states in a theories predicting cosmic strings (left), shown in a 2D plane, and monopoles (right). The position on the vacuum manifold is represented by arrows, and the points of normal phase are the central dots.

Other theories where more complex symmetries are broken can produce vacua described by the S^2 group (a sphere), this can lead to configurations such as those seen in Figure 2.3, which produce 0-dimensional point defects known as monopoles. Before even encountering topological defects one would have usually heard of monopoles from cosmic inflation. Many GUT theories predict the production of monopoles in the early Universe, but in such large abundances that they should have been observed by now [177]. This was one of the motivations for a period of exponential expansion in the early Universe (inflation), along with the (almost) isotropic CMB and apparent flatness of our Universe [35, 36].

2.2.1 Homotopy Groups

Thus far we have discussed topological defects qualitatively in order to a establish basic ideas upon which to build. Here we delve into the involved symmetries and topologies, and the importance of homotopy groups.

When a symmetry is broken in a theory the topology of the vacuum manifold, $\mathcal{M}$, will determine what type of defects will form (if any). This may be defined as

$$\mathcal{M} = \{\phi : V(\phi) = V_{\min}\}, \tag{2.14}$$

however we would like to express this in terms of the symmetry groups describing the phase transition. In general, one starts with a theory that is invariant under a symmetry group G, which upon symmetry breaking produces a theory that is now invariant under the subgroup H. If we define ϕ_0 as a single point on the vacuum manifold, then $g\phi_0$ where $g \in G$, is also on the vacuum manifold. Furthermore, there are elements of G which leave ϕ_0 unchanged, *i.e.* they act trivially ($g\phi_0 = \phi_0$), in this case $g \in H$. Given $h\phi_0 = \phi_0 \,\forall\, h \in H$, then elements of a left coset gH will give the same state when acting on ϕ_0. Thus G/H, the set of left cosets of H in G, is equivalent[1] to the set of all elements of G which have non-trivial action on ϕ_0, *i.e.* the vacuum manifold $\mathcal{M} = G/H$.

The topology of the vacuum manifold informs us what stable defects can form, or more specifically the homotopy groups $\pi_n(\mathcal{M})$ tells us. By definition $\pi_n(\mathcal{M})$ is the set of homotopy classes of the maps

$$f : S^n \to \mathcal{M}. \tag{2.15}$$

To elucidate this further we will consider the first homotopy group $\pi_1(\mathcal{M})$ concerning the mapping of $S^1 \to \mathcal{M}$, this is called the fundamental group. $\mathcal{M}$ will be some topological space and starting at a given basepoint one may consider paths traversing this space. Those which end at the same basepoint are the various mappings of S^1 to our topological space, which are referred to as *loops*. Two different loops are homotopic if they can be continuously deformed into one another within $\mathcal{M}$, and a homotopy class is the set of all homotopically equivalent loops (mappings). The set of all possible classes is then the homotopy group $\pi_1(\mathcal{M})$.

[1] One can have distinct elements of G, whose left cosets are equal ($gH = g'H$). These are not "double-counted" in the set of left cosets G/H, instead they are a singular element.

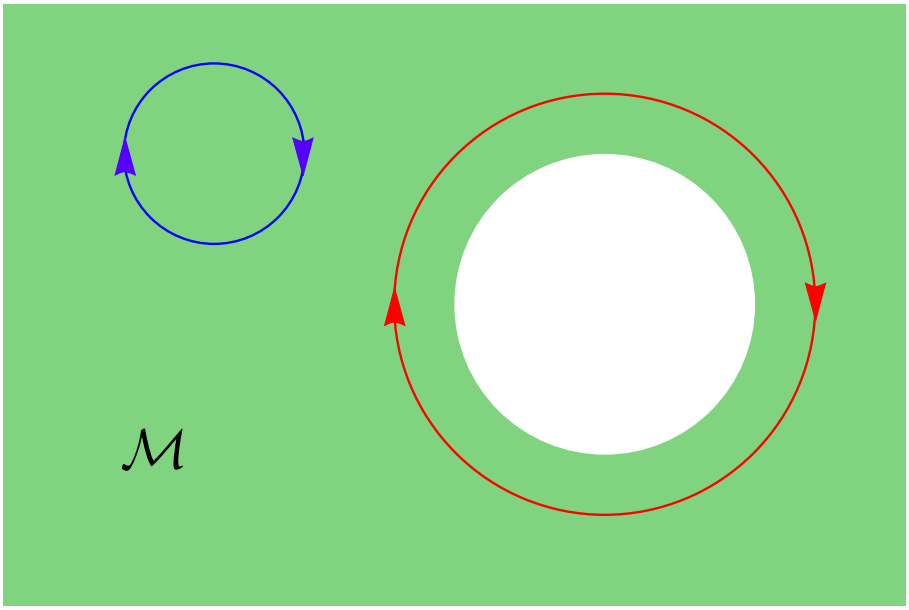

Figure 2.4: An illustration of contractible and non-contractible loops in a vacuum manifold. The green shaded region represents the vacuum manifold, which contains a hole. Loops not enclosing this hole, such as the blue loop shown, are contractible (to a point). Otherwise if it encloses the loop, such as the red one shown, then it is non-contractible.

Like all groups, the fundamental group has identity, reverse, and product elements (or classes). The identity class is the set of all contractible loops, *i.e.* all loops which are homotopic to the trivial loop: a loop whose path always lies on the basepoint (an infinitely small loop if you will). The difference between contractible and non-contractible loops is highlighted in Figure 2.4. The reverse class is the group of loops which traverse $\mathcal{M}$ in the opposite way, *e.g.* a class of non-contractible loops with a "clockwise" path will have a reverse with an "anticlockwise" path. The product classes consist of (non-contractible) mappings homotopic to one which loops multiple times around the same path of the manifold. These correspond to string solutions with higher winding numbers n, *i.e.* those which traverses a loop in $\mathcal{M}$ n times as one moves through a single loop in space.

If a homotopy group only contains the identity class, it is trivial and we say the manifold is *simply-connected*. A necessary condition for string formation is the non-triviality of the fundamental group of the vacuum manifold. As an example, consider the fundamental group of the vacuum manifold in the Abelian Higgs model (2.5), where $\mathcal{M} = \mathrm{U}(1)$. Here the vacuum

Condition	Defect
$\pi_0(\mathcal{M}) \neq \mathbb{1}$	Domain Walls
$\pi_1(\mathcal{M}) \neq \mathbb{1}$	Cosmic Strings
$\pi_2(\mathcal{M}) \neq \mathbb{1}$	Monopoles
$\pi_3(\mathcal{M}) \neq \mathbb{1}$	Textures

Table 2.1: A list of conditions on the homotopy groups of the vacuum manifold $\pi_n(\mathcal{M})$, in order for defects of the listed types to form.

manifold is easily visualised (as a circle), and one can, without any strenuous mathematical exercise, see that non-contractible loops are possible, thus the fundamental group is non-trivial and cosmic strings can therefore form. Similarly the non-triviality of the other homotopy groups allows the possibility of other types of defects forming; this is summarised in Table 2.1. For a more vigorous mathematical treatment see for example [173, 178].

Given these criteria for defect formation, and the discussion earlier on electroweak symmetry breaking, one might question if such defects arise in the SM. However while the fundamental homotopy group of the electroweak vacuum manifold is non-trivial, no stable string solutions are possible. This reflects an important caveat: while the homotopy conditions discussed are necessary for defects to form, they do not guarantee it [179].

In this section, a brief review of topological defects and their formation has been given in which issues with domain walls and monopoles were highlighted. These problems motivated us to focus on cosmic string physics in the works presented here, and as such a provision of further detail on the subject is appropriate.

2.3 Cosmic Strings

In the previous section we briefly reviewed how cosmic strings are generated through a spontaneous symmetry breaking phase transition, and through what kind of breaking do they arise. Derivations of string solutions from the field theory have not been touched upon however, which shall be discussed here. To demonstrate this, we shall once more consider the Abelian Higgs model (2.13) in the case of invariance under a global U(1) symmetry. For this

discussion, the Lagrangian is more appropriately given in the form

$$\mathcal{L} = |\partial_\mu \phi|^2 - \lambda(|\phi|^2 - \frac{1}{2}\eta^2)^2, \tag{2.16}$$

where a constant term has been added to insure the potential is non-negative everywhere.

The equation of motion of ϕ is then

$$[\partial^2 + 2\lambda(|\phi|^2 - \frac{1}{2}\eta^2)]\phi = 0, \tag{2.17}$$

to which the vacuum states are possible solutions, but there are also others — string solutions. We can derive these by considering a cylindrically symmetric ansatz

$$\phi = \frac{\eta}{\sqrt{2}} f(m_0 r) e^{in\theta}, \tag{2.18}$$

where m_0, as seen in (2.13), is the mass of the Higgs boson, and the form of the exponent reflects the requirement that the system must loop around the circular vacuum manifold an integer number of times (the winding number, n) as θ goes from 0 to 2π.

The form of $f(m_0 r)$ is not immediately known, however we need $f(0) = 0$ and $f(m_0 r \to \infty) \to 1$, in order to get symmetry restoration in the string center, and an ordered phase outside. The full form of $f(m_0 r)$ may be found by inserting the ansatz into the equation of motion, doing so one obtains

$$f'' + \frac{1}{\rho} f' - \frac{n^2}{\rho^2} f - \frac{1}{2}(f^2 - 1) f = 0, \tag{2.19}$$

where $\rho = m_0 r$ and a prime means the derivative with respect to ρ. This non-linear second-order differential equation has no known analytic solution, leaving $f(\rho)$ to be found numerically.

Here the solutions arose from the breaking of a global symmetry and as such are known as global strings or vortices. The energy density for these solutions goes as ρ^{-2} for large ρ, thus the energy (mass) per unit length μ (found by integrating over the plane perpendicular to the direction of the string), is infinite. Axion strings, produced via symmetry breaking in models with axions, are an example of such strings [180, 181].

Considering the same theory (2.16), but with a *local* U(1) symmetry, one obtains more a complex Nielsen-Olesen string solution [182]. In this case there is also a gauge field and so a set of equations of motion

$$\begin{aligned} (D^2 + 2\lambda(|\phi|^2 - \frac{1}{2}\eta^2))\phi = 0, \\ \partial_\nu F^{\mu\nu} + ie(\phi^\dagger D^\mu \phi - D^\mu \phi^\dagger \phi) = 0, \end{aligned} \tag{2.20}$$

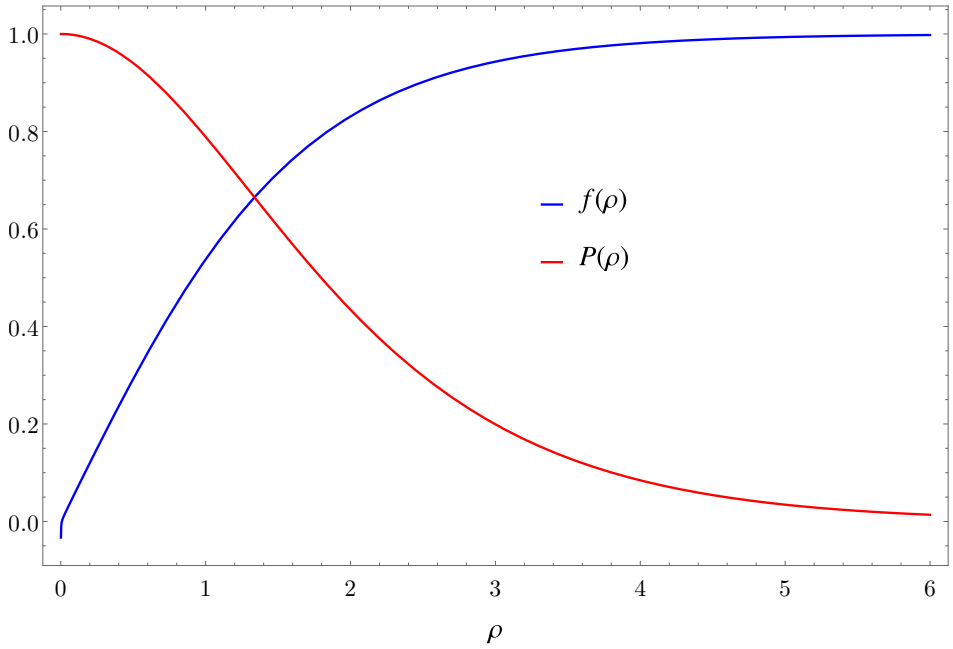

Figure 2.5: Radial string functions $f(\rho)$ and $P(\rho)$ from (2.22) in the case that $\beta = 1$ representing the cosmic string solutions to an Abelian Higgs model with a local U(1) symmetry.

where D_μ is the covariant derivative necessary for gauge invariance. As before, we again consider cylindrically symmetric ansatzes

$$\begin{aligned} \phi &= \frac{\eta}{\sqrt{2}} f(\rho) e^{in\theta}, \\ A^\mu &= \frac{1}{e}(P(\rho) - n)\partial^\mu \theta. \end{aligned} \tag{2.21}$$

Inserting these ansatzes into the Euler-Lagrange equations, we obtain[1]

$$\begin{aligned} f'' + \frac{1}{\rho} f' - \frac{n^2}{\rho^2} f - \frac{1}{2}(f^2 - 1)f - \frac{1}{\rho^2} P^2 f = 0, \\ P'' - \frac{1}{\rho} P' - \frac{1}{\beta} P f^2 = 0, \end{aligned} \tag{2.22}$$

where $\beta = m_0^2/m_v^2$ with $m_v = e\eta$ (the mass of the gauge boson). Figure 2.5 plots $f(\rho)$ and $P(\rho)$, showing how $f(\rho)$ smoothly varies from 0 to 1, *i.e.* from the normal to ordered phase, and how $P(\rho)$ peaks at $\rho = 0$ and flattens off as ρ increases. Since the gauge field's vacuum state is varying within the cosmic string, from $\vec{B} = \vec{\nabla} \times \vec{A}$ this tells us a magnetic field is produced, given by

$$B_z = \frac{m_0^2}{e\rho} P'. \tag{2.23}$$

[1]For more details on these derivations see [179, 183].

This translates to a magnetic flux of

$$\Phi_B = \oint_{\partial S} \vec{A}.d\vec{l} = \lim_{r\to\infty} \int_0^{2\pi} \frac{1}{e}|P(m_0 r) - n|d\theta = \frac{2\pi n}{e}, \tag{2.24}$$

which is quantized in units of $2\pi/e$ and is proportional to winding number of the string.

The mass per unit length of the cosmic string may be found from the energy density ϵ, which in terms of $f(\rho)$ and $P(\rho)$ is

$$\epsilon(\rho) = \frac{m_0^2\eta^2}{2}\left[f'^2 + \frac{\beta^2}{\rho^2}P'^2 + \frac{1}{\rho^2}f^2P^2 + \frac{1}{2}(1-f^2)^2\right], \tag{2.25}$$

thus μ is given by

$$\mu = \int \epsilon(r) r dr d\theta = \pi\eta^2 \int_0^\infty \left\{f'^2 + \frac{\beta^2}{\rho^2}P'^2 + \frac{1}{\rho^2}f^2P^2 + \frac{1}{2}(1-f^2)^2\right\}\rho d\rho. \tag{2.26}$$

Inspecting f and P in Figure 2.5, which is for the case when $\beta = 1$ (a typical value since both m_0 and m_v are set by the VEV), one may estimate that the term in the parentheses in (2.26) will be of order unity; given this we expect $\mu \sim \eta^2$. From numerical studies the term in the parentheses actually goes as $\ln\beta$, thus β need not be near unity for the μ approximation to hold. Cosmic strings are typically characterised by the parameter $G\mu$ (where G is the gravitational constant), which is referred to as the string tension. From its form, one can see that this gauges a string's gravitational strength.

Local strings are categorised into type I and type II dependent on the value of β. Type I strings occur if $\beta < 1$, where strings of any winding number n are stable. If instead $\beta > 1$ we get type II strings, where only the $n = 1$ solution is stable. The strings of higher winding number will decay in this scenario, splitting into n strings of unit flux $2\pi/e$. This reflects the interplay of two forces acting in the system: the first arises from the scalar field wanting to minimize the energy and thus join with other strings (an attractive force), and the second is the repulsive force between the magnetic fluxes of the strings. Given the width of these forces is characterised by $1/m_0$ and $1/m_v$ respectively, one can see how β's value determines the string type.

2.3.1 Gravitational Interactions

Cosmic strings are massive structures, and as such can have important gravitational consequences. The field equations of general relativity [25] which describe these interactions are

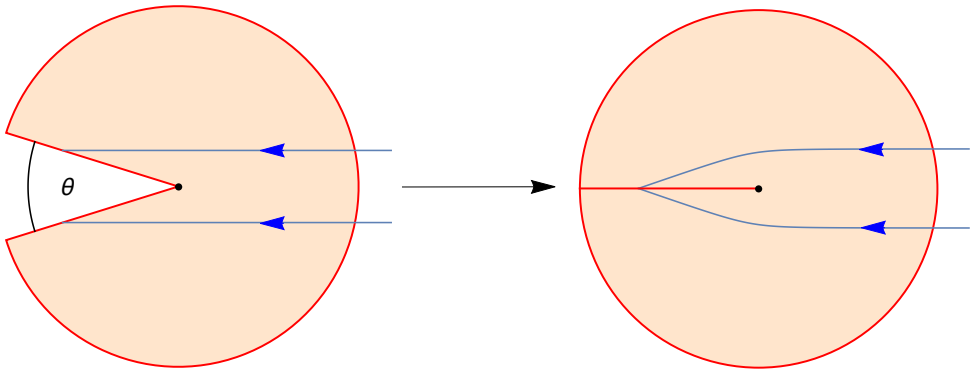

Figure 2.6: An illustration of how the conical space around a cosmic string allows the gravitational lensing of light. A cylindrical space (represented in red) has a slice of angular width θ removed from it. The edges are then pushed together "stretching" the space and transforming the geodesic path of light (shown as blue lines) travelling nearby.

dependent on the energy-stress tensor, which in the case of static straight local strings [176] is given by

$$T_{\mu\nu} = \mu \ \mathrm{diag}(1, 0, 0, -1)\delta(x)\delta(y). \tag{2.27}$$

This presumes the string is orientated along the z-axis and that the typical distances being considered are far greater than the width of the string, such that the latter has been taken to be zero. The T_{tt} term represents the energy density, while the T_{zz} term represents pressure along the z-axis. We can see that this latter quantity is negative, thus there is negative pressure along the string, that is to say, there is tension in the string. We also see that this tension, $T = -\mu$, is equal to the energy density, a relation which can be derived from lorentz invariance and conservation of energy.

Inserting this into the field equations one finds an intriguing result — the metric is flat, but conical (that is the angular coordinate runs from 0 to $2\pi - \delta$) in the vicinity of the string; this means the string can act as a gravitational lens. In Figure 2.6 we illustrate what is meant by conical space and how light is bent by it. Consequently an image of a source positioned behind a string may emerge on both sides of it. Several of these pairs of images aligned along a path would be a distinctive signal for the presence of a cosmic string.

By considering moving or non-straight strings, one finds a gravitational attraction is now exerted by the cosmic string (as opposed to simply a conically shaped spacetime). This

means, for example, that kinks (discontinuous turns in the path of a string) will be sources of gravitational attraction, and a moving string will affect the CMB [184]. Light from the surface of last scattering passing ahead of a cosmic string moving orthogonally to the line of sight will be redshifted, and the light behind will be blueshifted. This leads to temperature discontinuities along lines in the CMB, a distinct signature of cosmic strings.

Cosmic strings were originally a favoured explanation for the primordial perturbations required for structure formation in the early Universe [185, 186]. This was as an alternative to inflationary models, which also could create these fluctuations. However when acoustic peaks were seen in the CMB [187, 188], these were counter to cosmic string predictions, and ruled them out as the sole source of perturbations [189]. It was still thought that they could play a subdominant role, although CMB bounds on $G\mu$ limits this contribution to at most $\mathcal{O}(1)\%$ [190–195].

Having been ruled out as the main source of primordial perturbations, interest in cosmic strings waned [189]. However it was later renewed when cosmic strings were shown to arise in some models of string theory [196–200], opening a path for experimental tests of the theory. These cosmic *superstrings* are fundamental strings which have grown via an inflationary mechanism to cosmic sizes. Indeed, the numerous channels through which cosmic strings could arise makes their formation generic [201–204] and so studies of their possible consequences important.

2.3.2 Condensates and Superconductivity

Previously we saw how cosmic string formation in the case of a local U(1) symmetry also gave rise to structures on the gauge field. Interactions between the scalar field breaking the symmetry and other fields can generate further structures called *condensates* [205–207]. Section 2.1 established how mass terms can be generated upon the spontaneous symmetry breaking of a field, however in the core of a string the symmetry is restored and thus these consequences are reversed. If this regime change within the vicinity of the string means the interacting field sees a similar change, then this field is said to have condensed onto the string.

As an establishing example we will examine SM Higgs condensates, which are important in the works discussed here. Consider string production in the case of the Abelian Higgs model (2.16); taking into account the presence of the SM Higgs field, H, the scalar potential

of this theory may be written in the form

$$\begin{aligned} V(\phi, H) = \frac{1}{2}\lambda_1(|H|^2 - \frac{1}{2}v^2)^2 + \frac{1}{2}\lambda_2(|\phi|^2 - \frac{1}{2}M^2)^2 \\ + \lambda_3(|H|^2 - \frac{1}{2}v^2)(|\phi|^2 - \frac{1}{2}M^2), \end{aligned} \tag{2.28}$$

where both H and ϕ undergo spontaneous symmetry breaking, gaining non-zero VEVs $\langle H \rangle^2 = v^2/2$ and $\langle \phi \rangle^2 = M^2/2$ respectively.

Assuming ϕ breaks the additional U(1) symmetry at a scale much greater than the electroweak (*i.e.* $M \gg v$), there will be period after this phase transition where the electroweak symmetry is still intact and $\langle H \rangle$ is zero. Here strings have formed upon the ϕ field, but within their cores there is a false vacuum ($\langle \phi \rangle = 0$). Subsequently, the potential within the string includes the quadratic term $-\frac{1}{2}\lambda_3 M^2|H|^2$, as we see by inspection of (2.28). This contribution means the Higgs field's symmetry could be broken in the core of the string, but remain unbroken outside. The SM Higgs field's VEV, $\langle H \rangle$, inside will be of the order of M, so when the electroweak phase transition occurs, the VEV of the condensate will not be significantly affected as $M \gg v$.

This was an example of a bosonic condensate, which is any arbitrary scalar field whose symmetry is also broken within the vicinity of the string. Note here the genericity of these condensates; they form through scalar portal couplings which arise regardless of the symmetries each field is charged under.

Suppose now we have a bosonic condensate of a new scalar singlet S, charged under the electromagnetic $\mathrm{U}(1)_{\mathrm{EM}}$ symmetry. In the core of the string, the field solution is of the form $S = \frac{1}{\sqrt{2}}s(r)e^{i\alpha(x)}$. Taking the phase to vary linearly space and time, *i.e.* $\alpha = kz - \omega t$, it can be shown that the electromagnetic (Noether) current along the length of the string obeys

$$\frac{\partial j_z}{\partial t} = q^2 s(r)^2 E_z, \tag{2.29}$$

which is a London equation of superconductivity [208]. Therefore by allowing the bosonic condensate to be charged under the $\mathrm{U}(1)_{\mathrm{EM}}$ gauge symmetry, the string is now superconducting with the condensate field carrying the current.

This phenomenon was first suggested in [205] showing how superconducting fermionic condensates could also be rise. This occurs when a fermion field obtains its mass via a Yukawa coupling with the scalar field, thus at the core of the string you get fermion zero

modes of zero energy [209]. If the fermion field is also charged under the $U(1)_{EM}$ symmetry, then it can carry the current and make the string superconducting.

Issue arises in models predicting superconducting cosmic strings in what is referred to as the *vorton catastrophe* [210, 211]. Vortons are loop solutions predicted in such models which have non-zero angular momentum, and can stabilise. This can present a problem akin to that of monopoles; vortons produced in the early Universe can come to dominant the energy density of the Universe. Such scenarios are to be avoided, unless one requires very light strings, and so one must advocate an effect or mechanism by which the vorton relic abundance can be reduced. One way in which this could occur is via the consideration of quantum tunnelling permitting vorton decays.

Here we looked further into cosmic strings (one dimensional topological defects), reviewing the string solutions of the field theory, their gravitational effects, and the condensates which can form upon the string, and subsequently become superconducting. In order to further understand how DM can be produced from these strings, one must study their evolution and decays.

2.4 Cosmic String Evolution and Decay

Upon a phase transition (with the appropriate symmetry being broken) a cosmic network of strings form, which evolve under their own tension and under the expansion of the universe; doing so, they lose energy (decay) by radiating it into different forms. Firstly, they may lose energy via gravitational radiation as the oscillations of cosmic strings produce gravitational waves [212–214]. They can also emit particle radiation of various forms dependent on the particular model considered, *e.g.* in the case of an Abelian Higgs model, strings will emit Higgs and gauge bosons (associated with the symmetry and its breaking) [215, 216], or if we had superconducting strings, electromagnetic radiation may be emitted [205]. In the works described here, we consider the scenario when DM is amongst the particle radiation emitted, and can effect standard freeze-out physics.

Strings come in two types: long strings and loops[1], the former enter and exit at points on the horizon and in the case of the latter the ends meet. As the Universe evolves, long strings

[1]Earlier we referred to loops in the context of a vacuum manifold space, but here it is attributed to loops in *physical* space. From this point onwards that is the intended meaning, unless otherwise specified.

will straighten and loops will shrink and eventually disappear. Long strings can also create loops by intersecting with other strings or themselves; Figure 2.7 illustrates this procedure.

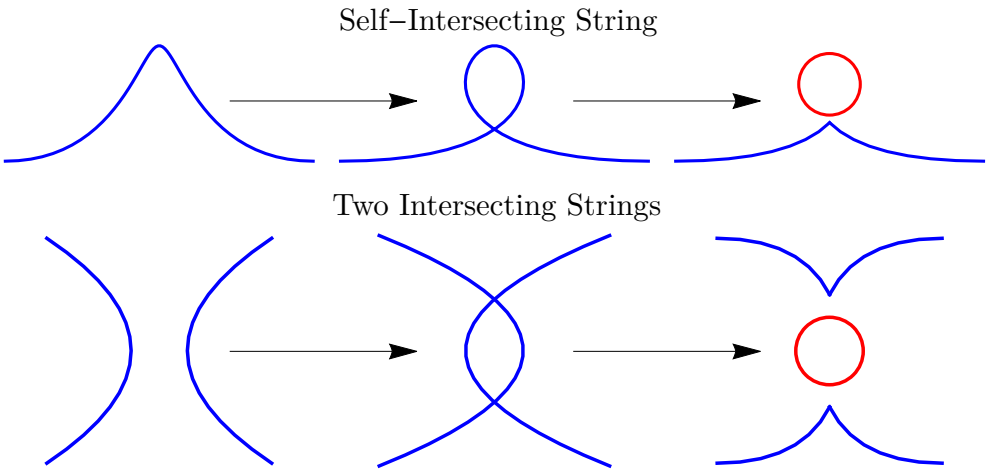

Figure 2.7: A diagram showing the mechanism for loop formation by the intersection of long strings. The top diagram shows formation through self-intersection, and the bottom shows formation from two different strings.

How the string network evolves, and into which channels with which fraction it loses its energy is a topic of debate. Here, two scenarios will be considered: one based on simulations of the Abelian Higgs model [217,218], and the other on the Nambu-Goto action of the string [173,179,183,219].

2.4.1 Abelian Higgs Field Simulations

Strings evolve on an expanding spacetime described by the FRW metric, which in conformal time is given by $ds^2 = a(\tau)^2(d\tau^2 - d\mathbf{x}^2)$, where $a(\tau)$ is the scale factor. Considering Nielsen-Olesen strings in the Abelian Higgs model (2.5), but now on the FRW metric, the action is

$$S = \int d^4x\sqrt{-g}\left(g^{\mu\nu}D_\mu\phi^\dagger D_\nu\phi - V(\phi) - \frac{1}{4}g^{\mu\rho}g^{\nu\sigma}F_{\mu\nu}F_{\rho\sigma}\right), \tag{2.30}$$

where $g^{\mu\nu}$ is the FRW metric tensor and g is its determinant.

The equations of motion under this new metric in the temporal gauge ($A_0 = 0$) are

$$\begin{aligned}\ddot{\phi} + 2\frac{\dot{a}}{a}\dot{\phi} - |\mathbf{D}|^2\phi + 2\lambda a^2\phi(|\phi|^2 - \frac{1}{2}\eta^2) = 0 \\ \partial_\nu F^{\mu\nu} + iea^2(\phi^\dagger D_\nu\phi - D_\nu\phi^\dagger\phi) = 0.\end{aligned} \tag{2.31}$$

These equations have been numerically solved by discretizing space into a lattice, then running simulations of the string networks evolution [215]. Here the majority of the energy loss was into particle, rather than gravitational radiation, and the system reached a scaling solution. In this regime the general structure in a comoving volume does not change, *e.g.* the network within a cube of length ct_1 at a time t_1 will appear similar to that at a later time t_2 in a cube of length ct_2. The energy density in this case goes as $\rho_{\rm cs} \propto t^{-2}$, thus the density parameter $\Omega_{\rm cs} = \rho_{\rm cs}/\rho_{\rm c}$ is constant.

2.4.2 Nambu-Goto Strings

If one assumes strings have zero width[1], then they can be described by a Nambu-Goto action, where the evolution and decay of the string network differs to what simulations of the Abelian Higgs model predict. In this formulation, one reduces from a 4D field theory to a 2D worldsheet[2] description — strings described in this manner are referred to as Nambu-Goto strings. The coordinates of the worldsheet are labelled by σ_a $(a = 0, 1)$, where typically σ_0 is time and σ_1 is the position along the string. The 4D spacetime coordinates X_μ of each point of the worldsheet are then a function of σ_a, that is $X_\mu = X_\mu(\sigma_a)$. The metric in this new coordinate system γ_{ab} is given by

$$\gamma_{ab} = \frac{\partial X^\mu}{\partial \sigma^a}\frac{\partial X^\nu}{\partial \sigma^b} g_{\mu\nu}, \tag{2.32}$$

and the action is

$$S = -\mu \int d^2\sigma \sqrt{-\gamma} = -\mu \int d^2\sigma (-\dot{\mathbf{X}}^2 \mathbf{X}'^2 + (\dot{\mathbf{X}}.\mathbf{X}')^2), \tag{2.33}$$

where γ is the determinant of the metric, and the dot and prime denote differentiation with respect to σ_0 and σ_1 respectively.

It is from this Nambu-Goto action that one can derive the strings behaviour. Again, one finds that the string enters a scaling regime as it did in the simulations of the Abelian Higgs model, however loop energy losses are dominantly into gravitational radiation in this scenario [213]. Particle radiation can still occur though via structural features called kinks and cusps. These are sharp (discontinuous) bends in the string and are illustrated in Figure 2.8.

[1] Such an assumption is reasonable when typical curvature radii in a network are far greater than the width of the strings [220].

[2] The path of a point in space through time is a worldline, the path of a string is a *worldsheet.*

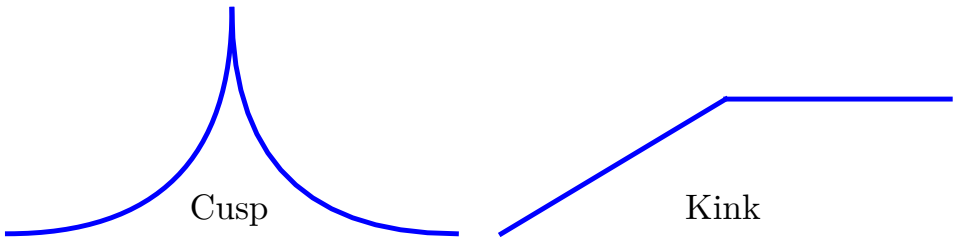

Figure 2.8: Illustrations of kinks and cusps on strings.

Cusps form on string loops during oscillations, when a point on the loop attains the speed of light and doubles back on itself. At such a point the string is self-interacting and particle radiation can be emitted upon their collapse. Kinks are the remnants of strings intersecting, and form on all strings involved, as illustrated in Figure 2.7. They also decay and are a source of particle radiation. Thus while gravitational radiation dominants loop energy losses, there is a secondary source of particles from cusps and kinks; this allows us to use this scenario as another channel through which DM could have been produced in the early Universe. These scenarios and their role in a mechanism for DM genesis is the focus of Chapter 3.

Symmetry topics are deeply entrenched in modern particle physics, and the works discussed here are indeed based heavily on such ideas. This chapter began with a review of spontaneous symmetry breaking, discussing the Higgs mechanism, and its place in the SM. Proceeding this, in Section 2.2, we moved onto topological defects, massive structures which can arise after symmetry breaking phase transitions. This section covered how they are formed, and how the symmetry involved determines if and what defects can arise.

Given their importance to this thesis, 1-dimensional topological defects called cosmic strings were further detailed in Section 2.3. Cosmic string solutions to global and local symmetries were discussed here, before their gravitational implications, condensates, and possible superconductivity were reviewed. Lastly in Section 2.4 we saw how cosmic strings evolve and decay, highlighting two scenarios in which particles may be radiated. For a reader searching for further information on topological defects there are books [173,183], and articles [179, 219, 221–223] which will enlighten them further.

Chapter 3

Dark Matter from Topological Defect Decays

> It is reminiscent of what distinguishes the good theorists from the bad ones. The good ones always make an even number of sign errors, and the bad ones always make an odd number.
>
> — Anthony Zee

Section 1.2 discussed DM genesis, mechanisms through which the observed relic density of DM could have been produced. These defined how our particle theory is connected to the astrophysical processes governing the relic density, and consequently, how it will be constrained by it. Typically this is assumed to occur via freeze-out [53–55], and the subsequently, the model under study can be highly constrained. Therefore if an alternative production mechanism was to be considered, these bounds will change, and the phase space could be opened up. In the work [1] we explored this idea, by considering the effect of decaying topological defects as a new source of DM in the early Universe[1]. Other mechanisms were discussed in Section 1.2, and there are further examples in [72].

Chapter 2 saw how the spontaneous symmetry breaking of a local U(1) symmetry gives

[1] DM from decaying strings was also considered in [224] where a specific production mechanism was assumed, in which DM states were generated, in small numbers, only when the loops of string had shrunk to radii the same order as the string width.

rise to 1-dimensional topological defects called cosmic strings. Within the particle radiation emitted by the decays of said strings and their condensates, there can be DM or a heavier particle which can decay into it. Remnant U(1) symmetries are generic in BSM theories, such as in GUT and string theories [201–204], and they must be broken to insure new massless gauge fields do not arise. Thus there is clear motivation for cosmic string formation, and so the possible effects on DM phenomenology should be considered.

In Section 3.1 we will discuss top-down DM production from decaying topological defects, considering how the decays can be parameterised, and the Boltzmann equation describing the mechanism. Numerical analyses of this equation are presented in Section 3.2, revealing how the yield of DM evolves in different scenarios. By making approximations, analytic solutions are also found and shown to be in excellent agreement with numerical results.

In Section 3.3, we consider DM constraints on the mechanism, and how this can be used to limit the string parameters. The analysis here is intended to be as model-independent as possible; later, in Chapter 4 we will implement this mechanism in the Inert Doublet Model and discuss the benefits of doing so [2].

3.1 Top-Down Dark Matter Production from Topological Defects

We utilise a top-down[1] production mechanism first considered as a possible explanation for the ultra high energy ($\sim 10^{11}$ GeV) cosmic rays [225]. In this scenario, cosmic strings decay into undefined states labelled X, which then in turn decay into χ particles. They take these radiated states to be cosmic rays, however we will assume they are DM particles. In such scenarios, the total energy density injection rate of X particles is modelled as

$$Q(t) = Q_\chi \left(\frac{t}{t_\chi}\right)^{p-4}, \tag{3.1}$$

where t_χ is a reference time, which for the sake of simplification is chosen to be when the temperature is equal to the DM mass m_χ. Q_χ is the energy density injection rate from

[1] Top-down scenarios are those which arise from physics at a higher scale, *e.g.* DM being produced via decays of heavier states, or small structures arising from the fragmentation of larger ones. Conversely, if something is produced from lower scale physics, such scenarios are labelled bottom-up.

decaying defects evaluated at that time and p is a power law index which depends on the string scenario.

A fraction f_X of the energy injected by the string goes into producing X states, which have an average energy of $\overline{E}_X$. These X particles will decay into N_χ χ particles on average, so the number density injection rate of χ particles is

$$j_\chi^{\rm inj} = \frac{f_X N_\chi Q_\chi}{\overline{E}_X} \left(\frac{t}{t_\chi}\right)^{p-4}, \tag{3.2}$$

where the value of p depends on the decay scenario.

Section 2.4 discussed how cosmic strings may decay and saw there were two schools of thought. The first is based on simulations of the Abelian Higgs field theory (as discussed in Section 2.4.1), where the majority of the energy loss is via particle radiation (*i.e.* $f_X \approx 1$) and $p = 1$, we label this the FT scenario. Section 2.4.2 saw how one can study the Nambu-Goto equations of motion to find the string energy loss; this motivates a cusp emission (CE) scenario, where while the dominant loop energy loss is via gravitational radiation, there is subdominant particle emission from the collapsing of cusps. In this latter scenario, the power law index $p = 7/6$.

In Appendix A, particle radiation in each scenario is discussed in further detail, where loop energy loss calculations are reviewed. Here, the choices of p are also justified, and relations between q_X and the string tension parameter $G\mu$ are derived.

3.1.1 Adding Defects to the Boltzmann Equation

Our mechanism only requires DM to be produced from decaying strings, and makes no further assumptions on the particle model. Subsequently, one can assume DM was still once in thermal equilibrium undergoing the same processes as in freeze-out, however now there is an additional non-thermal source of DM from defects. Section 1.2.1 derived the standard freeze-out Boltzmann equation for a DM particle undergoing $2 \to 2$ annihilation and creation processes. In order to take into account decaying defects, the injection rate (3.2) found in the previous section is added to this Boltzmann equation and one finds

$$\dot{n_\chi} + 3Hn_\chi = -\langle\sigma_\chi v\rangle \left(n_\chi^2 - n_{\chi,\rm eq}^2\right) + j_\chi^{\rm inj}, \tag{3.3}$$

which in terms of parameters $Y_\chi = n_\chi/s$ and $x = m_\chi/T$ (as defined in Section 1.2.1) becomes

$$\frac{dY_\chi}{dx} = -\frac{A}{x^{n+2}} \left(Y_\chi^2 - Y_{\chi,\rm eq}^2\right) + \frac{B}{x^{4-2p}}, \tag{3.4}$$

where as before (repeated here for convenience): $n = 0(1)$ in the case of s(p)-wave dominant annihilations, $A = \sqrt{\frac{\pi}{45}} g_* m_\chi M_{\rm Pl} \sigma_0$, and the effective relativistic degrees of freedom is approximated to be constant, *i.e.* $g_* \approx 100$, in accordance with the SM degrees of freedom.

There is also a new term B, defined as

$$B = \frac{3}{4} \left(\frac{N_\chi m_\chi}{\overline{E}_X} \right) \left(\frac{Q_\chi f_X}{\rho_\chi H_\chi} \right), \tag{3.5}$$

where ρ_χ and H_χ are the energy density and the Hubble parameter evaluated at the reference time ($x = 1$ when $t = t_\chi$, as it was defined). To simplify further, we define

$$q_X \equiv \frac{Q_\chi f_X}{\rho_\chi H_\chi}, \qquad \text{and} \qquad r_\chi \equiv \frac{N_\chi m_\chi}{\overline{E}_X}, \tag{3.6}$$

where q_X parameterises the X injection rate; this will be used as a free parameter in the model, and we will study how it may be constrained.

The parameter r_χ, gives the fraction of the decaying X state's energy that goes into the production of DM particles (that is, into total DM mass energy); the larger its value, the more efficient DM production will be. There are two main cases to consider for the value of r_χ. The first is where a few X states with $m_X \sim 10^{15}$ GeV (of the order of the VEV) are produced with a large average energy, $\overline{E}_X \sim 10^{15}$ GeV. The number of DM particles produced by X decays is model-dependent. This scenario will not be considered further as DM production will not be optimal. Instead, we will study a second scenario for X production, where many lower mass states are produced with low average energies. We shall consider the case $\overline{E}_X \sim 10^3$ GeV, appropriate for defects produced in SUSY theories where the VEV is in (a combination of) fields in a flat direction [226] or to strings with condensates of light fields [206]. We assume that the X states decay to a low number of DM particles, likely to be even due to the symmetry stabilising them. However, we will conservatively take $N_\chi = 1$, and set $m_\chi = 500$ GeV (that of a typical WIMP), thus $r_\chi = 0.5$.

When DM is still firmly in thermal equilibrium with the bath, the injection of DM from decaying defects is not expected to have a noticeable impact on the yield, as the number density changes they produce will be removed as the equilibrium yield is rapidly re-established. Only when the system approaches the point of freeze-out, where it departs thermal equilibrium, will the new source start taking effect. How it does this is quantitatively analysed in the coming section.

3.2 Solving the Boltzmann Equation

Evaluating the Boltzmann equation (3.4) presented in the previous section informs us how the DM yield evolves with x (which is closely related to time, $x \propto \sqrt{t}$). It is controlled by two free variables σ_0, the annihilation cross-section, and q_X, the X injection rate parameter. There is also n and p to consider, for which there are two choices each, and therefore four cases in total to consider, which we will label using (n, p).

3.2.1 Numerical Solutions

As in the case of standard freeze-out, the Boltzmann equation (3.4) has no exact analytic solution, therefore in order to see how the yield evolves, one must analyse it numerically. In Figure 3.1 the results of this analysis are shown, where the yield is plotted against x for all four cases of (n, p) using a 500 GeV DM mass. Here, σ_0 was chosen to be the value required to produce the observed abundance by standard freeze-out (2.0×10^{-26} cm^3 s^{-1} for s-wave dominating annihilations and 9.9×10^{-25} cm^3 s^{-1} for p-wave), while four different q_X values were considered (including $q_X = 0$, *i.e.* standard freeze-out).

These plots demonstrate how the presence of decaying defects increases the relic abundance, which one would intuitively expect given they are a *source* of DM, and so can not remove it. Likewise anticipated, the abundance increases with q_X, which controls the injection rate of DM particles from the decaying defects.

The trend seen post-freeze-out differs from the behaviour one sees in standard freeze-out curves (Figure 1.5), furthermore it varies between scenarios. In the $(0, 1)$ case, the yield flattens quickly, while in the other cases, it actually *increases* before plateauing. This effect can be understood by looking back at the Boltzmann equation (3.4); the first term controls the annihilation rate from standard scattering processes and the second term controls the production rate from decaying defects. In standard freeze-out, the yield departs from the equilibrium curve when the annihilation rate approximately equals the expansion rate of the Universe (the point of freeze-out x_{fr}). However now, the point where it departs (which we will label x_{d}) occurs when the two terms in the Boltzmann equation are balanced, and the

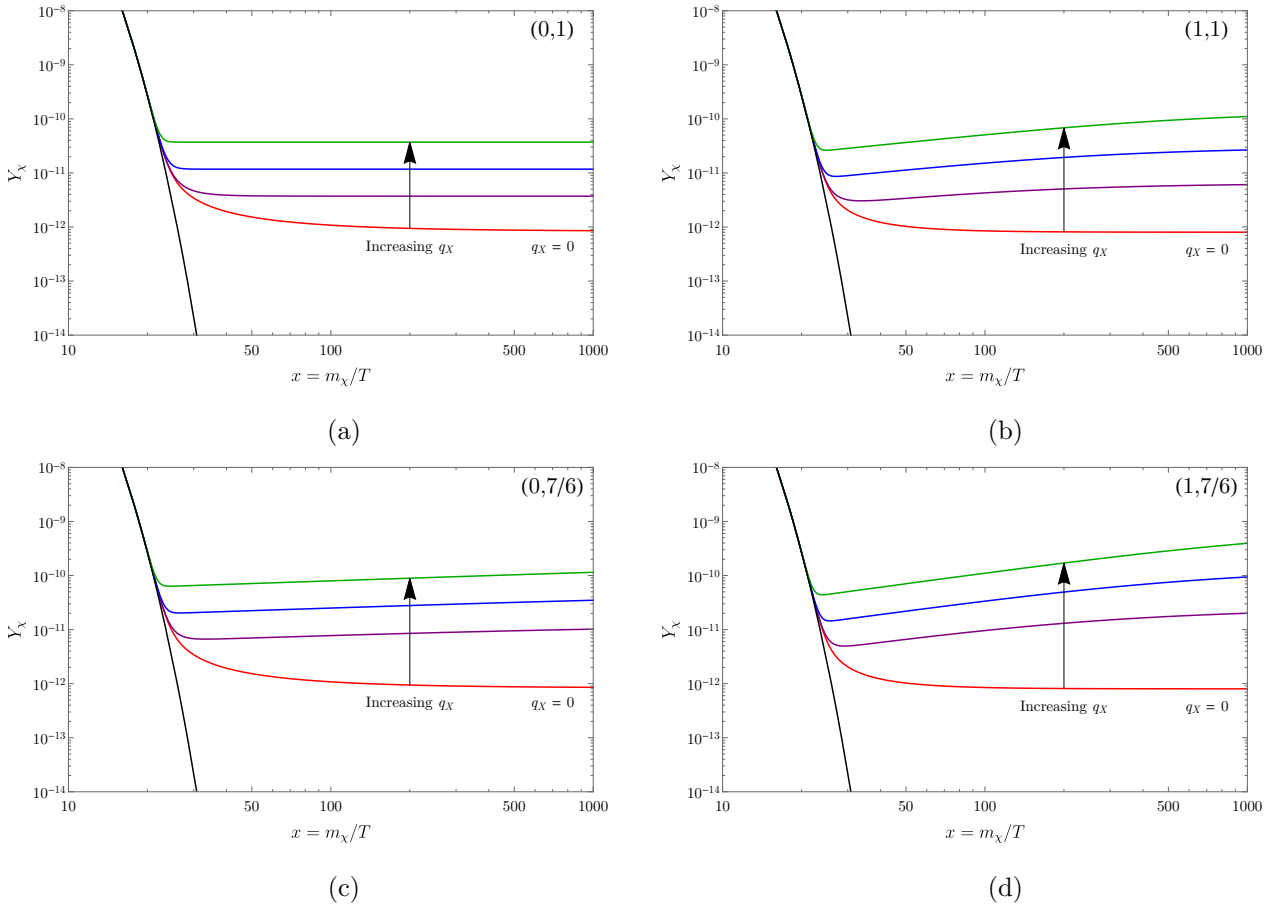

Figure 3.1: The yield of DM against $x = m_\chi/T$ from numerical evaluations of (3.4), which describes freeze-out with an additional source of DM from decaying topological defects. Each sub-figure is for one of the four different cases of (n, p) considered: $(0, 1)$ (a), $(1, 1)$ (b), $(0, 7/6)$ (c), and $(1, 7/6)$ (d). Plotted in each case are curves for when $q_X = 0$ (red), *i.e.* standard freeze-out, $q_X = 10^{-9}$ (purple), $q_X = 10^{-8}$ (blue), and $q_X = 10^{-7}$ (green). Also shown is the thermal equilibrium curve (black). In all cases, $m_\chi = 500$ GeV, $r_\chi = 0.5$, and σ_0 was chosen such that one obtains the observed relic abundance [17] in standard freeze-out; this is 2.0×10^{-26} cm^3 s^{-1} for dominant s-wave annihilations and 9.9×10^{-25} cm^3 s^{-1} for p-wave.

curve becomes flat (as $\frac{dY_\chi}{dx} = 0$), but this is *not* when the system leaves thermal equilibrium[1].

Past this point, the behaviour of the yield depends on the relative values of the exponents, $n + 2$ and $4 - 2p$. If $n + 2 = 4 - 2p$, then the annihilation and production rate terms decrease by the same amount as x increases, thus past x_d they will continue to cancel each other out

[1]The point of departure occurs when the yield is greater than that in the standard freeze-out case, so one expects the annihilation rate to be higher, and so the system to still be in thermal equilibrium.

and the curve remains flat. This condition is fulfilled in the $(0, 1)$ scenario, which is shown in Figure 3.1a. If instead $n + 2 > 4 - 2p$, then after $x_{\rm d}$ the annihilation rate will decrease faster than the production rate, and so the overall abundance increases with x. However the annihilation rate is by no means to be treated as negligible after $x_{\rm d}$, as without it the predicted abundance would be significantly higher (which one can calculate by integrating just the second term from $x_{\rm d}$). Therefore the behaviour after $x_{\rm d}$ is determined by the interplay between production and annihilation mechanisms, and the point where the system leaves chemical equilibrium is not manifest.

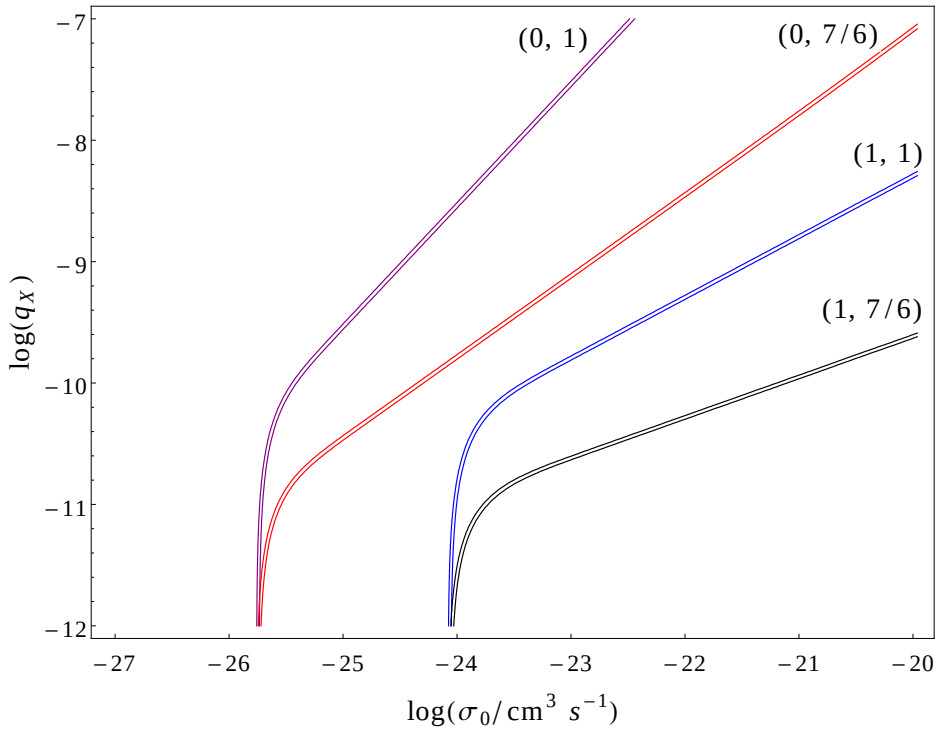

Figure 3.2: Contours of constant yield in (σ_0, q_X) space showing the required values in order to produce 1σ either side of the observed abundance of DM [17]. Four cases are considered: $(0, 1)$ (purple), $(1, 1)$ (blue), $(0, 7/6)$ (red), and $(1, 7/6)$ (black).

In each (n, p) case the residual yield generated is determined by σ_0 and q_X, it is therefore instructive to plot contours in (σ_0, q_X) space for which the observed relic density of DM is obtained. Figure 3.2 shows contours of constant yield for the four scenarios, set to 1σ either side of the relic density value [17]. The contours display two regions of distinct behaviour: at low q_X they are approximately vertical (independent of q_X), and at high q_X there is a positive correlation with σ_0. In the vertical region, q_X is too low to make any significant contribution,

thus the contours are independent of it and σ_0 is well approximated by standard freeze-out. In the positive correlation region there are significant contributions from decaying defects, so increasing q_X increases the production rate, and a higher σ_0 (and therefore annihilation rate) is needed to counteract this in order to maintain a constant yield.

In the regions to right of these curves at higher σ_0, there will be an under-abundance of DM, which is phenomenologically viable, but leaves some fraction of the DM abundance unaccounted for. Regions to the left of the curves at lower σ_0 predict an over-abundance of DM, and further new physics would be needed to bring this down to its observed value.

In Section 1.2.1 we stated annihilations could be dominantly s- or p-wave depending on whether the first or second term of the expansion $\sigma v = a + bv^2$ dominated respectively, which meant the thermally-averaged cross-section was then $\langle \sigma v \rangle = \frac{\sigma_0}{x^n}$. Comparing these scenarios in Figure 3.2, for dominant p-wave annihilations the contours are shifted to higher σ_0, as the factor of v^2 in σv suppresses the annihilation rate, and so σ_0 must increase to compensate (as is the case in standard freeze-out). Moving onto string scenarios, one sees smaller q_X values are required for a given σ_0 in the CE scenario, as the production rate drops more slowly and so would generate a larger amount of DM, unless q_X is lowered.

One also notices how the gradients in the high q_X region depend on the difference between exponents, *i.e.* $(n+2) - (4-2p)$. The gradient is shallowest when this difference is largest, which is in the $(1, 7/6)$ scenario. This may be understood by reflecting on Figure 3.1: in the $(0, 1)$ scenario if q_X is increased, $x_{\rm d}$ occurs at a higher yield (which dictates the relic yield), and to counteract this one increases σ_0 until the yield drops by the same amount. However in the other scenarios considered, you must also compensate for the excess production past $x_{\rm d}$, which will be greater when the production rate drops more slowly than the annihilation rate, *i.e.* when $(n+2) - (4-2p)$ is largest. This means σ_0 will need to increase more when compensating for increases in q_X when this difference is greatest.

The phenomenological consequences of this production mechanism are now clear; by accepting that topological defects can arise quite naturally and could be a source of DM in the early Universe, $\langle \sigma v \rangle$ is allowed to be larger than that required by standard freeze-out, as the reduction in abundance it predicts can be compensated for by the additional production from topological defects.

3.2.2 Analytic Solutions

As aforementioned, the Boltzmann equation (3.4) as it stands cannot be solved exactly analytically, however with approximations analytic solutions may be found. A simple integration of the production term from $x_{\rm d}$ to ∞ in order to find the relic abundance is insufficient as annihilations play a vital role in this region (as discussed in the previous section). However, by following similar steps to those used to approximate the standard freeze-out relic yield in [50] (which were also given in Section 1.2.1), an approximate analytic solution may be found.

It is clear from Figure 3.1 that after $x_{\rm d}$, the yield swiftly becomes much greater than the equilibrium yield, therefore in the region $x \gtrsim x_{\rm d}$ one may approximate the Boltzmann equation to be

$$\frac{dY_\chi}{dx} \approx -\frac{A}{x^{n+2}} Y_\chi^2 + \frac{B}{x^{4-2p}}, \tag{3.7}$$

which is in the form of a Riccati equation. This may now be analytically solved using the condition $Y_\chi(x_{\rm d}) \approx Y_{\chi,{\rm eq}}(x_{\rm d})$, and taking the relic yield to be the solution in the $x \to \infty$ limit, one finds

$$\begin{aligned} Y_\chi(\infty) = (\alpha+\beta)^{\frac{\beta-\alpha}{\alpha+\beta}} \frac{B^{\frac{\alpha}{\alpha+\beta}}\Gamma\left(\frac{\beta}{\alpha+\beta}\right)}{A^{\frac{\beta}{\alpha+\beta}}\Gamma\left(\frac{\alpha}{\alpha+\beta}\right)} \\ \times \frac{\left[I_{-\frac{\alpha}{\alpha+\beta}}\left(\frac{2\sqrt{AB}}{(\alpha+\beta)x_{\rm d}^{(\alpha+\beta)/2}}\right) - \sqrt{\frac{Bx_{\rm d}^{\alpha-\beta}}{AY_{\chi,{\rm eq}}(x_{\rm d})^2}} I_{\frac{\beta}{\alpha+\beta}}\left(\frac{2\sqrt{AB}}{(\alpha+\beta)x_{\rm d}^{(\alpha+\beta)/2}}\right)\right]}{\left[I_{\frac{\alpha}{\alpha+\beta}}\left(\frac{2\sqrt{AB}}{(\alpha+\beta)x_{\rm d}^{(\alpha+\beta)/2}}\right) + \sqrt{\frac{Bx_{\rm d}^{\alpha-\beta}}{AY_{\chi,{\rm eq}}(x_{\rm d})^2}} I_{-\frac{\beta}{\alpha+\beta}}\left(\frac{2\sqrt{AB}}{(\alpha+\beta)x_{\rm d}^{(\alpha+\beta)/2}}\right)\right]}, \end{aligned} \tag{3.8}$$

where $\alpha = n+1$, $\beta = 3-2p$, and $I_\nu(x)$ is the modified Bessel function of the first kind. This equation is valid for all possible n in the standard $\langle\sigma v\rangle$ expansion and for $p < 3/2$, thus is valid for all cases considered. If $p \geq 3/2$, then $Y_\chi \to \infty$ as $x \to \infty$, *i.e.* the abundance is continually increasing and does not plateau; however we are unaware of any such scenarios.

If the solution (3.8) in the $B \to 0$ (*i.e.* no defects) limit is considered, one would expect the standard freeze-out analytic solution (1.25) to be returned, however instead one gets a more complex expression. In order to be consistent with (1.25), the solution must be approximated further, as was done in the standard freeze-out case. One can show that the coefficient term

$\sqrt{\frac{Bx_{\rm d}^{\alpha-\beta}}{AY_{\chi,\rm eq}(x_{\rm d})^2}} \ll 1$, and so the solution simplifies to

$$Y_\chi(\infty) = (\alpha+\beta)^{\frac{\beta-\alpha}{\alpha+\beta}} \frac{B^{\frac{\alpha}{\alpha+\beta}}\Gamma\left(\frac{\beta}{\alpha+\beta}\right) I_{-\frac{\alpha}{\alpha+\beta}}\left(\frac{2\sqrt{AB}}{(\alpha+\beta)x_{\rm d}^{(\alpha+\beta)/2}}\right)}{A^{\frac{\beta}{\alpha+\beta}}\Gamma\left(\frac{\alpha}{\alpha+\beta}\right) I_{\frac{\alpha}{\alpha+\beta}}\left(\frac{2\sqrt{AB}}{(\alpha+\beta)x_{\rm d}^{(\alpha+\beta)/2}}\right)}, \tag{3.9}$$

which now returns the standard freeze-out analytic solution in the $B \to 0$ limit.

The solution is now in a more manageable form, and is valid for any choice of A and B (that is σ_0 and q_X). However, we are more interested in the regions of large σ_0 and q_X seen in Figure 3.2, where defect decays are making a significant difference. In this high AB limit, the Bessel functions are approximately equal, and the solution simplifies to

$$Y_\chi(\infty) = (\alpha+\beta)^{\frac{\beta-\alpha}{\alpha+\beta}} \frac{B^{\frac{\alpha}{\alpha+\beta}}\Gamma\left(\frac{\beta}{\alpha+\beta}\right)}{A^{\frac{\beta}{\alpha+\beta}}\Gamma\left(\frac{\alpha}{\alpha+\beta}\right)}. \tag{3.10}$$

By inspection, the Bessel functions cancel when their argument is ~ 2, therefore this solution is valid for

$$q_X\sigma_0 \gtrsim 10^{-38} x_{\rm d}^{\alpha+\beta}\ \text{cm}^3\text{s}^{-1}\left(\frac{500\ \text{GeV}}{m_\chi}\right)\left(\frac{0.5}{r_\chi}\right). \tag{3.11}$$

In Figure 3.3 these analytic solutions are compared to the numerical result by plotting contours of fixed yield (set to the measured amount) in (σ_0, q_X) space (as in Figure 3.2). This is in the $(1,1)$ scenario, and shows the original numerical solution in red, alongside contours found from the analytic expression (3.9), and its approximation in the high AB limit (3.10), in dashed and dotted blue lines respectively.

One sees the analytic solution (3.9) matches the numerical contours very closely in this scenario (in other scenarios the difference is comparable, if not better), especially in the higher AB region. In the lower region, where the process is effectively standard freeze-out, there is some small disagreement, however we know our analytic solution is equivalent to that commonly used for standard freeze-out (1.25).

Inspecting the high AB limit solution's contour, excellent agreement with the numerical result is seen within said region, although diverges away at low AB values. This means that despite starting from a non-linear, non-homogeneous Boltzmann equation with no exact analytic solution, an approximation with a simple form (3.10) is possible which closely matches

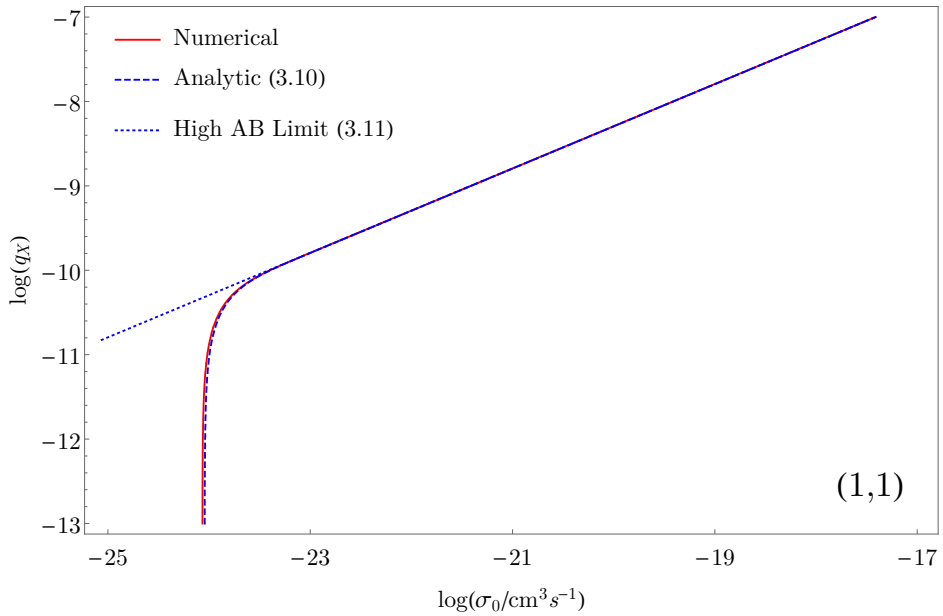

Figure 3.3: Contours of constant DM yield in (σ_0, q_X) space, fixed to the the observed abundance [17]. Shown are contours derived by three means: numerical analysis (red), using (3.9), an approximate analytic solution (dashed blue), and using (3.10), the analytic solution in the high AB limit (dotted blue). This is in the $(1, 1)$ scenario, where the disagreement between numerical and analytic results is maximal.

the numerical results, only diverging in an uninteresting region, where topological defect contributions are small and the system can be approximated by standard freeze-out.

Having established its validity, the high AB limit solution (3.10) can be used to find the relic abundance $\Omega_\chi \equiv \frac{\rho_\chi}{\rho_c} = \frac{m_\chi s_0}{\rho_c} Y_\chi(\infty)$, where ρ_χ and ρ_c are the χ and critical density respectively, and s_0 is the present entropy density. By inserting (3.10) into this one can rearrange for an expression for q_X. This tells us the q_X value required to produce the DM abundance Ω_χ, given a σ_0 value (as well as other parameters, which have been fixed for this study). Doing so, one obtains

$$q_X = \frac{4}{3}\frac{1}{r_\chi}(\alpha+\beta)^{\frac{\alpha-\beta}{\alpha}} \left(\sqrt{\frac{\pi g_*}{45}} M_{\rm Pl} m_\chi \, \sigma_0\right)^{\beta/\alpha} \left[\frac{\Gamma(\frac{\alpha}{\alpha+\beta})}{\Gamma(\frac{\beta}{\alpha+\beta})} \frac{\Omega_\chi \rho_c}{s_0 m_\chi}\right]^{\frac{\alpha+\beta}{\alpha}} . \tag{3.12}$$

Using the observed relic abundance [17] along with typical parameter values, this becomes

$$\begin{aligned} q_X \lesssim 2 \times 10^{-8} &\left(\frac{\alpha+\beta}{10^4}\right)^{\frac{\alpha-\beta}{\alpha}} \left(\frac{\Gamma(\frac{\alpha}{\alpha+\beta})}{\Gamma(\frac{\beta}{\alpha+\beta})}\right)^{\frac{\alpha+\beta}{\alpha}} \left(\frac{0.5}{r_\chi}\right) \left(\frac{500\ \text{GeV}}{m_\chi}\right) \\ &\times \left(\frac{\sqrt{g_*}}{10}\right)^{\frac{\beta}{\alpha}} \left(\sigma_0^{23}\right)^{\frac{\beta}{\alpha}} \left(\frac{\Omega_\chi h^2}{0.1186}\right)^{\frac{\alpha+\beta}{\beta}}, \end{aligned} \tag{3.13}$$

where $\sigma_0^{23} = \sigma_0 / 10^{-23} \text{cm}^3 \text{s}^{-1}$.

As discussed, the analytic solution found here was derived following the work in [50]. By inspecting its derivation of the point of freeze-out x_{fr} (seen in Section 1.2.1), this may again be used to find an approximate analytic form for x_{d}. Repeating the same steps, we start by defining the point of departure as the value of x for which the difference $\Delta \equiv Y_\chi - Y_{\chi,\text{eq}} = cY_{\chi,\text{eq}}$, where $\frac{\partial \Delta}{\partial x} \approx 0$ and c is a constant of order unity. With similar manipulations, one finds the reciprocal formula

$$\begin{aligned} x_{\text{d}} = \log[Akc(c+2)] &- \log\left[x_{\text{d}}^{n+1/2}\left(1 - \frac{3}{2x_{\text{d}}}\right)\right] \\ &- \log\left[\frac{1}{2}\left(1 + \sqrt{1 + \frac{4ABc(c+2)}{\left(1-\frac{3}{2x_{\text{d}}}\right)^2 x_{\text{d}}^{6-2p+n}}}\right)\right], \end{aligned} \tag{3.14}$$

where as before, $k = 0.145 g / g_{*S}$ (and $g_{*S} \approx g_*$).

By inserting the first term (the dominant contribution) of this equation into itself, and making the approximation $\frac{3}{2x_{\text{d}}} \ll 1$ (as one expects $x_{\text{d}} \gg 1$), an expression for x_{d} may be found:

$$\begin{aligned} x_{\text{d}} = \log[Akc(c+2)] &- \left(n + \frac{1}{2}\right) \log\left[\log[Akc(c+2)]\right] \\ &- \log\left[\frac{1}{2}\left(1 + \sqrt{1 + \frac{4ABc(c+2)}{(\log[Akc(c+2)])^{6-2p+n}}}\right)\right]. \end{aligned} \tag{3.15}$$

According to this as B increases, x_{d} will decrease, which agrees with what is seen in Figure 3.1. Conversely, taking the $B \to 0$ limit the expression reduces to the approximation for the point of freeze-out (1.27), so long as we take $c(c+2) = n+1$, as was done for x_{fr}. Immediately prior to this derivation, we discussed how (3.10) is a good approximation for the relic yield as long as the defects are contributing significantly. This result is independent of x_{d} however[1], thus where x_{d} significantly deviates from x_{fr} it has a negligible effect on the relic yield, and so this analytic result is of limited use.

[1] There is a dependence through $g^*(x_{\text{d}})$ in A, but its variation is minimal, and can be neglected.

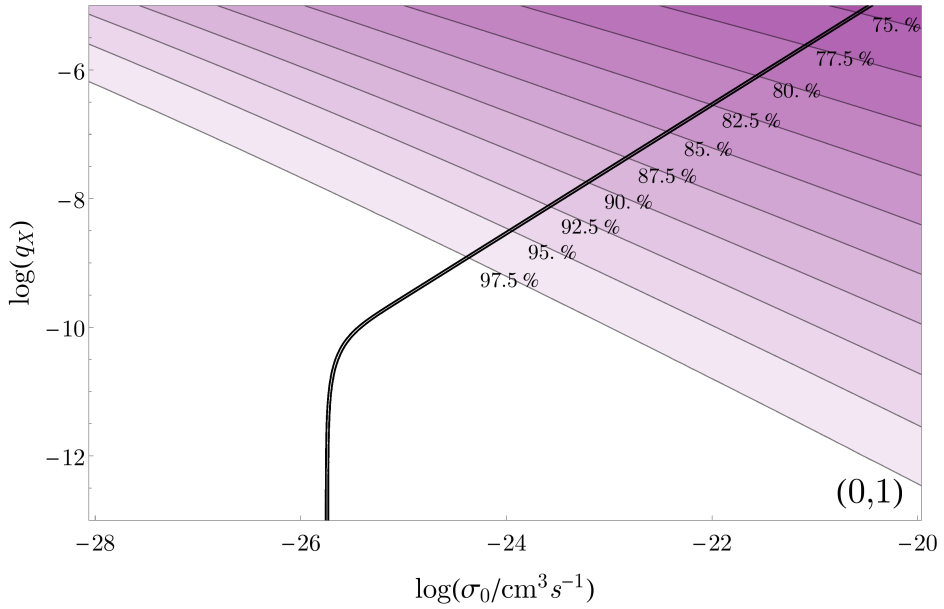

Figure 3.4: Contours of constant $(x_{\rm d}/x_{\rm fr})\%$ in (σ_0, q_X) space alongside those of constant yield set to 1σ either side of the observed abundance [17]. The point of departure, $x_{\rm d}$, was found using the recursive analytic approximation (3.14) and the yield contours were plotted using the approximate analytic solution (3.9). This was for the $(0,1)$ scenario, chosen as an illustrating example.

In Figure 3.4 contours of constant $(x_{\rm d}/x_{\rm fr})$ in (σ_0, q_X) space are shown along with those of constant yield already seen in Figure 3.2 for the $(0,1)$ scenario. This shows that for $x_{\rm d}$ to differ from $x_{\rm fr}$ by just a few percent, one must go well into the high AB region, where defects are playing a significant role and the relic yield is well approximated by (3.10), which is independent of $x_{\rm d}$. This supports the assertion in the proceeding paragraph, illustrating the limited use of $x_{\rm d}$, which is true for all (n,p) scenarios.

3.3 Constraints

Standard freeze-out asserts that the DM annihilation cross-section should hold some particular value at freeze-out, but in the preceding section one saw how, by allowing for defect decays, this cross-section could be increased and the observed abundance could still be obtained. However this boost will be limited by experimental and theoretical results, and thus so will q_X. Here, keeping the discussion model-independent, the bounds considered will either not depend on the theory, or be treated as an example of one which does.

The unitarity bound [154], which was discussed in Section 1.4.4, can be applied without knowledge of the specific model. Repeated here for convenience, this limits the annihilation cross-section to be

$$\langle \sigma v \rangle \lesssim \frac{4\pi(2n+1)}{m_\chi^2}\sqrt{\frac{x_\mathrm{d}}{\pi}}, \tag{3.16}$$

which presumes it remains approximately constant during freeze-out. This bound only depends on whether the annihilations are s-wave or p-wave dominated. Inserting (3.16) into (3.13), this bound on σ_0 is translated into one on q_X. That is, it tells us the q_X needed to produce the observed relic abundance, if σ_0 was at the unitarity bound. This is

$$\begin{aligned} q_X \leq 2\times 10^{-12}\left(4\times 10^5\right)^{\frac{\beta}{\alpha}}(\alpha+\beta)^{\frac{\alpha-\beta}{\alpha}}(2\alpha-1)^{\frac{\beta}{\alpha}}\left(\frac{\Gamma(\frac{\alpha}{\alpha+\beta})}{\Gamma(\frac{\beta}{\alpha+\beta})}\right)^{\frac{\alpha+\beta}{\alpha}} x_d^{(2\alpha-1)\frac{\beta}{2\alpha}}\left(\frac{0.5}{r_\chi}\right) \\ \times\left(\frac{500\ \mathrm{GeV}}{m_\chi}\right)^{\frac{2\beta+\alpha}{\alpha}}\left(\frac{\sqrt{g_*}}{10}\right)^{\frac{\beta}{\alpha}}\left(\frac{\Omega_\chi h^2}{0.1186}\right)^{\frac{\alpha+\beta}{\beta}}. \end{aligned} \tag{3.17}$$

In order to consider direct and indirect detection, and collider constraints, some model dependence must be introduced. Aiming to show how such results might constrain the mechanism, we considered indirect detection limits from Fermi-LAT [227] (discussed in Section 1.4.2), a satellite-based experiment measuring the γ-ray sky. Fermi-LAT results limit the annihilation cross-section directly, and so one needs only specify the final states of the process, rather than a full model, in order to extract limits. We used a preliminary 4 year Pass 7 combined analysis of Fermi-LAT data from several dwarf spheroidal satellite galaxies (dSphs) [228], and assumed dominant annihilations into W bosons.

In the case of dominant s-wave annihilations, $\langle \sigma v \rangle$ limits are velocity-independent, and so would have been the same during freeze-out as they are now in dSphs. The limit in this scenario is

$$\langle \sigma v \rangle \lesssim 8\times 10^{-25}\ \mathrm{cm}^3\ \mathrm{s}^{-1}. \tag{3.18}$$

The situation is more complicated when the annihilations are dominantly p-wave, since there is now a velocity dependence. However these limits are expected to be much weaker, as the mean velocity is $\mathcal{O}(10)$ km s^{-1} in dSphs [229, 230], whereas $\sim c/3$ at freeze-out. This means the limit in the case of dominantly p-wave annihilations will be orders of magnitude above those of s-wave. Consequently, these will be weaker than the unitarity bound and so can be safely ignored.

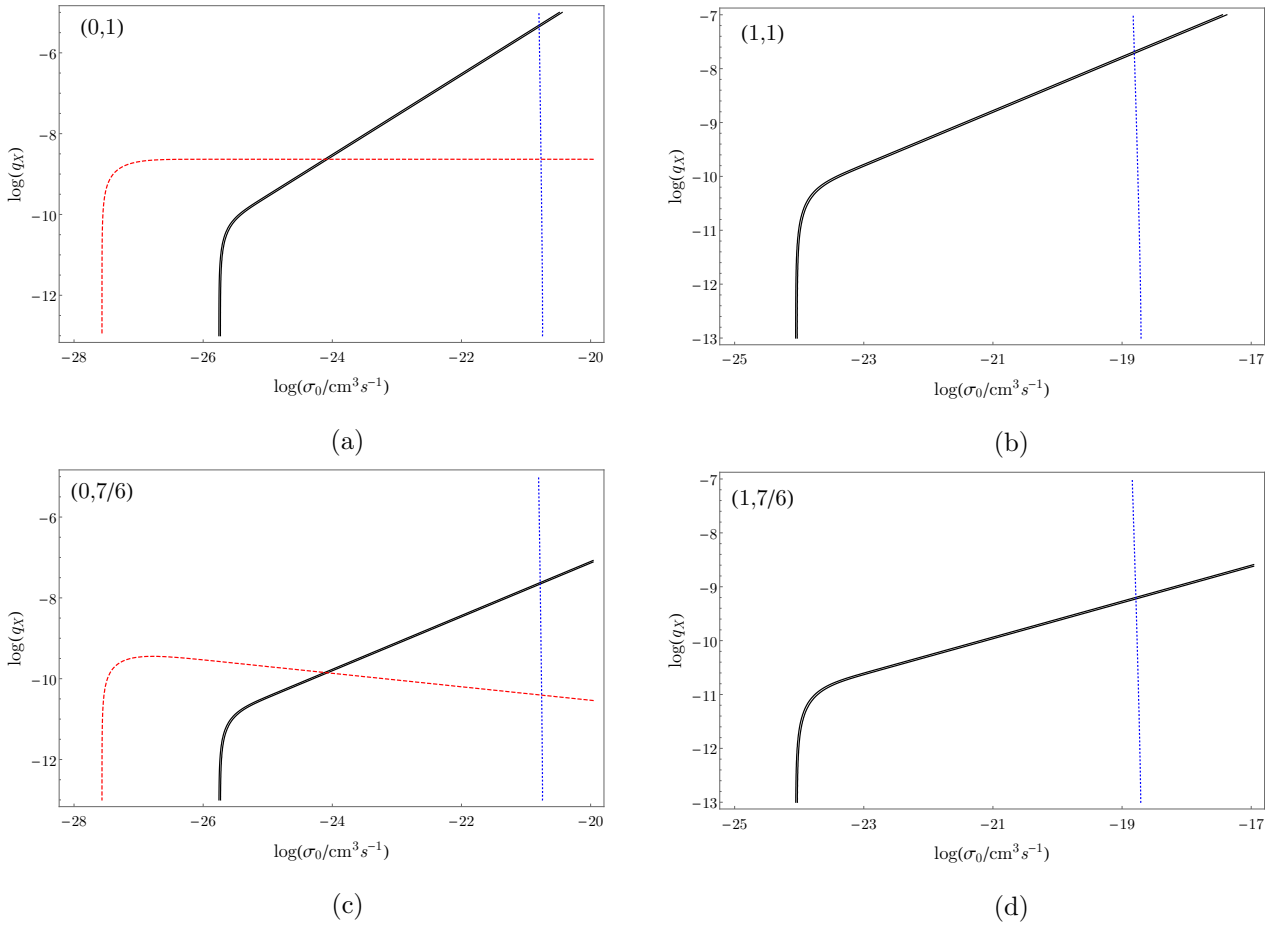

Figure 3.5: Plots of (σ_0, q_X) space constrained by unitarity (blue dotted) and Fermi-LAT (red dashed) bounds in four cases of (n, p); $(0, 1)$ (a), $(1, 1)$ (b), $(0, 7/6)$ (c), and $(1, 7/6)$ (d). The double black lines are contours of constant yield set to 1σ either side of the observed relic abundance [17], which were applied using the approximate analytic solution (3.9). The Fermi-LAT bound is from a combined analysis of several dSphs [228] and assumes dominant annihilations into W bosons. The unitarity bound (3.16) was taken from [154].

Figure 3.5 shows plots of (σ_0, q_X) space in the four (n, p) scenarios considered with unitarity and Fermi-LAT bounds applied. These are plotted alongside contours of constant yield set to 1σ either side of the observed relic abundance, as originally seen in Figure 3.2. The unitarity limits here are fairly weak as expected, and slightly off-vertical due to the dependence on σ_0 and q_X via that on x_d, whereas the Fermi-LAT bounds provide far stronger limits, but only in the cases with s-wave annihilations dominating. One might intuitively expect the Fermi-LAT bounds to be vertical (independent of q_X), however they are more horizontal

(independent of σ_0), which is exactly true in the $(0,1)$ case (unless σ_0 is below the standard freeze-out value).

To understand this, note that while Fermi-LAT limits may not directly depend on q_X, they do on Ω_χ, which itself varies under changes to the string parameter. The limits depend on Ω_χ^2 and so $Y_\chi(\infty)^2$, which is given in (3.10); this means that in the $(0,1)$ scenario, where $Y_\chi(\infty) = \sqrt{B/A} \propto \sqrt{q_X/\sigma_0}$ in the high AB region, the rate $R \propto Y_\chi(\infty)^2\langle\sigma v\rangle \propto q_X$, and so is independent of σ_0. In the $(0,7/6)$ scenario, the Fermi-LAT limits will have some dependence on σ_0 as $Y_\chi(\infty) \propto B^{3/5}/A^{2/5} \propto q_X^{3/5}/\sigma_0^{2/5}$, which means the rate goes as $R \propto q_X^{6/5}\sigma_0^{1/5}$. This predicts the limit on q_X to decrease when σ_0 increases, which agrees with the behaviour seen in Figure 3.5c.

(n,p)	DM density	Unitarity	dSph γ emission
$(0,1)$	$q_X \lesssim 2.9\times10^{-8}(\sigma_0^{23})$	$q_X \lesssim 4.6\times10^{-6}$	$q_X \lesssim 2.3\times10^{-9}$
$(1,1)$	$q_X \lesssim 1.6\times10^{-10}(\sigma_0^{23})^{\frac{1}{2}}$	$q_X \lesssim 2.0\times10^{-8}$	-
$(0,7/6)$	$q_X \lesssim 7.6\times10^{-10}(\sigma_0^{23})^{\frac{2}{3}}$	$q_X \lesssim 2.3\times10^{-8}$	$q_X \lesssim 1.4\times10^{-10}$
$(1,7/6)$	$q_X \lesssim 2.4\times10^{-11}(\sigma_0^{23})^{\frac{1}{3}}$	$q_X \lesssim 6.1\times10^{-10}$	-

Table 3.1: Limits on q_X in four different (n,p) scenarios. The second column gives the values required to produce the measured relic abundance, using (3.12), where $\sigma_0^{23} = \sigma_0/10^{-23}$ cm^3 s^{-1}. The third and fourth columns are limits from unitarity and Fermi-LAT respectively.

Table 3.1 summarises the various limits on q_X originating from DM bounds for all four scenarios. First one may consider how the measured DM relic abundance limits q_X, this is presented in the second column of the table. This will depend on σ_0, representing the q_X value required to produce the relic abundance, therefore beyond this DM is being over-produced. All limits presented are found using the high AB limit solution (3.12)[1], whose validity is lost (and so that of the limits) when $\langle\sigma v\rangle$ is approximately less than its value predicted in standard freeze-out.

In the third and fourth columns, q_X limits from unitarity and Fermi-LAT bounds respectively, are given. These also presume the required relic abundance is being produced, however now σ_0 is limited by these bounds. In relation to Figure 3.5, these represent the q_X values

[1]While the full analytic solution (3.9) could have been used, q_X's dependence on σ_0 would have been significantly more complex, and the only thing gained would be accuracy in the standard freeze-out regime.

at which the limit curves intersect the constant yield contours. For this analysis we chose $r_\chi = 0.5$; to obtain q_X limits in the case of an arbitrary r_χ value one can simply multiply the limits in Table 3.1 by a factor of $(0.5/r_\chi)$. However, this must be done at constant DM mass as limits depend non-trivially on m_χ, as seen in (3.12).

(n,p)	DM density	Unitarity	dSph γ emission
$(0,1)$	$G\mu < 1.1\times10^{-10}(\sigma_0^{23})P_{\rm FT}^{-1}$	$G\mu < 1.7\times10^{-8}P_{\rm FT}^{-1}$	$G\mu < 8.7\times10^{-12}P_{\rm FT}^{-1}$
$(1,1)$	$G\mu < 6.0\times10^{-13}(\sigma_0^{23})^{\frac{1}{2}}P_{\rm FT}^{-1}$	$G\mu < 7.5\times10^{-11}P_{\rm FT}^{-1}$	-
$(0,7/6)$	$G\mu < 3.3\times10^{-14}(\sigma_0^{23})^{\frac{2}{3}}P_{\rm CE}^{-1}$	$G\mu < 1.0\times10^{-12}P_{\rm CE}^{-1}$	$G\mu < 6.1\times10^{-15}P_{\rm CE}^{-1}$
$(1,7/6)$	$G\mu < 1.1\times10^{-15}(\sigma_0^{23})^{\frac{1}{3}}P_{\rm CE}^{-1}$	$G\mu < 2.7\times10^{-14}P_{\rm CE}^{-1}$	-

Table 3.2: Limits on the string tension parameter, $G\mu$, in four different (n,p) scenarios. The second column gives the values required to produce the measured relic abundance, while the third and fourth are limits from unitarity and Fermi-LAT respectively. These are translated from the q_X values presented in Table 3.1, using the relations (A.8) and (A.21). $P_{\rm FT}$ and $P_{\rm CE}$ are order unity parameters, which are defined in Appendix A.

While q_X is a convenient parameter for this study, the string tension parameter, $G\mu$ (where μ is the mass per unit length of the string, and $G = 6.7\times10^{-39}$ GeV^{-2} is the gravitational constant), is a more commonly used and physically meaningful parameter. Using the relations in Appendix A, (A.8) and (A.21), we present limits in Table 3.2 on $G\mu$ calculated from those on q_X. These are in terms of $P_{\rm FT}$ and $P_{\rm CE}$, parameters of order unity defined in Appendix A. All of the limits presented here are stronger than $G\mu \lesssim 10^{-7}$, which comes from Planck's CMB power spectrum [195].

Since $\mu \sim v^2$ (where v is the VEV), one can also use Table 3.2 to find upper limits on the VEV of the theory generating the cosmic strings. In the CE scenario, this means VEVs of up to $\mathcal{O}(10^{12})$ GeV are allowed before one of our limits comes in. In the FT scenario, one can have $v \lesssim \mathcal{O}(10^{13})$ GeV and $v \lesssim \mathcal{O}(10^{14})$ GeV, in the case of dominant s- and p-wave annihilations respectively.

The limits coming from DM search experiments have the potential to be much more constraining than the unitarity limit, but they are highly model-dependent. Further sources of indirect constraints can be derived from data obtained from searches for DM in the Galactic centre [231] for example, and in a specific DM model, limits from direct detection may also

be applied. The details of a fully model-dependent analysis of the allowed parameter space for a particular DM model is left to work presented in Chapter 4. The aim of this section was to demonstrate the potential interplay between DM search limits and our parameter space.

With the source term it is possible to increase the size of the annihilation cross-section beyond the standard freeze-out value, whilst still generating the correct relic abundance. This may lead to a possible source of "boost factors" for indirect detection needed to explain possible anomalies and issues. For example, in Chapter 5 this mechanism is used in a model with dominant p-wave annihilations for the Galactic centre excess [232], which allows tensions with dSph limits to dissipate, while keeping the observed relic density.

In principle the size of the boost factor can be several orders of magnitude with a model-independent maximum coming from the unitarity limit. Of course, model-dependent limits coming from both direct and indirect detection bounds for a specific DM candidate need to be applied but even with the Fermi-LAT dSph limit applied above we still have nearly two orders of magnitude in terms of a possible boost factor for both (0, 1) and (0, 7/6) cases.

In this Chapter, the work in [1] was discussed in detail. A DM production mechanism was presented, which stipulated that decaying topological defects can be a new source of DM in the early Universe, and would alter the standard freeze-out process. The formation of 1-dimensional topological defects called cosmic strings is generic, as it can just require an additional local $U(1)$ symmetry. Such symmetries arise in many GUT and string theories [201–204], and so one must consider the possible impact cosmic strings could have on DM physics.

In Section 3.1, the mechanism was introduced, where the injection rate from strings was parameterised by q_X, and the FT and CE scenarios describing string decays were discussed. This mechanism still presumed DM was once in a thermal equilibrium with the bath, although now an additional source from decaying defects was present; a Boltzmann equation was constructed which reflected this. In Section 3.2, this equation was analysed numerically allowing us to see how the DM yield evolved over time, and how by increasing q_X, larger and larger annihilation cross-sections were allowed, as the reduction in abundance they predicted could be compensated for by the production from decaying defects. Using approximations, analytic solutions for the Boltzmann equation were also derived and found to be in excellent agreement with the numerical results.

Possible constraints on the mechanism were considered in Section 3.3. Bounds on the annihilation cross-section arising from unitarity (a model-independent constraint), were translated into those on q_X. This showed the cross-section could be boosted orders of magnitude higher than its standard freeze-out value. Furthermore, to demonstrate how model-dependent limits could be much more constraining than this, we considered Fermi-LAT limits on dSphs, assuming dominant annihilations into W bosons.

This chapter illustrated how the mechanism works, and the benefits of implementing it. In the proceeding chapter, we do so, applying it in the Inert Doublet Model.

Chapter 4

The Inert Doublet Model with Topological Defects

> They cheer me because they all understand me, and they cheer you because no one understands you.
>
> — Charlie Chaplin to Albert Einstein

The topic of [1] and of the previous chapter, was a new mechanism for DM genesis using topological defect decays, where the dynamics and key features of the process were detailed through a model-independent approach. The mechanism proposed that a DM model in which cosmic strings arise (after a spontaneous symmetry breaking phase transition), can have larger $\langle \sigma v \rangle$ values than is permitted under standard freeze-out; this is because the strings can decay producing enough DM to compensate for the loss predicted by larger annihilation cross-sections. Ergo, it is important to test this conjecture by implementing the mechanism in an example model, which is the subject of [2] and of this chapter.

The simplest way in which cosmic strings may arise is via the spontaneous breaking of an additional local $\mathrm{U}(1)'$ symmetry. Furthermore, in a working example of a model with this genesis mechanism, these cosmic strings must then be permitted to decay into DM. In extending the SM from a bottom up perspective, we need to add DM states, and may also wish to supplement the SM gauge group with additional gauge symmetries, such as $\mathrm{U}(1)'$. The associated gauge boson can play a role in connecting the DM state to the SM sector.

Such a connection is required in most models of DM relying on the freeze-out mechanism to determine the relic abundance.

We may also expect additional Abelian gauge symmetries from a top down perspective. Whether one considers heterotic strings, type II string theory with D-branes or F-theory, it is common that in attempts to recover the SM gauge group, additional unbroken Abelian gauge symmetries are generated (see for example [202–204]). Whatever the source of the extra symmetry, the Z' in these models must be sufficiently massive to have escaped detection, and so the $\mathrm{U}(1)'$ must be spontaneously broken (at a symmetry breaking scale v').

As seen in the previous chapter, the connection the mechanism makes between DM and the topological defects can also be exploited to find constraints on the properties of the cosmic strings. There are a number of ways in which such a connection can be realised. Whether the DM states are charged under the additional symmetry or not, we generically expect that the decays of the defects formed in these models will have a branching fraction to the DM states at some level. If the DM is not charged under the $\mathrm{U}(1)'$, but is a scalar state χ, it can couple to the complex scalar, ϕ, responsible for spontaneously breaking the $\mathrm{U}(1)'$. It can do so via a quartic "portal" coupling $\mathcal{L} \supset |\phi|^2|\chi|^2$, which provides a connection between the DM states and the states that will form the cosmic string.

One could also consider the additional $\mathrm{U}(1)'$ kinetically mixing with the SM gauge group $\mathrm{U}(1)_\mathrm{Y}$. If the DM is charged under the electroweak gauge group we again have a direct connection between the $\mathrm{U}(1)'$ sector and the DM states. A further example, is where the DM state is charged under the $\mathrm{U}(1)'$. In this case the connection is straightforward with the DM states being produced directly from defect decays. In all these cases it is clear that DM will be produced in the decays of these defects with some branching fraction.

Increasing the injection rate of DM states from decaying defects, the annihilation cross-section needs to increase in order to bring the relic abundance down to the measured value. This can only be increased up to the unitarity limit, and hence there is an upper limit on the DM injection rate. For a given DM mass, this translates to constraints on the properties of the cosmic string network, or specifically, the mass per unit length of the strings μ. A further effect of increasing the annihilation rate is generically an enhancement of the indirect and direct detection signals, which can further limit the model. Conversely, the extra source of DM particles changes the predictions of specific DM models.

Scenarios in which DM production by decaying defects could play a positive role involve WIMP models where DM annihilation into SM particles naturally yields a relic density significantly below the observed one. This is, for example, the case for WIMP scenarios where DM annihilates dominantly via $SU(2)_L \times U(1)_Y$ gauge interactions, as in most of the parameter space of the minimal DM [233,234] and Inert Doublet Model (IDM) [235–237] scenarios. These models constitute rather minimal extensions of the SM, and are very appealing phenomenologically since the DM annihilation properties can be purely dictated by their $SU(2)_L \times U(1)_Y$ gauge quantum numbers. However, this same feature greatly restricts the range of DM masses that yield the observed relic abundance via thermal freeze-out.

In this work we explore the impact of DM production by defect decays on the available parameter space, taking as a case study the IDM supplemented by an additional $\mathrm{U}(1)'$ gauge symmetry. This model has already been considered in [238,239], however the motivation there was to dynamically create the symmetry stabilising the DM state.

In this chapter we will first review the IDM in Section 4.1, discussing its theoretical and phenomenological bounds. We furthermore define a choice of parameterisation, appropriate for our study. Later in Section 4.2 we add the $\mathrm{U}(1)'$ local symmetry to the IDM, and introduce a scalar field to break it. The phenomenological impact of the symmetry breaking is then discussed.

Next, in Section 4.3, we derive the Boltzmann equation describing DM genesis in the IDM with a source of DM from decaying defects, whereafter it is solved numerically and the relic yield's dependence on masses and couplings is explored. Lastly, experimental DM constraints from direct and indirect detection, and collider searches are considered in Section 4.4, along with limits directly on cosmic strings from Big Bang Nucleosynthesis and the diffuse γ-ray background. Here we will see how much more of the IDM's phase space is viable after cosmic strings have been introduced and experimental bounds applied.

4.1 The Inert Doublet Model

As reviewed in Section 2.1.2, the SM contains a single Higgs doublet charged under the electroweak symmetry group $\mathrm{SU(2)_L} \times \mathrm{U(1)_Y}$. The Higgs doublet then gains a VEV, which breaks this symmetry down to $\mathrm{U(1)_{EM}}$, and leaves behind a remnant scalar, the SM Higgs boson. The other degrees of freedom in the doublet are "eaten" by the W and Z bosons,

which become massive after the phase transition. Yukawa couplings also arise with left-handed fermion doublets charged under the electroweak symmetry group and right-handed singlets charged under just the $\mathrm{U}(1)_\mathrm{Y}$; post-symmetry breaking, these terms generate the fermion masses. There are multiple generations of fermions, which naturally leads one to question whether similarly, there may be additional Higgs doublets.

In the simplest realisation of this, there is a single extra Higgs doublet, which is also charged under the electroweak symmetry and gains a VEV. This is referred to as the two Higgs doublet model (2HDM), and has a rich and varied phenomenology [240]. Limits on flavour-changing neutral currents heavily constrain such models, but one way to avoid these limits is to make the extra Higgs doublet odd under an additional $\mathbb{Z}_2$ symmetry. This protects the theory from these unwanted currents, so long as the doublet does not gain a VEV and break the $\mathbb{Z}_2$ symmetry, *i.e.* the doublet should be *inert*. Given this discrete symmetry, the lightest degree of freedom in the doublet will be stable and so a DM candidate. This is the IDM.

Allowing the inert Higgs doublet to be odd forbids it from having Yukawa couplings with SM fermions, thus couples only to itself, the electroweak gauge bosons, and the SM Higgs doublet[1]. Under the gauge and $\mathbb{Z}_2$ symmetries, the addition of this extra Higgs Doublet admits several new terms to the scalar potential, which becomes

$$\begin{aligned} V = &-\mu_1^2|H_1|^2 + \mu_2^2|H_2|^2 + \lambda_1|H_1|^4 + \lambda_2|H_2|^4 + \lambda_3|H_1|^2|H_2|^2 \\ &+ \lambda_4|H_1^\dagger H_2|^2 + \frac{\lambda_5}{2}\left\{(H_1^\dagger H_2)^2 + \text{h.c.}\right\}, \end{aligned} \tag{4.1}$$

where H_1 is the SM Higgs doublet and H_2 is the inert Higgs doublet.

The potential has 7 parameters, although two of them (λ_1 and μ_1) are from the SM and can be calculated using electroweak observables, leaving us with 5 free parameters. With the SM Higgs doublet expanded about its VEV, v, the Higgs doublets are defined as follows

$$H_1 = \begin{pmatrix} G^+ \\ \frac{1}{\sqrt{2}}(v + h + G^0) \end{pmatrix}, \text{ and } H_2 = \begin{pmatrix} H^+ \\ \frac{1}{\sqrt{2}}(H^0 + iA^0) \end{pmatrix}, \tag{4.2}$$

where h is the SM Higgs boson. The scalars G^0 and G^+ are the would-be Goldstone bosons, which are "eaten" by the electroweak gauge bosons. The remaining four degrees of freedom,

[1]The SM Higgs doublet is sometimes referred to as the *active* doublet, as it gains a VEV and breaks the electroweak symmetry.

$H^{\pm}$, A^0, and H^0 are the new Higgs bosons, which are odd under the $\mathbb{Z}_2$ symmetry. The $H^{\pm}$ states carry electromagnetic charge, and therefore cannot be our DM candidate, leaving either A^0 (the CP-odd Higgs) or H^0 (the CP-even Higgs) as our DM candidate, depending on which is lighter.

Post-symmetry breaking, the masses of the odd sector Higgs bosons are given by

$$\begin{aligned} m_{H^0}^2 &= \mu_2^2 + \frac{1}{2}\left(\lambda_3 + \lambda_4 + \lambda_5\right) v^2, \\ m_{A^0}^2 &= \mu_2^2 + \frac{1}{2}\left(\lambda_3 + \lambda_4 - \lambda_5\right) v^2, \\ m_{H^{\pm}}^2 &= \mu_2^2 + \frac{1}{2}\lambda_3\, v^2. \end{aligned} \tag{4.3}$$

For this study H^0 was taken to be the lightest and therefore our DM candidate, which given the relations above, means $\lambda_5 < 0$ and $\lambda_4 + \lambda_5 < 0$. We would like to parameterise the IDM in terms of physically meaningful observables, which are appropriate to this study, rather than the more abstract parameters seen in (4.1). Of the 5 parameters to be defined, a logical first choice is the DM mass m_{H^0}. We also use, as is typically done in studies of the IDM, the combination of couplings $\lambda_L \equiv (\lambda_3 + \lambda_4 + \lambda_5)/2$. This combination controls a number of interactions, most importantly the hH^0H^0 coupling, which if switched off suppresses DM scattering off of fermions via SM Higgs exchange, and therefore quenches the direct detection signal.

The following squared mass splittings can also be taken as free parameters

$$\Delta m_0^2 \equiv m_{A^0}^2 - m_{H^0}^2 = -\lambda_5\, v^2 > 0, \tag{4.4}$$

$$\Delta m_+^2 \equiv m_{H^{\pm}}^2 - m_{H^0}^2 = -\frac{1}{2}(\lambda_4 + \lambda_5)\, v^2 > 0. \tag{4.5}$$

Summarising, the IDM can be described by the variables m_{H^0}, Δm_0^2, Δm_+^2, λ_L, and λ_2. However all the processes considered in this study (annihilation, scattering off SM nuclei, and production at colliders) are independent of λ_2 at tree-level (higher order diagrams will not be considered here), and so it may be ignored as a parameter in this study.

Furthermore, the square mass differences are set to be equal, *i.e.* $\Delta m^2 \equiv \Delta m_0^2 = \Delta m_+^2$, which simplifies the model, and also protects against conflicts with electroweak precision tests (discussed in the coming section). The intention of this study was to show how topological defects can be added to the IDM and its allowed parameter space could be expanded, therefore a simplification of this nature does not discard any key features integral to our aims. We are

now left with a more manageable 3-dimensional parameter space consisting of λ_L, Δm^2, and m_{H^0}.

4.1.1 Theoretical Bounds and Electroweak Precision Tests

The IDM has a rich phenomenology, and before considering the typical experimental constraints in Section 4.4, we will look at the theoretical bounds and limits from electroweak precision tests (EWPTs) to find the regions of parameter space to start our study within.

The requirement for the potential (4.1) to have stable minima is essential, as discussed in Section 1.4.4. To be bounded from below, and so not have minima at infinities, the couplings in the potential must obey the following conditions

$$\lambda_{1,2} > 0, \quad \lambda_3 > -2\sqrt{\lambda_1\,\lambda_2}, \quad \lambda_3 + \lambda_4 - |\lambda_5| = 2\,\lambda_L > -2\sqrt{\lambda_1\,\lambda_2}. \tag{4.6}$$

A global minimum preserving the $\mathbb{Z}_2$ symmetry is also required, that is there cannot be another minimum which breaks the symmetry into which ours might tunnel. To avoid this one requires

$$\frac{\mu_1^2}{\sqrt{\lambda_1}} < \frac{\mu_2^2}{\sqrt{\lambda_2}}. \tag{4.7}$$

With the above conditions a stable vacuum is assured.

As well as vacuum stability, it is also desired that calculations within the model remain perturbative across the energy scales of the processes considered, this may be guaranteed if

$$|\lambda_i| \leq 8\pi \;\forall\; i = 1, \ldots, 5. \tag{4.8}$$

Lastly, processes in the IDM should not break unitarity; this is insured by imposing the bounds

$$|e_i| \leq 8\pi \;\forall\; i = 1, \ldots, 12, \tag{4.9}$$

where

$$e_{1,2} = \lambda_3 \pm \lambda_4, \qquad e_{3,4} = \lambda_3 \pm \lambda_5, \qquad e_{5,6} = \lambda_3 + 2\lambda_4 \pm 3\lambda_5, \tag{4.10}$$

$$e_{7,8} = -\lambda_1 - \lambda_2 \pm \sqrt{(\lambda_1 - \lambda_2)^2 + \lambda_4^2}, \qquad e_{9,10} = -\lambda_1 - \lambda_2 \pm \sqrt{(\lambda_1 - \lambda_2)^2 + \lambda_5^2}, \tag{4.11}$$

$$e_{11,12} = -3\lambda_1 - 3\lambda_2 \pm \sqrt{9\,(\lambda_1 - \lambda_2)^2 + (2\lambda_3 + \lambda_4)^2}. \tag{4.12}$$

Across the parameter space we will consider here, the couplings obey all vacuum stability, perturbativity, and unitary bounds.

When considering BSM theories, it is often important to see how they are constrained by precision tests. A measurable process can be well predicted by the SM, and so contributions from new physics need to be small as to not spoil the agreement. For the IDM, EWPTs [241, 242], which constrain the size of new physics contributions to electroweak observables, offer the best limits.

For EWPTs, it is standard procedure to consider all contributions to the electroweak observables in just three oblique parameters S, T, and U. To do, three assumptions are made [243]:

1. Electroweak interactions are described by the gauge group $\mathrm{SU(2)_L \times U(1)_Y}$.
2. The couplings to light fermions introduced by the new physics are suppressed relative to the fermion couplings to electroweak gauge bosons.
3. The scale of the new physics is larger than the W and Z boson masses.

Electroweak observable precision measurements involve light fermions exchanging electroweak gauge bosons. With the assumptions above, one can neglect new physics contributions from vertex and box corrections, as vacuum polarization diagrams (the oblique corrections) give the dominant contributions.

The oblique parameter U only affects charged current observables, such as m_W, whereas S and T influences these as well as neutral current and low energy observables. Typically U is expected to be small, and furthermore much less than T [242]. Subsequently, one often adds the further assumption that $U = 0$, allowing all observables to be in terms of S and T.

In the IDM, the contributions to S and T (taken from [236]) are

$$\Delta S = \frac{1}{2\pi}\int_0^1 dx\, x\,(1-x)\,\log\left(\frac{x m_{H^0}^2 + (1-x)m_{A^0}^2}{m_{H^\pm}^2}\right), \tag{4.13}$$

and

$$\Delta T = \frac{\left[F\left(m_{H^\pm}, m_{A^0}\right) + F\left(m_{H^\pm}, m_{H^0}\right) - F\left(m_{A^0}, m_{H^0}\right)\right]}{32\pi^2 \alpha_{\mathrm{EM}} v^2}, \tag{4.14}$$

where

$$F\left(m_1, m_2\right) = \frac{m_1^2 + m_2^2}{2} - \frac{m_1^2 m_2^2}{m_1^2 - m_2^2}\log\left(\frac{m_1^2}{m_2^2}\right). \tag{4.15}$$

Work by the GFitter group [244] offers the best measurements of the oblique parameters, which under the same assumption that $U = 0$ with $m_t = 173$ GeV and $m_h = 125$ GeV, are

$$\Delta S \equiv S - S_{\mathrm{SM}} = 0.06 \pm 0.09, \qquad \text{and} \qquad \Delta T \equiv T - T_{\mathrm{SM}} = 0.10 \pm 0.07. \tag{4.16}$$

The contributions to S (4.13) and T (4.14) from the IDM must then be within error of these values in order to not conflict with EWPTs.

In the case of T, the IDM's contribution $\Delta T = 0$ when $\Delta m_0^2 = \Delta m_+^2$, which has already been assumed, pre-empting this result. This is the consequence of a $\mathrm{SU}(2)_\mathrm{L} \times \mathrm{SU}(2)_\mathrm{R}$ *custodial symmetry* arising in this limit, which may be seen when one recasts the potential (4.1) in terms of 2×2 matrices: $\mathbf{\Phi}_1 = (i\sigma_2 H_1^*, H_1)$, and $\mathbf{\Phi}_2 = (i\sigma_2 H_2^*, \pm H_2)$. Doing so one finds

$$\begin{aligned} V = &- \frac{\mu_1^2}{2}\,\mathrm{Tr}\left[\mathbf{\Phi}_1^\dagger \mathbf{\Phi}_1\right] + \frac{\mu_2^2}{2}\,\mathrm{Tr}\left[\mathbf{\Phi}_2^\dagger \mathbf{\Phi}_2\right] + \frac{\lambda_1}{4}\left(\mathrm{Tr}\left[\mathbf{\Phi}_1^\dagger \mathbf{\Phi}_1\right]\right)^2 + \frac{\lambda_2}{4}\left(\mathrm{Tr}\left[\mathbf{\Phi}_2^\dagger \mathbf{\Phi}_2\right]\right)^2 \\ &+ \frac{\lambda_3}{4}\,\mathrm{Tr}\left[\mathbf{\Phi}_1^\dagger \mathbf{\Phi}_1\right]\,\mathrm{Tr}\left[\mathbf{\Phi}_2^\dagger \mathbf{\Phi}_2\right] + \frac{\lambda_4 + \lambda_5}{16}\left(\mathrm{Tr}\left[\mathbf{\Phi}_1^\dagger \mathbf{\Phi}_2\right] + \mathrm{Tr}\left[\mathbf{\Phi}_2^\dagger \mathbf{\Phi}_1\right]\right)^2 \\ &- \frac{\lambda_4 - \lambda_5}{16}\left(\mathrm{Tr}\left[\mathbf{\Phi}_1^\dagger \mathbf{\Phi}_2 \sigma_3\right] - \mathrm{Tr}\left[\sigma_3 \mathbf{\Phi}_2^\dagger \mathbf{\Phi}_1\right]\right)^2, \end{aligned} \tag{4.17}$$

where if $\lambda_4 = \lambda_5$, then there is a global $\mathrm{SU}(2)_\mathrm{L} \times \mathrm{SU}(2)_\mathrm{R}$ symmetry which causes a cancellation between gauge self-energies such that $\Delta T = 0$. Furthermore if rewritten in terms of $\tilde{\mathbf{\Phi}}_2 = \mathbf{\Phi}_2 \sigma_3$ instead, one finds a similar potential which conserves the same global symmetry in the limit that $\lambda_4 = -\lambda_5$. Therefore $\Delta T = 0$ when $\lambda_4 = \pm\lambda_5$, which corresponds to either $\Delta m_+^2 = \Delta m_0^2$ or $\Delta m_+^2 = 0$.

Let us now consider ΔS when $\Delta m_+^2 = \Delta m_0^2$, in this case

$$\Delta S \simeq \frac{1}{2\pi}\int_0^1 dx\, x\,(1-x)\,\log\left(1 - x\,a^2\right) \leq 0, \qquad a^2 \equiv \frac{m_{A^0}^2 - m_{H^0}^2}{m_{A^0}^2} \in [0,1]. \tag{4.18}$$

This takes its largest (absolute) value when $a^2 = 1$ which is, $\Delta S \simeq -0.022$. Furthermore $\Delta S \to 0$ as $a^2 \to 0$, therefore given (4.16) ΔS remains within error of the measured value. In conclusion, by requiring $\Delta m_+^2 = \Delta m_0^2$ we avoid constraints from EWPTs.

4.2 An Inert Doublet Model with a U(1)′ Gauge Symmetry

Having reviewed the IDM, we now wish to see how the theory can be extended in order to for cosmic strings to form, and in such a way as to allow DM to be produced in the decays of these defects. There are many ways in which the IDM could be extended to accommodate this new physics, however as we seek just an illustrative example of defects in a DM model, then a simple extension will be studied.

As mentioned at the start of this chapter, the simplest way for strings to arise is in the spontaneous breaking of an additional local U(1)′ symmetry. Such breaking is necessary to

allow the gauge boson to become massive enough to escape detection, and requires just a single additional field ϕ, charged under the symmetry, to gain a VEV. Doing so allows cosmic strings to form in the model.

Interestingly, these strings can then decay into DM particles with no further requirements on, or additions to the theory. This may be understood by inspection of the potential, which with the addition of the ϕ field becomes

$$\begin{aligned} V = &- \mu_1^2|H_1|^2 + \mu_2^2|H_2|^2 - \mu_\phi^2|\phi|^2 + \lambda_1|H_1|^4 + \lambda_2|H_2|^4 + \lambda_\phi|\phi|^4 + \tilde{\lambda}_1|\phi|^2|H_1|^2 \\ &+ \tilde{\lambda}_2|\phi|^2|H_2|^2 + \lambda_3|H_1|^2|H_2|^2 + \lambda_4|H_1^\dagger H_2|^2 + \left\{\frac{\lambda_5}{2}(H_1^\dagger H_2)^2 + h.c.\right\}. \end{aligned} \tag{4.19}$$

As mentioned, ϕ breaks the U(1)′ symmetry by gaining a VEV, v', and can be expanded about its minimum, which in the unitary gauge is

$$\phi = \frac{1}{\sqrt{2}}(v' + X), \tag{4.20}$$

where X is a remnant real scalar.

Inspecting the potential (4.19), one sees portal coupling terms, $|\phi|^2|H_1|^2$ and $|\phi|^2|H_2|^2$, have arisen. These terms mean the H_1 and H_2 Higgs fields can condense upon the string, and these condensates (which were discussed in Section 2.3.2) can radiate both SM and inert Higgs bosons. The latter means the decaying strings produced in the theory will be a source of DM, and the former introduces interesting string constraints [245], which will be studied further in Section 4.4.2.

There are two new particles now in our model: X, and Z', the U(1)′ gauge boson, whose masses post-symmetry breaking will both be proportional to v'. Significant DM production from cosmic string decays requires v' to be far greater than the electroweak scale, thus these new degrees of freedom will be massive enough to be integrated out. This leaves us with an effective field theory, whose potential is

$$\begin{aligned} V = &- \left(\mu_1^2 - \frac{\tilde{\lambda}_1 v'^2}{2}\right)|H_1|^2 + \left(\mu_2^2 + \frac{\tilde{\lambda}_2 v'^2}{2}\right)|H_2|^2 + \left(\lambda_1 - \frac{\tilde{\lambda}_1^2}{8\lambda_\phi}\right)|H_1|^4 \\ &+ \left(\lambda_2 - \frac{\tilde{\lambda}_2^2}{8\lambda_\phi}\right)|H_2|^4 + \left(\lambda_3 - \frac{\tilde{\lambda}_1\tilde{\lambda}_2}{8\lambda_\phi}\right)|H_1|^2|H_2|^2 + \lambda_4|H_1^\dagger H_2|^2 \\ &+ \left\{\frac{\lambda_5}{2}(H_1^\dagger H_2)^2 + h.c.\right\}. \end{aligned} \tag{4.21}$$

This is in fact just the same as the original IDM potential (4.1), when the following redefinitions are made:

$$\mu_1^2 - \frac{\tilde{\lambda}_1 v'^2}{2} \to \mu_1^2, \qquad \mu_2^2 + \frac{\tilde{\lambda}_2 v'^2}{2} \to \mu_2^2, \qquad \lambda_1 - \frac{\tilde{\lambda}_1^2}{8\lambda_\phi} \to \lambda_1,$$
$$\lambda_2 - \frac{\tilde{\lambda}_2^2}{8\lambda_\phi} \to \lambda_2, \qquad \text{and} \qquad \lambda_3 - \frac{\tilde{\lambda}_1 \tilde{\lambda}_2}{8\lambda_\phi} \to \lambda_3. \tag{4.22}$$

This mapping back to the usual IDM is clearly advantageous, although the first two redefinitions show fine-tuning will be required in order to allow $\mu_{1,2}^2$ (and therefore the Higgs bosons' masses) to remain near the electroweak scale. Such fine-tunings are common in theories of this type, and can be viewed a sensitivity to high scale physics, which we recognise as part of the gauge hierarchy problem. This could be solved, for example, if we supersymmetrise the model, however this is beyond the scope of this work.

This model is arguably the simplest way in which cosmic strings may be introduced into the IDM, although we could have embellished and allowed the inert doublet to also be charged under U(1)′ symmetry. This would have permitted the $\mathbb{Z}_2$ symmetry, which stabilises the DM candidate, to arise dynamically upon the U(1)′ breaking. However the λ_5 term would be forbidden by gauge invariance in this model, which means H^0 and A^0 will be mass degenerate, as evident from (4.4). This mass degeneracy causes a conflict with direct detection searches.

In the IDM, $H^0 N \to H^0 N$ scattering (where N is a SM nucleon) proceeds via the exchange of the SM Higgs boson, and direct detection bounds can be avoided by lowering λ_L. However mass degenerate H^0 and A^0 states allows $H^0 N \to A^0 N$ scattering (and vice versa) via Z boson exchange, which is determined by fixed gauge couplings, and generates a direct detection signal far above current limits. This problem will be avoided if a mass splitting, *i.e.* a λ_5 term, can be reintroduced. However the mass splitting will need to be greater than the typical recoil energies imparted in the scatterings ($\sim \mathcal{O}(100)$ keV) in order to close this channel.

The λ_5 term can be reintroduced via a higher-order effective operator, such as

$$\frac{1}{\Lambda}\phi\,(H_1^\dagger H_2)^2, \tag{4.23}$$

which is allowed when ϕ and H_2 carry $+1$ and -2 charge under the U(1)′ symmetry respectively. Post-symmetry breaking, (4.23) will produce a λ_5 term like that seen in the potential (4.19). Such a theory was considered, but for different reasons, in [239], where the U(1)′ was

broken near the TeV scale. This allowed DM annihilations into Z' bosons, which meant lighter DM states could produce the correct relic abundance (according to standard freeze-out).

Regardless of whether or not the inert doublet is charged under the U(1)$'$ symmetry, our effective field theory at the electroweak scale will be the standard IDM, with the additional presence of cosmic strings, which can decay into SM and inert Higgs bosons. This means we have a source of DM from decaying defects in the early Universe, and we must consider the genesis mechanism presented in Chapter 3, as standard freeze-out is no longer appropriate for this model.

4.3 Increasing the Relic Abundance

The previous section introduced cosmic strings into the IDM, showing how condensates of both the SM and inert Higgs doublets could form on the defect. Consequently, defect decays radiate not just DM, but all odd sector states. Given this, the derivation of the Boltzmann equations in this section will be slightly more involved than what was presented in Section 3.1.1. As there is now a sector of odd particles, rather than a single species, a set of Boltzmann equations must be evaluated in order to take into account co-annihilations (reviewed in Section 1.2.1), and all particle production from defect decays.

Before, when deriving the Boltzmann equation in the case of a single DM species in Section 3.1.1, the energy density injection rate of the string was taken to have the form (3.1). A fraction f_X of this went into X states, which in turn decayed producing DM. Now, the string decays are producing the odd sector Higgs bosons directly, with a fraction f_i (where i represents an odd sector state) of the energy density injected going into i particles with an average energy of $\overline{E}_i$. The number density of each odd sector state, n_i, evolves according to

$$\begin{aligned}\frac{dn_i}{dt} =& -3Hn_i - \sum_j \langle\sigma_{ij}v_{ij}\rangle(n_i n_j - n_i^{\rm eq} n_j^{\rm eq}) \\ &- \sum_{j\neq i}\Big[\langle\sigma'_{ij}v_{ij}\rangle(n_i n_X - n_i^{\rm eq} n_X^{\rm eq}) - \langle\sigma'_{ji}v_{ij}\rangle(n_j n_{X'} - n_j^{\rm eq} n_{X'}^{\rm eq})\Big] \\ &- \sum_{j\neq i}\Big[\Gamma_{ij}(n_i - n_i^{\rm eq}) - \Gamma_{ji}(n_j - n_j^{\rm eq})\Big] + \frac{f_i Q(t)}{\overline{E}_i},\end{aligned} \tag{4.24}$$

where the cross-sections and decay rates are the same as defined before in (1.31), although here X and X' only comprise of SM particles, due to the $\mathbb{Z}_2$ symmetry conserved in each of the processes.

Proceeding as with co-annihilations in the case of standard freeze-out (see Section 1.2.1) [58], the Boltzmann equations are summed obtaining

$$\frac{dn}{dt} = -3Hn - \langle\sigma_{\text{eff}}v\rangle(n^2 - n_{\text{eq}}^2) + \sum_i \frac{f_i Q(t)}{\overline{E}_i}, \tag{4.25}$$

where $n = \sum_i n_i$ and

$$\langle\sigma_{\text{eff}}v\rangle \equiv \sum_{ij}\langle\sigma_{ij}v_{ij}\rangle\frac{n_{i,\text{eq}}n_{j,\text{eq}}}{n_{\text{eq}}^2}. \tag{4.26}$$

Given only the lightest odd sector particle, H^0, is stable, then we expect the present total number density of odd sector states to be entirely in the form of H^0, *i.e.* $n(t_0) = n_{H^0}(t_0)$.

In terms of $Y = n/s$ and $x = m_{H^0}/T$ (as defined in Section 1.2.1), the Boltzmann equation becomes

$$\frac{dY}{dx} = -\frac{A(x)}{x^2}\left[Y^2 - Y_{\text{eq}}^2\right] + \frac{B}{x^{4-2p}}, \tag{4.27}$$

where

$$A(x) = \sqrt{\frac{\pi g_*}{45}}m_{H^0}M_{\text{Pl}}\langle\sigma_{\text{eff}}v\rangle(x), \qquad B = \frac{3}{4}r_0 q_0, \tag{4.28}$$

with

$$q_0 = \sum_i \frac{\overline{E}_{H^0}}{\overline{E}_i}\frac{f_i Q_\chi}{\rho_\chi H_\chi}, \text{ and } r_0 = m_{H^0}/\overline{E}_{H^0}. \tag{4.29}$$

The equilibrium yield now sums over all odd sector states, and so takes the form[1]

$$Y_{\text{eq}}(x) = \frac{45x^2}{4\pi^4 g_{*S}}\sum_i g_i\left(\frac{m_i}{m_{H^0}}\right)^2 K_2\left(x\frac{m_i}{m_{H^0}}\right), \tag{4.30}$$

where g_i is the internal degrees of freedom of particle i.

The model's Boltzmann equation (4.27), despite the added complexities, has the same form as that of a single DM species (3.4). In this previous derivation, the injection rate of a single particle species was parameterised using a variable q_X. Now the variable q_0 is used which acts in the same way, although for the injection of multiple odd sector states. We set $r_0 = 0.5$ for this study, which is typical for condensates of light fields [206].

Both FT and CE scenarios (introduced in Section 2.4) of cosmic string decay will be considered, where $p = 1$ and $p = 7/6$ respectively. For this study we focus on benchmark points in the IDM parameter space, where $\Delta m^2 = 1000$ or 10000 GeV^2, and $\lambda_L = 0$ or 0.1.

[1]The equilibrium yield was earlier defined in a different form (1.22), which was valid in the non-relativistic regime. This helped us to derive an approximate analytic expression of x_{fr} (1.27). Here we use the full form of equilibrium yield.

The chosen values for the mass splitting allow us to examine regions of parameter space where co-annihilations are important ($\Delta m^2 = 1000$ GeV^2), and when they are not ($\Delta m^2 = 10000$ GeV^2). One can see this by considering a 200 GeV H^0 state; with $\Delta m^2 = 1000$ GeV^2, this means $m_{A^0} = m_{H^\pm} \approx 202$ GeV, while with $\Delta m^2 = 10000$ GeV^2, we get $m_{A^0} = m_{H^\pm} \approx 224$ GeV. Given that coannihilations can be expected to become important roughly when the linear mass splitting drops below the temperature at freeze-out, *i.e.* when $\delta m \sim T_f \approx m_{H^0}/25 = 8$ GeV, then one can see our choices of Δm^2 are suitable for the study of regimes with and without coannihilations playing a significant role. As mentioned earlier, λ_L controls the connection to SM fermions via the hH^0H^0 coupling, so by choosing these values as benchmark points, one can see how severing this connection impacts the phenomenology.

To use the Boltzmann equation (4.27) to find the evolution of the yield, one must calculate the effective cross-section $\langle \sigma_{\text{eff}} v \rangle$, which we found using MicrOMEGAS [246]. Through numerically evaluating the equation, the relic abundance of DM is plotted against m_{H^0} in Figure 4.1, for the four benchmark points in our parameter space in the FT scenario. Within each plot are curves showing the predicted relic abundance of DM in our IDM with topological defects for various values of q_0, as well that predicted by standard freeze-out. It is clear from these plots that increasing q_0 increases the predicted relic abundance. Below the standard freeze-out curves in all of these cases, an over-abundance of DM is being produced.

From the standard freeze-out curves, one finds only one or two m_{H^0} values along these slices in parameter space at which the observed relic abundance is produced. However with cosmic string decays the correct relic density may be generated within a large range of m_{H^0} values by tuning q_0. Therefore anywhere in parameter space where the relic abundance previously predicted by standard freeze-out to be equal to or less than what is measured, can now be acceptable.

The general shape of each plot is the same: they feature a major dip at around $m_{H^0} \sim 100$ GeV and rise either side. This dip emerges as annihilation channels into W and Z bosons become kinematically accessible. Below these thresholds, annihilations into fermions dominate, but in the case when $\lambda_L = 0$ these channels are cut-off; consequently, the predicted abundance sharply increases, as is evident in Figure 4.1b. However by decreasing the mass splitting, co-annihilation channels are opened up and the predicted relic abundance drops in these low mass regions, as is seen by comparing Figure 4.1a & 4.1b.

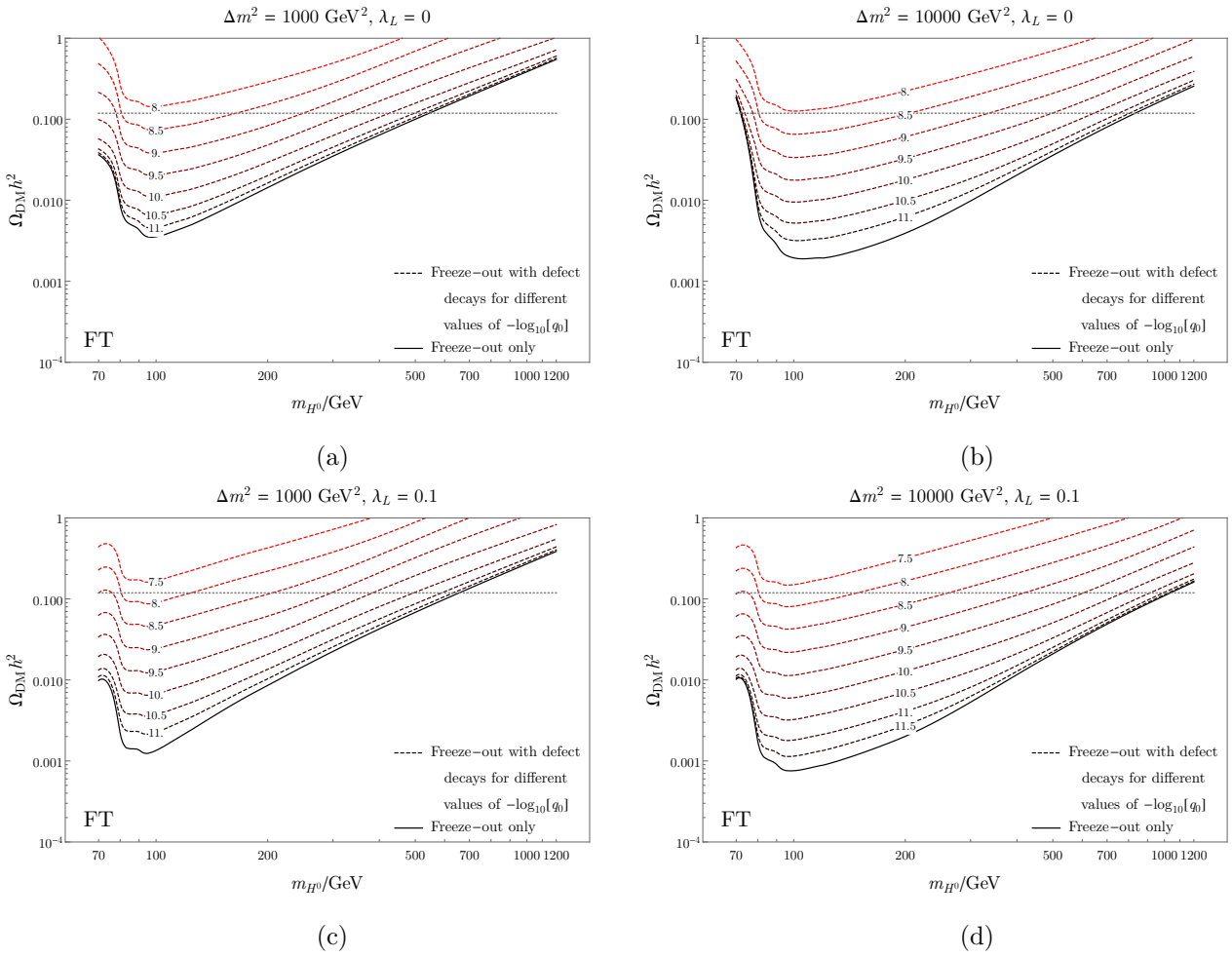

Figure 4.1: Plots of the predicted relic abundance against m_{H^0} in the FT scenario for four different benchmark points of $(\Delta m^2, \lambda_L)$; (1000 GeV^2, 0) (a), (10000 GeV^2, 0) (b), (1000 GeV^2, 0.1) (c), and (10000 GeV^2, 0.1) (d). Each plot shows the predicted relic abundance for the IDM with topological defects for various values of q_0, as well as for standard freeze-out. The horizontal dotted line is the observed relic abundance [17].

One would assume that this effect from a decreased mass splitting would also be true in the high mass region, and the relic abundance would likewise drop. Somewhat surprisingly however, one finds the relic abundance actually *increases*. This is due to the decrease in the mass splitting causing the model to go towards what is referred to as the pure gauge limit. In the high mass region, annihilations into W and Z bosons are dominant, however in the pure gauge limit the contribution from their longitudinal modes vanishes. Subsequently, this suppresses the cross-section and so increases the relic abundance enough to counteract

co-annihilation effects. In Appendix B we go over this point in further detail, showing the contributing diagrams and the behaviour of the squared matrix elements.

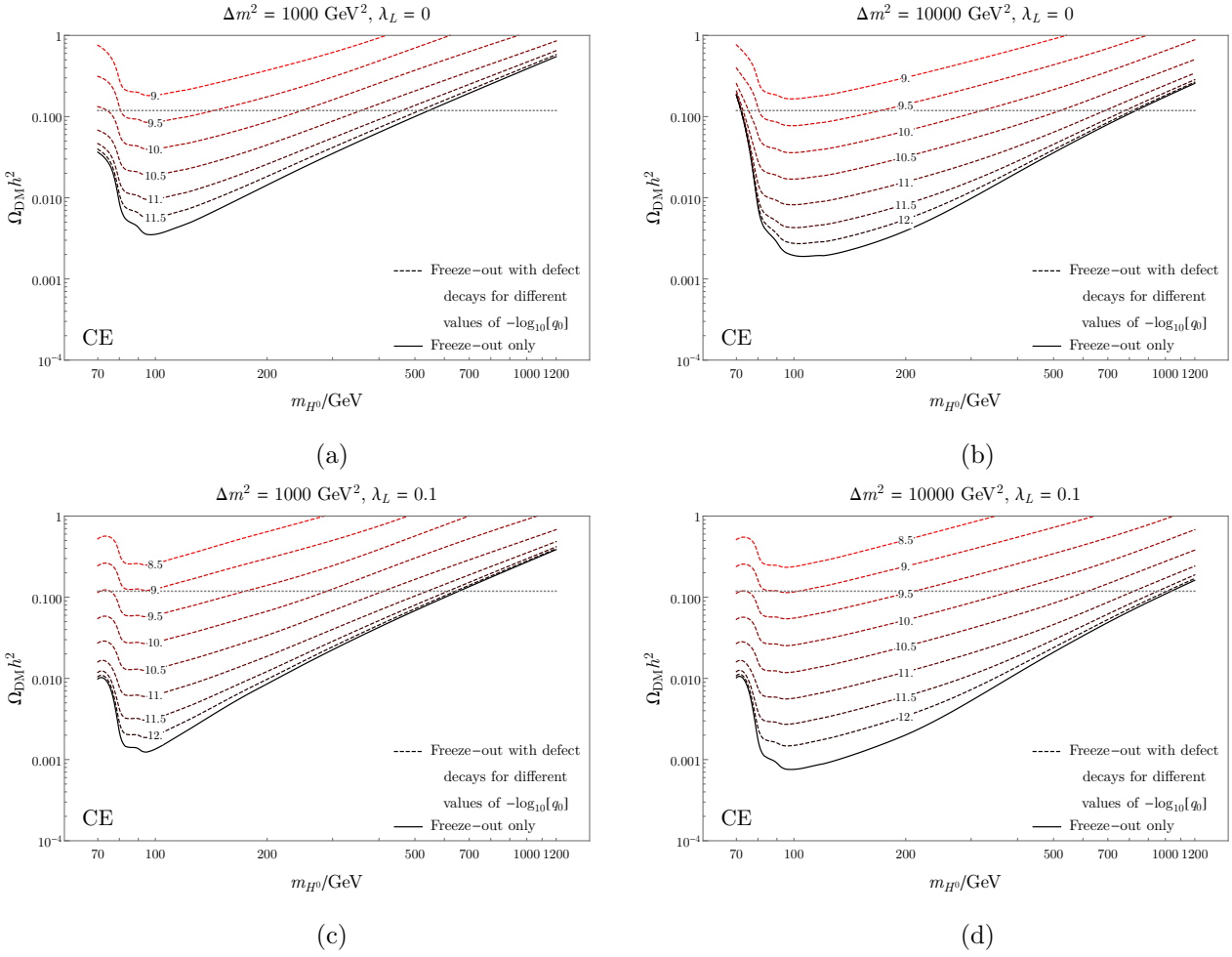

Figure 4.2: Plots of the predicted relic abundance against m_{H^0} in the CE scenario for four different benchmark points of $(\Delta m^2, \lambda_L)$; (1000 GeV^2, 0) (a), (10000 GeV^2, 0) (b), (1000 GeV^2, 0.1) (c), and (10000 GeV^2, 0.1) (d). Each plot shows the predicted relic abundance for the IDM with topological defects for various values of q_0, as well as for standard freeze-out. The horizontal dotted line is the observed relic abundance [17].

Figure 4.2 contains the same plots as before, except now in the CE scenario. They have the same shape as those in Figure 4.1, although smaller q_0 values are required to produce the same relic abundance. This is because the production rate from string decays drops at a slower rate in the CE scenario and so the total contribution to the relic density will be larger, meaning q_0 must be lower in order to balance this out.

For this study we will consider the case where H^0's mass is greater than the electroweak gauge bosons'. Above this threshold, annihilations into these states are allowed, and drive the cross-section up and so the relic abundance down. This is where our mechanism for DM genesis will have the most use. Furthermore, below this mass threshold there are several strong collider constraints, which will be discussed later in Section 4.4

The Boltzmann equations dictate how the yield of DM will evolve over time, in this section we have derived these equations for an extended IDM in which cosmic strings form and decay into the odd sector particles. These showed us how the relic abundance can be increased by the contributions from defects; this subsequently meant the observed relic abundance could be generated across a larger range of parameter space. The discussion in this section thus far has been void of experimental constraints, which will restrict these newly opened up regions of parameter space; the coming section addresses these.

4.4 Constraints

In the previous section the benefits of our mechanism were seen: it allowed the correct relic density to be generated for a range of m_{H^0} values in benchmark (Δm^2, λ_L) cases, as opposed to the discrete points permitted by standard freeze-out. Here we study a range of phenomenological bounds on the IDM and our mechanism arising from both DM and cosmic string considerations. Direct and indirect detection bounds from DM physics are examined along with those from collider searches, while bounds on cosmic strings from Big Bang Nucleosynthesis and the diffuse γ-ray background are studied.

4.4.1 Bounds from Dark Matter Physics

Direct Detection

We have already seen how direct detection limits can constrain the IDM, forbidding the mass splitting between H^0 and A^0 falling below a few hundred keV. Now we can consider their constraints on the general phase space. Currently the strongest direct detection limits, in the m_{H^0} range we considered, came from the Large Underground Xenon (LUX) experiment at the Sanford Underground Research Laboratory. LUX is a scintillation and ionization detector with a 118 kg fiducial volume of liquid xenon as a target. From 85.3 live-days of data, it limited

the spin-independent scattering cross-section at 90% CL to be 7.6×10^{-46} cm^3 s^{-1} at a WIMP mass of 33 GeV [95]. In the IDM, the WIMP-nucleon scattering proceeds via the exchange of a SM Higgs, whose hH^0H^0 vertex factor is proportional to λ_L. Thus if one sets λ_L to zero, the direct detection signal is cut-off at tree-level. We implement the limits from LUX by calculating the scattering cross-section using MicrOMEGAS [246].

Indirect Detection

Of the indirect detection searches, Fermi-LAT (discussed in Section 1.4.2) can provide the most stringent bounds. For this study we took limits from an analysis which examined the γ-ray continua (in the 20 MeV and 300 GeV energy range) in several dSphs [130]. DM annihilations can produce such γ-rays and so the annihilation cross-section may be limited by this analysis. The γ-ray flux Φ from a celestial object is given by

$$\Phi = \Phi_{\rm PP} \times J, \tag{4.31}$$

where $\Phi_{\rm PP}$ is the "particle physics input" containing all our knowledge of the particle model, and J is the "astrophysical input", which likewise holds all information regarding the astronomical object under study. They are given by

$$\Phi_{\rm PP} = \frac{\langle\sigma v\rangle}{8\pi m_{H_0}^2}\int_{E_0}^{E_{\rm max}}\frac{dN}{dE}dE, \qquad J = \int_{\Delta\Omega(\psi)}\int_{l}[\rho(l,\psi)]^2 dl d\Omega(\psi). \tag{4.32}$$

The astrophysical factor, J, depends on the density profile of DM around the object, a quantity that is poorly understood leading to significant uncertainties in resulting bounds. In the study considered, each dSph was weighted by its J value, obtaining a combined 95% CL limit on $\Phi_{\rm PP}$ of

$$\Phi_{\rm PP} < 5.5^{+4.3}_{-4.5}\times10^{-30}\ {\rm cm}^3\ {\rm s}^{-1}\ {\rm GeV}^{-2}. \tag{4.33}$$

MicrOMEGAS [246] was then used to scan across phase space and find the predicted value of $\Phi_{\rm PP}$ at each point.

DM annihilations can also effect recombination via reheating and ionization, therefore limits on $\langle\sigma v\rangle$ can be extracted from CMB data. Taking an analysis which uses WMAP 5-year data [247], it was found that the limits were weaker than those from LUX across our chosen phase space. However the limits from Planck data are expected to be an order of magnitude stronger, and will be competitive with current direct detection bounds.

Collider Searches

As with most theories, the IDM can be probed using several different collider searches. Already in Section 4.1.1 we have discussed the constraints from EWPTs.

The strongest collider limits typically come from monojet searches. The coupling λ_L is the controlling parameter in these analyses; if set to zero, monojet signals from $pp \to H^0 H^0 +$ jet are suppressed as they occur via the mediation of a SM Higgs. We take limits from an analysis of simplified models of DM using $\sqrt{s} = 8$ TeV LHC data, which considers a scalar DM candidate coupling to the SM Higgs in the same way as H^0 in the IDM [248]. It shows the 90% CL monojet limits only come in approximately when m_{H^0} drops below half the SM Higgs boson mass, $m_h/2$, which is outside the parameter space considered here.

If Δm^2 is sufficiently small, monojet signals could arise from $pp \to A^0 H^0 +$ jet processes (in which a Z is exchanged), since the decays of A^0 are expected to emit soft SM particles, which could be below ATLAS's and CMS's trigger threshold. The same analysis we used above [248], could be used here to limit this process. However we find the limits are very weak, requiring only that $A^0 H^0 Z$ coupling be approximately less than 5 for $m_{H^0} > m_W$.

If the mass splitting is large enough, then the visible decay products of A^0 and $H^\pm$ could be detected within ATLAS and CMS. Such searches closely match those of chargino/neutralino pair production in SUSY theories, which look for missing transverse energy and multilepton signatures. An analysis of $\sqrt{s} = 8$ TeV ATLAS data constrains the neutralino mass to be $\lesssim 110$ GeV [249] when it decays the same way as the odd sector particles in the IDM could. However, the limits will be weaker in the case of the IDM, where the odd sector particles are scalars, as the production cross-sections are smaller than for charginos and neutralinos. These searches put no relevant constraints on the IDM parameter space for $m_{H^0} > m_W$.

With the discovery of the SM Higgs boson [250,251], came measurements from ATLAS and CMS of the $h \to \gamma\gamma$ decay rate, which at the time were slightly above the SM prediction, and so indicated possible new physics. After improved analyses from ATLAS [252] and CMS [253], the excesses dropped and came within $1\,\sigma$ of the SM prediction, measuring the signal strengths to be

$$R_{\gamma\gamma}^{\text{CMS}} = 1.14^{+0.26}_{-0.23} \qquad \text{and} \qquad R_{\gamma\gamma}^{\text{ATLAS}} = 1.17 \pm 0.27. \tag{4.34}$$

The IDM contains a charged Higgs, which contributes to $h \to \gamma\gamma$ via a loop. The signal

strength for $h \to \gamma\gamma$ in the IDM is

$$\begin{aligned} R_{\gamma\gamma} &\equiv \frac{\sigma(pp \to h \to \gamma\gamma)^{\mathrm{IDM}}}{\sigma(pp \to h \to \gamma\gamma)^{\mathrm{SM}}} \\ &\approx \frac{\sigma(gg \to h)^{\mathrm{IDM}} BR(h \to \gamma\gamma)^{\mathrm{IDM}}}{\sigma(gg \to h)^{\mathrm{SM}} BR(h \to \gamma\gamma)^{\mathrm{SM}}} = \frac{BR(h \to \gamma\gamma)^{\mathrm{IDM}}}{BR(h \to \gamma\gamma)^{\mathrm{SM}}}. \end{aligned} \tag{4.35}$$

This may be simplified further by approximating the total decay rate of the Higgs in the IDM and SM to be the same for $m_{H^0} > m_h/2$. Therefore the signal strength can be approximated as the ratio of $h \to \gamma\gamma$ decay rates in the IDM and SM. These quantities were calculated analytically in [254], where just the dominant SM contributions from top and W loops were considered. Using these expressions, one finds the signal strength never deviates more than 10% from the SM result across all of our parameter space, which is within 1σ of both ATLAS and CMS measurements and so we are unaffected by this limit.

There is also the limit from the invisible decays of the SM Higgs boson, which given we are looking at DM masses larger than $m_h/2$, would not affect this study as the process is kinematically forbidden. Similarly LEP limits on m_{A^0} and m_{H^+} as a function of m_{H^0} are only relevant when $m_{H^0} < m_W$, which does not enter into our parameter space, thus these constraints can be ignored [255, 256].

From the discussion above, one can see that while there are a large range of collider constraints to consider, they enter in the low m_{H^0} regime, which is beyond the parameter space considered here, and are therefore irrelevant.

4.4.2 Bounds from Cosmic String Physics

Considering string phenomenology, there are also cosmological bounds on q_0 [245, 257–261]. Searches for line-like discontinuities in CMB data put limits on cosmic string scenarios requiring the string tension parameter $G\mu \lesssim 10^{-7}$ [195]. However we can now use DM phenomenological bounds to constrain q_0, and the model-independent unitarity limit (as seen in Section 3.3), while much weaker than experimental bounds, places stronger limits on q_0 than those from CMB searches.

In our model, both inert and SM Higgs doublets can condense upon the string formed, this subsequently means strings decay radiating not just the odd sector Higgs particles needed for our genesis mechanism, but also SM Higgs bosons. Here cosmic string bounds arising in the

case of a large[1] Higgs condensates [245] will be examined, which come from considerations of BBN and the diffuse γ-ray background (DGRB).

These limits constraint the energy injection rate into "visible" SM particles (γ, e, p, n), which will be denoted $Q_{\rm vis}$, with a dimensionless $q_{\rm vis}$ defined analogously to q_0 (4.29). It turns out that BBN constrains the CE scenario (p = 7/6) most strongly, while the DGRB constraints and BBN constraints from the deuterium abundance are about the same for the FT model (p = 1).

Big Bang Nucleosynthesis

BBN is a process through which the aggregation of SM nucleon bound states occurs, which dictates the atomic composition of the Universe. The measured abundance of the light elements is well predicted from SM nuclear physics, therefore a theory significantly disrupting the SM BBN scenario will be constrained. BBN occurs approximately when the temperature drops to around the same level as the binding energy of nucleons, $\mathcal{O}$(1-10) MeV.

BBN has been used to limit long-lived states [262] produced during an earlier freeze-out period, which then decay later during BBN, injecting high energy particles which can disrupt the process. Cosmic strings may affect BBN in a similar way; their decays may carry on during BBN, injecting high energy particles through the SM Higgs condensates. In the CE scenario the bound with the best combination of strength and robustness comes from the deuterium abundance [245], which limits the energy injected per unit entropy to

$$(E_{\rm vis} Y_X)_{\rm max} \simeq 10^{-13}\ \text{GeV}, \tag{4.36}$$

where $E_{\rm vis}$ is the average energy emitted in the form of non-weakly interacting "visible" particles, and Y_X is the yield of the X particles with a lifetime $\tau_X = 400$ s.

Approximating the energy density injected at a time t by $Q_{\rm vis} t$, then

$$q_{\rm vis}(t_{\rm BBN}) \lesssim \frac{8}{3} \frac{(E_{\rm vis} Y_X)_{\rm max}}{T_{\rm BBN}}, \tag{4.37}$$

where $t_{\rm BBN} = 400$ s and $T_{\rm BBN}$ is the temperature at that time.

Knowing the time-dependence of $q_{\rm vis}$ in the CE scenario, we can translate this bound at the BBN epoch to that during freeze-out, which gives

$$q_{\rm vis}(t_\chi) \lesssim \frac{8}{3} \frac{(E_{\rm vis} Y_X)_{\rm max}}{T_{\rm BBN}} \left(\frac{t_\chi}{t_{\rm BBN}} \right)^{\frac{1}{6}}, \tag{4.38}$$

[1] A large Higgs condensate has an amplitude of the order of the string mass scale.

where t_χ is a reference time during freeze-out, which as before is when the temperature equals the DM mass. Substituting in the numerical values, the limit in terms of the DM mass is

$$q_{\rm vis}(t_\chi) \lesssim 4 \times 10^{-11} \left(\frac{100 \text{ GeV}}{m_{H^0}}\right)^{1/3}. \tag{4.39}$$

Diffuse γ-ray Background

Visible particle injection post-recombination will cause electromagnetic cascades via interactions with the cosmic medium, which will contribute to the DGRB. A Fermi-LAT analysis limits the energy injection into SM particles to be $\omega_{\rm cas}^{\rm max} = 5.8 \times 10^{-7}$eV cm^{-3} [263, 264], therefore we require

$$\int_{t_c}^{t_0} dt \left(\frac{a(t)}{a(t_0)}\right)^4 Q_{\rm vis} \lesssim \omega_{\rm cas}^{\rm max}, \tag{4.40}$$

where t_c is the time at which the Universe becomes transparent to the γ-rays detected by Fermi-LAT, and t_0 is the present time.

In the FT scenario, this corresponds to a limit on $q_{\rm vis}$ of

$$q_{\rm vis} \lesssim \left(\frac{t_0}{t_c}\right)^{2/3} \frac{\omega_{\rm cas}^{\rm max}}{\rho_0}, \tag{4.41}$$

where $\rho_0 = 5.6 \times 10^3$ eV cm^{-3} is the present energy density. Inputting numerical values, one finds

$$q_{\rm vis} \lesssim 6 \times 10^{-9} \left(\frac{10^{15}\text{s}}{t_c}\right)^{2/3}. \tag{4.42}$$

4.4.3 Results

Section 4.3 saw how adding topological defects to the IDM opened up the parameter space, as regions where DM was under-produced in standard freeze-out could now meet the relic density requirement. Here the experimental bounds discussed in the previous section are implemented as well in order to see the viable regions of parameter space which remain.

In Figure 4.3 there are plots of q_0 vs m_{H^0} for the FT and CE scenarios. They show the q_0 values required to produced the measured relic density, against m_{H^0} for the four benchmark cases of (Δm^2, λ_L). As such, they could be viewed as inversions of Figure 4.1 & 4.2, which is reflected in their shapes. The q_0 values plummet towards the high mass end of the plots, this corresponds to the points at which the correct abundance is obtained via standard freeze-out, thus any further contributions from topological defect decays will spoil this agreement and so

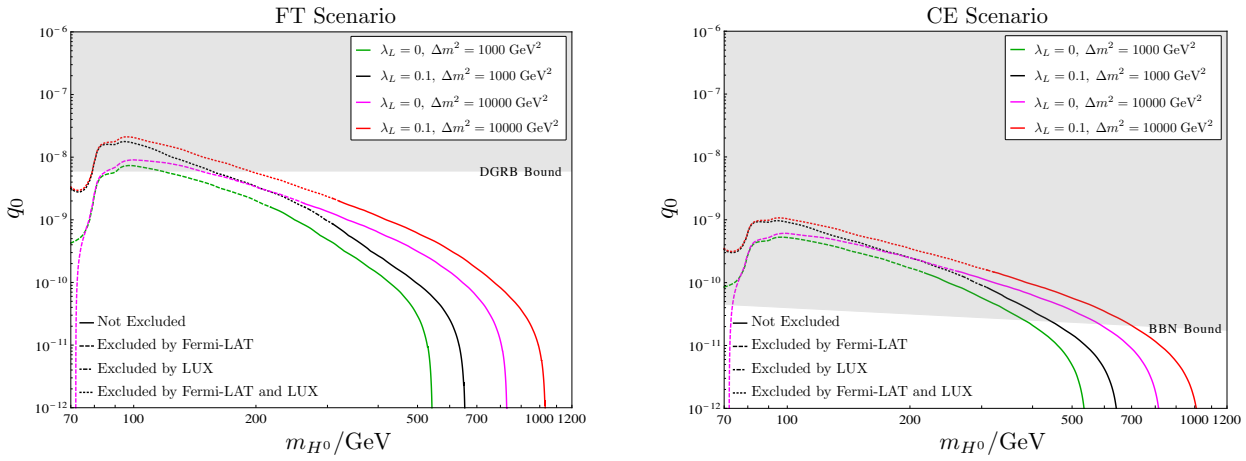

Figure 4.3: Plots of the q_0 values which generate the measured relic density, against m_{H^0} in the FT (a) and CE (b) scenarios. In each plot four benchmark cases of (Δm^2, λ_L) are shown; (1000 GeV^2, 0) (green), (1000 GeV^2, 0.1) (black), (10000 GeV^2, 0) (purple), and (10000 GeV^2, 0.1) (red). In the FT plot, the gray shaded region represents DGRB bounds and in the CE plot it represents BBN bounds. Where the lines are dashed and dot dashed, are where they are ruled out by Fermi-LAT limits from dSphs [130] and LUX limits [95] respectively. The regions where the lines are dotted or solid are ruled out by both or neither respectively.

$q_0 \to 0$. Past this point the annihilations are so inefficient that an over-abundance of DM is predicted, which cannot be reduced via our mechanism.

In each plot, the region of parameter space ruled out by Fermi-LAT/LUX experimental data is indicated with broken line styles, while the grey shaded region is ruled out by cosmological bounds on q_0. Therefore in the regions where the curves are solid and not in the gray shaded area, the measured relic abundance is being produced, while all experimental bounds are avoided. By inspection of these plots, one can see DM states can now be as light as ~ 200 GeV, whereas with standard freeze-out, the DM mass could be no lower than ~ 500 GeV, or at least across these slices in parameter space.

It is interesting to note the complementarity of DM and cosmic string bounds; in the FT scenario the DM bounds place stronger limits than the string bounds on q_0, but the opposite occurs in the CE scenario. The BBN bound in the latter case is particularly strong, but one can still reduce the DM mass by nearly 300 GeV and be consistent with all experimental constraints.

$(\lambda_L, \Delta m^2/\text{GeV}^2)$	m_{H^0}/GeV		q_0	
	FT	CE	FT	CE
$(0, 1000)$	$220 - 550$	$380 - 550$	$\lesssim 2 \times 10^{-9}$	$\lesssim 3 \times 10^{-11}$
$(0.1, 1000)$	$310 - 660$	$440 - 660$	$\lesssim 9 \times 10^{-10}$	$\lesssim 2 \times 10^{-11}$
$(0, 10000)$	$260 - 830$	$580 - 830$	$\lesssim 2 \times 10^{-9}$	$\lesssim 2 \times 10^{-11}$
$(0.1, 10000)$	$320 - 1040$	$690 - 1040$	$\lesssim 2 \times 10^{-9}$	$\lesssim 2 \times 10^{-11}$

Table 4.1: A table listing the possible mass ranges and maximum q_0 values allowed in an IDM in which cosmic strings arise. These are given for FT and CE scenarios for the four benchmark values of (Δm^2, λ_L). The second column lists the range of m_{H^0} values consistent with all experimental bounds, in which the observed relic density may be produced. The third column lists the maximum q_0 allowed in each of the cases, beyond this value q_0 is ruled out by either BBN or DGRB bounds, or requires $\langle \sigma v \rangle$ to be an unacceptably large value (*i.e.* conflicts with direct or indirection bounds) in order produce the observed relic density.

Table 4.1 summarises the valid mass ranges for each of the benchmark points considered, along with the maximum value of q_0 required in order to open up this whole range of mass values. The upper limits on the mass ranges correspond to the only valid values (of those considered) allowed when considering standard freeze-out. The limits on q_0 in the FT scenario arise from DM bounds, as if it were any higher, the annihilation cross-section would have to be an unacceptably large value in order for the correct relic abundance to be obtained. Whereas in the CE scenario the q_0 limits arise from cosmic string BBN bounds.

As was done in the previous chapter in Table 3.2, it is instructive to convert these limits on q_0 into limits on the string tension parameter $G\mu$. In the case of a single DM species, where the energy injection rate was parameterised by q_X, the relationships with $G\mu$ in the FT and CE scenarios were calculated in Appendix A to be (A.8) and (A.21) respectively. Now, the energy injection rate is parameterised by q_0 instead, however equivalent relationships with $G\mu$ can be derived by letting $q_X \to q_0 \equiv \sum_i \frac{\overline{E}_{H^0}}{\overline{E}_i} q_i$ in the same expressions. This results in slight redefinitions of P_{FT} and P_{CE}, which are now given by

$$P_{\text{FT}} \equiv \frac{\overline{E}_{H^0}}{\overline{E}_i} f_i \left(\frac{1 - 3\omega_{\text{d}}}{2} \right) \left(\frac{0.25}{\xi H} \right)^2 , \tag{4.43}$$

$(\lambda_L, \Delta m^2/\mathrm{GeV}^2)$	$G\mu$	
	FT	CE
$(0, 1000)$	$\lesssim 6 \times 10^{-12} P_{\mathrm{FT}}^{-1}$	$\lesssim 1 \times 10^{-15} P_{\mathrm{CE}}^{-1}$
$(0.1, 1000)$	$\lesssim 3 \times 10^{-12} P_{\mathrm{FT}}^{-1}$	$\lesssim 1 \times 10^{-15} P_{\mathrm{CE}}^{-1}$
$(0, 10000)$	$\lesssim 7 \times 10^{-12} P_{\mathrm{FT}}^{-1}$	$\lesssim 1 \times 10^{-15} P_{\mathrm{CE}}^{-1}$
$(0.1, 10000)$	$\lesssim 7 \times 10^{-12} P_{\mathrm{FT}}^{-1}$	$\lesssim 1 \times 10^{-15} P_{\mathrm{CE}}^{-1}$

Table 4.2: A table listing the maximum allowed values of $G\mu$ in the four benchmark (Δm^2, λ_L) points in the FT and CE scenarios. These were translated from the q_0 values seen in Table 4.1 using the same formulae for q_X in (A.8) and (A.21), although now P_{FT} and P_{CE} are defined differently, as shown in (4.43) and (4.44) respectively. Both parameters are still $\mathcal{O}(1)$.

and

$$P_{\mathrm{CE}} = \nu \beta_{\mathrm{CE}}^{2/3} \frac{\overline{E}_{H^0}}{\overline{E}_i} f_i \left(\frac{100}{g_*}\right)^{1/12} \left(\frac{m_X}{\mathrm{TeV}}\right)^{1/6} \left(\frac{500\ \mathrm{GeV}}{T_\chi}\right)^{1/3}. \tag{4.44}$$

Table 4.2 shows the limits on $G\mu$ calculated from the q_0 limits seen in Table 4.1, using the formulae described in the previous paragraph. These bounds on $G\mu$ mean the $\mathrm{U}(1)'$ symmetry breaking scale can be limited to $v' \lesssim 10^{13}$ GeV in the FT scenario, and $v' \lesssim 10^{12}$ GeV in the CE scenario.

While the (Δm^2, λ_L) benchmark approach has been convenient in highlighting the main consequences of an IDM with topological defects, a broader view of the phase space would inform further.

In Figure 4.4 are plots of (m_{H^0}, λ_L) space for $\Delta m^2 = 1000$ and $10000\ \mathrm{GeV}^2$ in the FT and CE scenarios. Shown in each plot are the regions ruled out by Fermi-LAT (shaded blue) and LUX (shaded green), where the limits of the latter disappear as $\lambda_L \to 0$, as expected. Also shown are contours of constant yield set to the observed DM abundance for different values of q_0, along with those in the case of standard freeze-out. The q_0 contours become dotted when the DGRB (in the FT scenario) or BBN (in the CE scenario) bound forbids it from holding that value. The contours of q_0 at which these bounds are met are shown by blue curves in these plots.

In the standard IDM one is forced to lie along the standard freeze-out contour seen in

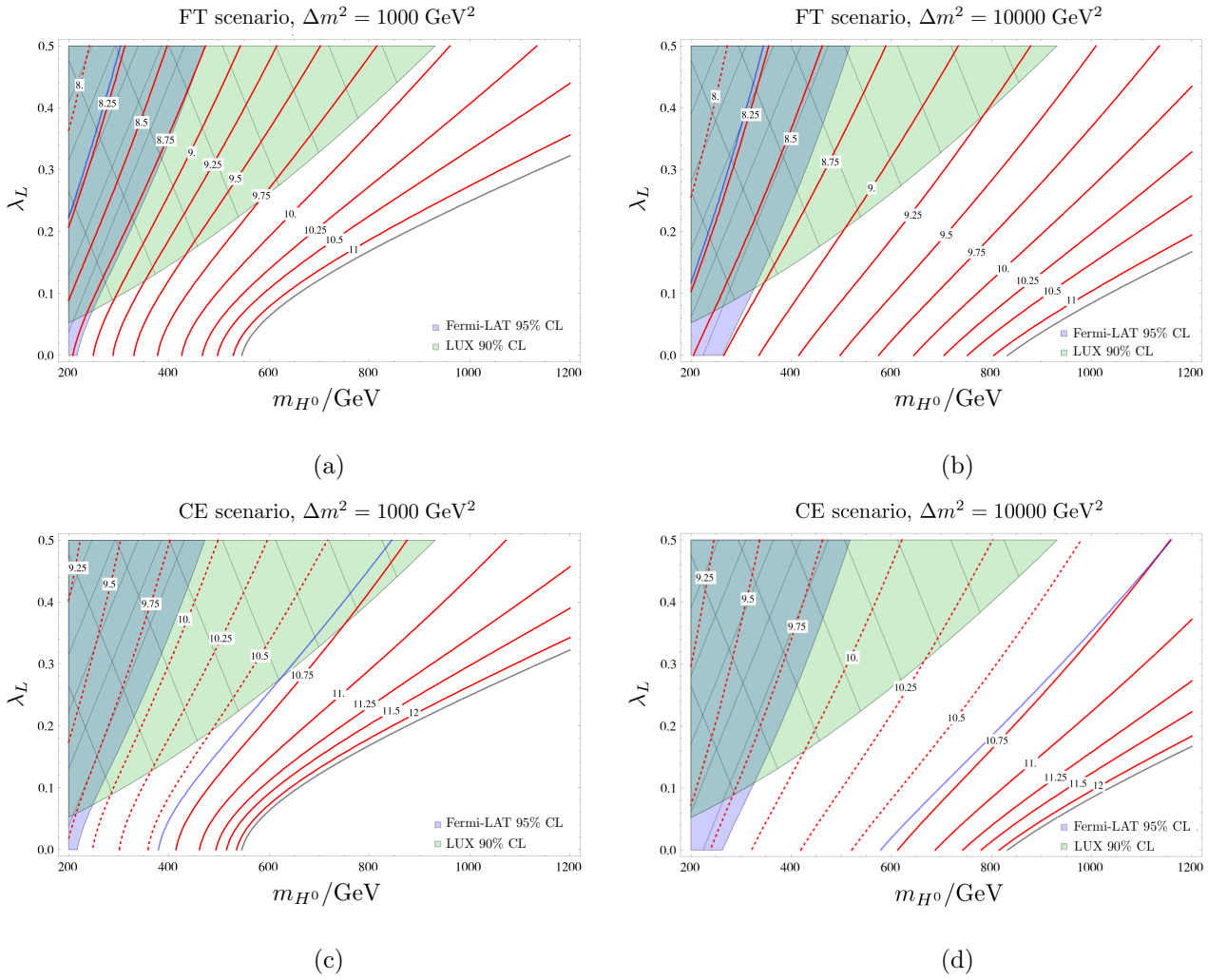

Figure 4.4: Plots in (m_{H^0}, λ_L) space for $\Delta m^2 = 1000$ GeV^2 (left) and $\Delta m^2 = 10000$ GeV^2 (right) in the FT (top) and CE (bottom) scenarios. The shaded regions show 90% CL limits from LUX (shaded green) and 95% CL limits from Fermi-LAT (shaded blue). Contours of constant yield set to the measured abundance for different values of $-\log_{10}[q_0]$ are shown in red, along with that in the case of standard freeze-out, seen in gray. When the contours become dotted, they are no longer consistent with DGRB and BBN bounds. The blue contour shows when the required q_0 value hits one of these cosmic string bounds, *i.e.* DGRB in the FT scenario and BBN in the CE scenario.

Figure 4.4, whereas in our model with topological defects added, the model may lie anywhere to the left of this up until the DM and cosmic string bounds come in. This has opened up a much larger region of phase space; the parameters have gone from being restricted to a 1-dimensional curve, to being allowed within a 2-dimensional area, *i.e.* the viable phase

space has had a "dimensional" boost. With standard freeze-out, only DM masses down to ~ 550 GeV are permitted, but now with the addition of topological defects these plots show this may go down to around 200 GeV, a significant reduction.

In the discussion of Figure 4.3 it was noted that the cosmic string limits were stronger than the DM bounds in the CE scenario for the benchmark cases considered. What is now seen here in Figure 4.4c, where $\Delta m^2 = 1000$ GeV^2 and we are in the CE scenario, is that at around $\lambda_L \sim 0.26$ LUX bounds surpass the BBN bounds to be become the leading constraint. This could also occur in the $\Delta m^2 = 10000$ GeV^2 case at a λ_L value beyond the boundaries of this plot, although perturbativity or unitarity bounds may come into play before this value is reached.

Figure 4.5 is the same as Figure 4.4, but now in $(m_{H^0}, \Delta m^2)$ space in the cases where $\lambda_L = 0$ and $\lambda_L = 0.1$. As one would expect the LUX limits disappear in as $\lambda_L \to 0$ and the direct detection signals vanish. These plots infer the same as Figure 4.4: that with the addition of topological defects to the IDM large regions of parameter space have been opened up, and we are no longer restricted to lie along the standard freeze-out contours.

4.5 Discussion

This chapter details [2], where the freeze-out with decaying topological defects mechanism discussed in Chapter 3 was implemented into the IDM. In order to generate cosmic strings, an additional local U(1)$'$ symmetry was added to the IDM. This supplementary symmetry was then broken by a scalar field, creating cosmic strings, and two massive particles: Z', the associated gauge boson, and X, the remnant scalar field.

Since the symmetry is thought to break at a scale far greater than the electroweak, these new degrees of freedom were far more massive than the others in the IDM. Given this, they could be integrated out to make an effective field theory, which was identical to the IDM. This required some fine-tuning, which was seen as part of the larger gauge hierarchy problem, and beyond the scope of this work. We saw how the addition of topological defects raised the relic abundance in the IDM, and discussed several experimental bounds on the IDM and cosmic strings. Of the former, LUX limits and Fermi-LAT bounds from an analysis of several dSphs were used to constrain the phase space. Direct limits on q_0 were also taken from [245], which considered BBN and DGRB bounds on cosmic strings. The main result was that large

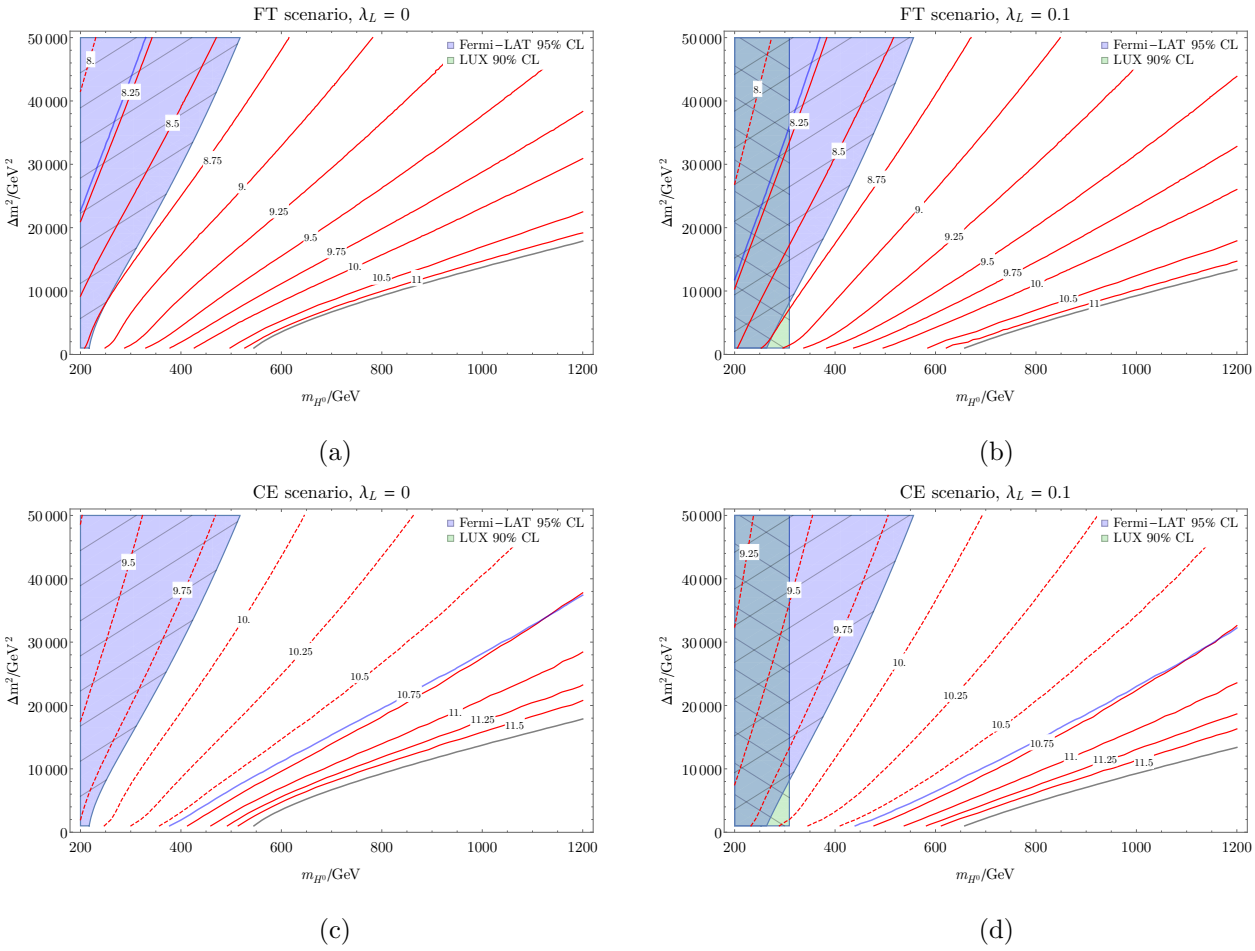

Figure 4.5: Plots in $(m_{H^0}, \Delta m^2)$ space for $\lambda_L = 0$ (left) and $\lambda_L = 0.1$ (right) in the FT (top) and CE (bottom) scenarios. The shaded regions show 90% CL limits from LUX (shaded green) and 95% CL limits from Fermi-LAT (shaded blue). Contours of constant yield set to the measured abundance for different values of $-\log_{10}[q_0]$ are shown in red, along with that in the case of standard freeze-out, seen in gray. When the contours become dotted, they are no longer consistent with DGRB and BBN bounds. The blue contour shows when the required q_0 value hits one of these cosmic string bounds, *i.e.* DGRB in the FT scenario and BBN in the CE scenario.

swathes of the IDM's parameter space was now opened up, *i.e.* they could produce the correct relic abundance and be consistent with all experimental bounds. This allowed the CP-even Higgs H^0 to be as light as ~ 200 GeV, whereas in the standard freeze-out scenario it could only go down to ~ 550 GeV.

Chapter 5

The Galactic Centre Excess with Topological Defects

> Reality is frequently inaccurate.
>
> — Douglas Adams

A high density of DM is thought to lie within the Galactic Center (GC) of the Milky Way, and as such is a logical target for indirect detection searches. Fermi-LAT, as discussed in Section 1.4.2, has been detecting the 20 MeV to 300 GeV γ-ray sky. Using Fermi-LAT data an excess was found in the region of the GC after known sources were removed [127], which was shown to be consistent with DM annihilations into b-quarks. Furthermore, the cross-section required to produce the excess came close to the value needed to generate the correct DM abundance according to standard freeze-out. Since then further analyses on the GC excess (GCE) have been carried out, studying the morphology, background systematics, possible annihilation modes, and other interpretations of the signal [129, 232, 265–269]. Millisecond pulsars have gained the most attention as an alternative source of the GCE; an explanation which has been studied and scrutinized by various groups [270–274].

Aside from the GC, dSphs also provide good targets for DM indirect detection as they have high mass-to-light ratios, and Fermi-LAT limits on these are in tension with DM interpretations of the GCE [275]. In order to circumvent this contradiction, one can assume the DM annihilations are dominantly p-wave, as was shown recently in [276]. Since DM annihi-

lates at lower mean relative velocities within dSphs than the GC, limits from the former are more suppressed and the tension is avoided.

However in order to compensate for the velocity-suppression in the GC, the annihilation cross-section (σ_0, as defined in (1.20)) needs to be large, which means the relic abundance is predicted to be orders of magnitude below the observed value. In [276], as a solution to this problem, there is a second heavier state which undergoes freeze-out with dominant s-wave annihilations, which later decays into the p-wave annihilating DM state responsible for the GCE.

Here, we will show how instead the deficit can be accounted for by allowing topological defect decays to be a source of DM in early Universe, via the mechanism proposed in [1], which was discussed in Chapter 3. In the previous chapter, this mechanism was implemented into an example DM model (the IDM), which subsequently meant large regions of its parameter space opened up and lighter DM states were permitted (under all phenomenological bounds). We implement it again here, in order to resolve an issue with a signal of DM, rather than a model. In both cases however, the core problem was the same: the relic abundance needed to be increased to the correct value. Considering the effects of decaying defects solves such issues, which could arise in other models and signals, and more. In the case of the IDM, it did so while keeping the effective particle theory unchanged at the electroweak scale.

As σ_0 has to be large to generate the GCE when the annihilations are dominantly p-wave, one needs to be wary of conflicts with direct detection and collider bounds. These can be avoided in cascade annihilation models, where the final states are on-shell mediators, which can then decay into SM fermions. Alternatively, there could be several mediator states, which decay into one another in a long chain (or cascade), before the SM fermions are finally emitted. This means the annihilation rate is set just by the DM-(heaviest) mediator coupling, while the scattering and production rates are dependent on the mediator-SM fermion couplings as well. Subsequently, we can fix the former coupling such that the GCE is generated, while the latter couplings can be suppressed to avoid direct detection and collider bounds. While this means the mediators' lifetimes can be large, this will not be nearly enough to effect of the morphology of the GCE.

Cascade annihilations have been used before to generate the GCE [276–281], however this has mostly been in the case of dominant s-wave annihilations. In such scenarios, DM

is a fermion with either vector, axial-vector, or pseudoscalar interactions. Annihilation into two pseudoscalars is actually p-wave dominated, however the three pseudoscalar final state channel is s-wave and is the leading contribution. Here we shall consider a model with DM annihilating into scalars, whose leading contribution is p-wave dominant. A benefit of such a theory is that mixing with the SM Higgs boson can arise, and given the SM Yukawa couplings follow a mass hierarchy, naturally allows annihilations into b-quarks to dominate (a preferred channel for the GCE).

This chapter is laid out as follows: in Section 5.1 we look at the GCE, showing how it can arise from DM annihilations and providing details of the fitting analysis. Limits from dSphs are then considered and the tension with DM as the source of the GCE is shown. This is subsequently demonstrated to be avoided when DM annihilations are dominantly p-wave. In Section 5.2 we detail our cascade annihilation model, and the mixing between the mediator and the SM Higgs. Following this, we examine how cosmic strings can be introduced into this model, and allow for sufficient DM production. In Section 5.4, we fit our model to the GCE and find the values of the string tension parameter, $G\mu$, required for the correct relic abundance to be produced. Cosmic string bounds on this parameter are then examined, before we conclude in Section 5.5.

5.1 The Galactic Centre Excess and dSph Limits

The DM models here will be fitted to the GCE using the analysis of Fermi-LAT data presented in [265], where spectral data with statistical and systematic errors is provided in the appendix. This analysis considered γ-rays in the range 200 MeV to 100 GeV observed during the period August 4th 2008 - June 6th 2012. The region of interest (ROI) is a 7°$\times$ 7° box centred on Sagittarius A*, the supermassive black hole at the centre of the galaxy, which itself is modelled as a point source of γ-rays. To illustrate the tension with dSph limits, a model of dominantly s-wave annihilating DM is fitted to the data.

The differential γ-ray flux from an astronomical source was given in Section 4.4.1, but repeated here for convenience with a change of variables more appropriate for this study, it is expressed as a function of the photon energy (E_γ), longitude (l), and latitude (b)

$$\Phi(E_\gamma, b, l) = \frac{\langle \sigma v \rangle}{8\pi m_\chi^2} \frac{dN}{dE_\gamma} J(b, l), \tag{5.1}$$

where m_χ is the DM mass, $\langle\sigma v\rangle$ is the velocity-averaged[1] annihilation cross-section times relative velocity, and $\frac{dN}{dE_\gamma}$ is the photon spectrum per annihilation. The term $J(b,l)$ is an astrophysical factor, given by

$$J(b,l) = \int_{\text{l.o.s.}} \rho(r)^2 ds, \tag{5.2}$$

where $\rho(r)$ is the DM density as a function of the radial distance to the GC. The integral is performed along the line of sight, *i.e.* $r^2 = s^2 + r_\odot^2 - 2sr_\odot\cos(b)\cos(l)$, where $r_\odot = 8.5$ kpc is the distance between the Earth and the GC.

For the DM density, we will use the generalised Navarro-Frenk-White (NFW) profile [282, 283]

$$\rho(r) = \frac{\rho_0}{\left(\frac{r}{r_s}\right)^\gamma \left(1+\frac{r}{r_s}\right)^{3-\gamma}}, \tag{5.3}$$

where the scale radius $r_s = 20$ kpc, the slope factor $\gamma = 1.2$, and ρ_0 is set such that $\rho(r_\odot) = \rho_\odot = 0.4$ GeV cm^{-3}, the density of DM in the vicinity of the Earth. These astrophysical factor values were chosen as to be in line with previous studies of the GCE and analyses of the DM halo [266, 267, 284, 285].

The annihilation spectra are generated using PPPC 4 DM ID [286, 287], a *Mathematica* package which has a database of photon spectra. These are generated by considering the possible products of DM annihilations/decays and the particles produced via the decays or hadronizations of said products. PPPC calculates the predicted fluxes of electrons/positrons, antiprotons, antideuterium, γ-rays, and neutrinos, after these latter processes have ceased. It then takes into account changes to these prompt spectra as they propagate through the Milky Way on their way to us, into order to give their observed spectra. For the charged cosmic ray fluxes, this takes into account energy loss due to processes such as synchrotron radiation from the galactic magnetic fields, and the inverse Compton scattering of the CMB, dust-rescattered light and starlight. These processes not only alter the charged cosmic ray fluxes, but also contribute to the photon spectra, which is accounted for in PPPC. It also computes the contribution of extragalactic photons.

A χ^2 analysis across a range of $\langle\sigma v\rangle$ and m_χ values is presented in Figure 5.1, which assumes dominant annihilations into $\bar{b}b$ final states. Also shown are the limits from a combined analysis of 15 dSphs using Fermi-LAT data [131], and the relic density curve, along which the

[1] Not to be confused with the thermally-averaged quantity used in the freeze-out calculation (1.20).

observed abundance of DM is produced in standard freeze-out.

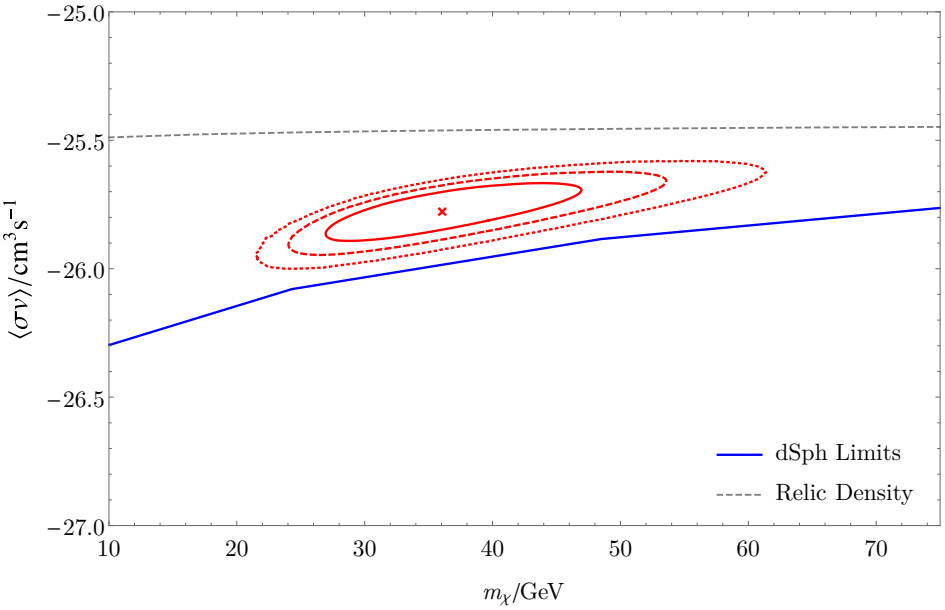

Figure 5.1: A fit of $(m_\chi, \langle\sigma v\rangle)$ space via a χ^2 analysis of GCE data [265] to a model of DM with dominant s-wave annihilations, assuming $\bar{b}b$ final states only. The cross shows the point of best fit, while the red bold, dashed, and dotted lines are contours highlighting $1\,\sigma$, $2\,\sigma$, and $3\,\sigma$ significance. Also shown are the thermal values of $\langle\sigma v\rangle$ required to produce the observed relic abundance according to standard freeze-out [17] (dashed gray), and the Fermi-LAT 95% limits from dSphs [131] (blue).

The best fit parameter values from the χ^2 analysis are

$$\langle\sigma v\rangle = (1.71 \pm 0.29) \times 10^{-26}\ \text{cm}^3\ \text{s}^{-1} \qquad m_\chi = 36.1^{+7.4}_{-5.8}\ \text{GeV}, \tag{5.4}$$

which is in approximate agreement with other analyses, and close to the value required to produce the observed relic abundance. However the limit from dSphs is below the fit, outside the $3\,\sigma$ CL contour, which puts pressure on the DM interpretation of the GCE (when assuming the annihilations are dominantly s-wave). This tension is explored further in [275], which finds it may be avoided by using a highly concentrated DM halo. Such a profile could arise due to the adiabatic contractions instigated by baryonic infall, but this situation is ruled out in [288].

5.1.1 P-wave Annihilating Dark Matter

One way to resolve the disagreement discussed in the previous section is by considering velocity-dependent annihilation cross-sections, as the velocity distributions vary between the

astronomical bodies. As discussed in Section 1.2.1, the annihilation cross-section may be expanded in relative velocity, v, as $\sigma v = a + bv^2 + \mathcal{O}(v^4)$. This expansion may be approximated by its lowest order non-zero term, which may be a or bv^2 corresponding to dominant s- or p-wave annihilations respectively.

The velocity-averaged cross-section is defined as

$$\langle \sigma v \rangle = \int f(\vec{v}_1) f(\vec{v}_2) (\sigma v_{rel}) d^3\vec{v}_1 d^3\vec{v}_2. \tag{5.5}$$

Following the work in [289], the velocity distribution in a given celestial object is taken to be a Maxwell-Boltzmann distribution with a cutoff at the escape velocity, *i.e.*

$$f(v) = N \begin{cases} v^2 \exp\left(-\frac{v^2}{2v_d^2}\right) & v < v_{\rm esc} \\ 0 & v > v_{\rm esc} \end{cases}, \tag{5.6}$$

where v_d is the velocity dispersion and N is a normalisation factor given by

$$N^{-1} = 2^{5/2} \pi v_d^3 \left(\frac{\sqrt{\pi}}{2} \mathrm{erf}\left(\frac{v_{\rm esc}}{\sqrt{2} v_d}\right) - \frac{v_{\rm esc}}{\sqrt{2} v_d} e^{-\frac{v_{\rm esc}^2}{2v_d^2}} \right). \tag{5.7}$$

In the limit that $v_d \ll v_{\rm esc}$, we can approximate $\langle \sigma v \rangle = \sigma_0 \left(\frac{v_d}{c}\right)^2$, where σ_0 is the same as in (1.20).

The velocity dispersion is dependent of the distance to the body's centre, and as such, the differential γ-ray flux for dominant p-wave annihilations will now be

$$\Phi(E_\gamma, b, l) = \frac{\sigma_0}{8\pi m_\chi^2} \frac{dN}{dE_\gamma} J_{\rm p}(b, l), \tag{5.8}$$

where

$$J_{\rm p} = \int_{\rm l.o.s.} \rho(r)^2 \left(\frac{v_d(r)}{c}\right)^2 ds. \tag{5.9}$$

Following [276, 289], the velocity dispersion of the Milky Way is taken to be

$$v_d(r)^3 = v_0^3 \left(\frac{r}{r_\odot}\right)^\chi \left(\frac{\rho(r)}{\rho_\odot}\right), \tag{5.10}$$

where $v_0 = 260$ km s^{-1}, in accordance with simulations of the DM halo [290] and $\chi = 1.64$ from [291], which takes baryonic effects into account.

Comparing (5.1) and (5.8), the best fit σ_0 value in the case of dominant p-wave annihilation (assuming no other changes) may be found by scaling the s-wave cross-section fit by the ratio of

J factors (integrated over the ROI). Doing so, one finds we would need $\sigma_0 \approx 9 \times 10^{-20}$ cm^3 s^{-1} in order to explain the GCE.

The velocity dispersion of a dSph is approximately constant, which means its limit on p-wave annihilating DM can be found by scaling the s-wave limit by a factor of $\left(\frac{v_d}{c}\right)^2$, but the situation is more complex as we are using a combined analysis of several dSphs. However by scaling by the largest velocity dispersion we produce a limit which is stronger than the true value, which is fine for our purposes (as was done in [276]). In the case of the 15 dSphs considered in [131], Fornax has the highest velocity dispersion at a value of $v_d = 11.7 \pm 0.9$ km s^{-1} [230]. This means in the p-wave dominated case $\sigma_0 \lesssim 8 \times 10^{-18}$ cm^3 s^{-1}, which is far above the value required to produce the GCE, and so the tension is avoided.

However the cross-section from the GCE fit is many orders of magnitude over the value required to produce the correct relic abundance when assuming the DM was generated via standard freeze-out, which is $\sigma_0 \sim 10^{-24}$ cm^3 s^{-1} for a p-wave dominated theory. As with the IDM, by letting decaying defects be a source of DM, this disagreement may be corrected.

5.2 A Toy Model

We now present an example model which can explain the GCE, and produce the correct relic abundance. The theory needs to satisfy two requirements: the DM's dominant annihilation channel is p-wave, and the model permits the formation of cosmic strings which can decay producing DM. First we shall consider how the former may realised, before the implementation of the latter in discussion in Section 5.3.

As discussed in the introduction, we shall consider a model with cascade annihilations where the mediators are light enough to be produced on-shell in DM annihilations. The mediators are unstable and will decay into SM particles, or into other unstable mediators which do, extending the chain (or cascade). Here, the simplest cascade will be considered, where there is only one new mediator.

One of the simplest ways in which such a scenario could arise with p-wave annihilations is if DM is a Dirac fermion χ, which couples to a scalar ϕ, *i.e.*

$$\begin{aligned}\mathcal{L} = \mathcal{L}_{\rm SM} + i\bar{\chi}\partial\!\!\!/\chi + m_\chi\bar{\chi}\chi + \frac{1}{2}(\partial_\mu\phi)^2 \\ - \frac{1}{2}m_\phi^2\phi^2 - \frac{\mu_\phi}{2\sqrt{2}}\phi^3 - \frac{\lambda_\phi}{4}\phi^4 - \lambda_\chi\phi\bar{\chi}\chi - \lambda_f\phi\bar{f}f,\end{aligned} \tag{5.11}$$

where f represents the SM fermion fields. In this case DM annihilations proceed via the chain $\bar{\chi}\chi \to \phi\phi \to \bar{f}f\bar{f}f$.

The photon spectrum in the case of cascade annihilations is given in [280, 292], where it is calculated by boosting the mediator's (at rest) decay spectrum dN_ϕ/dE_γ, *i.e.*

$$\frac{dN}{dE_\gamma} = \frac{2}{x_+ - x_-}\int_{E_\gamma x_-}^{E_\gamma x_+} \frac{dE'_\gamma}{E'_\gamma}\frac{dN_\phi}{dE'_\gamma}, \tag{5.12}$$

where $x_\pm = \frac{m_\chi}{m_\phi} \pm \sqrt{\left(\frac{m_\chi}{m_\phi}\right)^2 - 1}$.

5.2.1 Higgs Portal Couplings

The GCE is best fit by models predicting dominant annihilations into b-quarks, which for our toy model means ϕ decays should be likewise. This can occur naturally if the mediator mixes with the SM Higgs, which is indeed possible in our model as the following portal couplings are also permitted

$$\mathcal{L} \supset -\frac{\mu_H}{\sqrt{2}}\phi|H|^2 - \frac{\lambda_H}{2}\phi^2|H|^2, \tag{5.13}$$

where H is the SM Higgs doublet. Post-electroweak symmetry breaking a mixing emerges between the mediator and the SM Higgs boson h, and so diagonalizing, one finds

$$\begin{aligned} \phi &= \tilde{\phi}\cos\theta + \tilde{h}\sin\theta, \\ h &= \tilde{h}\cos\theta - \tilde{\phi}\sin\theta, \end{aligned} \tag{5.14}$$

where θ is the mixing angle, and $\tilde{\phi}$ and $\tilde{h}$ are the physical mass states. The ϕ field itself does not gain a non-zero VEV.

This mixing allows the mediator to couple to fermions via the SM Higgs boson's hierarchical (in mass) Yukawa terms, with a strength $y_f \sin\theta$. Subsequently $\phi \to \bar{b}b$ decays can dominate, provided the mediator's original Yukawa couplings, λ_f, are small enough. Such a scenario is always possible since λ_f can be decreased almost indefinitely without affecting the GCE signal, which is a defining concept of cascade annihilation models. We shall assume λ_f can be ignored and so the hierarchical coupling, $y_f \sin\theta$, controls the mediator's interactions with SM fermions. In an extension to this model, the original λ_f couplings to the SM fermions could be forbidden under some symmetry, whereby leaving them to be generated via mixing with the SM Higgs.

The mixing also generates a direct coupling between DM and the SM Higgs, which opens up new channels for direct detection and collider searches. Furthermore, there will also be lower limits on the decay rate of the mediator (and thus $\sin\theta$) coming from BBN; a long-lived particle decaying during this period will disrupt the process which is in the most part already well described by SM physics. In Appendix C we derive these bounds on $\sin\theta$, finding they are not strong enough to forbid the mixing, and so hierarchical couplings can arise through this channel.

5.3 Generating Cosmic Strings

DM production from decaying topological defects proceeds here as it did in Section 3.1, *i.e.* cosmic strings decay emitting X states with average energy $\overline{E}_X$, which in turn decay into N_χ DM states of mass m_χ. The Boltzmann equation is once again

$$\frac{dY_\chi}{dx} = -\frac{A}{x^n}\left(Y_\chi^2 - Y_{\chi,\mathrm{eq}}^2\right) + \frac{B}{x^{4-2p}}, \tag{5.15}$$

where

$$A = \sqrt{\frac{\pi g_*}{45}} M_{\mathrm{Pl}} m_\chi \sigma_0, \qquad \text{and} \qquad B = \frac{3}{4}\left(\frac{N_\chi m_\chi}{\overline{E}_X}\right)\left(\frac{Q_\chi f_X}{\rho_\chi H_\chi}\right), \tag{5.16}$$

whose parameters are defined as they were in Section 3.1. We again use the cosmic string variables

$$q_X \equiv \frac{Q_\chi f_X}{\rho_\chi H_\chi}, \qquad \text{and} \qquad r_\chi \equiv \frac{N_\chi m_\chi}{\overline{E}_X}. \tag{5.17}$$

As discussed in Section 2.3 and utilised in Chapter 4, one of the simplest ways in which cosmic strings may be generated is via the spontaneous breaking of a $\mathrm{U}(1)'$ symmetry by a scalar gaining a VEV. We will call this scalar the string field and label it Y. DM can then be produced from the decays of the string itself, or from the decays of condensates which form upon the string.

Considering the former case, the emitted particle, X, could be the remnant scalar of the string field Y, whose mass is expected to be of the order of the VEV, v'. For sufficient particle production, a large (much greater than the electroweak scale) VEV is required, therefore in this case $\overline{E}_X \sim v' \sim \mathcal{O}(10^{10}\text{-}10^{15})$ GeV. Given this, one would expect r_χ to be very small, as $m_\chi \sim \mathcal{O}(10)$ GeV and typically $N_\chi \sim \mathcal{O}(1)$. Although N_χ is model-dependent, it will not be close to the value required for $r_\chi \sim \mathcal{O}(1)$. Having an r_χ value of this size is problematic, as

q_X would need to be very large to generate the correct relic abundance, and such values will be in conflict with CMB string constraints [195].

This issue is remedied by assuming X is a different state with a mass around the electroweak scale, which couples to Y in such a way as to be produced from the string decays. For example, if X is a scalar field, it will have a portal coupling with the string field, $|Y|^2|X|^2$, which would allow X to form a condensate upon the string field. In this scheme, $\overline{E}_X$ will be around the electroweak scale.

In order for r_χ to be large enough, we need a significant branching fraction of X decays into DM, which means a coupling to DM must be introduced. One way in which this could be realised is if X is also charged under the U(1)$'$ symmetry, but with opposite charge to Y. One could then consider the effective operator, $\frac{1}{\Lambda}|Y^\dagger X|\bar{\chi}\chi$, which upon the symmetry breaking phase transition would generate the Yukawa term $\frac{v'}{\sqrt{2}\Lambda}X\bar{\chi}\chi$.

Alternatively the coupling to DM could arise through mixing with the mediator, ϕ, which is expected to have a large coupling to DM, such that the GCE can be produced. If X gains a VEV, a mixing may be generated via a term like $\phi|X|^2$. In this case, the remnant scalar of X, would mix with ϕ and be the field which decays producing DM. For the rest of this study, we presume DM production via decaying defects proceeds in ways such as those explored above, and subsequently take $r_\chi \approx 1$.

In Chapter 4 a field such as Y, which breaks the U(1)$'$ symmetry, was added to the IDM. As it broke the symmetry close to the GUT scale, it did not change the effective particle model at the electroweak scale. This was because it introduced particles which were massive enough to be integrated out. One can see that the situation will be the same here in our toy model, and like before, we expect fine-tuning will be needed to deal with large mass corrections generated from terms such as $\phi^2|X|^2$. This is recognised as part of the larger gauge hierarchy problem, which could be solved by supersymmetrising the model, however this is beyond the scope of this work.

5.4 Fitting and Constraining

With a working toy model established, we are now in a position to fit to the GCE, and consider further constraints. Thus far we have discussed how Fermi-LAT dSph limits are avoided with dominantly p-wave annihilating DM, but have not considered other indirect

detection limits, which cannot be suppressed in the same way as direct detection and collider bounds can be. When assuming dominantly s-wave annihilating DM, limits from clusters are weaker than those from dSphs, however with p-wave annihilations they can be stronger since the average DM velocity is higher. Out of the clusters, Virgo with an approximately flat velocity dispersion of 643^{+41}_{-30} km s^{-1} [293], provides the strongest limits on the p-wave annihilation cross-section [294]. Fitting our toy model to the GCE cannot simply be done

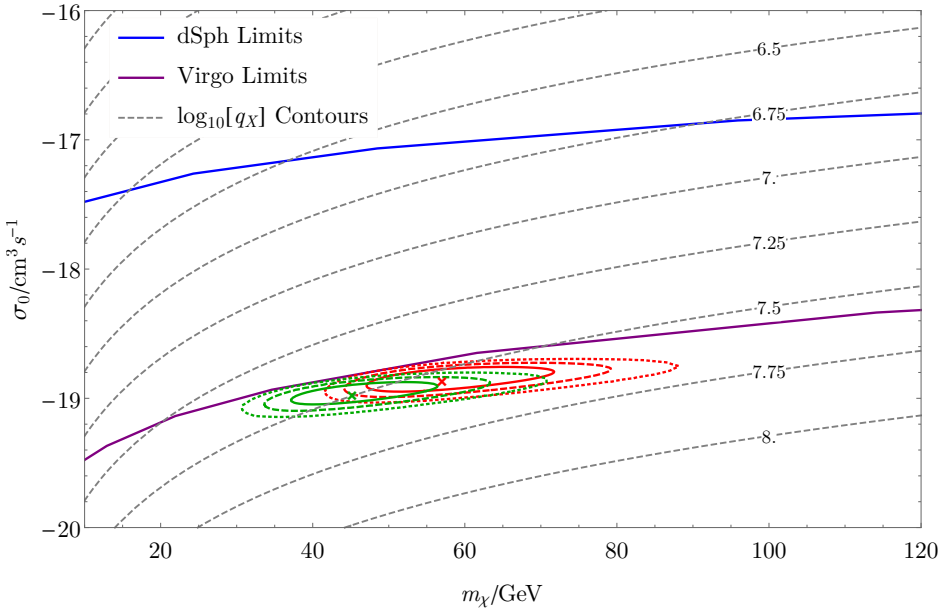

Figure 5.2: A fit of (m_χ, σ_0) space via a χ^2 analysis of GCE data [265] to a cascade annihilation model of DM where $\bar{\chi}\chi \to \phi\phi \to \bar{b}\bar{b}b\bar{b}$ for $m_\phi = 15$ GeV (green) and 40 GeV (red). The crosses show the points of best fit, while the bold, dashed, and dotted lines represent the $1\,\sigma$, $2\,\sigma$, and $3\,\sigma$ CL contours respectively. Also shown are the Fermi-LAT 95% CL limits from dSphs [131] (blue) and the Virgo Cluster [294] (purple). Contours along which the correct relic abundance is generated are plotted for various values of $-\log_{10}[q_X]$ (gray dashed lines) in the FT scenario.

by scaling the fit of the s-wave annihilation model, as was done at the end of Section 5.1.1. Since we are using a cascade annihilation model, the situation is more complex, as the photon spectrum is now found using (5.12). Figure 5.2 shows two fits in (m_χ, σ_0) space for our toy model with $m_\phi = 15$ and 40 GeV, along with Fermi-LAT limits from dSphs and Virgo. The point of best fit for $m_\phi = 15$ GeV is

$$\sigma_0 = (1.10 \pm 0.17) \times 10^{-19}\ \text{cm}^3\ \text{s}^{-1} \qquad m_\chi = 45.2 \pm 8.7\ \text{GeV}. \tag{5.18}$$

and for $m_\phi = 40$ GeV is

$$\sigma_0 = (1.42 \pm 0.26) \times 10^{-19} \text{ cm}^3 \text{ s}^{-1} \qquad m_\chi = 57.0^{+12.1}_{-8.3} \text{ GeV}. \tag{5.19}$$

These cross-sections are approximately a factor of 10^7 greater than the s-wave fit (5.4). As a check, we can crudely approximate the expected cross-section by scaling the s-wave fit by $\left(\frac{\overline{v_d}}{c}\right)^2$, where $\overline{v_d}$ is the average velocity dispersion. The velocity dispersion according to our model (5.10) peaks and plateaus around 185 km s^{-1}, however given the form of the γ-ray flux (5.8), we can see we'll get the largest contributions from the more central region where the density is highest and the velocity dispersion is lower. Given this, we can take $\overline{v_d} \sim 100$ km s^{-1} and doing so we would expect the p-wave cross-section fit to be $\sim 10^7$ times larger than the s-wave, in agreement with the results above. One could also take into account the increase in multiplicity given there are now cascade annihilations, and the increase in DM mass, however the resultant change would be negligible (less than a factor of 2).

As expected, dSph limits are no longer conflicting with the GCE fits. Limits from the Virgo cluster are now far stronger than those from dSphs, although not enough to create a new tension with the GCE fit. The gray dashed lines seen are contours along which the correct relic abundance is generated when assuming DM production from decaying topological defects; this is plotted for various values of $-\log_{10}[q_X]$ and assumes we are in the FT scenario.

With a smaller mediator mass, the best fit values for m_χ and σ_0 decrease. By inspection of (5.8) we can see that the decrease in σ_0 (which is an overall scaling factor) can be considered as compensating for the decrease in m_χ, in such a way as to keep the coefficient $\frac{\sigma_0}{m_\chi^2}$ constant. Physically this decrease in m_χ is causing the number density to rise, which would boost the signal unless σ_0 is scaled down appropriately.

However while σ_0 is overall at a lower value when m_χ is smaller, it is larger than what would be expected if the system was purely governed by this effect on the number density. Therefore a second effect is in play, which drives σ_0 up. The only other dependence on m_χ and m_ϕ is in the photon spectrum, thus σ_0 increases because the amplitude of the photon spectrum is lower when m_ϕ and m_χ are also. The photon spectrum for a one step cascade (5.12) is derived through the boosting of ϕ's decay spectra. By lowering the mediator's mass, the total number photons emitted on average is smaller as the b-quarks are emitted with less energy. This decreases the amplitude of the mediators decay spectra, and therefore the convolved DM annihilation spectrum. Subsequently the cross-section must be increased to

counter this secondary effect.

While the origin of the changes to σ_0 can be put down to the changes in m_ϕ and m_χ, we have yet to examine why m_χ decreases. This may be understood by considering two effects lowering m_ϕ has on the spectrum. Firstly, as the b-quarks are produced with less energy, the decay spectrum is more sharply peaked, and secondly, the mass splitting between m_χ and m_ϕ is larger. The latter means the ϕ's have higher momentum and so the decay spectra are boosted across a larger range of energy values, which increases the integration window in (5.12). This second effect dominates over the first, and smears the annihilation spectrum out. Therefore to regain approximately the same shape as before, which fitted the GCE, the mass splitting must be decreased by lowering m_χ.

5.4.1 Implications for Cosmic Strings

With the fits to the GCE seen in Figure 5.2, it is instructive to know how the large DM production from cosmic strings (reflected in the value of q_X) needs to be in order for the observed relic abundance to be produced. This can be found using the expression in (3.12), which tells us the required value of q_X for a given value of σ_0. These values are presented in Table 5.1 for both mediator masses in the FT and CE scenarios. In the case where the mediator is lighter, q_X is slightly greater, to counter the increase in the annihilation cross-section. In the FT scenario q_X is larger as the production rate drops more quickly, thus a greater value is required.

	q_X	
m_χ/GeV	FT Scenario	CE Scenario
15	$q_X = 3.25^{+0.24}_{-0.26} \times 10^{-8}$	$q_X = 1.17^{0.06}_{0.06} \times 10^{-9}$
40	$q_X = 2.92^{+0.25}_{-0.28} \times 10^{-8}$	$q_X = 1.01^{+0.06}_{-0.07} \times 10^{-9}$

Table 5.1: Values of q_X required to produce the observed relic abundance of DM [17] when the annihilation cross-section is fitted to the GCE signal, as seen in Figure 5.2. This is for $m_\chi = 15$ and 40 GeV, and is found for both the FT and CE scenarios.

As was done in the previous two chapters, the q_X values are converted into those of the more commonly used string tension parameter $G\mu$. This can be done by using the expressions (A.8) and (A.21) for the FT and CE scenarios respectively. These can be rescaled by $\frac{1}{r_\chi}$ to

find the value of $G\mu$ for any r_χ. In the FT scenario, $G\mu \gtrsim 1 \times 10^{-10} \left(\frac{1}{r_\chi}\right)$, and in the CE scenario, $G\mu \gtrsim 5 \times 10^{-14} \left(\frac{1}{r_\chi}\right)$, in order for the correct relic abundance to be produced, which correspond to VEV values for the string field of $v' \sim 10^{14} \left(\frac{1}{r_\chi}\right)^{1/2}$ and $v' \sim 10^{12} \left(\frac{1}{r_\chi}\right)^{1/2}$ GeV respectively. CMB string searches limit $G\mu \lesssim 10^{-7}$ [195], which our values easily avoid, since we are assuming $r_\chi = 1$. However taking r_χ as a free variable, this limit will still be avoided if $r_\chi \gtrsim 10^{-3}$ in the FT scenario and $r_\chi \gtrsim 5 \times 10^{-7}$ in the CE scenario.

There are further limits on $G\mu$, which could be strong enough to conflict with the required values, however these are model-dependent. For example, in the FT scenario, limits from the DGRB using EGRET data [225, 295] require $G\mu \lesssim 10^{-10} f^{-1}$, where f is the fraction of the energy going into γ-rays. Unless strings are dominantly decaying into photons, this bound will be avoided. In the CE scenario, the gravitational radiation may be searched for using pulsar timing arrays, and one such analysis requires $G\mu \lesssim 2.8 \times 10^{-9}$ [296]. This bound does not significantly constrain our model, and r_χ can still be as low as $\sim 2 \times 10^{-5}$.

Other limits also arise when large SM Higgs condensates form [245] upon the string, coming from BBN and DGRB bounds (discussed in Section 4.4.2). These will limit $q_{\rm vis}$, a parameter defined in the same way as q_X, but for "visible" SM particles. Following the discussion in Section 4.4.2, the DGRB bound in the FT scenario is found to be

$$q_{\rm vis} \lesssim 6 \times 10^{-9}. \tag{5.20}$$

The BBN limit in the FT scenario is comparable to this, while in the CE scenario it provides the strongest limit, given by

$$q_{\rm vis} \lesssim 5 \times 10^{-11}. \tag{5.21}$$

Comparing these limits to the required values in (5.1) one can see a strong tension. However this presumes $q_{\rm vis} \sim q_X$, *i.e.* the fraction of energy going into DM and SM particles (via Higgs radiation) is comparable. Furthermore this requires the formation of "large" Higgs condensates, and one can easily consider a region of parameter space where the condensates are not "large", as discussed in [297].

5.5 Discussions

In this chapter we examined the unexplained γ-ray GeV excess coming from the GC of the Milky Way, which has been shown to be consistent with annihilating DM [127]. The cross-

section required to produce the signal is close to that of a thermal relic (assuming standard freeze-out), however limits from dSphs are in tension with it [275]. By considering dominant p-wave annihilations, this tension may be resolved [276] (as established in Section 5.1), but at the cost of spoiling the agreement with the thermal value.

Here, we have shown that by considering the effects of defect decays in the early Universe, the correct relic density may be obtained for a model generating the GCE with dominant p-wave annihilations. As explained in Chapter 3, the decaying defects can be a source of DM, and so allows the annihilation cross-section to be far greater than standard freeze-out permits.

To illustrate how such a scenario could relieve tensions with dSphs and the relic density, a toy model was considered in Section 5.2. This was based on cascade annihilation theories [277–280], where DM annihilates dominantly into on-shell mediators, and allowed for experimental bounds to be avoided. Taking the mediator to be a scalar meant the DM annihilations were dominantly p-wave. Furthermore it meant portal couplings to the SM Higgs doublet were permitted, which allowed the mediator to mix with the Higgs boson. This subsequently gave the mediator hierarchical couplings to SM fermions determined by their masses, and therefore provided a natural explanation for dominant $\bar{b}b$ final states in mediator decays.

Cosmic strings were then introduced into this model in Section 5.3 by adding a new scalar Y which gained a VEV breaking an additional local $\mathrm{U}(1)'$ symmetry. To avoid cosmic string bounds we required r_χ to be sufficiently large, which was an unrealistic assumption if the DM was being produced directly from the decays of Y's remnant scalar field. Therefore we considered a second field, X, with an electroweak scale mass, which could decay dominantly into DM.

Fitting our model to the GCE in Section 5.4, we found the annihilation cross-section was required to be $\sigma_0 \sim 10^{-19}$ cm^3 s^{-1} with a larger DM mass than in the s-wave case. Furthermore these fits were shown to be consistent with dSph limits, as well as those from the Virgo cluster, which are stronger than dSph limits in the p-wave case. In order for the correct relic abundance to be produced, the string tension parameter describing cosmic strings was required to be $G\mu \sim 10^{-10}$ and $\sim 10^{-14}$ in the FT and CE scenarios respectively. This avoided most cosmic string bounds, apart from large Higgs condensates limits, however these presume a large SM Higgs condensate forms, which needs not be the case.

Chapter 6

Direct Detection Signatures of Nuclear Dark Matter

> It is a capital mistake to theorize before one has data. Insensibly one begins to twist facts to suit theories, instead of theories to suit facts.
>
> — Sherlock Holmes

The previous three chapters concentrated on a mechanism for DM production, where there was an additional source of DM in the early Universe from decaying topological defects. In the work [4], the direct detection signatures of a DM model also with atypical early Universe dynamics and genesis mechanism are considered. This uses a model of Nuclear Dark Matter (NDM) [298–303], where DM consists of bound states of strongly-interacting dark nucleons (DN) with short-range interactions, akin to SM nuclear bound states. In the early Universe, the DNs undergo an aggregation period, whereby through fusion processes larger and larger bound states form. These *dark nuclei* are spatially-extended objects, rather than the point-like candidates usually considered.

Compositeness has already been seen in the SM (emerging at different levels within atoms, nuclei, and nucleons) motivating DM models which follow suit. There are numerous models of composite DM, including [304–306] which study "WIMPonium", two particles bound under a Yukawa potential. The direct detection signatures of WIMPonium were fairly recently considered in [307, 308]. In analogy with SM atoms, a model of "dark hydrogen" was postulated

in [309], and "Q-balls", non-topological solitons of scalar fields, were presented in [310, 311]. Furthermore composite states can also be present in technicolor-like theories [312, 313].

We focus on the model of NDM hypothesised in [302, 303], and study the direct detection signatures and constraints arising from it. This class of model assumes that the dark nuclei have an approximately uniform density, with a hard core repulsion between the constituent DNs. This is in contrast to the DM "nuggets" described in [300, 301], where no hard core repulsion was assumed resulting in a more complicated internal structure.

In comparison to standard WIMP DM, the mass of a typical dark nucleus can be much larger. For example, in [302, 303] dark nuclei with a large number of constituents, each with masses in the GeV region, were considered leading to states with a total mass well in excess of the unitarity limit of thermal WIMP DM.

The composite and extended nature of these DM states will affect the way in which they scatter off SM nuclei in direct detection experiments. If all DM is in the form of composite states each with k dark nucleons (which we refer to as a k-DN state), and if the momentum transfer in the scattering process is less than the inverse radius of the state then the elastic scattering cross-section will be coherently enhanced by a factor of k^2 [298, 302, 303, 314]. However, as we increase k the number density of these k-DN states will decrease, leaving an overall event rate increasing only linearly with k [303].

The dependence of the scattering rate on the spatial properties of both the extended DM states and the SM nuclei is encoded in the product of their respective form factors. These form factors are as usual related to the Fourier transforms of the spatial densities of the particular composite object. If the radii of the DM states are larger than the SM nuclei, off which they are scattering, then direct detection experiments will start to probe the dark form factor at lower values of the momentum transfer compared to the SM form factor. This can lead to a striking structure in the recoil spectrum [303]. For example, if we assume that the composite DM states possess a uniform internal density, and model this density in terms of a spherical top hat function, the resulting form factor is a spherical Bessel function. The recoil energy spectrum will as a result include characteristic peaks and troughs. Whether these features are distinguishable from point-like WIMP recoil spectra depends on the individual experiment's energy resolution and threshold, and is the focus of this work.

The appearance of these distinctive peaks and troughs in the recoil spectrum also depends

on whether all DM states have the same number of DNs or whether there is a distribution of nuclei with different k values. The position of the troughs and peaks in the recoil spectrum is dependent on the value of k and it was shown in [303] that the compound recoil spectrum from a distribution of k values results in the peaks and troughs being smoothed out leaving a monotonically decreasing spectrum. While more difficult, in a single detector with a sufficiently high number of signal events the recoil spectrum in this case may still be distinguishable from that of a standard WIMP for a given DM velocity-distribution. Due to the uncertainty in the DM velocity-distribution a more effective way to distinguish between NDM and WIMP spectra is to perform a halo-independent analysis (see for example [315]) using data from several different detectors. In this paper however we wish to study the former and simpler case of dark nuclei existing predominantly with a fixed number of dark nucleons leaving the halo-independent analysis for future work.

In [303] a toy direct detection analysis of fixed k dark nuclei was performed using approximations of future detectors. In this paper we build on this work and perform an in-depth analysis of NDM at DEAP-3600 [98] and XENON1T [316] using the detectors' energy response functions, efficiencies and thresholds.

The first detector we consider is the liquid argon detector DEAP-3600, which will soon begin its 3 year run and will be approximately 20 times more sensitive to the WIMP scattering cross-section than current searches at a 100 GeV/c^2 WIMP mass [98]. We have chosen DEAP-3600 as one of our test cases as it has excellent energy resolution, which will be important if we hope to be able to identify peaks and troughs in the recoil energy spectrum. DEAP-3600 also has a better sensitivity to high mass DM states due to the slow (compared to xenon) fall off in the argon nuclear form factor.

The second direct detection experiment XENON1T is a liquid xenon detector which will also soon begin its physics run, and will be approximately 100 times more sensitive to the WIMP scattering cross-section than current searches in the mass range of 10-50 GeV/c^2 [316]. The use of the xenon target allows for a few-keV energy threshold, potentially giving sensitivity to features in the recoil energy spectrum at the lower energies where the scattering rate is largest.

Although our focus is to analyse the potential distinguishability of NDM from a standard WIMP signal, this paper includes an analysis of the current and future constraints on NDM if

no signal is observed. We use the limits from LUX [96] to calculate the current upper bounds on the DN-SM nucleon scattering cross-section for fixed k dark nuclei and go on to calculate the potential future limits arising from DEAP-3600 and XENON1T.

The paper is structured as follows; in Section 6.1 we outline our chosen model of NDM and review the calculation of the recoil spectrum including the energy efficiency and resolution of a direct detection experiment. Following this in Section 6.2.1 we explore the generic features of the recoil energy spectra for a selection of benchmark NDM scenarios at DEAP-3600, detailing the effect of the energy resolution and energy threshold on the observability of the features produced by the dark form factor. Following this we present the current and projected (if no signals are observed) limits on NDM from LUX and the two tonne-scale direct detection experiments respectively. In Section 6.3, we turn to the main component of this work and calculate the number of signal events required in order to distinguish a NDM spectrum from one generated by WIMPs. Finally we discuss our results and conclude in Section 6.4.

6.1 Nuclear Dark Matter Recoil Spectrum

The aim of this work is to analyse the direct detection phenomenology of a particular class of composite DM model termed Nuclear Dark Matter [302]. In particular, we extend the toy analysis of [303], in which a scenario of NDM with striking predictions for the recoil spectrum in direct detection experiments was examined. The specific scenario we wish to consider is one in which the DM abundance today consists of dark nuclei, each with the same number of DNs, *i.e.* all DM states are the same size or at least narrowly clustered around a specific value.

This scenario is a variant of the general picture described in [302], where dark nuclei generically exist in a wide distribution of sizes. The assumptions of [302] include the existence of a binding energy per dark nucleon that saturates leading to fusion processes that continue to produce larger and larger dark nuclei with the limit in size being determined by the temperature at which the fusion processes freeze-out. As a result we expect a distribution over different sizes of dark nuclei. In this case, however, the peaks and troughs in the recoil spectrum that we would hope to detect from a single size of dark nucleus are washed out when the full distribution is included [303].

The modified case where the distribution of dark nuclei sizes are focused around a par-

ticular value of k can in principle arise if the binding energy per dark nucleon turns over at some nucleon number, in the same way the SM nuclear binding energy per nucleon does at Iron. This turnover, for example, could arise in the dark sector in an analogous way to the SM by introducing a dark equivalent of the coulomb force. The direct detection prospects of this scenario is qualitatively different to that of the wide distribution and deserves detailed attention.

For simplicity in this analysis we will consider the underlying interaction between the DNs and SM quarks being due to the exchange of a heavy scalar mediator. In this case the elastic scattering rate of two spatially extended states will depend on the product of the respective form factors derived from the Fourier transforms of the individual spatial densities of the colliding objects.

The composite DM states we consider have an approximately uniform density of constituent matter and we can model the density as a spherical top hat function, leading to a spherical Bessel function form factor,

$$F_k(q) = \frac{3j_1(qR_k)}{qR_k}, \tag{6.1}$$

where R_k is the radius of the k-DN state and q is the momentum transfer in the collision. Under the assumption of a constant density and negligible binding energy, the radius is approximated by

$$R_k = k^{1/3}R_1, \tag{6.2}$$

where R_1 is the approximate radius of a single DN.

For the SM nuclear form factor, we use the Helm parameterisation [317]

$$F_N(q) = \frac{3j_1(qR_N)}{qR_N}e^{-q^2s^2/2}, \tag{6.3}$$

which represents a modification to the spherical hat density to include a finite-width drop off with skin depth $s = 0.9$ fm. For the SM nuclei's radius R_N, we employ the approximate analytic expression

$$R_N^2 = c^2 + \frac{7}{3}\pi^2a^2 - 5s^2, \tag{6.4}$$

from [318] with $c \approx 1.23A^{1/3} - 0.6$ fm (where A is the SM nucleon number), $a = 0.52$ fm.

The recoil spectrum, that is, the differential scattering rate per unit target mass for a DM

(whether a WIMP, NDM, or otherwise) particle to scatter off a SM nucleus, is given by

$$\frac{dR}{dE_R} = \frac{1}{m_N}\int_{v>v_{\min}} d^3\mathbf{v}\ \frac{\rho_X}{m_X} f(\mathbf{v}) v \frac{d\sigma_{XN}}{dE_R}\bigg|_v, \tag{6.5}$$

where $v_{\min} = \sqrt{\frac{E_R m_N}{2\mu_{XN}^2}}$ (for non-relativistic scattering) is the minimum velocity required to obtain recoil energy E_R, μ_{XN} is the reduced mass of the SM nuclei-DM state system, σ_{XN} is the DM-SM nuclei scattering cross-section, ρ_X is the local DM density, m_N and m_X are the masses of the SM-nucleus and DM state respectively, and $f(\mathbf{v})$ is the DM velocity distribution.

Now specifying to our case of a NDM state with k dark nucleons we follow [302] and assume that the underlying scattering process between the SM and DNs is isotropic and velocity independent. This allows us to write the differential event rate as

$$\frac{dR}{dE_R} = g(v_{\min})\frac{\rho_k}{2\mu_{kn}^2 m_1} A^2 k \sigma_0 F_N(q)^2 F_k(q)^2, \tag{6.6}$$

where σ_0 is defined as the zero-momentum transfer DN-SM nucleon scattering cross-section[1] (and so $F_k(0) = F_N(0) = 1$), μ_{kn} is the reduced mass of the DN-SM nucleon system, m_1 is the mass of a single DN, $q = \sqrt{2m_N E_R}$, and

$$g(v_{\min}) = \int_{v>v_{\min}} d^3\mathbf{v}\frac{f(\mathbf{v})}{v}. \tag{6.7}$$

Note that the event rate is proportional to a linear factor of k due to the cancellation of one power of the coherence factor (k^2) with a power of k in the denominator coming from the mass of the k-DN state, $m_k = km_1$. As we will only consider the case of a single size of dark nuclei, the density of k-DN, ρ_k, is the total local DM density.

In order to determine the recoil spectrum reconstructed by an experiment, one must take into account the detectors efficiency $\epsilon_{\text{eff}}(E_R)$, and energy resolution $\sigma(E_R)$. The reconstructed recoil spectra are then found using

$$\begin{aligned}\frac{dR_{\text{rec}}}{dE_R} &= \int dE'_R \epsilon_{\text{eff}}(E'_R)\kappa(E_R, E'_R)\frac{dR}{dE'_R} \\ &\approx \int dE'_R \frac{\epsilon_{\text{eff}}(E'_R)}{\sqrt{2\pi}\sigma(E'_R)} \exp\left(-\frac{(E_R - E'_R)^2}{2\sigma^2(E'_R)}\right)\frac{dR}{dE'_R}\end{aligned} \tag{6.8}$$

where $\kappa(E_R, E'_R)$ is the energy response function, which we have taken to be a Gaussian.

The predicted number of events seen by a detector is then

$$N = \left(\int_{E'_{\text{low}}}^{E'_{\text{up}}} dE_R \frac{dR_{\text{rec}}}{dE_R}\right) \times \text{Exposure}, \tag{6.9}$$

[1] Not to be confused with the annihilation cross-section parameter σ_0 used in the previous chapters.

where $E'_{\rm low}$ and $E'_{\rm up}$ are the limits of the reconstructed energy window used in the analysis, and the exposure is the fiducial mass of the detector multiplied by its livetime.

6.2 Nuclear Dark Matter in Tonne-Scale Direct Detection Experiments

6.2.1 Energy Resolutions, Efficiencies and Energy Windows.

In this section we detail the parameterisation of the energy resolution, detector efficiency and recoil energy window used in our analysis for each experiment we consider. The recoil energy spectrum generated by the dark form factor, (6.1), has two important features that will play an important role in the analysis. The first is the oscillatory nature of the Bessel function leading to non-decreasing sections of the recoil spectrum. In order to identify these features the experiment needs to have sufficiently good energy resolution. For this reason we have included an analysis with DEAP-3600, which has a particular focus on producing a leading energy resolution.

The second important feature of the NDM recoil spectrum is that the first few peaks at low energy will dominate the event rate. This means that a low recoil energy threshold will be an advantage for maximising the event rate. In addition, for large k states the frequency of oscillations will be higher and given that in order to distinguish between the NDM and WIMP models we need to detect as many events as possible in the non-decreasing part of the spectrum it is clear that the we need to have the recoil energy threshold as low as possible. For this reason, we have included an analysis with XENON1T, which has a low recoil energy threshold.

The size of the full signal energy window and the efficiency within the window for each experiment will also play a role in determining how many of the NDM form factor oscillations are in principle observable in each experiment. We start with the details of DEAP-3600.

DEAP-3600 is a single-phase scintillation detector with a 1000 kg fiducial mass target of liquid argon, which will begin its search in the near future and results are anticipated over the next few years. In the single-phase detector, an array of photomultiplier tubes (PMTs) views the target over the full solid angle of 4π to detect the scintillation light of any possible DM scatterings. This approach maximises the number of photoelectrons (PE) detected, which is

proportional to the recoil energy (in keV) imparted by the collisions. To predict how WIMPs and NDM will be reconstructed we ran Monte Carlo simulations of $\sim 8 \times 10^6$ events in a DEAP-like detector simulation. The efficiency and energy resolution were then found by fitting functions to the resulting distributions of measured PE versus generated recoil energy resulting in

$$\begin{gathered}\sigma(E_R) = 0.54 \text{ keV}\sqrt{E_R/ \text{ keV}} - 0.048 \text{ keV}(E_R/ \text{ keV}) + 0.0026 \text{ keV}(E_R/ \text{ keV})^{3/2}, \\ \epsilon(E_R) = 0.56\,\text{erf}(0.044\ E_R/ \text{ keV}).\end{gathered} \tag{6.10}$$

We consider events with $50 < E_R < 300$ PE ($19.4 < E_R < 122.4$ keV), since below this there are not enough photoelectrons to accurately reconstruct the position of the event, and above there are too few DM scatters.

XENON1T is a two-phase scintillation detector with 1000 kg fiducial mass of liquid xenon target. XENON1T is currently in the commissioning phase and will begin its physics run shortly. The relevant information for XENON1T was taken from [316], with an approximation for the energy resolution given by [319]. This and the efficiency were then taken to be

$$\begin{gathered}\sigma(E_R) = -0.47 \text{ keV} + 0.65 \text{ keV}\sqrt{E_R/ \text{ keV}} + 0.02 \text{ keV}(E_R/ \text{ keV}), \\ \epsilon(E_R) = 0.4,\end{gathered} \tag{6.11}$$

where the energy window $4 < E_R < 50$ keV is used.

We will calculate the bound on NDM from the existing published LUX results [96]. All requisite information about LUX was taken from a recent improved analysis of the 2013 data [96] and the first results report [95], except for the energy resolution. For this, we use the resolution for electron recoils from a more recent calibration of LUX using tritium decays [320], $\sigma(E_R) = 0.32 \text{ keV}\sqrt{E_R/ \text{ keV}}$. This was then converted into the energy resolution for nuclear recoils using a Lindhard model quenching factor [321] with a Lindhard factor of 0.174, as given in [96]. LUX's efficiency is taken directly from Figure 1 in [96], within an energy window $1.1 < E_R < 50$ keV.

6.2.2 Example Recoil Spectra

To illustrate the phenomenology of NDM scattering, we compare the reconstructed recoil spectra of NDM with that of a WIMP for DEAP-3600 and XENON1T. In Figure 6.1, the recoil energy spectra for a range of k are shown for each experiment. For each value of

k we display the spectra with and without the inclusion of the detector energy resolution detailed in Section 6.2.1. We have fixed the NDM model parameters R_1 and m_1 to 1 fm and 1 GeV respectively in analogy with the SM. We have no fundamental guide for what these parameters should be in the dark sector, so we have chosen to take the SM values as a place to start. These parameters will remain fixed at these values throughout the rest of this paper. Also shown in each plot of Figure 6.1 is the reconstructed recoil spectra of a standard WIMP with a mass and elastic scattering cross-section per SM nucleon of 100 GeV and 10^{-46} cm^2 respectively. We use a Maxwell-Boltzmann DM velocity distribution for the WIMP spectrum and assume the scattering is isotropic and momentum independent.

In most cases even with detector effects turned on the oscillations of the k-DN form factor can be seen, which contrasts with the monotonically decreasing WIMP spectrum[1]. The period of the oscillations in the NDM recoil energy spectrum decreases with k, as the size of the k-DN states increases. It is worth noting at this point that the slope enveloping these oscillations also steepens with k, due to the inverse dependence in (6.1).

Comparison of the solid and dashed curves in Figure 6.1 demonstrates the effect of the finite experimental energy resolution. The sharpness of the features are smoothed out leading to less significant troughs in the spectrum and simultaneously decreasing the height of the peaks. As k increases the period of the oscillations will decrease and the effect of the energy resolution smearing becomes more prominent. As the oscillation period approaches the energy resolution of the detector it is clear that there is a value of k, call it $k_{\max}$, beyond which the characteristic oscillations of the form factor can no longer be resolved. In particular, the non-decreasing parts of the spectrum will be smoothed away leaving a monotonically decreasing spectrum. This transition is important for our analysis as it will represent the value of k beyond which the distinguishability between the NDM spectrum and the WIMP spectrum is no longer determined by the non-decreasing sections of the spectrum but rather on its slope as a whole. As described earlier, the WIMP spectra used throughout this paper are all generated with a Maxwell-Boltzmann DM velocity distribution. Allowing for a non-standard velocity distribution may permit a WIMP spectrum that mimics the NDM spectrum for dark nuclei with $k > k_{\max}$, where as for lower k values the non-decreasing sections of the NDM

[1]The WIMP spectrum will start increasing again due to the oscillations in the SM form factor, but this occurs far beyond the maximum energy window of DEAP-3600 and XENON1T that we consider here.

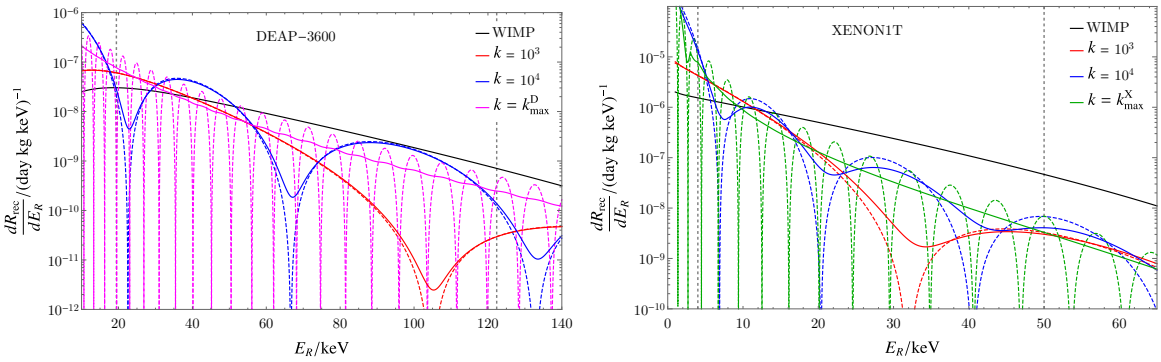

(a) (b)

Figure 6.1: (a): Comparison of the recoil energy spectra for NDM along with that of a 100 GeV WIMP for DEAP-3600. Spectra are plotted for three different k values: 10^3 (red), 10^4 (blue), and $k^{\rm D}_{\rm max} = 6.5 \times 10^6$ (purple). (b): Comparison of the recoil energy spectra for NDM along with that of a 100 GeV WIMP for XENON1T. Spectra are plotted for three different k values: 10^3 (red), 10^4 (blue), and $k^{\rm X}_{\rm max} = 5.8 \times 10^5$ (green). The bold and dashed lines represent the spectra with and without the finite energy resolution taken into account for each experiment using the experimental parameters in (6.10) and (6.11) for DEAP-3600 and XENON1T respectively. In the NDM cases we have set $R_1 = 1$ fm and $m_1 = 1$ GeV. Vertical dashed lines represent the limits of the energy windows of the two experiments. The WIMP-SM nucleon scattering cross-section was fixed to be 10^{-46} cm^2 and the NDM cross-sections were scaled such that the integrated rates were equal to that of the WIMP across the energy window of each experiment.

spectrum will still allow an experiment to distinguish it from a WIMP spectrum no-matter what the velocity distribution.

We can determine $k_{\rm max}$ by finding when the period of the oscillations at the threshold energy[1] is approximately equal to the width of the response function, $\sigma(E_R^{\rm th})$, where $E_R^{\rm th}$ is the threshold energy of the detector. This leads to

$$k_{\rm max} \sim \left(\frac{\pi^2}{4 m_N R_1^2 \left(E_R^{\rm th} - \sqrt{(E_R^{\rm th})^2 - \sigma(E_R^{\rm th})^2} \right)} \right)^{3/2} . \tag{6.12}$$

Beyond $k_{\rm max}$ we expect the dominant part of the NDM spectrum to be effectively a monotonically decreasing function of the recoil energy. In Figure 6.1, we have plotted the $k_{\rm max}$ for

[1] We compare at the threshold energy as this is where the dominant part of the signal will come from and is where the period of the oscillation is smallest.

each detector, $k^{\rm D}_{\rm max}$ for DEAP-3600 $k^{\rm X}_{\rm max}$ for XENON1T, and in each case we can see that the spectra including the detector effects have been smoothed out leaving no rising sections.

Conversely if we decrease the value of k sufficiently we will eventually generate a recoil spectrum that has no rising sections within the energy window of the experiment. The NDM form factor in this region only produces a modification in the slope of the recoil energy spectrum, which again could be mimicked easily by a WIMP spectrum. Defining $k_{\rm min}$ as the DN number at which the first trough in the recoil spectrum enters the energy window, we find

$$k_{\rm min} \sim \left(\frac{4.5}{R_1 \sqrt{2 m_N E_{\rm up}}} \right)^3 , \tag{6.13}$$

where $E_{\rm up}$ is the upper end of the sensitivity energy window for a given experiment. With these definitions, for each experiment there is a range of k values in which the distinctive rising features of the dark form factor may be seen within the energy window of a detector; outside this region we expect NDM spectra to be monotonically decreasing.

For DEAP-3600 this k range is

$$800 \lesssim k \left(\frac{R_1}{1\text{fm}} \right)^3 \lesssim 6.5 \times 10^6, \tag{6.14}$$

and for XENON1T it is

$$500 \lesssim k \left(\frac{R_1}{1\text{fm}} \right)^3 \lesssim 5.8 \times 10^5. \tag{6.15}$$

The lower bound in XENON1T is slightly lower than in DEAP-3600, as the first dip appears within the energy window sooner due to the larger mass of the xenon nucleus (leading to a shorter period in the form factor oscillation), despite XENON1T having a smaller energy window compared with DEAP-3600. Comparing DEAP-3600 and XENON1T for $k = 10^3$ and $k = 10^4$ we note that for the same value of k the period of oscillations in the spectra is larger for DEAP-3600 due to the smaller mass of the argon nucleus producing a lower value for the momentum transfer, q, for a given recoil energy. In addition for the majority of the relevant range of recoil energies, DEAP-3600 has a better energy resolution potentially allowing it to distinguish (using rising sections of the spectra) dark nuclei with larger k values compared to XENON1T as the transition to a monotonically decreasing spectrum will occur at larger values of k.

In Section 6.3 we perform an analysis to determine the number of signal events required to distinguish the NDM spectrum from that of a WIMP with a Maxwell-Boltzmann velocity

distribution. As we have stated above, due to the uncertainty in the DM velocity distribution, the NDM spectra for k values beyond $k_{\max}$ could be mimicked by WIMP spectra with a non-standard velocity distribution. However, asking whether the NDM spectrum can be distinguished from that of a WIMP with a Maxwell-Boltzmann velocity distribution is still a valuable question to answer.

For k values within the ranges in (6.14) and (6.15) the number of signal events required to identify the NDM spectrum will depend on two main properties; where the first (and sometimes subsequent) rising section of the spectrum appears in the energy window and what the amplitude of the oscillations are after the energy resolutions of the detectors have been taken into account.

6.2.3 Current and Projected Exclusion Limits

While our main focus is to examine whether we can distinguish the NDM from WIMP signal events, we finish this section with a discussion of the current and projected limits on models of NDM if neither DEAP-3600 or XENON1T observe any candidate signals. In Figure 6.2, we show a combination of limits on σ_0, the DN-SM nucleon scattering cross-section for NDM and compare this to the equivalent limits for a standard WIMP, plotting each as a function of the mass of the DM state. For NDM, the mass of the DM state is given as $m_k = k\, m_1$, where we have fixed the mass of an individual DN to $m_1 = 1$ GeV. As a result the x-axis is equivalent to the number of DNs, k, for the nuclear states.

In both the NDM and WIMP cases, we show the projected limits for DEAP-3600 and XENON1T, and the current limits derived from LUX. All NDM limits are calculated using (6.8) with the requisite detector information from Section 6.2.1. Our reconstructed WIMP limits (dashed lines in Figure 6.2) are in good agreement with the results presented in the analysis papers [96, 98, 316].

Comparing the NDM limits with those of the WIMPs, from (6.6) we see that the constraints on the DN-SM nucleon cross-section is much stronger than those for the WIMP. In the lower mass region below 100 GeV, the ratio of the NDM and WIMP limits for a given DM mass goes approximately as k^2 as in this region the dark form factor is still close to unity. As we move to higher masses the dark form factor suppresses the overall rate and therefore weakening the limits. The limiting behaviour of the event rate for large k goes as $\sim k^{-1/3}$

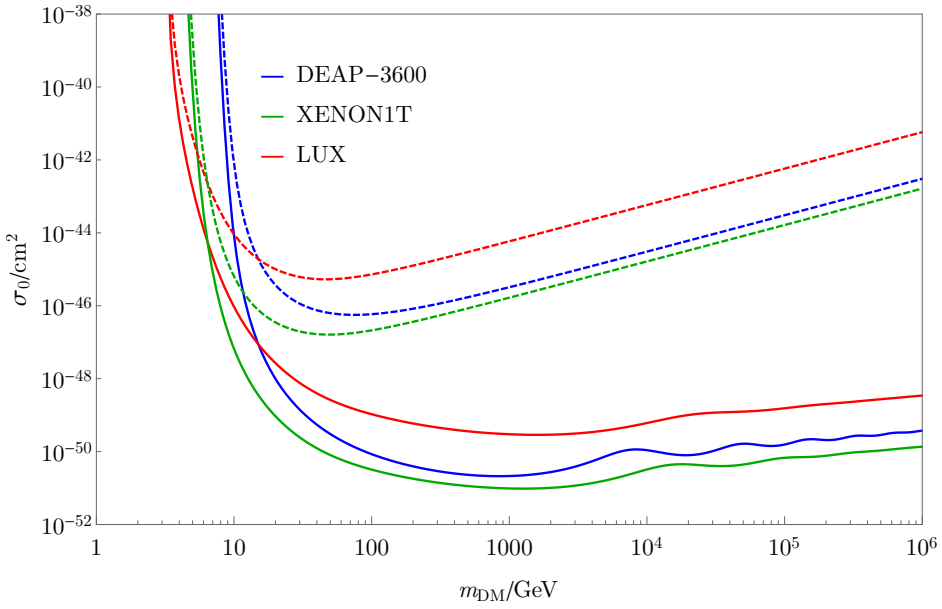

Figure 6.2: Projected limits at 90% CL for σ_0, the DN-SM nucleon scattering cross-section (in bold), against the DM mass for DEAP-3600 (blue) [98] and XENON1T (green) [96], and compared with the strongest current limits from LUX (red) [316]. Also shown are the WIMP limits in the same detectors (dashed lines). For the NDM limits we have taken $m_1 = 1$ GeV and $R_1 = 1$ fm.

and as a result the elastic scattering cross-section limit for dark nuclei increases as $k^{1/3}$ in contrast to the usual WIMP limit, which increases linearly with m_{DM}.

In the high mass region the NDM limits also exhibit oscillations (due to the dark form factor), which are more pronounced in the case of DEAP-3600. These arise as a result of the energy window enclosing varying configurations of form factor oscillations. As k (and therefore m_k) increases there are k values for which the energy window contains more peaks than troughs and visa-versa, which results in the observed oscillations. This effect is less pronounced in LUX and XENON1T as the energy resolution is not as good in the high recoil energy region, which means the amplitude of the oscillations in the recoil spectra will not be reconstructed as sharply resulting in the limit shape being flattened. An interesting result of these oscillations is that for some ranges of NDM mass a detector with a worse energy resolution could provide a slightly stronger limit compared to one with better (if all else is equal).

The overall scale of the limits on the DN-SM nucleon scattering cross-section is several orders of magnitude more restrictive than that for the WIMP case. In the example of a scalar

interaction between a SM quark and a DN (scalar or fermion) we can translate the limits from direct detection to an upper limit on the DN annihilation to SM quarks. We find a result that is many orders of magnitude below what is required for achieving the correct abundance via freeze-out. This is no great surprise as it has been known for some time [322] that it is very difficult to have a sufficiently large DM annihilation rate to SM quarks for asymmetric freeze-out to produce an abundance that is determined by the DM asymmetry. The limits from direct detection and monojet searches at the LHC rule out the viable parameter regions involving interactions with quarks or gluons. The process of asymmetric freeze-out in NDM models can proceed, however, via the annihilation into lighter hidden sector states [302]. These hidden sector states may also be limited in a model dependent way by astrophysical constraints, the details of which are beyond the scope of this work.

6.3 Identifying Nuclear Dark Matter

Perhaps the most interesting question is: if DEAP-3600 or XENON1T do see a candidate signal above the background, how many events are required to identify NDM? In this section we calculate the number of events required to distinguish between the NDM and WIMP hypotheses ($N_{\rm req}$) at a given confidence level.

In the absence of knowledge about the nature of DM particles, we compare each NDM spectrum (of varying k values) with the most similar WIMP-induced recoil energy distribution. This most similar WIMP mass can be different for each k, and therefore the number of events required to effectively distinguish between the hypotheses will be different in each case.

We start by finding the WIMP spectrum which is the most indistinguishable, *i.e.* requires the highest number of events to distinguish, from each hypothesised NDM spectrum. To this end we define a test statistic, λ, as a negative log likelihood (NLL) ratio;

$$\lambda = -2\ln\left(\frac{\mathcal{L}_{\rm NDM}}{\mathcal{L}_{\rm WIMP}}\right), \tag{6.16}$$

where $\mathcal{L}_{\rm NDM/WIMP}$ is the likelihood of an event occurring due to an NDM or WIMP DM candidate. In this case values greater than zero correspond to data sets which are more WIMP-like than NDM-like. An unbinned extended likelihood is used giving

$$\mathcal{L}_{\rm NDM/WIMP} = \text{Poisson}\left\{N_{\rm obs}, N_{\rm exp}(\sigma_0, k, m_1)\right\} \prod_{i=1}^{N_{\rm obs}} f(E_i|k, m_1). \tag{6.17}$$

where $f(E_i|k, m_1)$ is the reconstructed recoil energy PDF for the WIMP ($k = 1$) or NDM case. The mass m_1 (which in the case of NDM is the individual DN mass), and elastic scattering cross-section σ_0, is allowed take independent values for the NDM and WIMP cases. The scattering cross-section acts as an overall factor (under our assumptions of isotropic and velocity independent scattering) in both distributions; as such, it only appears in the integral number of expected events N_{exp}. The most indistinguishable case occurs when the expected number of events is the same for both NDM and WIMP DM, thus the Poisson term can be dropped from the likelihood ratio and only the shape of the distributions is compared.

For each hypothesised number of observed events a confidence level C is determined from the PDF of λ, $g(\lambda|N_{\text{obs}})$, where

$$1 - C = \int_0^\infty g(\lambda|N_{\text{obs}})d\lambda. \tag{6.18}$$

The PDF is built using a Monte Carlo where events are created under the NDM hypothesis for a given k. The value of C corresponds to the probability that a dataset will appear NDM-like under the NDM hypothesis.

The test was carried out at a range of 121 k values, logarithmically distributed between $k = 10$ and $k = 10^7$, with $m_1 = 1\,\text{GeV}$. For the WIMP distributions a table was built comprising 5000 WIMP mass spectra logarithmically distributed between $m = 10\,\text{GeV}$ and $m = 10^6\,\text{GeV}$. This range accounted for all possible WIMP distribution shapes; masses of 10 GeV and below are easily distinguishable from the NDM spectra in question, and those above 10^6 GeV are indistinguishable from each other.

The WIMP spectra table was scanned through for each value of k. The number of events required to distinguish between the NDM and WIMP hypotheses at $3\,\sigma$ CL was then determined for each WIMP mass. Generating adequate Monte Carlo statistics to produce distributions of $g(\lambda|N_{\text{obs}})$ for each of the masses and number of events is computationally expensive. Instead, a subset of values of N_{obs} were used and the distribution of confidence levels was determined by fitting a modified non-central chi-squared CDF:

$$C(N_{\text{obs}}) = 1 - Q_{\frac{a}{2}}\left(\sqrt{b}, \sqrt{\frac{N_{\text{obs}}}{c}}\right), \tag{6.19}$$

where $Q_{\frac{a}{2}}$ is the Marcum Q-function. Here the parameters a, b, and c are left as variables in the fit. This function fits well to the CL distribution as illustrated in Figure 6.3. Figure 6.3a

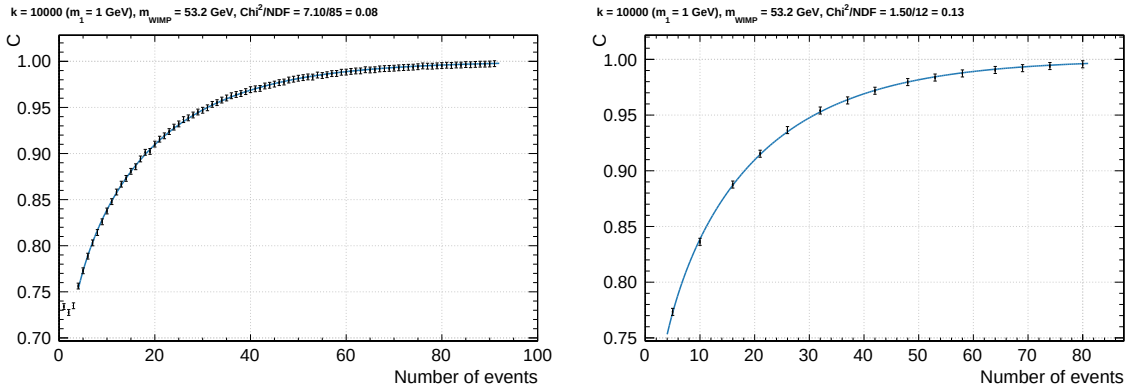

(a) (b)

Figure 6.3: (a): The CL up to $N_{\text{obs}} = 92$ for $k = 10^4$ ($m_1 = 1\,\text{GeV}$) compared to a 53.2 GeV WIMP (which gives the most indistinguishable spectrum. 10^5 pseudo-experiments were used to generate the $g(\lambda|N_{\text{obs}})$ distribution for each N_{obs}. (b): A subset of N_{obs} values, function (6.19) was fit to these points, shown as the solid line.

shows the CL for each value of N_{obs} up to $N_{\text{obs}} = 92$ for $k = 10^4$ ($m_1 = 1\,\text{GeV}$) compared to a 53.2 GeV WIMP. To generate the $g(\lambda|N_{\text{obs}})$ distribution, 10^5 pseudo-experiments were used in each case. Function (6.19) was fitted to these points with $1-C$ being used to determine the $3\,\sigma$ CL. In Figure 6.3b this fit is plotted alongside a subset of the N_{obs} values from Figure 6.3a, showing excellent agreement between the two.

Figure 6.4 shows a selection of NDM spectra as reconstructed by DEAP-3600, which are plotted across the energy window of the detector. In each sub-figure the spectrum is plotted alongside that of the most indistinguishable WIMP at that k value. The top left panel (Figure 6.4a) shows the spectra for $k = 1412$, which is the first bin in the k range in Figure 6.5, where the number of events required to distinguish up to a $3\,\sigma$ CL is plotted as a function of k. In the $k = 1412$ case, the first trough in the recoil spectrum has just entered into the energy window, and the WIMP spectrum closely matches that of NDM. Subsequently the number of events required to distinguish to $3\,\sigma$ is large (1294). As k decreases below this value, N_{req} gets larger and eventually the first trough leaves the energy window with distinguishability between WIMP and NDM spectra becoming effectively impossible. In the event of a signal in this case, one could only put an upper limit on k.

In Figure 6.4b where $k = 5012$, the first trough occurs earlier, and the WIMP spectrum

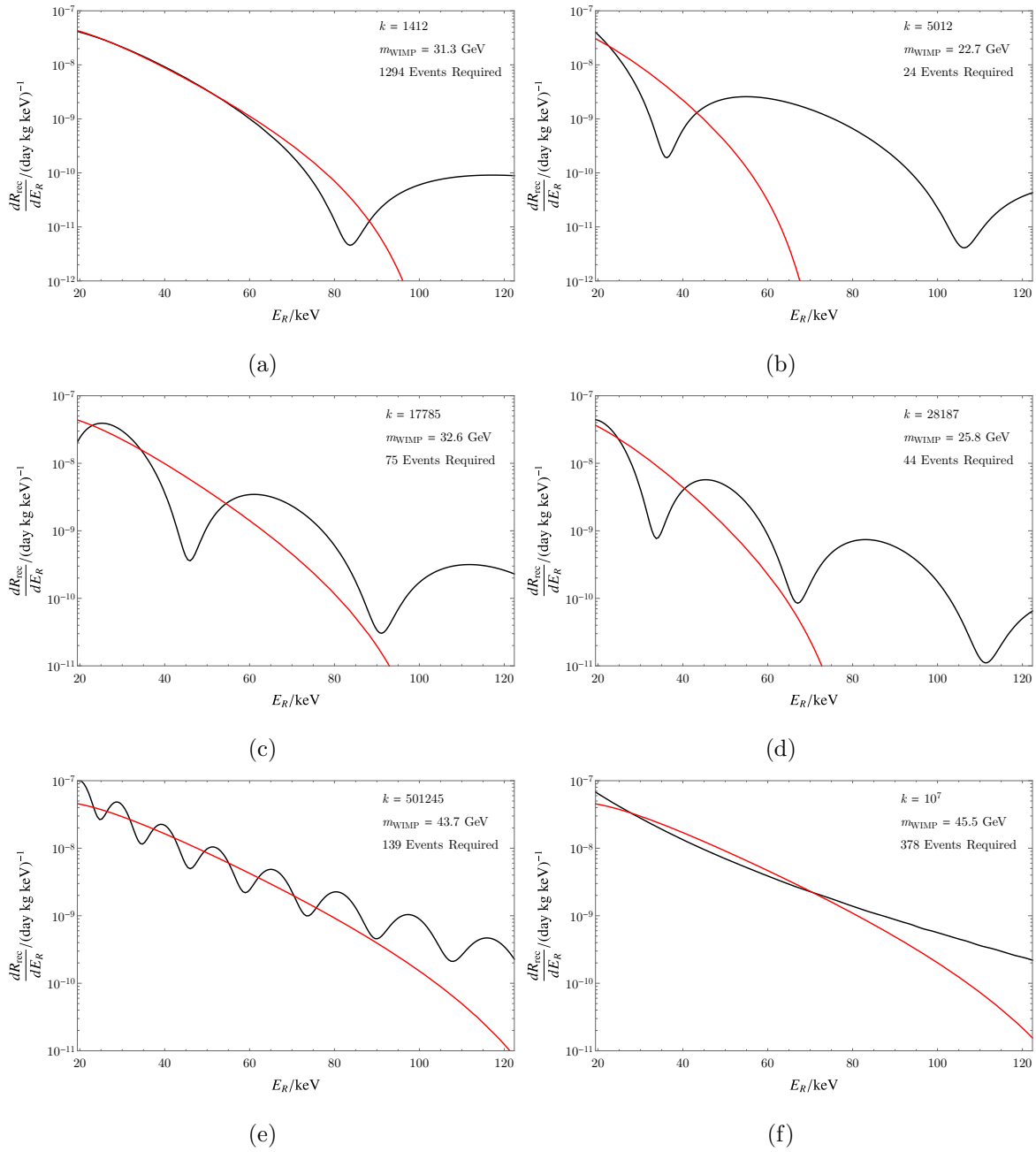

Figure 6.4: Example NDM spectra (black) reconstructed in DEAP-3600 along with the most indistinguishable WIMP spectra (red) resulting in the number of events shown in Figure 6.5. Inset into each plot are the k values, the mass of the best fitting WIMP (m_{WIMP}), and the number of events required to distinguish the spectra to a 3 σ confidence level. This is plotted across the energy window, where the total rate integrated over the window is equal for both WIMP and NDM.

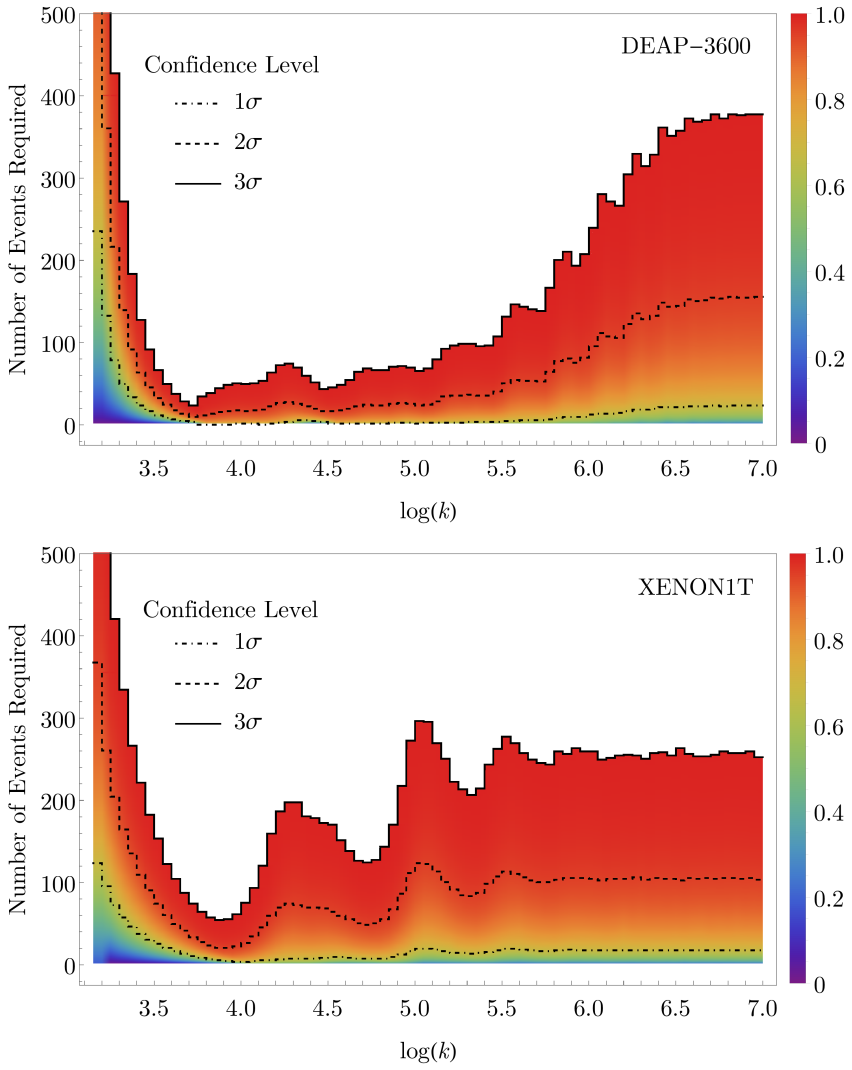

Figure 6.5: The number of events required to distinguish between values of k and all WIMP masses to the stated confidence level in DEAP-3600 (above) and XENON1T (below). Here the confidence level given by (6.19) is shown by the colour scale with 1, 2, and 3 σ shown as dot-dashed, dashed, and solid lines respectively.

no longer closely follows that of NDM. Here, the relative contribution of the second peak is much greater than in Figure 6.4a, by almost a factor of 100. Given that N_{req} decreases by around this factor as well, this suggests the rise in the spectrum, which is irreproducible with a standard WIMP, acts as the dominant distinguishing feature of the spectra. This claim is further supported when we notice that N_{req} in each of these cases is just enough to be able

to resolve the second peak (and consequently, the first trough)[1]. Only 24 events are required in the case that $k = 5012$, which corresponds to the lowest value across the entire range for DEAP-3600, *i.e.* the deepest minimum in Figure 6.5.

This distinguishing mechanism is also at work in the case that $k = 17785$ (seen in Figure 6.4c), which corresponds to the first peak following the central minimum at $k = 5012$ in Figure 6.5. Here the threshold is just at the beginning of a peak, which means the NDM spectrum follows the WIMP spectrum more closely than in the previous case and the second peak occurs later on, subsequently N_{req} is larger.

The next minimum in N_{req} lies at $k = 28187$, whose spectrum is seen in Figure 6.4d. Here the threshold intersects the oscillations approximately as it does in Figure 6.4b for $k = 5012$, however more events are required to distinguish in the $k = 28187$ case. This reflects the effect of the finite energy resolution which smears out the troughs, reducing their depth and making them less distinctive.

It is clear now that as k is increased, N_{req} oscillates as the spectra change between configurations such as those in Figure 6.4b & 6.4d, and that in Figure 6.4c. These fluctuations are seen in Figure 6.5 for both DEAP-3600 and XENON1T, the difference between them will be discussed later. The ability to distinguish between hypotheses for a particular value of k in this region is dependent on the chosen energy window. If we were to change the lower threshold of the window, this would change the relative size of the second peak and therefore N_{req}. The overall effect of this would be a phase change in the oscillations seen in Figure 6.5; the troughs and peaks would shift, but their amplitude would not change much. Changing the upper threshold by small amounts will have little effect, as the relative rate in this region is negligible (compared with the rate at threshold).

Looking now at the case where $k = 501245$ (Figure 6.4e), lying in the upwards trending region of Figure 6.5, we can see the period of the oscillations is significantly shorter here, which have also been smeared out significantly here. With just $\mathcal{O}(10)$ events, the first several oscillations in the spectrum can now be probed (as opposed to only the first), however their amplitude has been reduced to such an extent that 139 events are required to distinguish to $3\,\sigma$. The upwards rise in Figure 6.5 reflects the increase in smearing making distinction

[1] A crude criterion for a resolvable spectral feature is as follows: if the rate in the vicinity of the feature is a factor of $1/N$ smaller than the peak rate within the entire energy window, then at least N events will be needed before events appear in this region, allowing it to be "resolvable".

harder.

In the last case seen in Figure 6.4f where $k = 10^7$, the oscillations in the NDM spectrum are no longer visible, as their period is too small to be resolved by DEAP-3600. The shape of the slope is still distinct from all WIMP spectra, and so can still be distinguished. However this is under the assumption that the WIMP's velocity distribution is described by the SHM. By considering an alternative velocity distribution, a WIMP spectrum could mimic that of NDM's seen here. Past the point where the oscillations are no longer resolved, the shape of NDM spectra is fixed, and so N_{req} plateaus, as seen in Figure 6.5.

What one notices across the selection of spectra presented in Figure 6.4 is that the mass of the most indistinguishable WIMP, m_{WIMP}, approximately follows N_{req}. When N_{req} is smaller, so is m_{WIMP} as the NDM spectra start with sharp declines, which WIMP spectra best mimic by decreasing more quickly as well; this trend is created by decreasing the WIMP mass, which causes the distribution of recoil energies to drop off faster.

Comparing DEAP-3600 and XENON1T in Figure 6.5 one notices the range of k values where distinguishing could be possible (before the plateau region and after the divergence at low k) is greater for DEAP-3600, where N_{req} is also smaller. Both these qualities reflect the benefit of having a better energy resolution when searching for NDM. Furthermore the range of distinguishable k values seen in these plots is in good agreement with the those predicted earlier: (6.14) and (6.15) for DEAP-3600 and XENON1T respectively.

The oscillations in N_{req} have a larger period for XENON1T, which is counter-intuitive given that the period of the recoil spectra's oscillations is smaller. This is a result of the energy threshold being lower; as k increases the dips in the recoil spectrum contract towards the origin, and so get "bunched" around it. This means that by having a lower threshold, troughs will pass through this boundary at a slower pace with increasing k, and so the period of the oscillations in N_{req} increases.

As discussed, the minimum number of events required to distinguish to $3\,\sigma$ in DEAP-3600 is 24, which occurs when $k \sim 5000$. For XENON1T, the minimum is 55 events (as the energy resolution is worse), which occurs when $k \sim 8000$. As the position of the first trough in the recoil spectrum is at lower E_R in XENON1T, one might expect to find this global minimum at a lower k value than in DEAP-3600. However because the energy threshold is also lower, the relative differences are such that the minimum is pushed higher.

The final significant difference one notices between detectors, is the size of N_{req} in the plateau region, which is lower for XENON1T. While the characteristic troughs are not resolved here, the NDM spectra have different slopes. In the case of XENON1T, the slope is sharper and more easily distinguished as the target nuclei are larger.

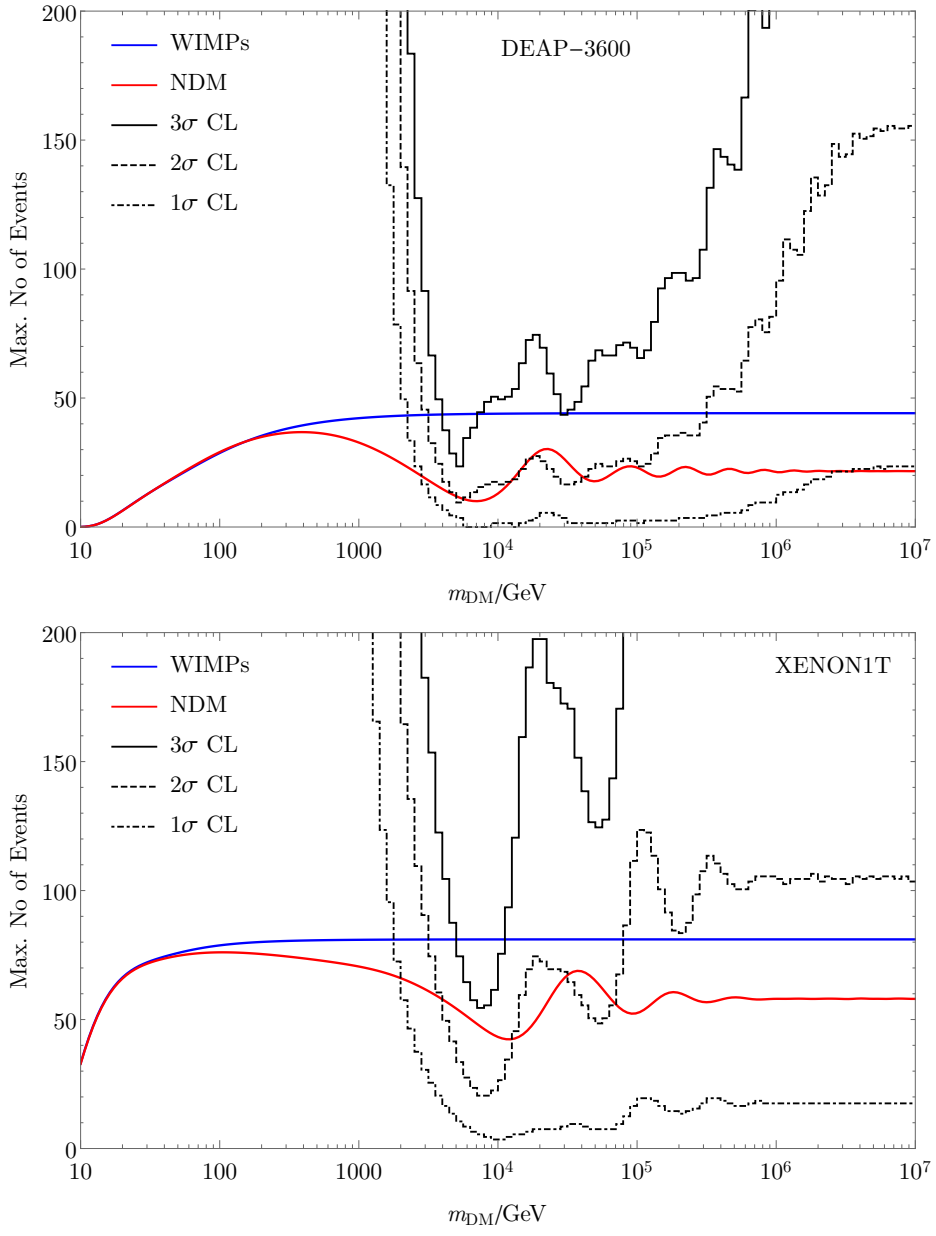

Figure 6.6: The maximum number of events that could be seen at DEAP-3600 (above) and XENON1T (below) against DM mass for NDM (red) and WIMPs (blue), plotted alongside the 1,2, & 3σ CL lines (the dotdashed, dashed, and bold lines respectively) for distinction as seen in Figure 6.5.

6.3.1 Discovery Potential

Finally, we examine the maximum number of events that could be seen ($N_{\max}$) in DEAP-3600 and XENON1T, and see how they compare to N_{req} in each case. This is estimated by taking the LUX limit as the cross-section, and is plotted against mass in Figure 6.6 for both NDM and WIMPs in the DEAP-3600 and XENON1T experiments. Included in the same plot are the N_{req} values at 1, 2, & 3 σ CL. For both WIMPs and NDM, $N_{\max}$ goes to zero at low mass, where LUX becomes more sensitive than DEAP-3600 and XENON1T[1]. The predicted $N_{\max}$ rises with mass as the experiments increase in sensitivity relative to the current LUX bound for both NDM and WIMPs, however the two models diverge around 100 GeV, where the value plateaus at $\sim$ 65 (120) for WIMPs, but oscillates around $\sim$ 20 (60) for NDM in DEAP-3600 (XENON1T). These oscillations occur for the same reason as those in the σ_0 limit in Figure 6.2; *i.e.* the energy window is enclosing varying configurations of the recoil spectra, which results in a fluctuating $N_{\max}$.

Comparing $N_{\max}$ to N_{req} for NDM, we see there are small ranges where distinguishing to $2\,\sigma$ CL could be possible in both DEAP-3600 and XENON1T. However this range is slightly larger in case of XENON1T, despite requiring a higher number of events to distinguish, as this is compensated for by its increased sensitivity. Furthermore XENON1T comes closer to distinguishing to $3\,\sigma$ than DEAP-3600. Changes to m_1 and R_1 are not expected to cause large shifts or gains to $N_{\max}$ relative to N_{req}, which would alter the discovery potential. Varying m_1 will just scale the recoil spectra in the high mass limit as the number density is changing, and N_{req} only depends on the relative shape of WIMP and NDM spectra, so is unchanged by such scaling factors. Similarly $N_{\max}$ is not affected as the change in the rate is exactly cancelled by an equivalent shift in the LUX limit.

Varying R_1 would change the size of the k-DN state, R_k, which affects the scattering rate via the form factor, and so if it were allowed to vary, the configuration of troughs would change. However this would be equivalent to varying k as this also changes R_k (it also scales the rate, but as mentioned, such factors are irrelevant), therefore shifting R_1 will simply stretch or contract $N_{\max}$ and N_{req} equivalently along the mass axis. While the situation may be more complex in the lower mass region, as distribution of imparted recoil energies is

[1]LUX becomes more sensitive than both XENON1T and DEAP-3600, because its energy threshold is lower, allowing it to probe lighter DM states with a higher sensitivity.

changing (*i.e.* $g(v_{\min})$), much of it is already constrained by LUX. Furthermore NDM expects high mass DM candidates, and so this region is less interesting.

Therefore while $2\,\sigma$ "hints" of NDM could be seen in the tonne-scale experiments coming online now, a distinction at the $3\,\sigma$ level is unlikely. However larger follow-on detectors employing argon (20T) and xenon (7T) targets are under consideration. Taking a 20T argon detector's specifications (the efficiency, *etc.*) to be the same as DEAP-3600's, then $N_{\max}$ in Figure 6.6 can simply be scaled to predict the same for the follow-on detector. Therefore we can expect $N_{\max}$ in this detector to oscillate around 400 events with a peak of 800, which is enough to distinguish almost the entire k range in (6.14) to at least $3\,\sigma$. Only where $k \lesssim 2000$ could distinguishing to $3\,\sigma$ still not be possible. Thus where the peaks and troughs are visible within the energy window, distinguishing NDM and WIMP signals will nearly always be possible.

Doing the same calculation for a 7T xenon detector with the same specifications as XENON1T, we can expect $N_{\max}$ also oscillate around 400 events with a peak of 650, which also allows the signals to be distinguished to at least $3\,\sigma$ across the most of the k range in (6.15). Furthermore, these projections as conservative estimates, as better efficiency, energy thresholds, and so forth, are to be expected.

It is clear that when searching for NDM, both DEAP-3600 and XENON1T have their own advantages. DEAP-3600's better energy resolution and smaller oscillation periodicity allows NDM spectra to be more easily distinguishable, while XENON1T's reduced lower energy threshold pushes the sensitivity higher.

6.4 Discussions

Typically DM is assumed to be a point-like particle, however composite DM forming spatially-extended bound states is an area of increasing interest. If DM is composite, it will have new interesting phenomenology; such as that in direct detection searches, which often provide our most stringent bounds. This paper studies the signals of NDM, following [302], in the tonne-scale argon and xenon experiments coming online now, DEAP-3600 and XENON1T respectively.

The model we considered is motivated from SM nuclear physics with composite DM states consisting of asymmetrically produced DNs bound together under an analogous strong nuclear

force. The binding energy per nucleon decreases with DN number, allowing for stable states of exceedingly high DN number (up to 10^8, but can be more [302]) and thus mass. A striking feature of this model are the oscillations in the dark form factors, which we find could be seen in future direct detection searches, including realistic detector energy response, threshold, and resolution.

We find predicted limits on benchmarks cases of NDM assuming no events are seen by DEAP-3600 or XENON1T, along with those already placed by the null result from LUX. The limits on σ_0, the DN-SM nucleon scattering cross-section, are orders of magnitude below the equivalent WIMP limits, owing to a k^2 enhancement arising in the scattering rate. The projected limits on WIMP and NDM scattering cross-sections are seen to be slightly stronger in XENON1T than in DEAP-3600. The benefit of argon over xenon targets in the high mass region is partially lost here, as the lower energy threshold is higher and so DEAP-3600 is probing deeper into the dark form factor where the rate is more suppressed. However if DEAP-3600's lower energy threshold could be reduced past ~ 8 keV, then it could be more sensitive to NDM in the high mass region.

Likelihood tests were also carried out to determine how many events DEAP-3600 and XENON1T would need in order to distinguish between WIMP and NDM spectra. The number of required events for each value of k was found to be dependent on the detector energy threshold, which determines the relative contribution of the second NDM peak in the energy window, and the energy resolution, which determines the amplitude of the characteristic oscillatory features.

The lowest number of events required for $3\,\sigma$ CL distinction was 24 events in DEAP-3600 and 55 in XENON1T, which occurred when $k \sim 4000$ and ~ 8000 respectively. After this point, the required number of events oscillates with k, as the configurations of the recoil spectra in the energy window vary. These fluctuations reflected the relative difficulty in resolving the second peak in the energy window, which was the dominant distinguishing feature.

Taking the limits from LUX, the maximum number of events which could be seen were derived and found to oscillate around 20 in DEAP-3600 and 60 in XENON1T. While this is likely only enough to see $2\,\sigma$ "hints" of NDM across a small range of k values, future upgrades to both detectors will be able to distinguish to $3\,\sigma$ CL over almost the entire k range

considered. Argon based detectors like DEAP-3600 can be ideal for NDM searches, as they can have greater sensitivity at higher mass, larger periods of oscillation in the recoil spectra, and smaller energy resolutions. However if the lower energy threshold is not sufficiently small, these benefits over xenon detectors may be hindered or lost.

Epilogue

> The most exciting phrase to hear in science, the one that heralds the most discoveries, is not 'Eureka!' (I found it!) but 'That's funny...'
>
> — Isaac Asimov

Highly abundant yet remarkably elusive, dark matter is one of the longest standing questions in physics. How it emerged in the early Universe from the primordial soup is a rich and interesting topic, and was the core theme of this thesis. Four works [1–4] were described here, in which atypical dark matter genesis mechanisms played an integral role. In the first three works, discussed across Chapters 3, 4 & 5, there was an additional source of dark matter from the decays of topological defects which was discussed and detailed, or used for varied purposes. Chapter 6 covered the last work, in which the direct detection signatures of nuclear dark matter were examined; in such models, dark matter fuses into bound states during a period of aggregation in the early Universe.

Chapter 1 was an introduction to dark matter physics, first taking a look at the evidence for it from a historical perspective. The modified gravity and invisible baryonic matter hypotheses were brought into question, and the case for a new beyond the standard model particle was established. Typically dark matter is presumed to have been generated through a process called freeze-out, which was reviewed in detail thereafter, alongside other alternative dark matter genesis mechanisms. Freeze-out assumes dark matter was once in thermal equilibrium with a primordial bath, until the Universe expanded and cooled sufficiently to allow dark matter to fall out of equilibrium leaving a residual yield. Assuming dark matter to be produced through these means can heavily constrain some models of dark matter, and not be possible in others — this highlights the value of alternative production mechanisms.

Proceeding this, we took a glance at arguably the most popular dark matter candidate, the neutralino, followed by a discussion of model building with effective field theories, and simplified models. Lastly we reviewed the searches for dark matter by means of direct and indirect detection, and well as collider analyses. Work in each of these fields is progressing well with fresh results coming regularly and many further experiments already planned. There have been several possible signatures of dark matter already seen in searches, which are part of an ongoing debate. These include the DAMA/LIBRA annual modulation, and the galactic centre excess seen by Fermi-LAT, the latter was a subject of our work [3].

Given its relevance to the works presented, a summary of topological defects was provided in Chapter 2. Topological defects are structures arising at symmetry breaking phase transitions in the early Universe; they are stable configurations on the vacuum, which evolve under their own tension and can emit particle radiation. Here spontaneous symmetry breaking was reviewed, as was its place in the standard model. Following this, we examined how topological defects can form during such phase transitions, and recognised how the topology of the vacuum manifold dictated which defects (monopoles, cosmic strings, domain walls, *etc.*) could be produced. If created, domain walls would quickly come to dominant the energy of the Universe, and are therefore under heavy experimental constraints. As are monopoles, which motivate a period of inflation in order to dilute them away sufficiently. Thus cosmic strings are one of the only cosmologically acceptable forms of topological defects. It was then discussed how cosmic strings can decay into gravitational and particle radiation by forming string loops, which then shrink releasing energy in these forms. The manner of string decays is of debate, and we discussed two possible cases based on simulations of the Abelian Higgs model, and on the Nambu-Goto equations of motion.

Examining the effect of topological defect decays during freeze-out was the subject of [1], and of Chapter 3. If via defects decays particle radiation is emitted, then this can be a new source of dark matter during freeze-out. A Boltzmann equation describing dark matter freezing out with this extra source was derived, and subsequently solved numerically. This revealed behaviour that theories of dark matter could benefit from: it allowed the annihilation cross-section to be increased beyond what standard freeze-out requires, and still generate the correct relic abundance, as contributions from decaying defects could compensate for the predicted loss in dark matter.

Despite the complexity of the Boltzmann equation, following the work of others [50], simple approximate analytic solutions were found which were in excellent agreement with the numerical results. Unitarity bounds and an example experimental constraint from indirect detection were then applied to the mechanism's phase space in order to provide an initial glance into what the phenomenology of such a mechanism could entail.

This work followed a model-independent approach, choosing to focus on the mechanism itself. Following on from this, in Chapter 4 the mechanism was implemented in an example dark matter theory: the inert doublet model [2]. After reviewing this model, we saw how cosmic strings could form in this theory by simply adding an extra scalar field charged under a $\mathrm{U}(1)'$ gauge symmetry. Such symmetries are typically remnant in grand unified theories and string theories [201–204], and their spontaneous breaking is necessary for the associated gauge boson to avoid detection and will always produce cosmic strings. String formation is consequently generic, and its possible phenomenological ramifications for dark matter should be explored. In the case of the inert doublet model, this meant the cosmic strings could decay into dark matter with no further requirements needed other than that they form.

By adding an extra $\mathrm{U}(1)'$ symmetry to the inert doublet model, two new particles are introduced: the remnant scalar and the associated gauge boson. Both of these had masses of the order of the vacuum expectation value, which needed to be far greater than the electroweak scale to allow sufficient dark matter production from decaying strings. The processes relevant to the study were of or below the electroweak scale, therefore these additional degrees of freedom could be integrated out, and the effective theory left was identical to the standard inert doublet model. This required some fine-tuning, which was seen as part of a broader gauge hierarchy problem and beyond the scope of the work. With the mechanism implemented in the model, experimental constraints from dark matter and cosmic string physics were applied to the parameter space of the model; it was seen that large regions could now produce the correct relic abundance and agree with all experimental bounds, which subsequently meant lighter dark matter states were allowed.

This chapter illustrated how by allowing cosmic strings to form in a model, the previously under-producing (according to standard freeze-out) regions of parameter space could be opened up. If implemented in other models of dark matter, similar consequences could be expected. Outside of model building, this mechanism can serve further purposes, *e.g.*

resolving issues with dark matter interpretations of experimental signals. Chapter 5 did as such, by considering how issues with the γ-ray excess seen by Fermi-LAT in the vicinity of the galactic centre might be resolved by putting this genesis mechanism into effect, which was the subject of [3].

After known sources were removed, an excess of GeV scale γ-rays was seen in the galactic centre, which was shown to be consistent with dark matter annihilations. The cross-section required to produce the signal was close to the thermal value required by standard freeze-out to produce the observed abundance, however it was also in tension with Fermi-LAT limits from dwarf spheroidal galaxies. By assuming the annihilations are p-wave, this conflict between results was resolved, however the agreement with the thermal value was lost. In this chapter this agreement was then restored, by allowing decaying defects to produce dark matter.

In the case of p-wave annihilating dark matter generating the galactic centre excess, issues with direct detection and colliders limits arise as the coupling values required to produce the excess are too large. To avoid these problems, a cascade model of dark matter was considered, where the annihilations into on-shell mediators dominated, which then decay into standard model fermions. This meant the dark matter-mediator coupling could be set to generate the excess, while the mediator-standard model fermion couplings could be suppressed to avoid direct detection and collider bounds. A benefit to considering scalar mediators was that the coupling to fermions could be generated through mixing with the Higgs boson. In this situation, the mediators decayed dominantly into b-quarks, which fits best to the excess.

As with the inert doublet model, cosmic strings were added by assuming an additional $\mathrm{U}(1)'$ symmetry which was broken by a new scalar field. However in order to allow for sufficient dark matter production from these defects, an additional field was added which had an electroweak scale mass. We explored how this second scalar could be produced in string decays, and then dominantly decay itself into dark matter. Subsequently, we found the requirements on the cosmic string necessary for the correct relic abundance of dark matter to be produced. Limits on the strings were then considered, and in the case of those coming from large Higgs condensates, could cause tension with our results. However these limits were model-dependent and could easily be avoided.

Chapter 6 investigated the direct detection phenomenology of nuclear dark matter at upcoming tonne-scale detectors, DEAP-3600 and XENON1T. Nuclear dark matter is a theory

of composite dark matter modelled on standard model nuclear physics, postulating that dark matter is comprised of bounds states of strongly-interacting dark nucleons. The scatterings of these dark nuclei off standard model nuclei were described by a form factor with distinctive oscillations, which could appear within the measured recoil spectrum at detectors, offering a strong signal for nuclear dark matter. Initially the case of null results from both detectors was considered, and subsequently we found the projected limits this would put on the spin-independent scattering cross-section and compared this with the existing limits from LUX.

In the case that a signal of dark matter is seen, the number of events the detectors needed to distinguish between WIMP and nuclear dark matter hypotheses was found using likelihood tests, which for a $3\,\sigma$ CL was as low as $\mathcal{O}(10)$ in some cases. For distinction to be possible, the number of dark nucleons forming each state had to lie within a range of values, beyond which distinguishing would be very difficult, as either the period of the oscillations was too small to be resolved, or these spectral features had not yet entered into the energy window. Comparing the number of events required to distinguish with the maximum number each detector is likely to see, told us that at most DEAP-3600 and XENON1T could see $2\,\sigma$ "hints" of nuclear dark matter. However upgrades to these detectors could distinguish almost the entire nucleon number range to 3σ CL. Future work in this area would consider different nucleon number distributions; these result in recoil spectra which can be mimicked by those of a WIMP with an atypical velocity distribution, and as such requires a halo-independent analysis of multiple detectors to distinguish between them.

Dark matter is a nearly 100 year old problem, and the works described here are a few of hundreds produced every year. The range of future dark matter searches probing the electroweak scale gives one reason to hope for a signal over the coming decades, especially for one loyal to the WIMP paradigm. This however may not be the case and popular theories may be replaced by the more exotic — arguably a more interesting outcome to many. Whatever your preferred theory, dark matter remains one of the biggest scientific questions of the our time, and many eagerly await the day it finally reveals itself to us, stepping into the light (but probably not scattering off it).

Appendix A

Particle Radiation from Cosmic Strings

Section 2.4 provided a qualitative overview of string decay dynamics, here we will discuss the involved mathematical formalism which will allow us to relate q_X, to the more commonly used string tension parameter $G\mu$ (where μ is the mass per unit length).

At the time of phase transition t_c, where the symmetry is broken, the cosmic strings are formed as a 3-dimensional random walk of a characteristic step length. They are in a dense tangled formation, where the bulk length of the string network is in a single Universe-sized long string, and the rest is in the form of loops. It is convenient to introduce a characteristic length ξ describing the string configuration, which is defined as

$$\xi \equiv \sqrt{\mu/\rho_\infty}, \tag{A.1}$$

where ρ_∞ is the energy density of long strings. It can be interpreted as a combination of the average curvature radius and the average separation of long string segments.

The long strings evolve under their own tension, subject to Hubble damping and friction from the cosmic fluid [323]. Straightening out, the overall length of the strings within the Hubble volume decreases, and so ξ increases. Eventually ξ will become comparable to the length of the horizon, and the long strings enter a scaling regime, where $\xi \propto t$. In this case, the defect density parameter is constant, *i.e.*

$$\Omega_d \equiv \frac{\rho_d}{\rho_c} = \frac{8\pi G\mu}{3\xi^2 H^2}, \tag{A.2}$$

where H is the Hubble parameter.

It is possible that ξ varies differently with time, that is it does not enter the scaling regime. If ξ varies less rapidly (causality prevents it varying more rapidly), then strings will dominate the energy density of the early Universe at some point. This would lead to a more inhomogeneous Universe, which would be inconsistent with observations. Numerical and analytical studies [173, 179] show however, that strings would most likely enter the scaling regime. In order for this regime to be maintained, there must be a particular rate of energy loss; if not, then ξ will vary less rapidly and one would end up with the unacceptable inhomogeneities described above. According to numerical simulations of the theory [217, 324], $\xi H \sim 0.25$.

During the scaling period, the loop length distribution remains a topic of active debate [218, 325]. The loops are freely oscillating, and can lose energy via a variety of channels. In the original cosmic string scenario, perturbative particle production from an oscillating string loop was shown to be negligible [326, 327], and the most important source of energy loss was argued to be gravitational radiation for sufficiently large loops [328]. However, direct numerical simulations of field theories with strings showed that there was an additional non-perturbative source of particle production in the form of classical field radiation [215, 218].

In either case the loop length ℓ shrinks at a constant rate

$$\dot{\ell} = -\beta, \tag{A.3}$$

where β is a constant dependent on the mode of energy loss. There are two significant ways in which the loops may lose their energy; non-perturbative particle production [215, 218], where $\beta \sim 1$, and via gravitational radiation, where $\beta = \Gamma G\mu$ (Γ is an $\mathcal{O}(100)$ efficiency parameter [328]).

Knowing the length loss rate, the energy injection rate of the process can be found using

$$Q(t) = -\int_0^\infty \mu\dot{\ell} n(\ell, t) d\ell, \tag{A.4}$$

where $n(\ell, t)$ is the loop length distribution. In the radiation dominated era, this is given by

$$n(\ell, t) = \frac{\nu}{t^{\frac{3}{2}} \ell_i^{\frac{5}{2}}}, \tag{A.5}$$

where ν is a dimensionless $\mathcal{O}(1)$ parameter, and ℓ_i is the average loop size at formation (t_i) [173, 179, 325].

The loop length shrinking rate is dependent on the (FT or CE) scenario under consideration, we will look at both in turn.

A.1 FT Scenario

Here non-perturbative particle radiation is the dominant source of loop energy loss, and we can relate q_X to other string parameters by first considering energy conservation, which tells us the energy injection rate

$$Q = 3(\omega - \omega_{\rm d})\Omega_{\rm d}\rho_{\rm c}H, \tag{A.6}$$

where ω ($\omega_{\rm d}$) is the total (string's) average equation of state parameter ($\omega_{\rm d} \gtrsim -1/3$ [173]). Using (A.6) and the definition of q_X (3.6), one finds

$$q_X = \frac{8\pi G\mu f_X}{\xi^2 H^2}(\omega - \omega_{\rm d}). \tag{A.7}$$

We now have a relationship between q_X and $G\mu$ in the FT scenario, which is linear and for our purposes is best represented in the form

$$q_X \simeq \frac{256\pi}{3} G\mu P_{\rm FT}, \tag{A.8}$$

where

$$P_{\rm FT} \equiv f_X \left(\frac{1-3\omega_{\rm d}}{2}\right)\left(\frac{0.25}{\xi H}\right)^2, \tag{A.9}$$

which is an $\mathcal{O}(1)$ parameter.

In this scenario, the loop length reduction rate is given by (A.3), and so $\ell_i = \ell + \beta t$. This means, according to (A.4), that $Q(t) \propto 1/t^3$. Comparing this with the general form expression for $Q(t)$ (3.1), we see that $p = 1$ in this case. Its value was defined as such in the FT scenario earlier, pre-empting this result.

A.2 CE Scenario

When the cosmic strings may be described by the Nambu-Goto equations of motion, loops lose most of their energy through gravitational radiation, but there is also particle emission via the collapse of cusps. This can happen in two ways: strings double back on themselves

and annihilate [329, 330], or they are a classical source of massive scalar radiation, strongly beamed from the cusps [206, 331]. In both cases, the length decreases as

$$\dot{\ell} = -\beta_{\rm CE}\frac{1}{\sqrt{m_X \ell}}, \tag{A.10}$$

where $\beta_{\rm CE}$ is a constant containing numerical factors and couplings [206, 330].

Loops must be smaller than $\ell_{\rm CE} = (\beta_{\rm CE}/\beta)^2 m_X^{-1}$ in order for cusp annihilations to significantly contribute to the energy loss. The mean length of a loop at the time it is created is given by $\ell \sim \Gamma G\mu t$, *i.e.* longer loops are created at later times, which one would expect from a system of dense strings, unravelling and straightening out. Therefore, combining these results, it is not until around

$$t_{\rm CE} = \frac{\beta_{\rm CE}^2}{(\Gamma G\mu)^3 m_X} \simeq 6.6\times 10^{-13}\beta_{\rm CE}^2 \left(\frac{100}{\Gamma}\right)^3 \left(\frac{10^{-7}}{G\mu}\right)^3 \left(\frac{\rm TeV}{m_X}\right)\ {\rm s}, \tag{A.11}$$

when loops of size $\ell_{\rm CE}$ are formed and cusp emissions become less important. This occurs during the radiation-dominated era of the early Universe, thus happens when the Universe's temperature drops to

$$\begin{aligned} T_{\rm CE} &= \left(\frac{45}{16\pi^3 g_*}\right)^{1/4} \frac{\sqrt{M_{\rm Pl} m_X}}{\beta_{\rm CE}} (\Gamma G\mu)^{3/2} \\ &\simeq 600 \frac{1}{\beta_{\rm CE}} \left(\frac{100}{g_*}\right)^{1/4} \left(\frac{\Gamma}{100}\right)^{3/2} \left(\frac{G\mu}{10^{-7}}\right)^{3/2} \left(\frac{m_X}{\rm TeV}\right)^{1/2}\ {\rm GeV}. \end{aligned} \tag{A.12}$$

Given the loop reduction rate from cusp emissions (A.10), the energy injection rate $Q(t)$ according to (A.4) in this scenario is

$$Q(t) = \int_0^\infty d\ell \frac{\mu\beta_{\rm CE}}{\sqrt{m_X\ell}} n(\ell, t). \tag{A.13}$$

In late times ($t \gg t_{\rm CE}$), where large loops dominate, the length contracts according to (A.3) and therefore $\ell_i \simeq \ell + \beta t$. However in early times ($t \ll t_{\rm CE}$) with small loops dominating, they contract as described by (A.10), and so

$$\ell_i = \ell_{\rm CE}\left[\left(\frac{\ell}{\ell_{\rm CE}}\right)^{3/2} + \frac{3t}{2t_{\rm CE}}\right]^{2/3}. \tag{A.14}$$

The energy injection rate depends on which of these regimes we are in, using the above results and (A.4), one may write $Q(t)$ in the form

$$Q(t) = \frac{\nu\beta_{\rm CE}}{\beta^{1/2}} \frac{\mu}{t^3} C\left(\frac{t}{t_{\rm CE}}\right), \tag{A.15}$$

where

$$C(\tau) \simeq \begin{cases} 1.0\,\tau^{1/6} & \text{for } \tau \ll 1 \\ \frac{4}{3}\tau^{-1/2} & \text{for } \tau \gg 1 \end{cases}. \tag{A.16}$$

Comparing this expression to the general form (3.1), one can see that $p = 7/6$ when $\tau \equiv \frac{t}{t_{\rm CE}} \ll 1$, and $p = 1/2$ when $\tau \gg 1$.

Converting (A.15) into expression for q_X, one obtains

$$q_X = \left.\frac{Q(t) f_X}{\rho H}\right|_{T_\chi} = \frac{64\pi}{3}\nu\beta_{\rm CE} f_X \sqrt{\frac{G\mu}{\Gamma}} C(\tau_\chi). \tag{A.17}$$

where given (A.12)

$$\begin{aligned} \tau_\chi \equiv \frac{t_\chi}{t_{\rm CE}} &= \left(\frac{45}{16\pi^3 g_*}\right)^{1/2} \frac{M_{\rm Pl} m_X}{\beta_{\rm CE}^2 T_\chi^2} (\Gamma G\mu)^3 \\ &\simeq 1.5 \frac{1}{\beta_{\rm CE}^2} \left(\frac{100}{g_*}\right)^{1/2} \left(\frac{\Gamma}{100}\right)^3 \left(\frac{G\mu}{10^{-7}}\right)^3 \left(\frac{m_X}{\rm TeV}\right) \left(\frac{500\ \text{GeV}}{T_\chi}\right)^2. \end{aligned} \tag{A.18}$$

Hence

$$q_X \simeq \begin{cases} 2.3\times 10^{-3} \left(\nu\beta_{\rm CE}^{2/3} f_X\right) \left(\frac{100}{g_*}\right)^{1/12} \left(\frac{G\mu}{10^{-7}}\right) \left(\frac{m_X}{\rm TeV}\right)^{1/6} \left(\frac{500\ \text{GeV}}{T_\chi}\right)^{1/3} & \text{for } G\mu \ll 10^{-7} D_\chi \\ 2.3\times 10^{-3} \left(\nu\beta_{\rm CE}^2 f_X\right) \left(\frac{100}{\Gamma}\right)^2 \left(\frac{g_*}{100}\right)^{1/4} \left(\frac{10^{-7}}{G\mu}\right) \left(\frac{\rm TeV}{m_X}\right)^{1/2} \left(\frac{T_\chi}{500\ \text{GeV}}\right) & \text{for } G\mu \gg 10^{-7} D_\chi \end{cases}, \tag{A.19}$$

where by fixing the other parameters to their reference values, the value of $G\mu$ determines the boundary between the regimes. The parameter D_χ, in the conditions is given by

$$D_\chi \simeq 0.88\,\beta_{\rm CE}^{2/3} \left(\frac{g_*}{100}\right)^{1/6} \left(\frac{100}{\Gamma}\right) \left(\frac{\rm TeV}{m_X}\right)^{1/6} \left(\frac{T_\chi}{500\ \text{GeV}}\right)^{2/3}. \tag{A.20}$$

CMB data [195] limits $G\mu \lesssim 10^{-7}$ and so we are interested in the $G\mu \ll 10^{-7} D_\chi$ regime where $p = 7/6$, which justifies choosing the p value to be as such in the CE scenario. Assuming this solution, q_X may be rewritten in the more convenient form

$$q_X \simeq 2.3\times 10^4\, G\mu P_{\rm CE}, \tag{A.21}$$

where $P_{\rm CE}$ is an $\mathcal{O}(1)$ parameter defined as

$$P_{\rm CE} = \nu\beta_{\rm CE}^{2/3} f_X \left(\frac{100}{g_*}\right)^{1/12} \left(\frac{m_X}{\rm TeV}\right)^{1/6} \left(\frac{500\ \text{GeV}}{T_\chi}\right)^{1/3}. \tag{A.22}$$

Using this and (A.8), one can now relate q_X to $G\mu$ in both the FT and CE scenarios.

Appendix B

Pure Gauge Limit

In Section 4.3, we saw how the relic abundance predicted in the IDM increased when the mass splitting Δm^2 was taken to small values in the high mass limit $m_{H^0} > 100$ GeV. This suggested that despite co-annihilation channels opening up in this limit, there was a decrease in the cross-section which was the over-riding effect.

This effect is perhaps most intuitively explained by recalling that the masses of H^0, A^0, and $H^\pm$ dictate the values of the coupling constants. By inspecting (4.4) and (4.5), one sees that both λ_4 and λ_5 will tend to zero in the limit that $\Delta m^2 \to 0$. Similarly, since $\lambda_3 = 2\lambda_L - \lambda_4 - \lambda_5$, taking this limit also decreases λ_3, which will go to zero if $\lambda_L = 0$ as well.

The pure gauge limit is when both λ_L and Δm^2 are zero, which means λ_3, λ_4, and λ_5 all vanish. In this case, all couplings between the inert and SM Higgs doublets in the potential (4.1) are zero, and only DM annihilations into gauge bosons are permitted at tree level. We may examine the consequences of this in more detail by considering the contributing diagrams.

In the high mass region, the dominant contribution to the annihilation cross-section is from W and Z final states. The diagrams for these processes are seen in Figure B.1. The matrix elements of these diagrams are [332]

$$\begin{gathered} i\mathcal{M}_p = i\frac{g_V^2}{2} g^{\mu\nu}\epsilon_\mu^*(p_3)\epsilon_\nu^*(p_4), \qquad i\mathcal{M}_s = i\frac{\lambda_L v^2 g_V^2}{s - m_h^2} g^{\mu\nu}\epsilon_\mu^*(p_3)\epsilon_\nu^*(p_4), \\ i\mathcal{M}_t = i\frac{g_V^2\, p_1^\mu p_2^\nu}{t - \Delta m^2 - m_{H^0}^2}\epsilon_\mu^*(p_3)\epsilon_\nu^*(p_4), \quad \text{and} \quad i\mathcal{M}_u = i\,\frac{g_V^2\, p_2^\mu\, p_1^\nu}{u - \Delta m^2 - m_{H^0}^2}\epsilon_\mu^*(p_3)\epsilon_\nu^*(p_4), \end{gathered} \tag{B.1}$$

where the subscripts indicate whether it represents the s-,t-, or u-channel, or the four point

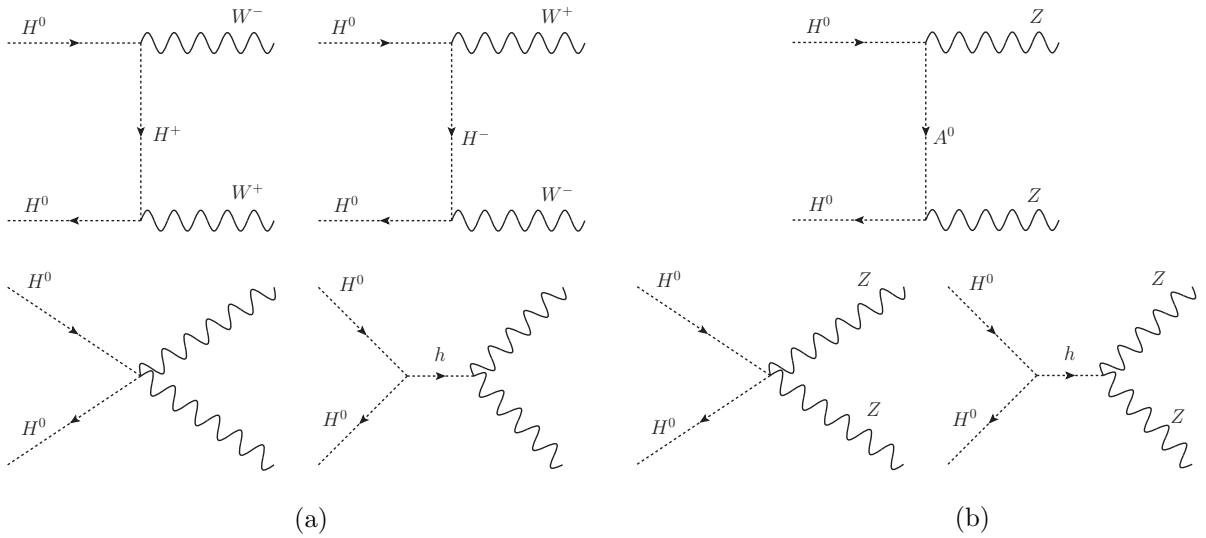

Figure B.1: Feynman diagrams for $H^0H^0 \to W^+W^-$ (a) and $H^0H^0 \to ZZ$ (b) processes which dominate the annihilation cross-section in the early Universe in the high mass region $m_{H^0} > 100$ GeV.

diagram, referred to as the "p"-channel. Here $g_V = g$ or $(g/\cos(\theta_W))$, depending on whether the annihilation is into W's or Z's, respectively.

In the pure gauge limit $\lambda_L = 0$, and given (B.1), the s-channel contribution must disappear. Considering just the dominant s-wave contribution, which is found by taking the zero relative velocity limit, *i.e.* $s = 4m_{H^0}^2$ and $t = u = m_V^2 - m_{H^0}^2$, the total squared amplitude can be found to be

$$\begin{aligned} |\mathcal{M}|^2 = g_V^4 \Bigg[& \frac{1}{\left(1+\frac{y}{2}-\frac{x}{2}\right)^2}\left(1-\frac{2}{x}+\frac{1}{x^2}\right) \\ & -\frac{1}{\left(1+\frac{y}{2}-\frac{x}{2}\right)}\left(1-\frac{3}{x}+\frac{2}{x^2}\right)+\frac{3}{4}-\frac{1}{x}+\frac{1}{x^2}\Bigg], \end{aligned} \tag{B.2}$$

where

$$x \equiv m_W^2/m_{H^0}^2 \qquad \text{and} \qquad y \equiv \Delta m^2/m_{H^0}^2. \tag{B.3}$$

In the high mass region (where $x \to 0$), and in the pure gauge limit (where $y \to 0$), the squared matrix element

$$|\mathcal{M}|^2 \to \frac{g_V^4}{2}. \tag{B.4}$$

Moving outside the pure gauge limit, in the regime $m_{H^0}^2 \gg \Delta m^2 > m_W$, one finds

$$|\mathcal{M}|^2 = g_V^4 \left[\frac{(\Delta m^2)^2}{4\, m_W^4} + \frac{1}{2} + \mathcal{O}(x,y)\right], \tag{B.5}$$

which is greater than (B.4). Thus when we move away from the pure gauge limit, the cross-section increases, and the relic density drops. This is a result of a cancellation between the point-like, and the t- and u-channels, which is related to gauge invariance.

This cancellation suppresses the contribution of the longitudinal mode final states ($H^0 H^0 \to V_L V_L$), as the longitudinal parts of the gauge bosons are contained in the Goldstones of the SM Higgs, which the inert doublet is decoupled from in this limit. Moving away from this limit, the longitudinal contribution is restored and the annihilation cross-section increases significantly enough to counteract the suppression of co-annihilations.

Appendix C

Cascade Annihilation Model: Higgs Mixing

In Chapter 5 a cascade annihilation model of DM is used to produce the GCE, where $\bar{b}b$ final states are assumed to dominate. The model is described by (5.11), which also permits portal couplings between the mediator, ϕ, and the SM Higgs boson, h (5.13). Through these couplings, a ϕ-h mixing arises, which allows the mediator to decay dominantly into $\bar{b}b$. However, if the mixing is too large, direct detection and collider limits could come in, and if it is too low, the mediator could be so long-lived as to interfere with BBN. Therefore these upper and lower limits on the mixing, $\sin\theta$, should be established in order to see if a viable range of values is permitted.

First, the λ_χ value required to produce the excess must be determined, which can be used to derive limits on $\sin\theta$. These are found using the best fit values in (5.19) and (5.18) from the χ^2 analysis of our toy model, and the expression for the cross-section expanded in terms of the relative velocity v, which is

$$\sigma v(\bar{\chi}\chi \to \phi\phi) = \frac{\lambda_\chi^4 v^2}{24\pi} \frac{m_\chi \sqrt{m_\chi^2 - m_\phi^2}}{\left(2m_\chi^2 - m_\phi^2\right)^2} \left(2 + \frac{m_\chi^4}{(2m_\chi^2 - m_\phi^2)^2}\right) + \mathcal{O}(v^4). \tag{C.1}$$

Using these we find $\lambda_\chi = 4.1$ and 5.1 for $m_\chi = 15$ and 40 GeV respectively.

Let us first examine bounds from direct detection searches, where two t-channel diagrams determine the scattering rate (at tree level), one in which h is exchanged and the other ϕ. The matrix elements of both diagrams are proportional to $|\lambda_\chi y_f \sin\theta|$, however there is a

relative minus sign between them. LUX currently provides the strongest limits [96] on the spin-independent DM-WIMP scattering cross-section, however the bounds presented assume the DM halo is described by the SHM. As we are not using the SHM, LUX's limits will need to be adapted for consistency. In [333], such an adjustment is considered, and limits using a generalised NFW profile are presented. As our DM profile parameter choices closely match their fitted values, these results shall be used. These can be related to $\sin\theta$ via the expression for the spin-independent DM-nucleon scattering cross-section (given in [151]) is

$$\sigma^{\mathrm{SI}}_{\chi\text{-}N} = \frac{\mu^2_{\chi\text{-}N} m_N^2}{\pi} \frac{\lambda_\chi^2 \sin^2\theta}{v^2} \left(\frac{1}{m_\phi^2} - \frac{1}{m_h^2} \right)^2 f_N^2 \tag{C.2}$$

where m_N is the nucleon mass, $\mu_{\chi\text{-}N}$ is the reduced mass of the DM-nucleon system, and f_N is the effective DM-nucleon coupling given in (1.44).

There are numerous collider bounds that could be studied, we will focus on monojet searches, direct searches for mediators, and invisible Higgs decays, which are amongst most promising channels. Through the first, DM may be detected as missing energy in events where $pp \to \bar{\chi}\chi +$ jet which may occur via a ϕ or h radiating off a fermion, although due to the mass difference the ϕ mediated diagram will dominate. Given the enhanced couplings to heavier quarks, missing energy searches with the mediator coupling to bottom and top quarks are ideal to probe our model. Such a study was carried out in [334], where an effective operator approach was used in the case of hierarchical couplings. Expected limits from ATLAS using $\sqrt{s} = 8$ TeV data are presented, which we will use here. While it has been shown that an effective field theory approach for LHC dark matter searches may not always be appropriate [335], the limits provided here will be more conservative than in a UV complete model, which is suits our purposes.

Given the mediator is light in our model, one can also search for it directly via searches for Higgs-like scalars. Such searches were explored extensively in [336, 337], which looked at various ATLAS, CMS, LEP, and DELPHI searches.

The last collider bounds we shall consider are those from the invisible decays of the SM Higgs, which can be into either DM or the mediators. However analyses of the latter will not allow us set rigid bounds on the mixing angle, as the process depends on the portal coupling λ_H, which is a free parameter. Assuming the invisible Higgs decays are then entirely into DM, we obtain limits from an analysis of similar simplified models [248].

Thus far several upper limits on the mixing angle have been discussed, however there is a lower limit from BBN to consider. If the mediator was long-lived enough, it could decay during BBN and interfere with the SM nuclear processes which already accurately predict the light element abundances; this could occur if ϕ's lifetime is larger than $t \gtrsim 0.1$ s [262]. The $h \to \bar{\chi}\chi$ decay rate, taken from [277], is

$$\Gamma(h \to \bar{\chi}\chi) = \sum_f N_c \frac{y_f^2 \sin^2\theta g_v^2 m_\phi}{16\pi} \left(1 - \frac{4m_f^2}{m_\phi^2}\right)^{3/2}, \tag{C.3}$$

which can be used to find the BBN limit on the mixing angle.

A long-lived mediator could also effect the morphology of the GCE, however this lower limit on $\sin\theta$ will be far weaker than that of BBN, due to the vast astronomical scales considered.

Table C.1 presents the upper and lower limits from all the sources discussed above: direct detection, monojet searches, direct searches for ϕ, invisible Higgs decays, and BBN. We can see that the lower limits from BBN are at least six orders of magnitude below the strongest upper limits (coming from direct detection). This means ϕ-h mixing is permitted, and thus we have a natural explanation for dominant $\phi \to \bar{b}b$ decays.

	$m_\phi = 15$ GeV	$m_\phi = 40$ GeV
Direct Detection	$\lesssim 0.0002$	$\lesssim 0.001$
Monojet	$\lesssim 0.01$	$\lesssim 0.08$
Direct ϕ searches	$\lesssim 0.015$	$\lesssim 0.02$
Inv. Higgs decays	$\lesssim 0.006$	$\lesssim 0.03$
BBN	$\gtrsim 1 \times 10^{-10}$	$\gtrsim 7 \times 10^{-11}$

Table C.1: Limits on $\sin\theta$, the mixing between the mediator ϕ, and the SM Higgs boson h. These take $\lambda_\chi = 4.1$ and 5.1 for $m_\chi = 15$ and 40 GeV respectively, provided by fits to the GCE. Bounds from direct detection, monojet searches, direct searches for ϕ, invisible Higgs decays, and BBN are listed. See the text for a discussion of these limits and references there within.

Bibliography

[1] M. Hindmarsh, R. Kirk, and S. M. West, "Dark Matter from Decaying Topological Defects," *JCAP* **1403** (2014) 037, 1311.1637.

[2] M. Hindmarsh, R. Kirk, J. M. No, and S. M. West, "Dark Matter with Topological Defects in the Inert Doublet Model," 1412.4821.

[3] R. Kirk and S. West, "Relieving Tensions on Dark Matter Interpretations of the Galactic Centre Excess using Topological Defects," *Work in Progress*.

[4] A. Butcher, R. Kirk, J. Monroe, and S. West, "Can Tonne-Scale Direct Detection Experiments Discover Nuclear Dark Matter?," *Work in Progress*.

[5] E. Opik *Bull. de la Soc. Astr. de Russie* **21** (1915) 150.

[6] J. Kapteyn, "First Attempt at a Theory of the Arrangement and Motion of the Sidereal System," *Astrophys.J.* **55** (1922) 302–328.

[7] J. H. Jeans, "The motions of stars in a Kapteyn universe," *Mon. Not. R. Astron. Soc.* **82** (Jan., 1922) 122–132.

[8] J. H. Oort, "The force exerted by the stellar system in the direction perpendicular to the galactic plane and some related problems," *Bull. Astron. Inst. Neth.* **6** (Aug., 1932) 249.

[9] F. Zwicky, "Die Rotverschiebung von extragalaktischen Nebeln," *Helv.Phys.Acta* **6** (1933) 110–127.

[10] V. C. Rubin and J. Ford, W. Kent, "Rotation of the Andromeda Nebula from a Spectroscopic Survey of Emission Regions," *Astrophys.J.* **159** (1970) 379–403.

[11] H. W. Babcock, "The rotation of the Andromeda Nebula," *Lick Observatory Bulletin* **19** (1939) 41–51.

[12] K. Begeman, A. Broeils, and R. Sanders, "Extended rotation curves of spiral galaxies: Dark haloes and modified dynamics," *Mon.Not.Roy.Astron.Soc.* **249** (1991) 523.

[13] **Troitsk** Collaboration, V. N. Aseev *et. al.*, "An upper limit on electron antineutrino mass from Troitsk experiment," *Phys. Rev.* **D84** (2011) 112003, 1108.5034.

[14] **ALEPH** Collaboration, R. Barate *et. al.*, "An Upper limit on the tau-neutrino mass from three-prong and five-prong tau decays," *Eur. Phys. J.* **C2** (1998) 395–406.

[15] K. Assamagan *et. al.*, "Upper limit of the muon-neutrino mass and charged pion mass from momentum analysis of a surface muon beam," *Phys. Rev.* **D53** (1996) 6065–6077.

[16] F. Capozzi, E. Lisi, A. Marrone, D. Montanino, and A. Palazzo, "Neutrino masses and mixings: Status of known and unknown 3ν parameters," *Nucl. Phys.* **B908** (2016) 218–234, 1601.07777.

[17] **Planck** Collaboration, P. A. R. Ade *et. al.*, "Planck 2015 results. XIII. Cosmological parameters," 1502.01589.

[18] **SLD Electroweak Group, DELPHI, ALEPH, SLD, SLD Heavy Flavour Group, OPAL, LEP Electroweak Working Group, L3** Collaboration, S. Schael *et. al.*, "Precision electroweak measurements on the Z resonance," *Phys. Rept.* **427** (2006) 257–454, hep-ex/0509008.

[19] B. W. Lee and S. Weinberg, "Cosmological Lower Bound on Heavy Neutrino Masses," *Phys.Rev.Lett.* **39** (1977) 165–168.

[20] M. Milgrom, "A Modification of the Newtonian dynamics as a possible alternative to the hidden mass hypothesis," *Astrophys. J.* **270** (1983) 365–370.

[21] B. Famaey and S. McGaugh, "Modified Newtonian Dynamics (MOND): Observational Phenomenology and Relativistic Extensions," *Living Rev. Rel.* **15** (2012) 10, 1112.3960.

[22] W. J. G. de Blok and S. S. McGaugh, "Testing modified Newtonian dynamics with low surface brightness galaxies: Rotation curve fits," *Astrophys. J.* **508** (1998) 132, astro-ph/9805120.

[23] J. Einasto, "Dark Matter," in *Astronomy and Astrophysics 2010, [Eds. Oddbjorn Engvold, Rolf Stabell, Bozena Czerny, John Lattanzio], in Encyclopedia of Life Support Systems (EOLSS), Developed under the Auspices of the UNESCO, Eolss Publishers, Oxford ,UK.* 2009. 0901.0632.

[24] S. van den Bergh, "The Early history of dark matter," *Publ.Astron.Soc.Pac.* **111** (1999) 657, astro-ph/9904251.

[25] A. Einstein, "The Foundation of the General Theory of Relativity," *Annalen Phys.* **49** (1916) 769–822.

[26] F. W. Dyson, A. S. Eddington, and C. Davidson, "A Determination of the Deflection of Light by the Sun's Gravitational Field, from Observations Made at the Total Eclipse of May 29, 1919," *Royal Society of London Philosophical Transactions Series A* **220** (1920) 291–333.

[27] **SDSS** Collaboration, K. N. Abazajian *et. al.*, "The Seventh Data Release of the Sloan Digital Sky Survey," *Astrophys. J. Suppl.* **182** (2009) 543–558, 0812.0649.

[28] B. Paczynski, "Gravitational microlensing by the galactic halo," *Astrophys. J.* **304** (1986) 1–5.

[29] **MACHO** Collaboration, C. Alcock *et. al.*, "The MACHO project: Microlensing results from 5.7 years of LMC observations," *Astrophys.J.* **542** (2000) 281–307, astro-ph/0001272.

[30] D. Clowe, M. Bradac, A. H. Gonzalez, M. Markevitch, S. W. Randall, *et. al.*, "A direct empirical proof of the existence of dark matter," *Astrophys.J.* **648** (2006) L109–L113, astro-ph/0608407.

[31] M. Bradac, S. W. Allen, T. Treu, H. Ebeling, R. Massey, *et. al.*, "Revealing the properties of dark matter in the merging cluster MACSJ0025.4-1222," *Astrophys.J.* **687** (2008) 959, 0806.2320.

[32] M. J. Jee, H. Ford, G. Illingworth, R. White, T. Broadhurst, *et. al.*, "Discovery of a Ringlike Dark Matter Structure in the Core of the Galaxy Cluster Cl 0024+17," *Astrophys.J.* **661** (2007) 728–749, 0705.2171.

[33] A. A. Penzias and R. W. Wilson, "A Measurement of excess antenna temperature at 4080-Mc/s," *Astrophys.J.* **142** (1965) 419–421.

[34] A. G. Lemaître, "Contributions to a British Association Discussion on the Evolution of the Universe.," *Nature* **128** (Oct., 1931) 704–706.

[35] A. H. Guth, "The Inflationary Universe: A Possible Solution to the Horizon and Flatness Problems," *Phys. Rev.* **D23** (1981) 347–356.

[36] K. Sato, "First Order Phase Transition of a Vacuum and Expansion of the Universe," *Mon. Not. Roy. Astron. Soc.* **195** (1981) 467–479.

[37] A. D. Linde, "A New Inflationary Universe Scenario: A Possible Solution of the Horizon, Flatness, Homogeneity, Isotropy and Primordial Monopole Problems," *Phys. Lett.* **B108** (1982) 389–393.

[38] A. Albrecht and P. J. Steinhardt, "Cosmology for Grand Unified Theories with Radiatively Induced Symmetry Breaking," *Phys. Rev. Lett.* **48** (1982) 1220–1223.

[39] A. D. Linde, "Chaotic Inflation," *Phys. Lett.* **B129** (1983) 177–181.

[40] G. F. Smoot, C. Bennett, A. Kogut, E. Wright, J. Aymon, *et. al.*, "Structure in the COBE differential microwave radiometer first year maps," *Astrophys.J.* **396** (1992) L1–L5.

[41] **Planck** Collaboration, R. Adam *et. al.*, "Planck 2015 results. I. Overview of products and scientific results," 1502.01582.

[42] J. R. Bond, G. Efstathiou, and J. Silk, "Massive Neutrinos and the Large Scale Structure of the Universe," *Phys. Rev. Lett.* **45** (1980) 1980–1984.

[43] C. S. Frenk, S. D. White, and M. Davis, "Nonlinear evolution of large-scale structure in the universe," *Astrophys.J.* **271** (1983) 417.

[44] J. R. Bond and A. S. Szalay, "The Collisionless Damping of Density Fluctuations in an Expanding Universe," *Astrophys. J.* **274** (1983) 443–468.

[45] G. Bertone, D. Hooper, and J. Silk, "Particle dark matter: Evidence, candidates and constraints," *Phys.Rept.* **405** (2005) 279–390, `hep-ph/0404175`.

[46] A. V. Maccio, B. Moore, J. Stadel, and J. Diemand, "Radial distribution and strong lensing statistics of satellite galaxies and substructure using high resolution lambda-CDM hydrodynamical simulations," *Mon. Not. Roy. Astron. Soc.* **366** (2006) 1529–1538, `astro-ph/0506125`.

[47] M. Boylan-Kolchin, J. S. Bullock, and M. Kaplinghat, "The Milky Way's bright satellites as an apparent failure of LCDM," *Mon. Not. Roy. Astron. Soc.* **422** (2012) 1203–1218, `1111.2048`.

[48] I. Ferrero, M. G. Abadi, J. F. Navarro, L. V. Sales, and S. Gurovich, "The dark matter halos of dwarf galaxies: a challenge for the LCDM paradigm?," *Mon. Not. Roy. Astron. Soc.* **425** (2012) 2817–2823, `1111.6609`.

[49] D. H. Weinberg, J. S. Bullock, F. Governato, R. Kuzio de Naray, and A. H. G. Peter, "Cold dark matter: controversies on small scales," in *Sackler Colloquium: Dark Matter Universe: On the Threshhold of Discovery Irvine, USA, October 18-20, 2012.* 2013. `1306.0913`.

[50] E. Kolb and M. Turner, *The Early Universe.* Westview Press, 1994.

[51] M. Roos, "Dark Matter: The evidence from astronomy, astrophysics and cosmology," `1001.0316`.

[52] K. Freese, "Review of Observational Evidence for Dark Matter in the Universe and in upcoming searches for Dark Stars," *EAS Publ. Ser.* **36** (2009) 113–126, `0812.4005`.

[53] Y. B. Zel'dovich *Zh. Eksp. Teor. Fiz* **48** (1965) 986.

[54] Y. B. Zel'dovich, L. B. Okun, and P. S. B. *Usp. Fiz. Nauk* **84** (1965) 113.

[55] H. Y. Chiu *Phys. Rev. Lett.* **17** (1966) 712.

[56] J. L. Feng and J. Kumar, "The WIMPless Miracle: Dark-Matter Particles without Weak-Scale Masses or Weak Interactions," *Phys.Rev.Lett.* **101** (2008) 231301, 0803.4196.

[57] K. Griest and D. Seckel, "Three exceptions in the calculation of relic abundances," *Phys.Rev.* **D43** (1991) 3191–3203.

[58] P. Gondolo and J. Edsjo, "Neutralino relic density including coannihilations," *Phys. Atom. Nucl.* **61** (1998) 1081–1097. [Yad. Fiz.61,1181(1998)].

[59] A. Sommerfeld, "The dark matter halos of dwarf galaxies: a challenge for the LCDM paradigm?," *Annalen Phys.* **403** (1931) 257.

[60] J. L. Feng, M. Kaplinghat, and H.-B. Yu, "Sommerfeld Enhancements for Thermal Relic Dark Matter," *Phys. Rev.* **D82** (2010) 083525, 1005.4678.

[61] Z.-P. Liu, Y.-L. Wu, and Y.-F. Zhou, "Sommerfeld enhancements with vector, scalar and pseudoscalar force-carriers," *Phys. Rev.* **D88** (2013) 096008, 1305.5438.

[62] L. Canetti, M. Drewes, and M. Shaposhnikov, "Matter and Antimatter in the Universe," *New J. Phys.* **14** (2012) 095012, 1204.4186.

[63] J. M. Cline, "Baryogenesis," in *Les Houches Summer School - Session 86: Particle Physics and Cosmology: The Fabric of Spacetime Les Houches, France, July 31-August 25, 2006*. 2006. hep-ph/0609145.

[64] M. Trodden, "Electroweak baryogenesis," *Rev. Mod. Phys.* **71** (1999) 1463–1500, hep-ph/9803479.

[65] A. Strumia, "Baryogenesis via leptogenesis," in *Particle physics beyond the standard model. Proceedings, Summer School on Theoretical Physics, 84th Session, Les Houches, France, August 1-26, 2005*, pp. 655–680. 2006. hep-ph/0608347.

[66] H. Iminniyaz, M. Drees, and X. Chen, "Relic Abundance of Asymmetric Dark Matter," *JCAP* **1107** (2011) 003, 1104.5548.

[67] M. T. Frandsen, S. Sarkar, and K. Schmidt-Hoberg, "Light asymmetric dark matter from new strong dynamics," *Phys. Rev.* **D84** (2011) 051703, 1103.4350.

[68] A. Falkowski, J. T. Ruderman, and T. Volansky, "Asymmetric Dark Matter from Leptogenesis," *JHEP* **05** (2011) 106, 1101.4936.

[69] L. J. Hall, J. March-Russell, and S. M. West, "A Unified Theory of Matter Genesis: Asymmetric Freeze-In," 1010.0245.

[70] L. J. Hall, K. Jedamzik, J. March-Russell, and S. M. West, "Freeze-In Production of FIMP Dark Matter," *JHEP* **03** (2010) 080, 0911.1120.

[71] S. Dodelson and L. M. Widrow, "Sterile-neutrinos as dark matter," *Phys.Rev.Lett.* **72** (1994) 17–20, hep-ph/9303287.

[72] F. D. Steffen, "Dark Matter Candidates - Axions, Neutralinos, Gravitinos, and Axinos," *Eur. Phys. J.* **C59** (2009) 557–588, 0811.3347.

[73] A. De Rujula, S. L. Glashow, and U. Sarid, "CHARGED DARK MATTER," *Nucl. Phys.* **B333** (1990) 173–194.

[74] S. D. McDermott, H.-B. Yu, and K. M. Zurek, "Turning off the Lights: How Dark is Dark Matter?," *Phys. Rev.* **D83** (2011) 063509, 1011.2907.

[75] P. Bode, J. P. Ostriker, and N. Turok, "Halo formation in warm dark matter models," *Astrophys. J.* **556** (2001) 93–107, astro-ph/0010389.

[76] J. R. Primack, "Cosmology: small scale issues revisited," *New J. Phys.* **11** (2009) 105029, 0909.2247.

[77] M. Taoso, G. Bertone, and A. Masiero, "Dark Matter Candidates: A Ten-Point Test," *JCAP* **0803** (2008) 022, 0711.4996.

[78] H. Baer, K.-Y. Choi, J. E. Kim, and L. Roszkowski, "Dark matter production in the early Universe: beyond the thermal WIMP paradigm," *Phys. Rept.* **555** (2015) 1–60, 1407.0017.

[79] S. P. Martin, "A Supersymmetry primer," hep-ph/9709356. Adv. Ser. Direct. High Energy Phys.18,1(1998).

[80] E. Fermi, "An attempt of a theory of beta radiation. 1.," *Z.Phys.* **88** (1934) 161–177.

[81] R. Peccei, "The Strong CP problem and axions," *Lect.Notes Phys.* **741** (2008) 3–17, hep-ph/0607268.

[82] L. D. Duffy and K. van Bibber, "Axions as Dark Matter Particles," *New J.Phys.* **11** (2009) 105008, 0904.3346.

[83] L. Visinelli and P. Gondolo, "Dark Matter Axions Revisited," *Phys.Rev.* **D80** (2009) 035024, 0903.4377.

[84] R. Adhikari *et. al.*, "A White Paper on keV Sterile Neutrino Dark Matter," *Submitted to: White paper* (2016) 1602.04816.

[85] H. P. Nilles, "Supersymmetry, Supergravity and Particle Physics," *Phys. Rept.* **110** (1984) 1–162.

[86] H.-C. Cheng, J. L. Feng, and K. T. Matchev, "Kaluza-Klein dark matter," *Phys. Rev. Lett.* **89** (2002) 211301, hep-ph/0207125.

[87] T. Piffl *et. al.*, "The RAVE survey: the Galactic escape speed and the mass of the Milky Way," *Astron. Astrophys.* **562** (2014) A91, 1309.4293.

[88] C. McCabe, "The Astrophysical Uncertainties Of Dark Matter Direct Detection Experiments," *Phys.Rev.* **D82** (2010) 023530, 1005.0579.

[89] M. Vogelsberger, A. Helmi, V. Springel, S. D. M. White, J. Wang, C. S. Frenk, A. Jenkins, A. D. Ludlow, and J. F. Navarro, "Phase-space structure in the local dark matter distribution and its signature in direct detection experiments," *Mon. Not. Roy. Astron. Soc.* **395** (2009) 797–811, 0812.0362.

[90] M. Kuhlen, N. Weiner, J. Diemand, P. Madau, B. Moore, D. Potter, J. Stadel, and M. Zemp, "Dark Matter Direct Detection with Non-Maxwellian Velocity Structure," *JCAP* **1002** (2010) 030, 0912.2358.

[91] M. Kuhlen, M. Lisanti, and D. N. Spergel, "Direct Detection of Dark Matter Debris Flows," *Phys. Rev.* **D86** (2012) 063505, 1202.0007.

[92] S. H. Hansen, B. Moore, M. Zemp, and J. Stadel, "A Universal velocity distribution of relaxed collisionless structures," *JCAP* **0601** (2006) 014, astro-ph/0505420.

[93] J. R. Ellis, A. Ferstl, and K. A. Olive, "Reevaluation of the elastic scattering of supersymmetric dark matter," *Phys. Lett.* **B481** (2000) 304–314, hep-ph/0001005.

[94] G. Jungman, M. Kamionkowski, and K. Griest, "Supersymmetric dark matter," *Phys.Rept.* **267** (1996) 195–373, hep-ph/9506380.

[95] **LUX Collaboration** Collaboration, D. Akerib *et. al.*, "First results from the LUX dark matter experiment at the Sanford Underground Research Facility," *Phys.Rev.Lett.* **112** (2014) 091303, 1310.8214.

[96] **LUX** Collaboration, D. S. Akerib *et. al.*, "Improved Limits on Scattering of Weakly Interacting Massive Particles from Reanalysis of 2013 LUX Data," *Phys. Rev. Lett.* **116** (2016), no. 16, 161301, 1512.03506.

[97] A. Manalaysay, "Dark-matter results from 332 new live-days of lux data." http://lux.brown.edu/LUX_dark_matter/Talks_files/LUX_NewDarkMatterSearchResult_332LiveDays_IDM2016_160721.pdf, July, 2016.

[98] P. A. Amaudruz, M. Batygov, B. Beltran, J. Bonatt, M. Boulay, *et. al.*, "DEAP-3600 Dark Matter Search," 1410.7673.

[99] **XENON1T** Collaboration, E. Aprile, "The XENON1T Dark Matter Search Experiment," *Springer Proc.Phys.* **C12-02-22** (2013) 93–96, 1206.6288.

[100] **DarkSide** Collaboration, T. Alexander *et. al.*, "DarkSide search for dark matter," *JINST* **8** (2013) C11021.

[101] **DARWIN Consortium** Collaboration, L. Baudis, "DARWIN: dark matter WIMP search with noble liquids," *J. Phys. Conf. Ser.* **375** (2012) 012028, 1201.2402.

[102] D. Malling, D. Akerib, H. Araujo, X. Bai, S. Bedikian, *et. al.*, "After LUX: The LZ Program," 1110.0103.

[103] **SuperCDMS** Collaboration, R. Agnese *et. al.*, "Search for Low-Mass Weakly Interacting Massive Particles with SuperCDMS," *Phys. Rev. Lett.* **112** (2014), no. 24, 241302, 1402.7137.

[104] L. Baudis, "WIMP Dark Matter Direct-Detection Searches in Noble Gases," *Phys.Dark Univ.* **4** (2014) 50–59, 1408.4371.

[105] A. K. Drukier, K. Freese, and D. N. Spergel, "Detecting Cold Dark Matter Candidates," *Phys. Rev.* **D33** (1986) 3495–3508.

[106] B. Cabrera, L. M. Krauss, and F. Wilczek, "Bolometric Detection of Neutrinos," *Phys. Rev. Lett.* **55** (1985) 25.

[107] J. Monroe and P. Fisher, "Neutrino Backgrounds to Dark Matter Searches," *Phys. Rev.* **D76** (2007) 033007, 0706.3019.

[108] L. E. Strigari, "Neutrino Coherent Scattering Rates at Direct Dark Matter Detectors," *New J. Phys.* **11** (2009) 105011, 0903.3630.

[109] P. Grothaus, M. Fairbairn, and J. Monroe, "Directional Dark Matter Detection Beyond the Neutrino Bound," *Phys. Rev.* **D90** (2014), no. 5, 055018, 1406.5047.

[110] **DAMA** Collaboration, R. Bernabei *et. al.*, "Search for WIMP annual modulation signature: Results from DAMA / NaI-3 and DAMA / NaI-4 and the global combined analysis," *Phys. Lett.* **B480** (2000) 23–31.

[111] R. Bernabei *et. al.*, "The Annual Modulation Signature for Dark Matter: DAMA/LIBRA-Phase1 Results and Perspectives," *Adv. High Energy Phys.* **2014** (2014) 605659.

[112] **CoGeNT** Collaboration, C. E. Aalseth *et. al.*, "Search for An Annual Modulation in Three Years of CoGeNT Dark Matter Detector Data," 1401.3295.

[113] **CoGeNT** Collaboration, C. Aalseth *et. al.*, "Results from a Search for Light-Mass Dark Matter with a P-type Point Contact Germanium Detector," *Phys.Rev.Lett.* **106** (2011) 131301, 1002.4703.

[114] **CoGeNT** Collaboration, C. Aalseth *et. al.*, "CoGeNT: A Search for Low-Mass Dark Matter using p-type Point Contact Germanium Detectors," *Phys.Rev.* **D88** (2013), no. 1, 012002, 1208.5737.

[115] G. Angloher *et. al.*, "Results from 730 kg days of the CRESST-II Dark Matter Search," *Eur. Phys. J.* **C72** (2012) 1971, 1109.0702.

[116] M. Kuźniak, M. G. Boulay, and T. Pollmann, "Surface roughness interpretation of 730 kg days CRESST-II results," *Astropart. Phys.* **36** (2012) 77–82, 1203.1576.

[117] **CDMS-II** Collaboration, Z. Ahmed *et. al.*, "Search for annual modulation in low-energy CDMS-II data," 1203.1309.

[118] **CDMS** Collaboration, R. Agnese *et. al.*, "Silicon Detector Dark Matter Results from the Final Exposure of CDMS II," *Phys. Rev. Lett.* **111** (2013), no. 25, 251301, 1304.4279.

[119] P. J. Fox, G. D. Kribs, and T. M. P. Tait, "Interpreting Dark Matter Direct Detection Independently of the Local Velocity and Density Distribution," *Phys. Rev.* **D83** (2011) 034007, 1011.1910.

[120] P. J. Fox, J. Liu, and N. Weiner, "Integrating Out Astrophysical Uncertainties," *Phys. Rev.* **D83** (2011) 103514, 1011.1915.

[121] J. Herrero-Garcia, T. Schwetz, and J. Zupan, "Astrophysics independent bounds on the annual modulation of dark matter signals," *Phys. Rev. Lett.* **109** (2012) 141301, 1205.0134.

[122] J. Herrero-Garcia, T. Schwetz, and J. Zupan, "On the annual modulation signal in dark matter direct detection," *JCAP* **1203** (2012) 005, 1112.1627.

[123] D. Hooper, J. Collar, J. Hall, D. McKinsey, and C. Kelso, "A Consistent Dark Matter Interpretation For CoGeNT and DAMA/LIBRA," *Phys.Rev.* **D82** (2010) 123509, 1007.1005.

[124] K. Freese, M. Lisanti, and C. Savage, "Colloquium: Annual modulation of dark matter," *Rev. Mod. Phys.* **85** (2013) 1561–1581, 1209.3339.

[125] E. Del Nobile, G. B. Gelmini, A. Georgescu, and J.-H. Huh, "Reevaluation of spin-dependent WIMP-proton interactions as an explanation of the DAMA data," *JCAP* **1508** (2015), no. 08, 046, 1502.07682.

[126] E. A. Baltz *et. al.*, "Pre-launch estimates for GLAST sensitivity to Dark Matter annihilation signals," *JCAP* **0807** (2008) 013, 0806.2911.

[127] L. Goodenough and D. Hooper, "Possible Evidence For Dark Matter Annihilation In The Inner Milky Way From The Fermi Gamma Ray Space Telescope," 0910.2998.

[128] V. Vitale, A. Morselli, and for the Fermi/LAT Collaboration, "Indirect Search for Dark Matter from the center of the Milky Way with the Fermi-Large Area Telescope," *ArXiv e-prints* (dec, 2009) 0912.3828.

[129] D. Hooper and T. Linden, "On The Origin Of The Gamma Rays From The Galactic Center," *Phys.Rev.* **D84** (2011) 123005, 1110.0006.

[130] A. Geringer-Sameth and S. M. Koushiappas, "Exclusion of canonical WIMPs by the joint analysis of Milky Way dwarfs with Fermi," *Phys.Rev.Lett.* **107** (2011) 241303, 1108.2914.

[131] **Fermi-LAT** Collaboration, M. Ackermann *et. al.*, "Searching for Dark Matter Annihilation from Milky Way Dwarf Spheroidal Galaxies with Six Years of Fermi Large Area Telescope Data," *Phys. Rev. Lett.* **115** (2015), no. 23, 231301, 1503.02641.

[132] E. Bulbul, M. Markevitch, A. Foster, R. K. Smith, M. Loewenstein, *et. al.*, "Detection of An Unidentified Emission Line in the Stacked X-ray spectrum of Galaxy Clusters," *Astrophys.J.* **789** (2014) 13, 1402.2301.

[133] A. Boyarsky, O. Ruchayskiy, D. Iakubovskyi, and J. Franse, "Unidentified Line in X-Ray Spectra of the Andromeda Galaxy and Perseus Galaxy Cluster," *Phys.Rev.Lett.* **113** (2014) 251301, 1402.4119.

[134] H. Ishida, K. S. Jeong, and F. Takahashi, "7 keV sterile neutrino dark matter from split flavor mechanism," *Phys.Lett.* **B732** (2014) 196–200, 1402.5837.

[135] T. Higaki, K. S. Jeong, and F. Takahashi, "The 7 keV axion dark matter and the X-ray line signal," *Phys.Lett.* **B733** (2014) 25–31, 1402.6965.

[136] M. T. Frandsen, F. Sannino, I. M. Shoemaker, and O. Svendsen, "X-ray Lines from Dark Matter: The Good, The Bad, and The Unlikely," *JCAP* **1405** (2014) 033, 1403.1570.

[137] F. Hofmann, J. S. Sanders, K. Nandra, N. Clerc, and M. Gaspari, "7.1 keV sterile neutrino constraints from X-ray observations of 33 clusters of galaxies with Chandra ACIS," 1606.04091.

[138] T. E. Jeltema and S. Profumo, "Deep XMM Observations of Draco rule out at the 99% Confidence Level a Dark Matter Decay Origin for the 3.5 keV Line," *Mon. Not. Roy. Astron. Soc.* **458** (2016), no. 4, 3592–3596, 1512.01239.

[139] **PAMELA** Collaboration, O. Adriani *et. al.*, "An anomalous positron abundance in cosmic rays with energies 1.5-100 GeV," *Nature* **458** (2009) 607–609, 0810.4995.

[140] **AMS** Collaboration, L. Accardo *et. al.*, "High Statistics Measurement of the Positron Fraction in Primary Cosmic Rays of 0.5–500 GeV with the Alpha Magnetic Spectrometer on the International Space Station," *Phys.Rev.Lett.* **113** (2014) 121101.

[141] M. Cirelli, M. Kadastik, M. Raidal, and A. Strumia, "Model-independent implications of the e+-, anti-proton cosmic ray spectra on properties of Dark Matter," *Nucl. Phys.* **B813** (2009) 1–21, 0809.2409. [Addendum: Nucl. Phys.B873,530(2013)].

[142] T. Linden and S. Profumo, "Probing the Pulsar Origin of the Anomalous Positron Fraction with AMS-02 and Atmospheric Cherenkov Telescopes," *Astrophys.J.* **772** (2013) 18, 1304.1791.

[143] W. H. Press and D. N. Spergel, "Capture by the sun of a galactic population of weakly interacting massive particles," *Astrophys. J.* **296** (1985) 679–684.

[144] **IceCube** Collaboration, M. G. Aartsen *et. al.*, "Improved limits on dark matter annihilation in the Sun with the 79-string IceCube detector and implications for supersymmetry," *JCAP* **1604** (2016), no. 04, 022, 1601.00653.

[145] **ANTARES** Collaboration, S. Adrian-Martinez *et. al.*, "Limits on Dark Matter Annihilation in the Sun using the ANTARES Neutrino Telescope," *Phys. Lett.* **B759** (2016) 69–74, 1603.02228.

[146] **Super-Kamiokande** Collaboration, K. Choi *et. al.*, "Search for neutrinos from annihilation of captured low-mass dark matter particles in the Sun by Super-Kamiokande," *Phys. Rev. Lett.* **114** (2015), no. 14, 141301, 1503.04858.

[147] **ATLAS, CMS** Collaboration, D. Zerwas, "Searches for Dark Matter in ATLAS and CMS," *PoS* **EPS-HEP2015** (2015) 150.

[148] **ATLAS** Collaboration, G. Aad *et. al.*, "Search for dark matter candidates and large extra dimensions in events with a jet and missing transverse momentum with the ATLAS detector," *JHEP* **1304** (2013) 075, 1210.4491.

[149] **CMS** Collaboration, S. Chatrchyan *et. al.*, "Search for dark matter and large extra dimensions in monojet events in pp collisions at $\sqrt{s} = 7$ TeV," *JHEP* **1209** (2012) 094, 1206.5663.

[150] G. Busoni, A. De Simone, E. Morgante, and A. Riotto, "On the Validity of the Effective Field Theory for Dark Matter Searches at the LHC," *Phys.Lett.* **B728** (2014) 412–421, 1307.2253.

[151] J. Abdallah *et. al.*, "Simplified Models for Dark Matter Searches at the LHC," *Phys. Dark Univ.* **9-10** (2015) 8–23, 1506.03116.

[152] O. Buchmueller, M. J. Dolan, S. A. Malik, and C. McCabe, "Characterising dark matter searches at colliders and direct detection experiments: Vector mediators," *JHEP* **01** (2015) 037, 1407.8257.

[153] M. E. Peskin and D. V. Schroeder, *An Introduction to quantum field theory.* 1995.

[154] K. Griest and M. Kamionkowski, "Unitarity Limits on the Mass and Radius of Dark Matter Particles," *Phys.Rev.Lett.* **64** (1990) 615.

[155] K. Garrett and G. Duda, "Dark Matter: A Primer," *Adv. Astron.* **2011** (2011) 968283, 1006.2483.

[156] D. Majumdar, *Dark Matter: An Introduction.* CRC Press, 2014.

[157] A. Einstein, "On the electrodynamics of moving bodies," *Annalen Phys.* **17** (1905) 891–921. [Annalen Phys.14,194(2005)].

[158] D. J. Gross, "The role of symmetry in fundamental physics," *Proc. Natl. Acad. Sci.* **93** (1996) 14256–14259.

[159] H. D. Politzer, "Reliable Perturbative Results for Strong Interactions?," *Phys. Rev. Lett.* **30** (1973) 1346–1349.

[160] D. J. Gross and F. Wilczek, "Ultraviolet Behavior of Nonabelian Gauge Theories," *Phys. Rev. Lett.* **30** (1973) 1343–1346.

[161] P. W. Higgs, "Broken Symmetries and the Masses of Gauge Bosons," *Phys. Rev. Lett.* **13** (1964) 508–509.

[162] F. Englert and R. Brout, "Broken Symmetry and the Mass of Gauge Vector Mesons," *Phys. Rev. Lett.* **13** (1964) 321–323.

[163] G. S. Guralnik, C. R. Hagen, and T. W. B. Kibble, "Global Conservation Laws and Massless Particles," *Phys. Rev. Lett.* **13** (1964) 585–587.

[164] P. W. Higgs, "Nobel Lecture: Evading the Goldstone theorem," *Rev. Mod. Phys.* **86** (2014), no. 3, 851.

[165] **CMS** Collaboration, W. de Boer, "The Discovery of the Higgs Boson with the CMS Detector and its Implications for Supersymmetry and Cosmology," in *Time and Matter 2013 (TAM2013) Venice, Italy.* 2013. 1309.0721.

[166] S. Weinberg, "A Model of Leptons," *Phys. Rev. Lett.* **19** (1967) 1264–1266.

[167] S. L. Glashow, "Partial Symmetries of Weak Interactions," *Nucl. Phys.* **22** (1961) 579–588.

[168] A. Salam, "Weak and Electromagnetic Interactions," *Conf. Proc.* **C680519** (1968) 367–377.

[169] **CMS** Collaboration, V. Khachatryan *et. al.*, "Precise determination of the mass of the Higgs boson and tests of compatibility of its couplings with the standard model predictions using proton collisions at 7 and 8 TeV," *Eur. Phys. J.* **C75** (2015), no. 5, 212, 1412.8662.

[170] **ATLAS** Collaboration, G. Aad *et. al.*, "Measurements of the Higgs boson production and decay rates and coupling strengths using pp collision data at $\sqrt{s} = 7$ and 8 TeV in the ATLAS experiment," *Eur. Phys. J.* **C76** (2016), no. 1, 6, 1507.04548.

[171] N. Cabibbo, "Unitary Symmetry and Leptonic Decays," *Phys. Rev. Lett.* **10** (1963) 531–533. [,648(1963)].

[172] M. Kobayashi and T. Maskawa, "CP Violation in the Renormalizable Theory of Weak Interaction," *Prog. Theor. Phys.* **49** (1973) 652–657.

[173] A. Vilenkin and E. P. S. Shellard, *Cosmic Strings and Other Topological Defects*. Cambridge University Press, 2000.

[174] Ya. B. Zeldovich, I. Yu. Kobzarev, and L. B. Okun, "Cosmological Consequences of the Spontaneous Breakdown of Discrete Symmetry," *Zh. Eksp. Teor. Fiz.* **67** (1974) 3–11. [Sov. Phys. JETP40,1(1974)].

[175] A. Vilenkin, "Cosmic Strings and Domain Walls," *Phys. Rept.* **121** (1985) 263–315.

[176] A. Vilenkin, "Gravitational Field of Vacuum Domain Walls and Strings," *Phys. Rev.* **D23** (1981) 852–857.

[177] Ya. B. Zeldovich and M. Yu. Khlopov, "On the Concentration of Relic Magnetic Monopoles in the Universe," *Phys. Lett.* **B79** (1978) 239–241.

[178] R. H. Brandenberger, "Topological defects and structure formation," *Int. J. Mod. Phys.* **A9** (1994) 2117–2190, `astro-ph/9310041`.

[179] M. B. Hindmarsh and T. W. B. Kibble, "Cosmic strings," *Rept. Prog. Phys.* **58** (1995) 477–562, `hep-ph/9411342`.

[180] G. Lazarides and Q. Shafi, "Axion Models with No Domain Wall Problem," *Phys. Lett.* **B115** (1982) 21–25.

[181] A. Vilenkin and A. E. Everett, "Cosmic Strings and Domain Walls in Models with Goldstone and PseudoGoldstone Bosons," *Phys. Rev. Lett.* **48** (1982) 1867–1870.

[182] H. B. Nielsen and P. Olesen, "Vortex Line Models for Dual Strings," *Nucl. Phys.* **B61** (1973) 45–61.

[183] M. R. Anderson, *The mathematical theory of cosmic strings: Cosmic strings in the wire approximation*. 2003.

[184] N. Kaiser and A. Stebbins, "Microwave Anisotropy Due to Cosmic Strings," *Nature* **310** (1984) 391–393.

[185] Ya. B. Zeldovich, "Cosmological fluctuations produced near a singularity," *Mon. Not. Roy. Astron. Soc.* **192** (1980) 663–667.

[186] A. Vilenkin, "Cosmic Strings," *Phys. Rev.* **D24** (1981) 2082–2089.

[187] **Boomerang** Collaboration, P. de Bernardis *et. al.*, "A Flat universe from high resolution maps of the cosmic microwave background radiation," *Nature* **404** (2000) 955–959, astro-ph/0004404.

[188] S. Hanany *et. al.*, "MAXIMA-1: A Measurement of the cosmic microwave background anisotropy on angular scales of 10 arcminutes to 5 degrees," *Astrophys. J.* **545** (2000) L5, astro-ph/0005123.

[189] L. Perivolaropoulos, "The Rise and fall of the cosmic string theory for cosmological perturbations," *Nucl. Phys. Proc. Suppl.* **148** (2005) 128–140, astro-ph/0501590.

[190] C. Dvorkin, M. Wyman, and W. Hu, "Cosmic String constraints from WMAP and the South Pole Telescope," *Phys. Rev.* **D84** (2011) 123519, 1109.4947.

[191] M. Wyman, L. Pogosian, and I. Wasserman, "Bounds on cosmic strings from WMAP and SDSS," *Phys. Rev.* **D72** (2005) 023513, astro-ph/0503364. [Erratum: Phys. Rev.D73,089905(2006)].

[192] N. Bevis, M. Hindmarsh, M. Kunz, and J. Urrestilla, "Fitting CMB data with cosmic strings and inflation," *Phys. Rev. Lett.* **100** (2008) 021301, astro-ph/0702223.

[193] R. Battye, B. Garbrecht, and A. Moss, "Tight constraints on F- and D-term hybrid inflation scenarios," *Phys. Rev.* **D81** (2010) 123512, 1001.0769.

[194] R. Battye and A. Moss, "Updated constraints on the cosmic string tension," *Phys. Rev.* **D82** (2010) 023521, 1005.0479.

[195] **Planck Collaboration** Collaboration, P. Ade *et. al.*, "Planck 2013 results. XXV. Searches for cosmic strings and other topological defects," 1303.5085.

[196] E. Witten, "Cosmic Superstrings," *Phys. Lett.* **B153** (1985) 243–246.

[197] S. Sarangi and S. H. H. Tye, "Cosmic string production towards the end of brane inflation," *Phys. Lett.* **B536** (2002) 185–192, hep-th/0204074.

[198] M. Sakellariadou, "Cosmic Strings and Cosmic Superstrings," *Nucl. Phys. Proc. Suppl.* **192-193** (2009) 68–90, 0902.0569.

[199] J. Polchinski, "Introduction to cosmic F- and D-strings," in *String theory: From gauge interactions to cosmology. Proceedings, NATO Advanced Study Institute, Cargese, France, June 7-19, 2004*, pp. 229–253. 2004. hep-th/0412244.

[200] M. Sakellariadou, "Cosmic Superstrings," *Phil. Trans. Roy. Soc. Lond.* **A366** (2008) 2881–2894, 0802.3379.

[201] R. Jeannerot, J. Rocher, and M. Sakellariadou, "How generic is cosmic string formation in SUSY GUTs," *Phys. Rev.* **D68** (2003) 103514, hep-ph/0308134.

[202] S. A. Abel, M. D. Goodsell, J. Jaeckel, V. V. Khoze, and A. Ringwald, "Kinetic Mixing of the Photon with Hidden U(1)s in String Phenomenology," *JHEP* **07** (2008) 124, 0803.1449.

[203] M. Goodsell and A. Ringwald, "Light Hidden-Sector U(1)s in String Compactifications," *Fortsch. Phys.* **58** (2010) 716–720, 1002.1840.

[204] E. Dudas and E. Palti, "On hypercharge flux and exotics in F-theory GUTs," *JHEP* **09** (2010) 013, 1007.1297.

[205] E. Witten, "Superconducting Strings," *Nucl. Phys.* **B249** (1985) 557–592.

[206] T. Vachaspati, "Cosmic Rays from Cosmic Strings with Condensates," *Phys. Rev.* **D81** (2010) 043531, 0911.2655.

[207] D. Haws, M. Hindmarsh, and N. Turok, "SUPERCONDUCTING STRINGS OR SPRINGS?," *Phys. Lett.* **B209** (1988) 255–261.

[208] F. London and H. London, "The Electromagnetic Equations of the Supraconductor," *Proceedings of the Royal Society of London Series A* **149** (Mar., 1935) 71–88.

[209] R. Jackiw and P. Rossi, "Zero Modes of the Vortex - Fermion System," *Nucl. Phys.* **B190** (1981) 681.

[210] R. L. Davis and E. P. S. Shellard, "The Physics of Vortex Superconductivity," *Phys. Lett.* **B207** (1988) 404–410.

[211] R. L. Davis and E. P. S. Shellard, "The Physics of Vortex Superconductivity. 2," *Phys. Lett.* **B209** (1988) 485–490.

[212] T. Damour and A. Vilenkin, "Gravitational wave bursts from cosmic strings," *Phys. Rev. Lett.* **85** (2000) 3761–3764, gr-qc/0004075.

[213] T. Damour and A. Vilenkin, "Gravitational radiation from cosmic (super)strings: Bursts, stochastic background, and observational windows," *Phys. Rev.* **D71** (2005) 063510, hep-th/0410222.

[214] S. Olmez, V. Mandic, and X. Siemens, "Gravitational-Wave Stochastic Background from Kinks and Cusps on Cosmic Strings," *Phys. Rev.* **D81** (2010) 104028, 1004.0890.

[215] G. Vincent, N. D. Antunes, and M. Hindmarsh, "Numerical simulations of string networks in the Abelian Higgs model," *Phys. Rev. Lett.* **80** (1998) 2277–2280, hep-ph/9708427.

[216] J. N. Moore, E. P. S. Shellard, and C. J. A. P. Martins, "On the evolution of Abelian-Higgs string networks," *Phys. Rev.* **D65** (2002) 023503, hep-ph/0107171.

[217] N. Bevis, M. Hindmarsh, M. Kunz, and J. Urrestilla, "CMB power spectrum contribution from cosmic strings using field-evolution simulations of the Abelian Higgs model," *Phys.Rev.* **D75** (2007) 065015, astro-ph/0605018.

[218] M. Hindmarsh, S. Stuckey, and N. Bevis, "Abelian Higgs Cosmic Strings: Small Scale Structure and Loops," *Phys. Rev.* **D79** (2009) 123504, 0812.1929.

[219] E. J. Copeland, L. Pogosian, and T. Vachaspati, "Seeking String Theory in the Cosmos," *Class. Quant. Grav.* **28** (2011) 204009, 1105.0207.

[220] K.-i. Maeda and N. Turok, "Finite Width Corrections to the Nambu Action for the Nielsen-Olesen String," *Phys. Lett.* **B202** (1988) 376–380.

[221] T. W. B. Kibble, "Topology of Cosmic Domains and Strings," *J. Phys.* **A9** (1976) 1387–1398.

[222] T. Vachaspati, "Lectures on cosmic topological defects," in *ICTP Summer School on Astroparticle Physics and Cosmology Miramare, Trieste, Italy, June 12-July 7, 2000.* 2000. hep-ph/0101270.

[223] M. Hindmarsh, "Signals of Inflationary Models with Cosmic Strings," *Prog. Theor. Phys. Suppl.* **190** (2011) 197–228, 1106.0391.

[224] R. Jeannerot, X. Zhang, and R. H. Brandenberger, "Non-thermal production of neutralino cold dark matter from cosmic string decays," *JHEP* **12** (1999) 003, hep-ph/9901357.

[225] P. Bhattacharjee and G. Sigl, "Origin and propagation of extremely high-energy cosmic rays," *Phys. Rept.* **327** (2000) 109–247, astro-ph/9811011.

[226] P. Bhattacharjee, Q. Shafi, and F. Stecker, "TeV and superheavy mass scale particles from supersymmetric topological defects, the extragalactic gamma-ray background, and the highest energy cosmic rays," *Phys.Rev.Lett.* **80** (1998) 3698–3701, hep-ph/9710533.

[227] **Fermi-LAT** Collaboration, W. B. Atwood *et. al.*, "The Large Area Telescope on the Fermi Gamma-ray Space Telescope Mission," *Astrophys. J.* **697** (2009) 1071–1102, 0902.1089.

[228] A. Drlica-Wagner, "Searching for dark matter in dwarf spheroidal satellite galaxies with the fermi-lat." http://fermi.gsfc.nasa.gov/science/mtgs/symposia/2012/program/fri/ADrlica-Wagner.pdf. [On behalf of Fermi-LAT collaboration at Fermi symposium 2012].

[229] J. D. Simon and M. Geha, "The Kinematics of the Ultra-Faint Milky Way Satellites: Solving the Missing Satellite Problem," *Astrophys. J.* **670** (2007) 313–331, 0706.0516.

[230] M. G. Walker, M. Mateo, E. W. Olszewski, J. Penarrubia, N. W. Evans, and G. Gilmore, "A Universal Mass Profile for Dwarf Spheroidal Galaxies," *Astrophys. J.* **704** (2009) 1274–1287, 0906.0341. [Erratum: Astrophys. J.710,886(2010)].

[231] D. Hooper, C. Kelso, and F. S. Queiroz, "Stringent and Robust Constraints on the Dark Matter Annihilation Cross Section From the Region of the Galactic Center," *Astropart. Phys.* **46** (2013) 55–70, 1209.3015.

[232] D. Hooper and L. Goodenough, "Dark Matter Annihilation in The Galactic Center As Seen by the Fermi Gamma Ray Space Telescope," *Phys. Lett.* **B697** (2011) 412–428, 1010.2752.

[233] M. Cirelli, N. Fornengo, and A. Strumia, "Minimal dark matter," *Nucl. Phys.* **B753** (2006) 178–194, hep-ph/0512090.

[234] M. Cirelli, A. Strumia, and M. Tamburini, "Cosmology and Astrophysics of Minimal Dark Matter," *Nucl. Phys.* **B787** (2007) 152–175, 0706.4071.

[235] E. Ma, "Verifiable radiative seesaw mechanism of neutrino mass and dark matter," *Phys. Rev.* **D73** (2006) 077301, hep-ph/0601225.

[236] R. Barbieri, L. J. Hall, and V. S. Rychkov, "Improved naturalness with a heavy Higgs: An Alternative road to LHC physics," *Phys. Rev.* **D74** (2006) 015007, hep-ph/0603188.

[237] L. Lopez Honorez, E. Nezri, J. F. Oliver, and M. H. G. Tytgat, "The Inert Doublet Model: An Archetype for Dark Matter," *JCAP* **0702** (2007) 028, hep-ph/0612275.

[238] P. Ko, Y. Omura, and C. Yu, "Dark matter and dark force in the type-I inert 2HDM with local $\mathrm{U}(1)_H$ gauge symmetry," *JHEP* **11** (2014) 054, 1405.2138.

[239] P. Ko, Y. Omura, and C. Yu, "Two Higgs doublet models with local $U(1)_H$ gauge symmetry and dark matter," 1406.1952.

[240] G. C. Branco, P. M. Ferreira, L. Lavoura, M. N. Rebelo, M. Sher, and J. P. Silva, "Theory and phenomenology of two-Higgs-doublet models," *Phys. Rept.* **516** (2012) 1–102, 1106.0034.

[241] M. E. Peskin and T. Takeuchi, "A New constraint on a strongly interacting Higgs sector," *Phys.Rev.Lett.* **65** (1990) 964–967.

[242] M. E. Peskin and T. Takeuchi, "Estimation of oblique electroweak corrections," *Phys.Rev.* **D46** (1992) 381–409.

[243] T. Takeuchi, "Estimation of oblique electroweak corrections," in *International Workshop on Electroweak Symmetry Breaking Hiroshima, Japan, November 12-15, 1991*. 1992.

[244] **Gfitter Group** Collaboration, M. Baak *et. al.*, "The global electroweak fit at NNLO and prospects for the LHC and ILC," *Eur.Phys.J.* **C74** (2014), no. 9, 3046, 1407.3792.

[245] H. F. Santana Mota and M. Hindmarsh, "Big-Bang Nucleosynthesis and Gamma-Ray Constraints on Cosmic Strings with a large Higgs condensate," *Phys. Rev.* **D91** (2015), no. 4, 043001, 1407.3599.

[246] G. Belanger, F. Boudjema, A. Pukhov, and A. Semenov, "micrOMEGAs_3: A program for calculating dark matter observables," *Comput.Phys.Commun.* **185** (2014) 960–985, 1305.0237.

[247] S. Galli, F. Iocco, G. Bertone, and A. Melchiorri, "CMB constraints on Dark Matter models with large annihilation cross-section," *Phys.Rev.* **D80** (2009) 023505, 0905.0003.

[248] A. De Simone, G. F. Giudice, and A. Strumia, "Benchmarks for Dark Matter Searches at the LHC," *JHEP* **1406** (2014) 081, 1402.6287.

[249] **ATLAS Collaboration** Collaboration, G. Aad *et. al.*, "Search for direct production of charginos and neutralinos in events with three leptons and missing transverse momentum in $\sqrt{s} = 8$TeV pp collisions with the ATLAS detector," *JHEP* **1404** (2014) 169, 1402.7029.

[250] **ATLAS** Collaboration, G. Aad *et. al.*, "Observation of a new particle in the search for the Standard Model Higgs boson with the ATLAS detector at the LHC," *Phys. Lett.* **B716** (2012) 1–29, 1207.7214.

[251] **CMS** Collaboration, S. Chatrchyan *et. al.*, "Observation of a new boson at a mass of 125 GeV with the CMS experiment at the LHC," *Phys. Lett.* **B716** (2012) 30–61, 1207.7235.

[252] **CMS** Collaboration, V. Khachatryan *et. al.*, "Observation of the diphoton decay of the Higgs boson and measurement of its properties," *Eur. Phys. J.* **C74** (2014), no. 10, 3076, 1407.0558.

[253] **ATLAS** Collaboration, G. Aad *et. al.*, "Measurement of Higgs boson production in the diphoton decay channel in pp collisions at center-of-mass energies of 7 and 8 TeV with the ATLAS detector," *Phys. Rev.* **D90** (2014), no. 11, 112015, 1408.7084.

[254] B. Swiezewska and M. Krawczyk, "Diphoton rate in the inert doublet model with a 125 GeV Higgs boson," *Phys.Rev.* **D88** (2013), no. 3, 035019, 1212.4100.

[255] E. Lundstrom, M. Gustafsson, and J. Edsjo, "The Inert Doublet Model and LEP II Limits," *Phys.Rev.* **D79** (2009) 035013, 0810.3924.

[256] A. Pierce and J. Thaler, "Natural Dark Matter from an Unnatural Higgs Boson and New Colored Particles at the TeV Scale," *JHEP* **0708** (2007) 026, hep-ph/0703056.

[257] J. H. MacGibbon and R. H. Brandenberger, "High-energy neutrino flux from ordinary cosmic strings," *Nucl. Phys.* **B331** (1990) 153–172.

[258] G. Sigl, K. Jedamzik, D. N. Schramm, and V. S. Berezinsky, "Helium photodisintegration and nucleosynthesis: Implications for topological defects, high-energy cosmic rays, and massive black holes," *Phys. Rev.* **D52** (1995) 6682–6693, astro-ph/9503094.

[259] U. F. Wichoski, J. H. MacGibbon, and R. H. Brandenberger, "High-energy neutrinos, photons and cosmic ray fluxes from VHS cosmic strings," *Phys. Rev.* **D65** (2002) 063005, hep-ph/9805419.

[260] A. J. Long and T. Vachaspati, "Cosmic Strings in Hidden Sectors: 2. Cosmological and Astrophysical Signatures," *JCAP* **1412** (2014), no. 12, 040, 1409.6979.

[261] V. Berezinsky, E. Sabancilar, and A. Vilenkin, "Extremely High Energy Neutrinos from Cosmic Strings," *Phys. Rev.* **D84** (2011) 085006, 1108.2509.

[262] M. Kawasaki, K. Kohri, and T. Moroi, "Big-Bang nucleosynthesis and hadronic decay of long-lived massive particles," *Phys.Rev.* **D71** (2005) 083502, astro-ph/0408426.

[263] **Fermi-LAT collaboration** Collaboration, A. Abdo *et. al.*, "The Spectrum of the Isotropic Diffuse Gamma-Ray Emission Derived From First-Year Fermi Large Area Telescope Data," *Phys.Rev.Lett.* **104** (2010) 101101, 1002.3603.

[264] V. Berezinsky, A. Gazizov, M. Kachelriess, and S. Ostapchenko, "Restricting UHECRs and cosmogenic neutrinos with Fermi-LAT," *Phys.Lett.* **B695** (2011) 13–18, 1003.1496.

[265] C. Gordon and O. Macias, "Dark Matter and Pulsar Model Constraints from Galactic Center Fermi-LAT Gamma Ray Observations," *Phys.Rev.* **D88** (2013), no. 8, 083521, 1306.5725.

[266] T. Daylan, D. P. Finkbeiner, D. Hooper, T. Linden, S. K. N. Portillo, N. L. Rodd, and T. R. Slatyer, "The characterization of the gamma-ray signal from the central Milky Way: A case for annihilating dark matter," *Phys. Dark Univ.* **12** (2016) 1–23, 1402.6703.

[267] F. Calore, I. Cholis, and C. Weniger, "Background model systematics for the Fermi GeV excess," *JCAP* **1503** (2015) 038, 1409.0042.

[268] K. N. Abazajian and M. Kaplinghat, "Detection of a Gamma-Ray Source in the Galactic Center Consistent with Extended Emission from Dark Matter Annihilation and Concentrated Astrophysical Emission," *Phys. Rev.* **D86** (2012) 083511, 1207.6047. [Erratum: Phys. Rev.D87,129902(2013)].

[269] D. Hooper and T. R. Slatyer, "Two Emission Mechanisms in the Fermi Bubbles: A Possible Signal of Annihilating Dark Matter," *Phys. Dark Univ.* **2** (2013) 118–138, 1302.6589.

[270] D. Hooper, I. Cholis, T. Linden, J. Siegal-Gaskins, and T. Slatyer, "Pulsars Cannot Account for the Inner Galaxy's GeV Excess," *Phys. Rev.* **D88** (2013) 083009, 1305.0830.

[271] I. Cholis, D. Hooper, and T. Linden, "Challenges in Explaining the Galactic Center Gamma-Ray Excess with Millisecond Pulsars," *JCAP* **1506** (2015), no. 06, 043, 1407.5625.

[272] N. Mirabal, "Dark matter vs. Pulsars: Catching the impostor," *Mon. Not. Roy. Astron. Soc.* **436** (2013) 2461, 1309.3428.

[273] Q. Yuan and B. Zhang, "Millisecond pulsar interpretation of the Galactic center gamma-ray excess," *JHEAp* **3-4** (2014) 1–8, 1404.2318.

[274] J. Petrović, P. D. Serpico, and G. Zaharijas, "Millisecond pulsars and the Galactic Center gamma-ray excess: the importance of luminosity function and secondary emission," *JCAP* **1502** (2015), no. 02, 023, 1411.2980.

[275] K. N. Abazajian and R. E. Keeley, "Bright gamma-ray Galactic Center excess and dark dwarfs: Strong tension for dark matter annihilation despite Milky Way halo profile and diffuse emission uncertainties," *Phys. Rev.* **D93** (2016), no. 8, 083514, 1510.06424.

[276] J. Choquette, J. M. Cline, and J. M. Cornell, "P-wave Annihilating Dark Matter from a Decaying Predecessor and the Galactic Center Excess," 1604.01039.

[277] M. Abdullah, A. DiFranzo, A. Rajaraman, T. M. P. Tait, P. Tanedo, and A. M. Wijangco, "Hidden on-shell mediators for the Galactic Center γ-ray excess," *Phys. Rev.* **D90** (2014) 035004, 1404.6528.

[278] A. Ibarra, S. Lopez Gehler, and M. Pato, "Dark matter constraints from box-shaped gamma-ray features," *JCAP* **1207** (2012) 043, 1205.0007.

[279] J. Mardon, Y. Nomura, D. Stolarski, and J. Thaler, "Dark Matter Signals from Cascade Annihilations," *JCAP* **0905** (2009) 016, 0901.2926.

[280] J. M. Cline, G. Dupuis, Z. Liu, and W. Xue, "Multimediator models for the galactic center gamma ray excess," *Phys. Rev.* **D91** (2015), no. 11, 115010, 1503.08213.

[281] G. Elor, N. L. Rodd, and T. R. Slatyer, "Multistep cascade annihilations of dark matter and the Galactic Center excess," *Phys. Rev.* **D91** (2015) 103531, 1503.01773.

[282] J. F. Navarro, C. S. Frenk, and S. D. M. White, "The Structure of cold dark matter halos," *Astrophys. J.* **462** (1996) 563–575, astro-ph/9508025.

[283] J. F. Navarro, C. S. Frenk, and S. D. M. White, "A Universal density profile from hierarchical clustering," *Astrophys. J.* **490** (1997) 493–508, astro-ph/9611107.

[284] F. Iocco, M. Pato, G. Bertone, and P. Jetzer, "Dark Matter distribution in the Milky Way: microlensing and dynamical constraints," *JCAP* **1111** (2011) 029, 1107.5810.

[285] R. Catena and P. Ullio, "A novel determination of the local dark matter density," *JCAP* **1008** (2010) 004, 0907.0018.

[286] M. Cirelli, G. Corcella, A. Hektor, G. Hutsi, M. Kadastik, P. Panci, M. Raidal, F. Sala, and A. Strumia, "PPPC 4 DM ID: A Poor Particle Physicist Cookbook for Dark Matter Indirect Detection," *JCAP* **1103** (2011) 051, 1012.4515. [Erratum: JCAP1210,E01(2012)].

[287] P. Ciafaloni, D. Comelli, A. Riotto, F. Sala, A. Strumia, and A. Urbano, "Weak Corrections are Relevant for Dark Matter Indirect Detection," *JCAP* **1103** (2011) 019, 1009.0224.

[288] J. Binney and T. Piffl, "The distribution function of the Galaxy's dark halo," *Mon. Not. Roy. Astron. Soc.* **454** (2015), no. 4, 3653–3663, 1509.06877.

[289] F. Chen, J. M. Cline, A. Fradette, A. R. Frey, and C. Rabideau, "Exciting dark matter in the galactic center," *Phys. Rev.* **D81** (2010) 043523, 0911.2222.

[290] J. F. Navarro, A. Ludlow, V. Springel, J. Wang, M. Vogelsberger, S. D. M. White, A. Jenkins, C. S. Frenk, and A. Helmi, "The Diversity and Similarity of Cold Dark Matter Halos," *Mon. Not. Roy. Astron. Soc.* **402** (2010) 21, 0810.1522.

[291] M. Cirelli and J. M. Cline, "Can multistate dark matter annihilation explain the high-energy cosmic ray lepton anomalies?," *Phys. Rev.* **D82** (2010) 023503, 1005.1779.

[292] P. Agrawal, B. Batell, P. J. Fox, and R. Harnik, "WIMPs at the Galactic Center," *JCAP* **1505** (2015) 011, 1411.2592.

[293] M. Girardi, D. Fadda, G. Giuricin, F. Mardirossian, M. Mezzetti, and A. Biviano, "Velocity dispersions and x-ray temperatures of galaxy cluster," *Astrophys. J.* **457** (1996) 61–76, astro-ph/9507031.

[294] **Fermi-LAT** Collaboration, M. Ackermann *et. al.*, "Search for extended gamma-ray emission from the Virgo galaxy cluster with Fermi-LAT," *Astrophys. J.* **812** (2015), no. 2, 159, 1510.00004.

[295] M. Hindmarsh, "Signals of Inflationary Models with Cosmic Strings," *Prog.Theor.Phys.Suppl.* **190** (2011) 197–228, 1106.0391.

[296] J. J. Blanco-Pillado, K. D. Olum, and B. Shlaer, "The number of cosmic string loops," *Phys. Rev.* **D89** (2014), no. 2, 023512, 1309.6637.

[297] J. M. Hyde, A. J. Long, and T. Vachaspati, "Dark Strings and their Couplings to the Standard Model," *Phys.Rev.* **D89** (2014) 065031, 1312.4573.

[298] G. Krnjaic and K. Sigurdson, "Big Bang Darkleosynthesis," 1406.1171.

[299] W. Detmold, M. McCullough, and A. Pochinsky, "Dark Nuclei I: Cosmology and Indirect Detection," 1406.2276.

[300] M. B. Wise and Y. Zhang, "Stable Bound States of Asymmetric Dark Matter," *Phys. Rev.* **D90** (2014), no. 5, 055030, 1407.4121. [Erratum: Phys. Rev.D91,no.3,039907(2015)].

[301] M. B. Wise and Y. Zhang, "Yukawa Bound States of a Large Number of Fermions," *JHEP* **02** (2015) 023, 1411.1772.

[302] E. Hardy, R. Lasenby, J. March-Russell, and S. M. West, "Big Bang Synthesis of Nuclear Dark Matter," *JHEP* **06** (2015) 011, 1411.3739.

[303] E. Hardy, R. Lasenby, J. March-Russell, and S. M. West, "Signatures of Large Composite Dark Matter States," *JHEP* **07** (2015) 133, 1504.05419.

[304] M. Pospelov and A. Ritz, "Astrophysical Signatures of Secluded Dark Matter," *Phys.Lett.* **B671** (2009) 391–397, 0810.1502.

[305] J. D. March-Russell and S. M. West, "WIMPonium and Boost Factors for Indirect Dark Matter Detection," *Phys.Lett.* **B676** (2009) 133–139, 0812.0559.

[306] W. Shepherd, T. M. Tait, and G. Zaharijas, "Bound states of weakly interacting dark matter," *Phys.Rev.* **D79** (2009) 055022, 0901.2125.

[307] R. Laha and E. Braaten, "Direct detection of dark matter in universal bound states," *Phys.Rev.* **D89** (2014), no. 10, 103510, 1311.6386.

[308] R. Laha, "Directional detection of dark matter in universal bound states," *Phys. Rev.* **D92** (2015), no. 8, 083509, 1505.02772.

[309] D. E. Kaplan, G. Z. Krnjaic, K. R. Rehermann, and C. M. Wells, "Atomic Dark Matter," *JCAP* **1005** (2010) 021, 0909.0753.

[310] J. A. Frieman, G. B. Gelmini, M. Gleiser, and E. W. Kolb, "Solitogenesis: Primordial Origin of Nontopological Solitons," *Phys. Rev. Lett.* **60** (1988) 2101.

[311] A. Kusenko and M. E. Shaposhnikov, "Supersymmetric Q balls as dark matter," *Phys. Lett.* **B418** (1998) 46–54, hep-ph/9709492.

[312] S. Nussinov, "TECHNOCOSMOLOGY: COULD A TECHNIBARYON EXCESS PROVIDE A 'NATURAL' MISSING MASS CANDIDATE?," *Phys. Lett.* **B165** (1985) 55.

[313] R. S. Chivukula and T. P. Walker, "TECHNICOLOR COSMOLOGY," *Nucl. Phys.* **B329** (1990) 445.

[314] G. Gelmini, A. Kusenko, and S. Nussinov, "Experimental identification of nonpointlike dark matter candidates," *Phys. Rev. Lett.* **89** (2002) 101302, hep-ph/0203179.

[315] J. F. Cherry, M. T. Frandsen, and I. M. Shoemaker, "Halo Independent Direct Detection of Momentum-Dependent Dark Matter," *JCAP* **1410** (2014), no. 10, 022, 1405.1420.

[316] **XENON** Collaboration, E. Aprile *et. al.*, "Physics reach of the XENON1T dark matter experiment," *JCAP* **1604** (2016), no. 04, 027, 1512.07501.

[317] R. H. Helm, "Inelastic and Elastic Scattering of 187-Mev Electrons from Selected Even-Even Nuclei," *Phys. Rev.* **104** (1956) 1466–1475.

[318] J. Lewin and P. Smith, "Review of mathematics, numerical factors, and corrections for dark matter experiments based on elastic nuclear recoil," *Astropart.Phys.* **6** (1996) 87–112.

[319] M. Selvi. Private Communications.

[320] **LUX** Collaboration, D. S. Akerib *et. al.*, "Tritium calibration of the LUX dark matter experiment," *Phys. Rev.* **D93** (2016), no. 7, 072009, 1512.03133.

[321] J. Lindhard, V. Nielsen, M. Scharff, and P. V. Thomsen, "Integral Equations Governing Radiation Effects," *Kong.Dan.Vid.Sel.Mat.Fys.Med.* **33** (1963), no. 10, 1–42.

[322] J. March-Russell, J. Unwin, and S. M. West, "Closing in on Asymmetric Dark Matter I: Model independent limits for interactions with quarks," *JHEP* **08** (2012) 029, 1203.4854.

[323] T. W. B. Kibble, "Some Implications of a Cosmological Phase Transition," *Phys. Rept.* **67** (1980) 183.

[324] N. Bevis, M. Hindmarsh, M. Kunz, and J. Urrestilla, "CMB power spectra from cosmic strings: predictions for the Planck satellite and beyond," *Phys.Rev.* **D82** (2010) 065004, 1005.2663.

[325] J. J. Blanco-Pillado, K. D. Olum, and B. Shlaer, "Large parallel cosmic string simulations: New results on loop production," *Phys. Rev.* **D83** (2011) 083514, 1101.5173.

[326] T. Vachaspati, A. E. Everett, and A. Vilenkin, "Radiation From Vacuum Strings and Domain Walls," *Phys. Rev.* **D30** (1984) 2046.

[327] M. Srednicki and S. Theisen, "Nongravitational Decay of Cosmic Strings," *Phys. Lett.* **B189** (1987) 397.

[328] A. Vilenkin, "Gravitational radiation from cosmic strings," *Phys. Lett.* **B107** (1981) 47–50.

[329] R. H. Brandenberger, "On the Decay of Cosmic String Loops," *Nucl. Phys.* **B293** (1987) 812–828.

[330] J. J. Blanco-Pillado and K. D. Olum, "The Form of cosmic string cusps," *Phys. Rev.* **D59** (1999) 063508, gr-qc/9810005.

[331] T. Damour and A. Vilenkin, "Cosmic strings and the string dilaton," *Phys. Rev. Lett.* **78** (1997) 2288–2291, gr-qc/9610005.

[332] L. Lopez Honorez and C. E. Yaguna, "A new viable region of the inert doublet model," *JCAP* **1101** (2011) 002, 1011.1411.

[333] D. G. Cerdeno, M. Fornasa, A. M. Green, and M. Peiro, "How to calculate dark matter direct detection exclusion limits that are consistent with gamma rays from annihilation in the Milky Way halo," 1605.05185.

[334] T. Lin, E. W. Kolb, and L.-T. Wang, "Probing dark matter couplings to top and bottom quarks at the LHC," *Phys. Rev.* **D88** (2013), no. 6, 063510, 1303.6638.

[335] O. Buchmueller, M. J. Dolan, and C. McCabe, "Beyond Effective Field Theory for Dark Matter Searches at the LHC," *JHEP* **01** (2014) 025, 1308.6799.

[336] A. Falkowski, C. Gross, and O. Lebedev, "A second Higgs from the Higgs portal," *JHEP* **05** (2015) 057, 1502.01361.

[337] T. Robens and T. Stefaniak, "Status of the Higgs Singlet Extension of the Standard Model after LHC Run 1," *Eur. Phys. J.* **C75** (2015) 104, 1501.02234.